# Planet Mercury: volatile release on a contracting world

## Thesis

# Planet Mercury:

## volatile release on a contracting world

Rebecca J. Thomas

BSc, MA (Hons)

Submitted 4th September 2015

A thesis submitted to the Open University in the subject of Planetary Science for the degree of Doctor of Philosophy.

Department of Physical Sciences

Open University

χαῖρ᾽. Ἑρμῆ χαριδῶτα, διάκτορε, δῶτορ ἐάων.

Hail, Hermes, giver of grace, guide, and giver of good things

Anonymous (English translation by H. G. Evelyn-White) (1914), Hymn 18 to Hermes, in The Homeric Hymns and Homerica, Harvard University Press, Cambridge, MA.

# Abstract

This thesis investigates the geological processes by which materials containing high concentrations of volatile substances have been delivered to the surface of the planet Mercury throughout its history, despite global contraction, which could be expected to impede the replenishment of these materials from depth. With the aid of high-resolution data from the MESSENGER (MErcury Surface, Space ENvironment, GEochemistry, and Ranging) spacecraft, I perform detailed analyses of the two types of geological features most indicative of the action of volatiles at Mercury's surface: flat-floored depressions known as 'hollows', and pits and deposits thought to be the products of explosive volcanism. For hollows, I seek to clarify the nature of the substance lost to form them and the mechanisms by which this has been introduced to, and lost from, the surface recently enough to explain their pristine appearance. I produce a global catalogue of hollows, study their local associations, and investigate their spectral character, finding evidence that they form primarily by sublimation of a moderately volatile substance, potentially a sulfide, from a specific low-reflectance substrate exhumed and exposed by meteorite impacts. To better understand explosive volcanism, I investigate its longevity and the processes promoting it at specific locations. Through identifying, dating and characterising proposed pyroclastic deposits and vents, I show that putative explosive volcanism was more long-lived than voluminous effusive eruptions, that its occurrence is tectonically controlled, and that its eruptive style indicates magma storage prior to eruption, at greater depths than on the more tectonically-neutral Moon. This indicates that, rather than precluding it, global contraction favoured volcanic explosivity by promoting magma storage during which volatiles could become concentrated in the magma. Furthermore, because processes concentrating volatiles have been important in the genesis of both hollows and explosive volcanism, their occurrence does not necessarily indicate a high planetary bulk volatile fraction.

# Acknowledgements

I extend my deepest thanks to my PhD supervisors: David Rothery, for curing me of 'which'-ery, Susan Conway, not only a GIS-guru but bringer of pork scratchings, Mahesh Anand for his gems of insight, and all of three for their unfailing help and support.

Thanks also to the MESSENGER team for the stunning data I've had the privilege to work with in the course of my PhD. Credit for excerpts from global mosaics used in figures in this thesis goes to NASA/Johns Hopkins University Applied Physics Laboratory/Carnegie Institution of Washington, and for NAC and WAC images, to NASA/JPL-Caltech. In particular, my thanks to Noam Izenberg, Dave Blewett and Larry Nittler for the collaboration that inspired Chapter 3, and to Peter James for providing me with his global crustal thickness model, so useful for Chapter 6.

My thanks go to Matteo Massironi, Alice Lucchetti and Gabriele Cremonese at the University and Astronomical Observatory of Padova for our fascinating and fruitful collaboration, and particularly to Matteo for his invaluable guidance and for taking such good care of me in Italy. Thanks also to Simone Marchi of the Solar System Exploration Research Virtual Institute, Southwest Research Institute, Boulder, CO for his invaluable help in producing model production function ages for Chapter 4.

Thanks to my fellow Mercury Girls, Valentina Galluzzi and Emma Fegan. You are both awesome.

Last but very much not least, my thanks to my family, Jeremy, Yvonne and Giles, and to Brigid, Fran, Robyn, Anya, Kirstin and Colin for keeping me sane and reminding me of the big picture.

And finally, a dedication:

For Jean

Inspiring woman, beloved grandmother.

I know you'd be proud.

# Table of Contents

# List of Figures

# List of Tables

# List of Supporting Digital Media

| Media | Filename | Description |
|---|---|---|
| CD | bepi_targets.shp and supporting files (bepi_targets.*) | ArcGIS shape file containing digitised polygons for all BepiColombo targets listed in Appendix F. |

# List of Abbreviations

| Abbreviation | Meaning |
|---|---|
| BCFD | Bright Crater Floor Deposit |
| HMR | High-Magnesium Region |
| HRP | High-Reflectance Plains |
| IT | Intermediate Terrain |
| LRP | Low-Reflectance blue Plains |
| LRM | Low-Reflectance Material |
| MASCS | Mercury Atmospheric and Surface Composition Spectrometer |
| MDIS | Mercury Dual Imaging System |
| MESSENGER | MErcury Surface, Space ENvironment, GEochemistry, and Ranging |
| NAC | Narrow Angle Camera |
| PSD | Photo Stimulated Desorption |
| WAC | Wide Angle Camera |
| XRS | X-Ray Spectrometer |

# Chapter 1. Introduction

## 1.1 The overarching question and approach

In recent years, there has been a paradigm shift in our understanding of the planet Mercury. Where once explanations for its high density implied that it would be depleted in volatile substances (e.g. *Cameron*, 1985; *Fegley and Cameron*, 1987), we now know that it is anything but. Not only is there a surprisingly high abundance of relatively volatile elements at the planet's surface (e.g. *Nittler et al.,* 2011; *Peplowski et al.*, 2012; *Evans et al.*, 2014), landforms seemingly created through loss of those volatiles are widespread (*Kerber et al.*, 2009; *Blewett et al.*, 2011). However, this realisation has given rise to a new problem:

> How has it been possible for concentrations of volatiles sufficient to result in these landforms to reach Mercury's surface over the course of its geological history, despite the absence of plate tectonics and in the state of crustal compression indicated by planet-wide thrust faulting?

This thesis, which evolved into a focussed study from the original concept of a more general look at Mercury's geology at 'high' resolution, aims to answer this fundamental question by investigating the geological features that appear to be most closely associated with volatile-release at Mercury's surface: the youthful flat-floored depressions known as 'hollows' and the products of explosive volcanism. By investigating how the processes that result in these landforms interact with other exogenic and endogenic processes, I seek to develop a deeper understanding of Mercury as a dynamic system.

## 1.2 Background

Mercury is the smallest planet in our Solar System, with a radius of 2,440 km. Though it is the planet with the highest uncompressed density (5.3 g/cm$^3$), its small size means it has a low gravitational attraction (3.7 m/s$^2$) and does not retain an atmosphere, though it has an exosphere (a volume in which particle density is too low for collisional interaction). Its heliocentric orbit is highly elliptical, taking it to 0.31 AU (46,000,000 km) at perihelion and

0.47 AU (70,000,000 km) at aphelion. Because it rotates slowly (three times for every two solar orbits), its solar days are long (176 Earth days from noon to noon) and there is a large diurnal temperature variation at the surface. This is greatest at 'hot poles' (0° and 180° E) where the Sun is overhead at perihelion, ranging from 100 K to 700 K (*Vasavada et al.*, 1999). Mercury is the only planet in the Solar System other than the Earth that has an intrinsic dipole magnetic field, though its strength is small (~1% of Earth's (*Ness et al.*, 1974)). Impactors strike Mercury faster than other bodies in the Solar System, at an average impact velocity of 20 km/s (*Cintala*, 1992), producing abundant impact craters that dominate the surface geology. Large areas are also resurfaced by smooth, flat-lying lavas, in particular a region near the north pole known as the Northern Volcanic Plains.

Notoriously difficult to view from Earth, little was known about Mercury prior to three flybys made by Mariner 10 in 1973–74 (e.g. *Sandner*, 1963). As a result of that ground-breaking mission, the literature regarding Mercury burgeoned in the 1970s and 1980s, providing new insights into the planet (e.g. *Howard et al.*, 1974), its surface (e.g. *Murray et al.*, 1975), exosphere (e.g. *Broadfoot et al.*, 1974) and magnetic field (e.g. *Ness et al.*, 1974). Mature reflection led to several books (*Strom*, 1987; *Vilas et al.*, 1988; *Strom and Sprague.*, 2003) that informed our understanding of the planet up until the arrival of NASA's MErcury Surface, Space ENvironment, GEochemistry, and Ranging (MESSENGER) spacecraft at Mercury. MESSENGER's fly-bys (2009–2010) and then its orbital mission (2011–2015) led to a large number of publications, including special issues of prestigious journals (e.g. *Earth and Planetary Science Letters*, 285, 2009; *Science*, 59, 2011), and, so far, one major book (*Rothery*, 2015). The work contained within this more recent literature has largely provided the background to the research presented in this thesis, and is reviewed accordingly in the Introduction or Background sections of Chapters 2–8.

Mercury's anomalously high uncompressed density (5.3 g/cm$^3$ versus Earth's 4.45 g/cm$^3$) has long been a subject for speculation (e.g. *Cameron et al.*, 1988). It implies that the planet has a much higher metal to silicate ratio than other terrestrial planets, corresponding, when moment of inertia measurements are taken into account, to a metallic core taking up over

80% of its radius and a silicate portion only ~ 400 km thick (*Hauck et al.*, 2013). In the period between the precise determination of the planet's high density using data from Mariner 10 (*Howard et al.*, 1974; *Anderson et al.*, 1987) and the arrival of the MESSENGER spacecraft at Mercury in 2008, three main mechanisms were proposed by which metal-silicate fractionation in the early solar system could account for this finding. The first is that the original building-blocks of Mercury were metal-rich, most likely due to differences in the susceptibility of denser iron-rich planetesimals and silicate planetesimals to orbital decay through gas drag in the inner solar nebula (*Weidenschilling*, 1978). In the second model, Mercury formed from planetesimals with a chondritic composition similar to that of other terrestrial planets, but, due to high temperatures in the early Solar System, the silicate portion was partially evaporated and carried away by the solar wind (*Cameron*, 1985; *Fegley and Cameron*, 1987). The third mechanism also posits the removal of part of the silicate portion after planet-formation, but in one or more giant impacts (*Benz et al.*, 1988, 2007; *Cameron et al.*, 1988). The vaporisation model and the original variants of the impact model predict a Mercury that is depleted in volatiles relative to chondrites and other terrestrial planets.

The evidence returned by MESSENGER indicates otherwise. Sulfur is relatively abundant at the surface, with an average concentration of 2 wt%, several orders of magnitude greater than in Earth's crust (*Nittler et al.*, 2011; *Evans et al.*, 2012; *Weider et al.*, 2015). Chlorine (*Evans et al.*, 2015) and sodium (*Peplowski et al.*, 2014) are also detected at average concentrations considerably and somewhat above average terrestrial crustal values, respectively. The K–Th ratio, ranging to values higher than those found for Mars, additionally argues against the removal of the volatile fraction from Mercury or its exclusion from the planet for thermal reasons, because potassium is more volatile than thorium (*Peplowski et al.*, 2011). More indirectly, two types of landform indicate the action of volatiles at the surface and their presence within the planet (Figure 1-1). The first are kilometre-scale morphologically-fresh, flat-floored, irregular depressions known as 'hollows' (*Blewett et al.*, 2011). Their closed morphology and clustered occurrence is most consistent with formation

by the loss of a moderately volatile substance from the planet's surface without melting, and their crisp scarps and lack of superposed impact craters indicate that they formed very recently or that formation is ongoing. The second landform type is irregular pits, a few to tens of kilometres across, which are commonly surrounded by a relatively bright and red-sloped spectral anomaly with diffuse margins. This association strongly suggests that the pits are vents, and that the spectral anomaly represents associated deposits, formed through explosive (and hence volatile-driven) volcanism (*Kerber et al.*, 2009; *Head et al.*, 2012).

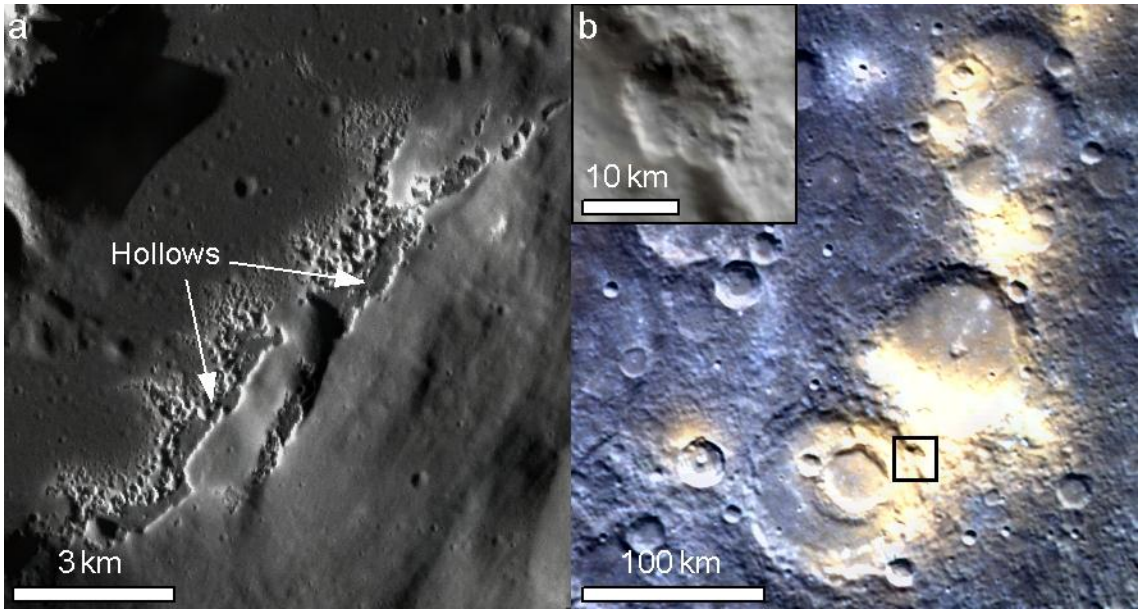


**Figure 1-1 Landforms revealed by MESSENGER and attributed to the action of volatiles. (a) Flat-floored depressions known as 'hollows' seen at 15 m/pixel resolution (image EN0258630853M; solar illumination from the left). (b) Relatively bright and red spectral anomalies (colour composite of images EW1005108006I, EW1005108026G and EW1005108010F in the red, green and blue bands) and (inset) pits (image EN0239040293M), attributed to explosive volcanism (solar illumination from the top in both parts).**

Both of these landform types have clear associations with volatiles, but in many ways they raise more questions than they answer. Hollows have been justly termed 'enigmatic' (e.g. *Blewett et al.*, 2012): their method of formation and the nature and provenance of the moderately-volatile substance lost during that formation were all initially unknown. Though pyroclastic vents and deposits are a better-known phenomenon on planetary surfaces (e.g. *West*, 1974; *Head*, 1976), their occurrence on Mercury is problematic. The widespread

occurrence of thrust faulting (indicated by lobate scarps and wrinkle ridges) indicates that Mercury has been in a state of crustal compression from at least 3.8 billion years ago (*Watters et al.*, 2009; *Banks et al.*, 2014), a condition that is unfavourable for magma ascent to the surface. However, the crisp morphology of the pits and the spectral distinctiveness of the surrounding anomalies appear to indicate that these are not ancient, and hence the magma involved in the eruptions that formed them was able to rise to the planet's surface despite these contractional forces.

## 1.3 Specific objectives

To address the significant outstanding issues relating to the above-mentioned volatile-driven processes at Mercury's surface, this thesis has the following objectives:

1. Fully document the occurrence of hollows and putative explosive volcanism on Mercury, as far as the spatial resolution of the available data allows.
2. For hollows, investigate:
    a. The process(es) by which they form.
    b. The substance(s) lost in their formation.
    c. The process(es) by which this material has been exposed at the planet's surface in the recent past.
3. For explosive volcanism, investigate:
    a. Its timing in relation to effusive volcanism and tectonic shortening, and in absolute terms.
    b. The processes that have dictated its spatial variability.
    c. The volcanic processes by which the observed landforms could have formed, including mechanisms by which volatile concentrations sufficient to create them became available.
4. Pinpoint those questions that cannot be answered using MESSENGER data, and identify sites where targeting by the forthcoming BepiColombo mission (*Benkhoff et al.*, 2010) has a high scientific return potential.

Through meeting these objectives, this work aims to significantly advance our understanding of how landforms associated with volatile release formed on Mercury, and what they can tell us about the nature and evolution of the planet as a whole.

## 1.4 Methodology

To fully catalogue these landforms, I have examined high-resolution image data from the MESSENGER spacecraft, which was in orbit around the planet throughout the course of the research (2012–2015), returning images at increasingly high resolutions as it approached Mercury at increasingly low altitudes. By examining all images with a resolution better than 180 m/pixel in conjunction with relevant images at lower resolutions I have been able to create the most comprehensive catalogues yet produced (Appendix A, Appendix C)

On the basis of these catalogues, and with the aid of multiple other datasets from MESSENGER, such as X-Ray spectrometer and laser altimetry data, I have studied the spatial and temporal distribution of hollows and sites of proposed explosive volcanism, their specific local settings, their association with other landforms, and their geochemical associations.

## 1.5 Thesis structure

This thesis broadly divides into three sections. The first section (Chapters 2 and 3) relates to hollows. Chapter 2 presents a global investigation of hollows, their distribution and associations, and assesses the implications of these findings for their formation mechanism and the source of the hollow-forming volatiles. Chapter 3 takes a detailed look at the spectral character of hollow floors to constrain the nature of the moderately-volatile substance responsible for their formation.

The second section (Chapters 4 to 8) relates to explosive volcanism. Chapter 4 considers the timing of this activity, showing that it continued into the most recent era of Mercury's geological history. Chapter 5 documents the global distribution of the activity, along with its local associations, and reaches conclusions about the structural mechanisms allowing explosive volcanism at so recent a date despite global contraction. As an extension of this

work, in Chapter 6 I consider whether the observation that sites of putative explosive volcanism are common at basin margins allows us to use such sites to identify ancient impact basins, and propose three locations at which this may be so.

In Chapter 7 I look at an unexpected and eye-catching landform on Mercury that cried out for explanation – a steep-sided cone at the centre of a deposit indicative of explosive volcanism. I find, with the help of modelling work undertaken by international collaborators, that such a cone can be formed by modification of a pre-existing impact crater by explosive volcanism surrounding the central peak, and tie this in with the common occurrence of crater-centred explosive volcanism on Mercury. This specific localisation presents a contrast with explosive volcanism on the Earth's Moon, which also commonly occurs in impact craters, but at the outer margins of fractured crater floors. Therefore in Chapter 8, I make a detailed comparison between crater-hosted explosive volcanism on Mercury and the Moon, drawing conclusions that further our understanding of both.

At many points in this work, it is clear that future data provided by the BepiColombo mission, due to begin science operations in orbit around Mercury in 2024, can help answer still-outstanding questions. In the final section, Chapter 9, I bring these questions together, discussing in detail what the enhanced capabilities of BepiColombo can tell us that MESSENGER's instruments could not, and suggesting specific sites that would warrant targeted data-collection. Appendix F provides a comprehensive list of targets consisting of vents, pyroclastic deposits and landforms associated with hollows, as an aid to planning BepiColombo science operations. Finally, in Chapter 10 I conclude by showing how this thesis has furthered its primary aims and objectives.

Chapters 2, 4, 5 and 7 have already been published in peer-reviewed journals (except that I have 'topped and tailed' them to better integrate them into the thesis), and Chapter 8 is under review at the time of thesis submission (Table 1-1). The text of the papers is unchanged apart from cosmetic details such as figure numbering and conversion to UK English in the first person. Figures that were published as supplementary material to published papers have been included in the body of the chapter where possible and all other published

supplementary material has been included in the Appendices. Apart from Chapter 7, the research for each Chapter is entirely my own, though I have of course benefitted from team discussions. My supervisors, Professor David Rothery, Dr Susan Conway and Dr Mahesh Anand, have all contributed by suggesting changes to wording and pointing out areas where my arguments or methods needed refinement. The paper that makes up Chapter 7 is a collaboration with researchers in Italy, which I led. Alice Lucchetti and Dr Gabriele Cremonese conducted hydrocode modelling and provided descriptions of their methods and results, Dr Matteo Massironi provided guidance in structural geology and crater-counting techniques, and Dr Cristina Re produced the digital elevation model for the main landform under consideration. Their contributions constituted 40% of the substance of the published paper.

**Table 1-1 Papers published or in peer-review included in this thesis**

| Chapter | Paper |
|---|---|
| 2 | Thomas, R. J., D. A. Rothery, S. J. Conway, and M. Anand (2014), Hollows on Mercury: Materials and mechanisms involved in their formation, *Icarus*, 229, 221–235, doi:10.1016/j.icarus.2013.11.018. |
| 4 | Thomas, R. J., D. A. Rothery, S. J. Conway, and M. Anand (2014), Long-lived explosive volcanism on Mercury, *Geophys. Res. Lett.*, 41(17), 6084–6092, doi:10.1002/2014GL061224. |
| 5 | Thomas, R. J., D. A. Rothery, S. J. Conway, and M. Anand (2014), Mechanisms of explosive volcanism on Mercury: implications from its global distribution and morphology, *J. Geophys. Res. Planets*, 119, 2239–2254, doi:10.1002/2014JE004692. |
| 7 | Thomas, R. J., A. Lucchetti, G. Cremonese, D. A. Rothery, M. Massironi, C. Re, S. J. Conway, and M. Anand (2015), A cone on Mercury: Analysis of a residual central peak encircled by an explosive volcanic vent, *Planet. Space Sci.*,108, 108–116, doi: 10.1016/j.pss.2015.01.005. |
| 8 | Thomas, R. J., D. A. Rothery, S. J. Conway, and M. Anand (2015), Explosive volcanism in complex impact craters on Mercury and the Moon: influence of tectonic regime on depth of magmatic intrusion. *Earth Planet. Sci. Lett*, 431, 164–172, doi: 10.1016/j.epsl.2015.09.029. |

# Chapter 2. Hollows on Mercury: materials and mechanisms involved in their formation

## 2.1 Introduction

The most unusual and surprising landforms attributed to volatiles at Mercury's surface are the flat-floored depressions known as 'hollows'. To better understand these, I set out to fully document their global occurrence and associations, and to use this data to investigate their mechanisms of formation and the source of the materials involved. This work is presented in the peer-reviewed *Icarus* paper (*Thomas et al.*, 2014a) comprising this chapter.

## 2.2 Background

The presence of morphologically fresh depressions on the surface of Mercury has been one of the most surprising discoveries of the MESSENGER (MErcury Surface, Space ENvironment, GEochemistry, and Ranging) spacecraft. Though areas of hollows had been imaged at low resolution by the Mariner 10 spacecraft in the 1970s, they appeared only as high–reflectance, spectrally relatively blue patches on the floors of impact craters (BCFDs – Bright Crater Floor Deposits) (*Dzurisin*, 1977; *Robinson et al.*, 2008; *Blewett et al.*, 2009). When MESSENGER went into orbit in 2011 and obtained higher-resolution images, these were revealed to be clusters of irregular rimless depressions with flat floors and steep walls (Figure 2-1). These were dubbed 'hollows' to distinguish them from deeper 'pits' with sloping floors, which are proposed to form through magmatic processes (*Gillis-Davis et al.*, 2009; *Kerber et al.*, 2011). They range from individual hollows tens of meters across to clusters of hollows tens of kilometres across (*Blewett et al.*, 2011) and shadow measurements indicate a consistent depth within a particular host crater in the range of tens of meters (*Blewett et al.*, 2011; *Vaughan et al.*, 2012). Though their consistent depths make them flat-floored overall, lumps of material do occur on hollow floors that may be degraded remnants of the original surface (*Blewett et al.*, 2011). The bright deposits that gave BCFDs their name are revealed from orbit to occur both on hollow floors and as surrounding haloes.

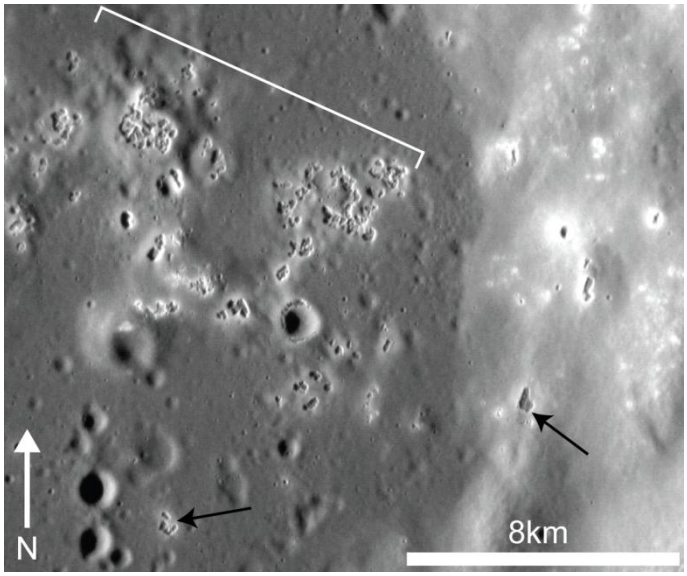


**Figure 2-1 Irregular, rimless hollows on the floor and terraced wall of an unnamed impact crater at 46.4°N, 318.7°E. Black arrows indicate individual hollows; the white bracket indicates a cluster (MESSENGER image ID 2760274).**

Hollows appear morphologically fresh and lack superposed impact craters. This implies a young age and suggests hollow formation may be an ongoing process (*Blewett et al.*, 2011). If so, it will be important to distinguish whether it is a gradual, continual process or a more rapid, episodic process.

The flat-floored, closed morphology of hollows and the lack of associated outflow features suggest that they form by the preferential loss of a volatile component from the surface without melting. The nature of this material is not known: sulfides or chlorides are possible candidates (*Vaughan et al.*, 2012; *Blewett et al.*, 2013) but the current resolution of surface elemental composition data (*Goldsten et al.*, 2007; *Hawkins et al.*, 2007; *Schlemm et al.*, 2007; *Nittler et al.*, 2011; *Peplowski et al.*, 2011; *Evans et al.*, 2012; *Weider et al.*, 2012) is not sufficient to verify this at the scale of hollows.

Several possible release mechanisms for this volatile substance have been suggested (*Blewett et al.*, 2011). The feasibility of these processes is dependent on the nature of the substance lost and the timescale of hollow formation. In light of the high daytime surface temperatures at Mercury and the morphological similarity between hollows and the 'Swiss cheese terrain' of Mars (*Thomas et al.*, 2000), sublimation is a strong candidate. However, various forms of

space weathering are believed to occur at Mercury, and these may be important release mechanisms if they are relatively intense in the material where hollows form. Along with thermal desorption (*Madey et al.*, 1998), photon stimulated desorption (PSD) releases alkalis from the surface and may be the most efficient form of space weathering supplying these elements to the exosphere (*Cheng et al.*, 1987; *Mura et al.*, 2009). On a shorter timescale and at particular localities, physical (*Killen et al.*, 2004) and perhaps chemical (*Potter*, 1995) sputtering by the solar wind may also be important, with its intensity depending on the time-variable interaction between the solar wind and the planet's magnetic field. Micrometeorite impact vaporization also releases material from the surface, and unlike the processes mentioned above, penetrates beyond the layer of atoms at the extreme surface (*Killen et al.*, 2007). The rate of hollow formation may however be too fast for this to apply (*Blewett et al.*, 2011).

Hollows usually occur in material with a low reflectance relative to the Hermean average. In some cases this is a regional deposit equating to the LRM (Low-Reflectance Material) spectral unit that has been mapped over large areas of the planetary surface (*Denevi et al.*, 2009), in others it is a localized deposit, and in a few cases it is a small 'dark spot' with even lower reflectance than LRM (*Xiao et al.*, 2013). Low-reflectance material may therefore be the volatile-bearing unit that degrades to form hollows. The question arises of how the volatile component in this material has been able to access the surface recently enough to form fresh landforms despite considerable evidence for global contraction (*Strom et al.*, 1975; *Watters et al.*, 2009): this stress state would tend to hinder migration of material through the crust. The correlation of hollow formation with impact craters strongly suggests that impacts are involved in bringing the hollow-forming volatiles to the surface. It has been suggested that this may occur through exposure in crater walls, floors and ejecta and exhumation in peak structures (*Blewett et al.*, 2013), or through differentiation of impact melt (*Vaughan et al.*, 2012).

A deeper understanding of the distribution and mode of occurrence of hollows is of great interest because of the probable relationship between hollows and volatile percentage in

Mercury's crust, now understood to be higher than previously thought (*Kerber et al.*, 2009, 2011; *Nittler et al.*, 2011; *Peplowski et al.*, 2011). I have therefore conducted a full survey of MESSENGER images of Mercury's surface. This comprehensive survey has allowed identification of many areas of hollow formation not previously recognized, building on the global inventory published by *Blewett et al.* (2013). I have recorded the extent, location and associations of the observed hollow clusters, and examined latitudinal and longitudinal variations in their areal extent. I consider how their occurrence and extent may be controlled by external factors such as insolation and ion sputtering or endogenic processes such as the formation of pyroclastic pits or surficial coverage by thick volcanic plains. On a local scale, I have examined the slope aspects in locations where hollows occur on slopes, in order to test whether there is a correlation with insolation intensity, and have studied the local settings of hollow formation to evaluate possible exposure mechanisms for hollow-forming volatiles.

## 2.3 Methods

### 2.3.1 MESSENGER imagery

I examined images taken by MESSENGER's Mercury Dual Imaging System (MDIS) (*Hawkins et al.*, 2007, 2009) up to the end of MESSENGER's fourth solar day in orbit around Mercury (product creation times up to March 17, 2013). Monochrome images were used to identify hollows and study them in detail, and lower resolution colour composites were used to determine the spectral character of their associated deposits and substrates.

#### *2.3.1.1 Monochrome images*

I examined all MESSENGER monochrome images with resolutions of less than 180 m/pixel, excluding images at lower resolutions because they do not reveal the irregular margins, flat floors and rimlessness that distinguish hollows from small impact craters. These images were obtained by the 1.5° field-of-view Narrow Angle Camera (NAC) and the 748.7 nm filter in the 10.5° field-of-view Wide Angle Camera (WAC) of MDIS. The highest-resolution images used were 7.7 m/pixel and the average resolution of those available was 106 m/pixel.

I applied radiometric and photometric correction to all images using the ISIS3 image processing package of the USGS. I then overlaid these onto the 250 m/pixel global monochrome mosaic version 9 produced by the MESSENGER team (released by NASA's Planetary Data System on 8 March 2013) and digitized features on this global mosaic.

#### *2.3.1.2 Colour images*

To characterize the spectral type of local and regional substrates, I examined colour composites created by combining data from three of the twelve spectral filters in the WAC. All major substrates on Mercury have red-sloped reflectance spectra (*Denevi et al.*, 2009), but the steepness of this slope varies, allowing some to be classified as red or blue relative to the Hermean average. By combining reflectance at 996 nm, 749 nm and 433 nm in the red, green and blue bands, I was able to see these variations and attribute substrates to the spectral types established by *Denevi et al.* (2009), which are believed to indicate real compositional and geological differences between surface units.

All images at a resolution of less than 1000 m/pixel were examined, as was the 1000 m/pixel global colour mosaic version 3 produced by the MESSENGER team (released by NASA's Planetary Data System on 8 March 2013). The highest-resolution composite created was 64 m/pixel and the average resolution was 455 m/pixel.

### 2.3.2 Data collected

#### *2.3.2.1 Hollows and pits*

Data on all non-impact-related depressions visible in the images were gathered in order to ensure that a distinction was made between hollows and pits with a probable magmatic (*Gillis-Davis et al.*, 2009) or pyroclastic (*Kerber et al.*, 2011) origin and to make spatial comparisons between this activity and hollow formation. Impact-related craters were distinguished from pits and hollows on the basis of their circular shape, raised rims and the characteristic geometry of their ejecta blankets.

The steepness of a depression's margins and the spectral signature of its associated deposits were used to distinguish between hollows and pits: hollows have steep margins leading to flat floors and bluer deposits while pits have gentler slopes, are deeper, and any surrounding deposits are redder (Table 2-1). I identified a third previously unidentified type of depression that is intermediate in character between pits and hollows: areas of pitted ground floored by relatively red deposits. These either lack defined margins or have steep margins that appear less crisp than those of hollows. Where they have defined margins, they are intermediate in depth between hollows and pits. The presence of relatively red deposits in these regions, the lack of relatively blue deposits and their smoother morphology suggests that these are not hollows. The similarity of the spectral character of their deposits to those of pits, which are suggested to be formed by explosive volcanism (*Kerber et al.*, 2011), may indicate a volcanic origin.

**Table 2-1 Characteristics distinguishing pits, hollows and spectrally red pitted ground**

| **Characteristic** | **Hollows** | **Pits** | **Spectrally red pitted ground** |
|---|---|---|---|
| Wall slope | Steep | Shallow | Lacking or steep |
| Floor slope | Flat, though lumps of material may occur | Sloping | Roughly horizontal but uneven |
| Surrounding deposits (when present) | High-reflectance, relatively blue | High-reflectance, relatively red | High-reflectance, relatively red |
| Depth | Tens of meters | Can be 1 km or more (*Gillis-Davis et al.*, 2009; *Rothery et al.*, 2014). | Tens of meters |

For each depression, I gathered data on its geographical location, area, association with tectonic structures such as thrust faults, the spectral type of the local and regional substrate, and the type of material hosting it. I identified the spectral type of the regional substrate by reference to global mapping by *Denevi et al.* (2009, 2013) and my own observations of colour composite images, distinguishing between regional low-reflectance material (LRM), intermediate terrain (IT), high-reflectance plains (HRP) and low-reflectance blue plains (LBP). On a local scale, I noted the presence of relatively red material, bright ejecta deposits

and localized low-reflectance material. To record the host material I distinguished between the walls, peak structure, ejecta blanket and smooth or rough floor of craters, and smooth and rough non-crater surfaces.

I grouped together hollows on the basis of occurrence within a particular host crater, or location within 50 km of each other where they lie outside craters. I calculated the areal extent of hollows within each group by mapping them individually and obtaining the spherical area (area of a polygon without the distortion caused by map projection) using the Graphics and Shapes tool for ArcGIS (*Jenness*, 2011).

As several of the proposed formation mechanisms for hollows are controlled by insolation, I investigated the possibility of preferential hollow formation on sun-facing slopes. I recorded the aspect of the slope where hollows within a group occurred on slopes of a particular orientation where that observed orientation could not be explained by compositional differences or differences in viewing conditions for nearby slopes at other orientations. This aspect was taken to be the bearing of a line normal to the horizontal alignment of hollows along the surface of the slope. This was drawn by eye and rounded to the nearest 5°, as no digital terrain model of adequate resolution was available.

In order to calculate the depths of hollows, I measured shadows at the margins of hollows in cases where high resolution (< 110 m/pixel) images were available. A precision of half a pixel was used to estimate the error. Where multiple images were available of the same hollow, I used the image with the highest resolution and lowest emission angle (angle off nadir) to minimize error. I also avoided measuring shadows falling on steep slopes.

Because pits are generally larger-scale features than hollows and since I wanted to investigate whether hollows occur in association with pits, I noted whether the resolution of the available images of pits would allow identification of hollows, if present.

#### *2.3.2.2 Impact craters*

Where hollows occur in association with an impact crater I noted the crater diameter as a proxy for depth of excavation. This was obtained from the *Herrick et al.* (2011) global crater

database or measured on a sinusoidal projection of the crater if it was not within that database. I also noted the crater's degree of degradation as a proxy for age using the scheme of *Barnouin et al.* (2012). Degradation classes range from 1 to 5 (oldest to youngest) and are defined on the basis of characteristics such as the preservation of the ejecta blanket, modification of terraces and amount of superposed impact craters. Any crater ages mentioned in this work are based on this scale.

## 2.4 Results

I found 445 groups of hollows, covering 57,400 km$^2$, which amounts to 0.08% of the surface area imaged at better than 180 m/pixel (locations indicated in Table A-1). These ranged in areal extent from 0.07 km$^2$ to 6771 km$^2$, with a mean of 129 km$^2$ (standard deviation = 475). 140 of these groups were at locations previously catalogued by *Blewett et al.* (2013). I also identified 173 groups of pits and 24 groups of spectrally red pitted ground (Figure 2-2).

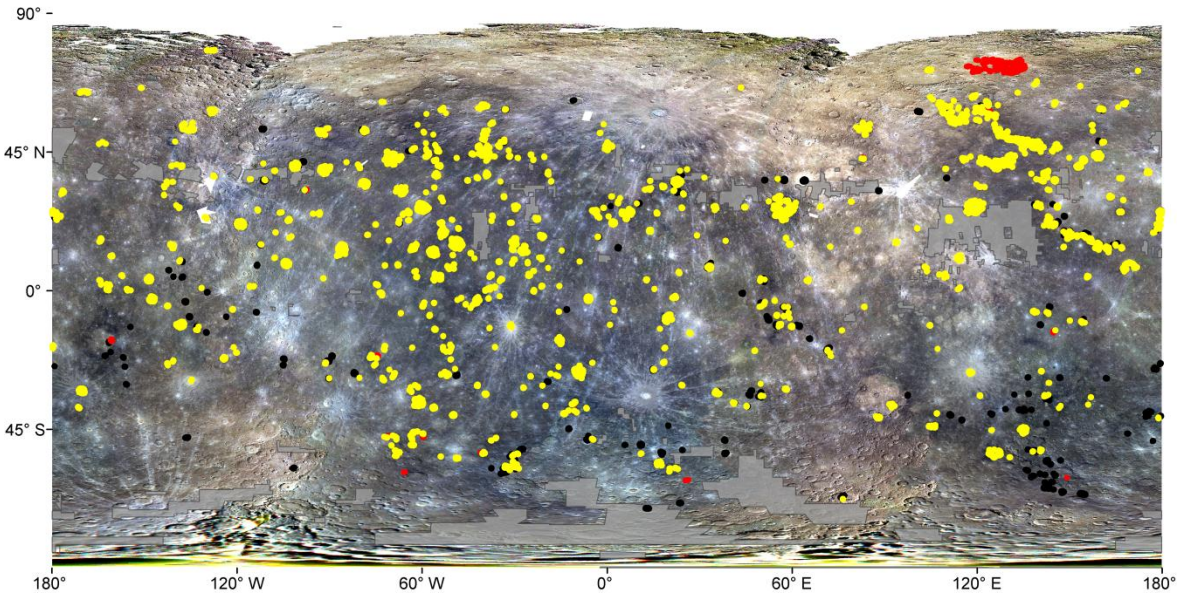


**Figure 2-2 Global occurrence of hollows, pits and spectrally red pitted ground. Yellow: hollows; black: pits; red: spectrally red pitted ground; grey: area not imaged at < 180 m/pixel. (Base mosaic: MESSENGER global colour v3).**

### 2.4.1 Global variations in the areal extent of hollows

Hollows occur globally, but are rare in the high reflectance plains at high northern latitudes and within basins such as Caloris (160° E, 32° N) and Rembrandt (88° E, -33° N). There is

good image coverage in these regions so this absence is not a product of observational bias. Though much of the interior of Caloris lacks hollows, hollows do occur within younger impact craters in its fill. Hollows also occur at its rim, often in association with pits of probable pyroclastic origin, and in two sublinear regions outside its northwest rim.

Though hollows are not observed at high southern latitudes, this could be largely attributable to observational bias: MESSENGER's highly elliptical orbit, with an initial periapsis altitude of 200 km at ~ 60° N and an apoapsis altitude of 15,200 km (*Hawkins et al.*, 2007), means this area is imaged at much lower resolutions than areas further north.

It has been suggested that hollow formation is controlled by insolation and that hollows rarely occur on smooth plains substrates (*Blewett et al.*, 2013). In order to assess these hypotheses with my global dataset, I investigated whether there is a correlation between longitudinal and latitudinal variations in the areal extent of hollows and in the intensity of insolation and the areal extent of non-plains substrates.

#### *2.4.1.1 Longitudinal variation*

The elliptical orbit of Mercury leads to a variation in mean insolation along the equator: two 'hot poles' (0° and 180° E) are under the sun at perihelion and experience mean temperatures estimated to be 100 K higher than those of two 'cold poles' (-90° and 90° E), under the sun at aphelion (*Melosh and McKinnon*, 1988). To investigate the relationship between hollow occurrence and this longitudinal variation, I calculated the total areal extent of hollows in 20° bins in a 30° S to 30° N equatorial strip, normalizing the hollowed area to the area that is imaged at < 180 m/pixel (Figure 2-3a). This region has the virtue of being imaged at high resolution and low to moderate solar incidence angles, which are favourable observation conditions for hollows. I found that the areal extent of hollows is low near the 'cold poles', as expected if the intensity of insolation controls their occurrence. The fraction of the surface hollowed between the -40° E to -20° E bin and the 60° E to 80° E bin peaks at the 'hot pole' at 0° E, but a similar pattern of increase is not seen around the other 'hot pole' at 180° E.

However, plains associated with the Caloris basin occupy a large part of the equatorial strip from 150° E to 180° E. To test whether the presence of these plains modifies the pattern of hollow occurrence, I normalized the areal extent of hollows to the fraction of non-plains in each bin, in effect removing the influence of this parameter from the data (Figure 2-3b). I then saw a stronger correlation between the extent of hollows and the intensity of mean insolation, indicating that intensity of insolation controls hollow occurrence but is not a sufficient condition for their formation in all substrates.

The large areal extent of hollows in the -60 to -40° E region is a clear anomaly, neither accounted for by the variation in mean insolation or the presence or absence of smooth plains.

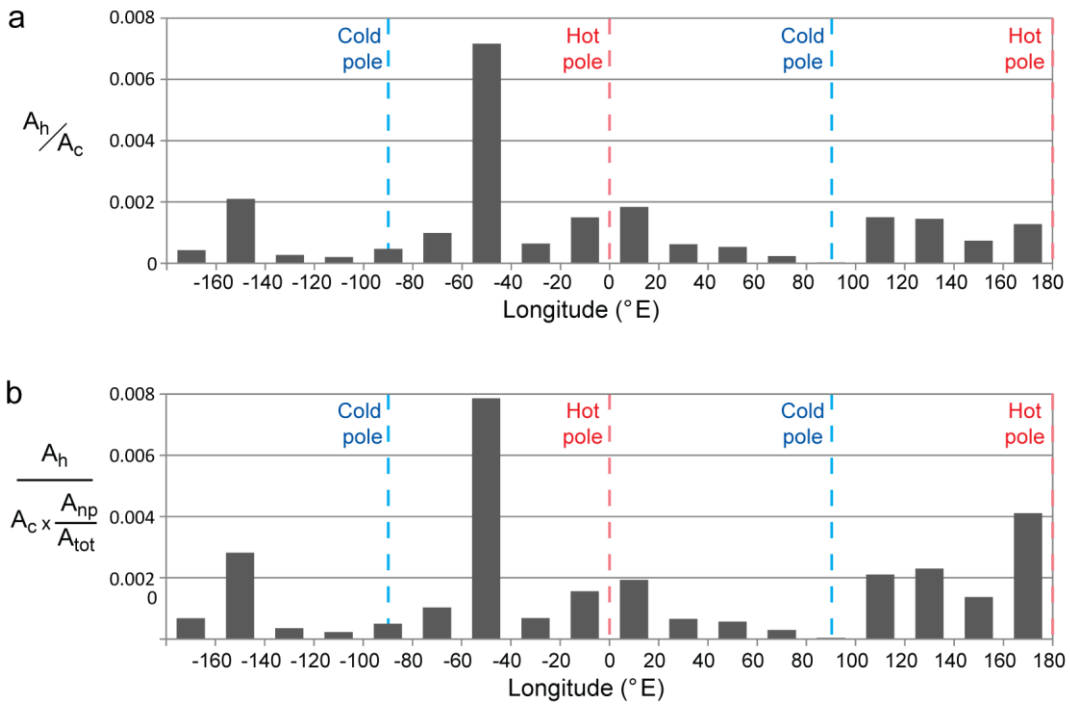


**Figure 2-3 Variation in the areal extent of hollows ($A_h$) by longitude bin in the region 30° S to 30° N, normalized to (a) area imaged at < 180 m/pixel ($A_c$), and (b) $A_c$ × the fraction of the surface that is not smooth plains ($A_{np}/A_{tot}$).**

### *2.4.1.2 Latitudinal variation*

The fraction of the surface area imaged at < 180 m/pixel that is hollowed varies widely at different latitudes (Figure 2-4a). This is in major part attributable to observational bias: this fraction is highest at low and mid-northern latitudes where MESSENGER is closest to the

planet and lowest at high southern latitudes where it is furthest away. At very high latitudes, high solar incidence angles (*Chabot et al.*, 2013) also preclude identification of hollows where they occur in craters because large parts of crater interiors are in shadow.

The lack of hollows at high northern latitudes is likely to be further controlled by the presence of a smooth plains substrate here. Normalizing to the fraction of non-plains does not entirely remove the disparity between hollow occurrence at low and high northern latitudes (Figure 2-4b), but as non-plains areas near the pole are imaged only with high solar incidence angles, it is possible that the remaining disparity is due to observational bias.

The areal extent of hollows at low southern latitudes (-30° to 0° N) is significantly lower than at low northern latitudes (0° to 30° N), and this contrast is not removed by normalizing to the fraction of non-plains (Figure 2-4b). This suggests a further factor discouraging hollowing at low southern latitudes or promoting it at low northern latitudes.

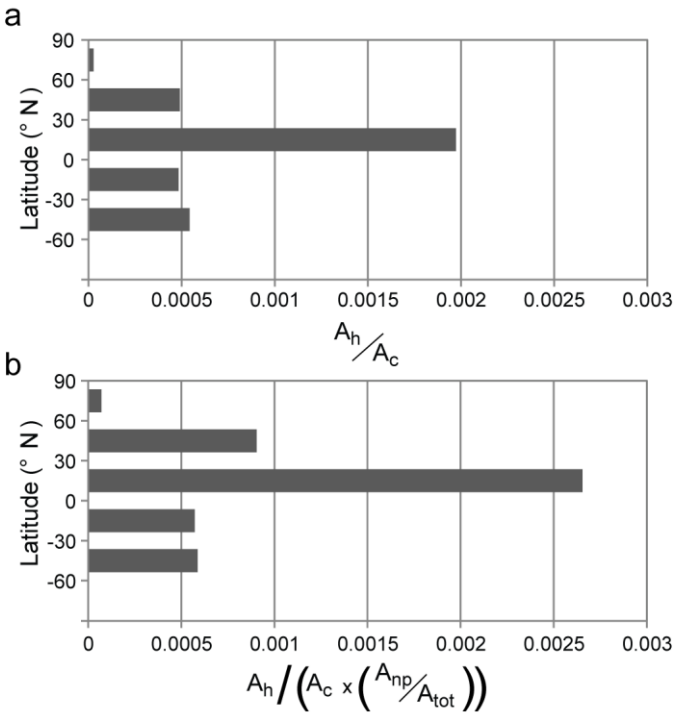


**Figure 2-4 Latitudinal variations in areal extent of hollows ($A_h$), normalized to (a) the area imaged at < 180 m/pixel ($A_c$) and (b) $A_c$ × the fraction of the surface that is non-plains ($A_{np}/A_{tot}$) within each latitude bin. Hollow extent varies broadly with image quality, though observational bias does not explain the small extent of hollowing in the 30° S to 0° N bin.**

### 2.4.2 Preferred slope aspect

It has been suggested that hollows preferentially form on sun-facing slopes and that this is evidence that their formation is linked to solar heating (*Blewett et al.*, 2013). I found some evidence in support of this phenomenon. A preferred aspect was found in only 8% of the groups of hollows observed, but in these cases there was a good correlation to the sun-facing slope (Figure 2-5). The small percentage of cases in which a preferred aspect was observed is partly attributable to the fact that only the sun-facing slope is illuminated in many of the available images of hollows at mid- to high latitudes, and in such cases preferential hollow formation on that slope was not recorded because lighting conditions were not good enough to rule out hollow formation on the opposing slope. However, most hollows are found on flat surfaces or on slopes of opposing aspects within a group so I do not find that preferential formation on sun-facing slopes is a common characteristic of hollows.

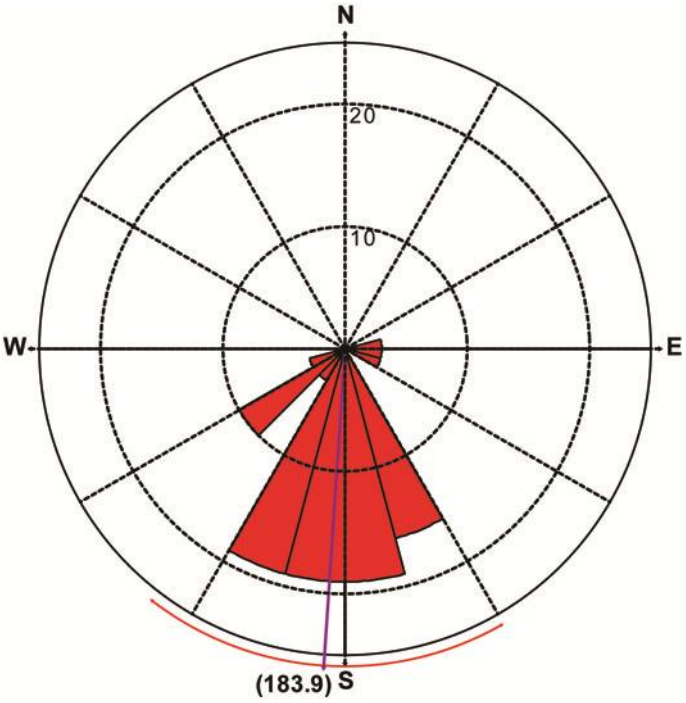


**Figure 2-5 Aspects of slopes on which hollows preferentially form in the northern hemisphere (N=31), showing a correlation with the sun-facing slope. Purple line indicates the mean, red circumferential line shows one standard deviation. Radial axis: percentage of the population of hollow groups with a preferred aspect within the northern hemisphere.**

### 2.4.3 Hollow depth

I calculated a mean depth for hollows of 47 m (standard deviation 21) on the basis of 108 shadow measurements within 27 hollow clusters. Depths ranged from 5 m ± 0.75 m to 98 m ± 19.5 m. These results are consistent with but more extensive and representative than previous studies showing a hollow depth of ~30m in Kertesz crater (*Vaughan et al.*, 2012) and 44 m in Raditladi basin (*Blewett et al.*, 2011).

Because of the limited resolution of available images, there is a large error in depth values and it is not possible to identify significant depth variations between different substrates (e.g. peak ring vs. crater floor) or craters of different ages.

### 2.4.4 Geological settings

The majority of hollows occur in clusters within impact craters and upon their proximal ejecta, as discussed by *Blewett et al.* (2013). However, my detailed survey also revealed two large areas of more distributed hollow formation lacking a close relationship with specific craters, and some association with pyroclastic pits in non-crater settings.

#### *2.4.4.1 Association with impact craters*

2.4.4.1.1 Observations

Hollows occur on a variety of crater surfaces. In simple craters, they commonly occur in a band on the inside rim of the crater (Figure 2-6a). In complex craters, they occur on the walls, central structures and smooth floor fill (Figure 2-6b) and occasionally on the ejecta blanket. Hollows are commonly clustered, either loosely with small (< 5 km) expanses of non-hollowed surface between individual hollows (Figure 2-1) or more tightly, as in Figure 2-6b, where they form a continuous hollowed area. At the rim of the Caloris basin, many small groups of hollows occur on peaks in the rim material and associated with probable pyroclastic pits.

Where hollows occur on crater fill, they often cluster around the central structures or near the walls (Figure 2-6c). In old, degraded craters, they commonly occur on the high inner walls

of smaller impacts into the crater or in the hanging walls of crater-crossing thrust faults (Figure 2-6d).

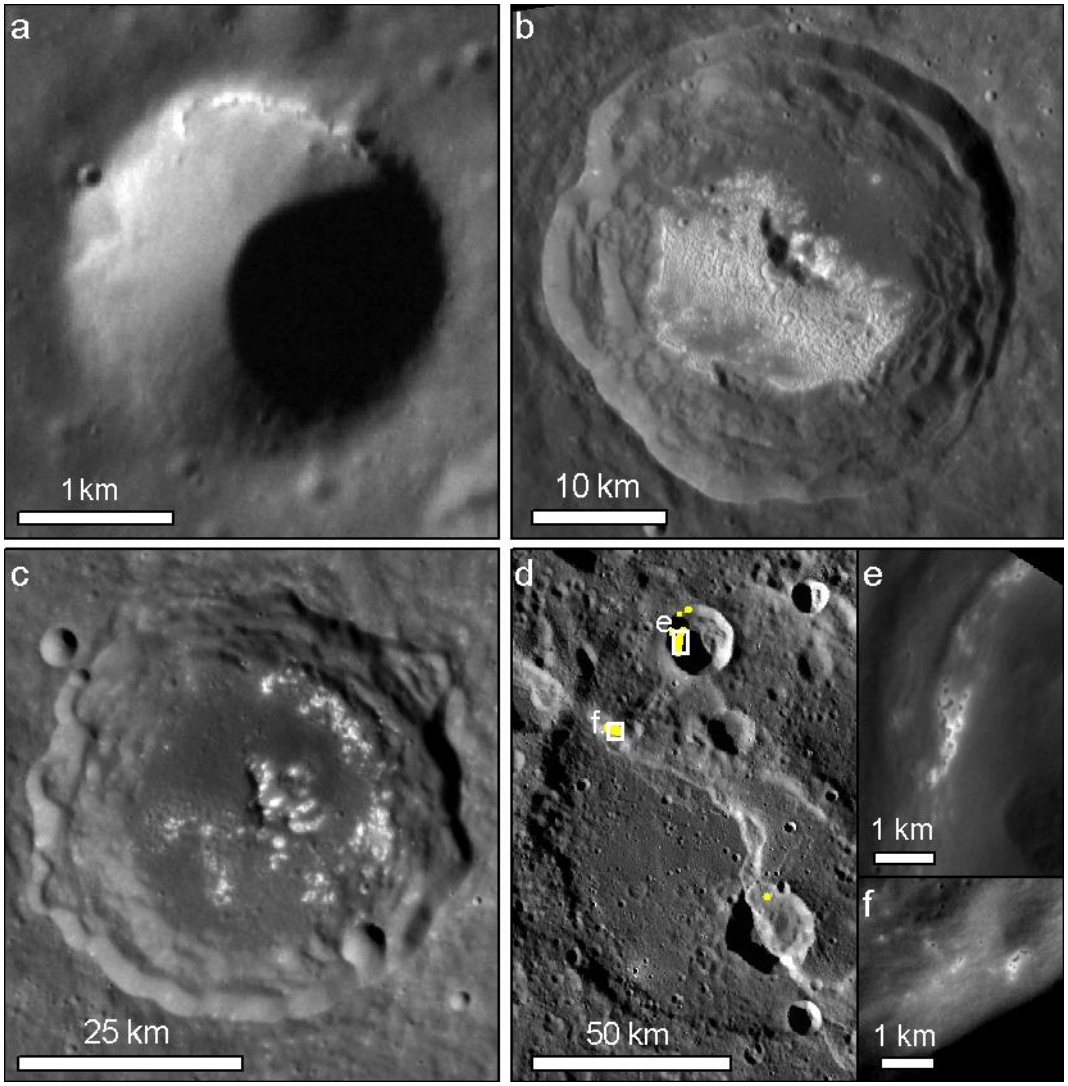


**Figure 2-6 Typical locations of hollows within impact craters (a) in a curvilinear band at inner rim of a simple crater (-58.6° E, 57.4° N, EN0238696485M). (b) Hollowing across a large part of the floor and peak structure of Hopper crater (Mansurian age, -55.8° E, -12.5° N, EN0223616383M). (c) Clustered in the area abutting the crater wall of Nampeyo crater (Mansurian age, -49.9° E, -40.3° N, EN0253678867M). (d) In a young impact into and on a thrust crossing the old, degraded Duccio crater (hollowed areas outlined in yellow) (Tolstojan age, -52.3° E, 58.2° N, MESSENGER global monochrome mosaic). (e) Close-up of hollows in a younger impact crater (EN0223658124M). (f) Close-up of hollows on a thrust (EN0223614937M). North is towards the top of each image.**

#### 2.4.4.1.2 Statistical correlation

Hollows occur within impact craters and their proximal ejecta in 84.5% of cases, and make up 97.5% of the total global hollowed area. Hollows are therefore strongly associated with craters.

If hollow-forming material is brought to the surface at the time of crater formation, then depending on the duration over which hollows (once formed) remain visible, a correlation could be expected between the age of the crater and the areal extent of hollowing. I therefore plotted the average extent of hollowing as a percentage of the crater's floor area ($\pi r^2$ where r = crater radius) in craters of each degradation state (Figure 2-7), using degradation state as a proxy for age (*Barnouin et al.*, 2012). I divided the data into crater diameter bins to allow for the possibility that a similar degree of degradation may occur in a shorter period for smaller craters than larger craters. I found no clear increase in the percentage of the crater area hollowed in older craters. In fact the average percentage hollowed is somewhat lower in older craters than younger craters (note the logarithmic vertical scale), though it can range up to 5.5% even in very old craters (degradation class 1, signifying a Pre-Tolstojan age). Because slope processes and burial by regolith can potentially obscure the characteristic morphology of hollows (in particular their steep, sharp margins), hollows seen clearly now can be assumed to either be still forming or to have ceased forming in the relatively recent past.

### *2.4.4.2 Hollows outside craters*

Hollows outside craters make up loose groupings rather than clusters, and in most cases (excluding those discussed below) the extent of hollowing within each group is small, averaging 15.2 $km^2$ (standard deviation = 38.0). This compares to a mean area of 148.6 $km^2$ (standard deviation = 514.0) for hollow groups within and in the proximal ejecta of craters. Hollows outside craters usually occur on hummocky surfaces or in a linear pattern cross-cutting geological units, suggesting they formed in distal ejecta (Figure 2-8). Some occur around pits with surrounding relatively spectrally red deposits, as reported below (Section 2.4.5).

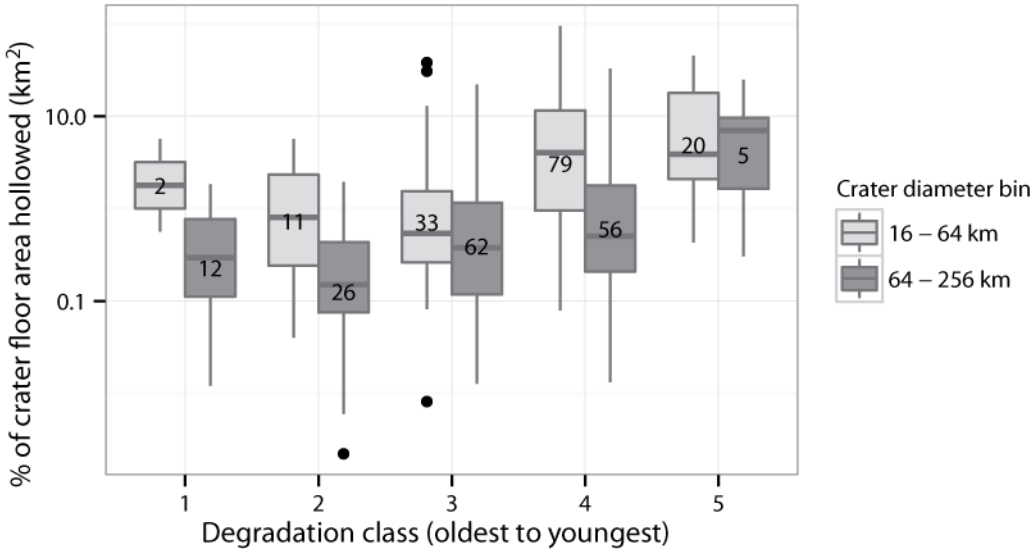


**Figure 2-7 Spread in area of hollows as a percentage of the calculated crater floor area against the degradation state of the host crater. Bottom and top of boxes indicate the first and third quartiles, band inside each box indicates the median, numbers indicate number of observations and are vertically centred to the mean; lines above and below boxes extend to the most extreme data point where it is no more than 1.5 times the interquartile range; dots indicate outliers.**

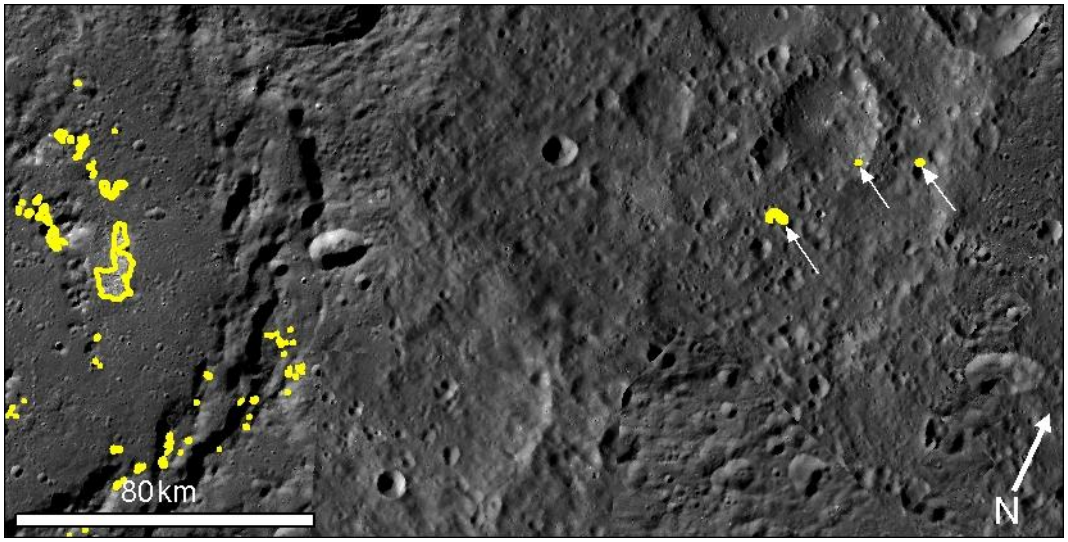


**Figure 2-8 Hollows of small areal extent (indicated by white arrows) occur approximately radial to a Mansurian-aged unnamed complex crater with hollows on its peak ring, floor and terraces (hollows outlined in yellow). This association suggests they formed in distal ejecta from the crater. (Figure centred at -65.0° E, 44.8° N; image: excerpt from global monochrome mosaic.)**

The detailed examination undertaken by this study has revealed for the first time two dispersed groupings of hollows covering large areas (136,000 km² and 52,000 km²) roughly

radial to the Caloris basin rim and extending to the west and northwest (Figure 2-9a). In the western grouping, hollows with an areal extent totalling ~ 150 $km^2$ occur on the partially-preserved, heavily-cratered raised rims of old craters that are floored by smooth plains (Figure 2-9b). The hollows do not appear to be particularly associated with any one crater but occur wherever this rougher, higher elevation substrate occurs. This substrate can be classified as low-reflectance material (LRM), whereas the crater fills are high reflectance plains (HRP). Hollows in the northwest grouping have an areal extent totalling ~498 $km^2$. The eastern part of this grouping lies in and around a wide graben outside the northwest rim of the Caloris basin, which may have been carved by ejecta during the Caloris impact event (*Fassett et al.*, 2009). From this area towards the west, hollows occur on the circum-Caloris low-reflectance blue plains (LBP) at the margins of a curvilinear unit of high reflectance material that appears contiguous with a region featuring several broad channels, possibly lava channels (*Byrne et al.*, 2013) near the margins of the northern smooth plains (Figure 2-9c). In the far northwest, hollows preferentially form in and around localized very low reflectance deposits (dubbed 'dark spots' by *Xiao et al.* (2013)), which occur on a non-plains substrate adjacent to the smooth-floored channels and to pits that are possible sources of fluid lava that carved the channels (*Byrne et al.*, 2013). The 'dark spots' occur on a rough, cratered substrate that appears superficially smoothed. This smoothing is particularly pronounced in lower elevation areas (Figure 2-9d).

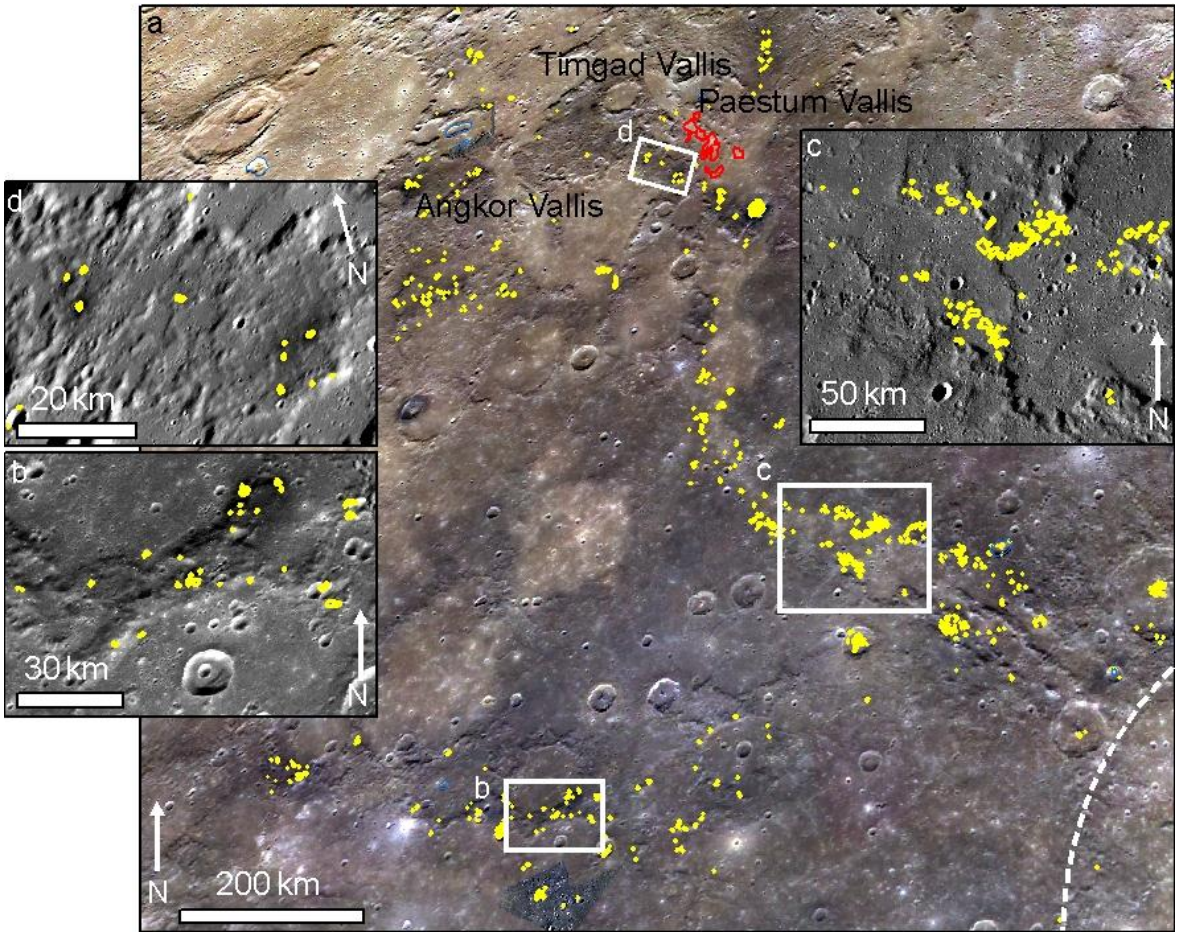


**Figure 2-9 Two dispersed groupings of hollows occur to the northwest of the Caloris basin (a) Regional view. Hollows outlined in yellow, dashed white line = basin rim. The northwest grouping extends to a region featuring several named valles, thought to be lava channels (*Byrne et al.*, 2013), several pits (outlined in blue and a group of areas of spectrally red pitted ground (outlined in red). Hollows associated with specific impact craters have been omitted from this diagram. Extent of insets indicated by white boxes (excerpt from the global colour mosaic). (b) Hollow formation in the southern grouping occurs on LRM forming degraded crater rims (image ID EW0264188888G). (c) Hollows in the mid-part of the northern grouping form at the margins and on the margin-proximal floor of a smooth, curvilinear unit of HRP (excerpt from the global monochrome mosaic). (d) Hollows (outlined in yellow) occur in 'dark spots' on regions of the non-plains surface that are adjacent to smooth channel floors and appear superficially smoothed (mosaic of image ID EW0231135561G, EW0231135600G and EW0231135586G).**

### 2.4.5 Association with pyroclastic features

Non-impact-related pits have hollows within 50 km of them in 74% of the cases where the resolution of the available images allows hollow identification, showing a strong association. 71% of these pits have surrounding spectrally-red deposits, proposed to be pyroclastic in origin (e.g. *Kerber et al.*, 2011). The association between hollows and pits within craters is stronger than the association of hollows and pits outside craters. 77% of pits within craters have nearby hollows, while only 47% of pits outside craters do. All of the areas of spectrally red pitted ground that were imaged at a high-enough resolution to identify hollows did have hollows within 50 km of them.

The reverse relationship is not as strong: only 22% of hollow groups lie within 50 km of a pit or pitted spectrally red area, 93% of which have associated bright red deposits indicating pyroclastic activity. The areal extent of these groups of hollows is higher than average: they total 52.5% of the total hollowed area and have a mean extent per group of 307 $km^2$ (standard deviation = 855) (compared to a mean of 129 $km^2$ (standard deviation = 475) for the total population). Formation of hollows in the vicinity of pits is more frequent in longitude bins crossing the 'cold poles' than near the 'hot poles' (Figure 2-10), but variations in percentage of the hollowed area within those bins do not follow this pattern (Figure 2-10b).

### 2.4.6 Association with regional substrates

Previous studies have indicated an association between hollow formation and low-reflectance material, both the regional LRM unit (*Blewett et al.*, 2013) and localized, possibly lower reflectance (*Xiao et al.*, 2013) deposits. The results of my survey support this: 96% of the total hollowed area occurs associated with either regional or localized low-reflectance material. The hollows incise the low-reflectance material and are floored and/or haloed by bright relatively blue material.

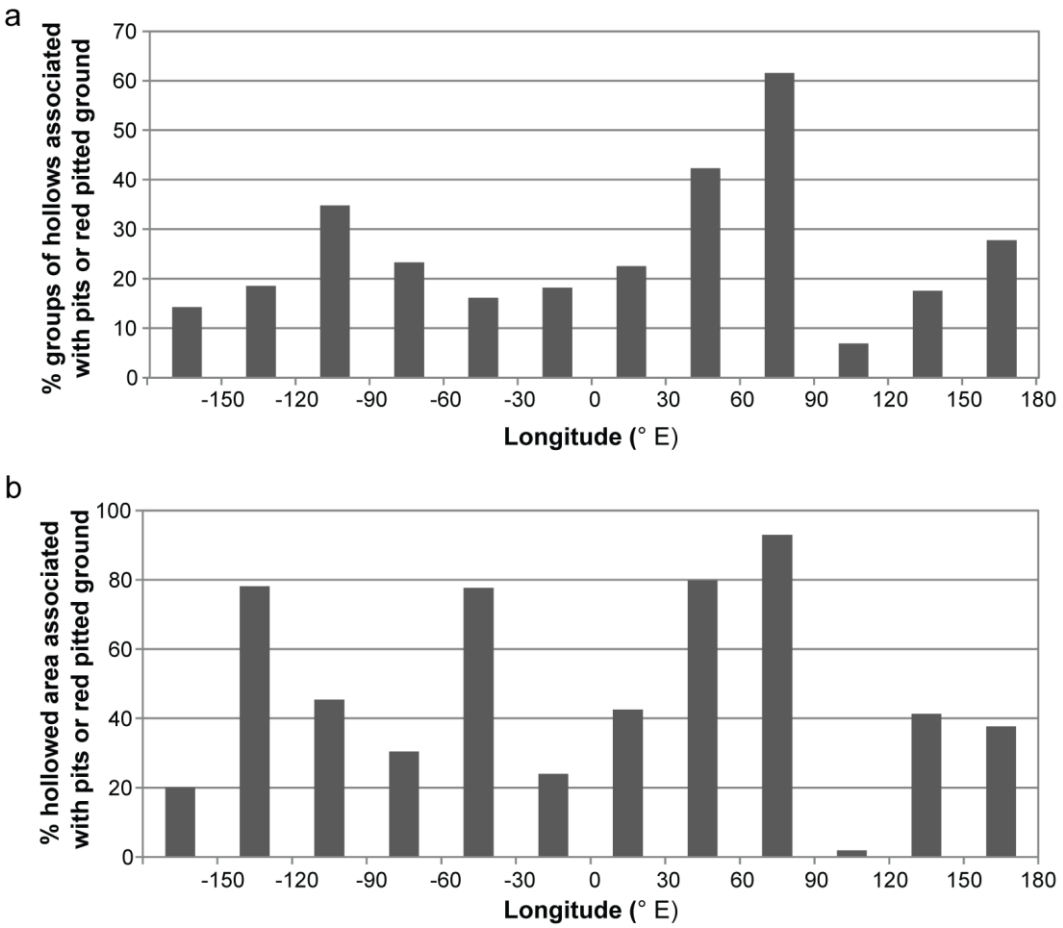


**Figure 2-10 Latitudinal variation in the association of hollows with pits and spectrally red pitted ground. (a) Hollows more commonly occur near these features at 'cold pole'-crossing latitudes (-90° E and 90° E) than at 'hot pole'-crossing latitudes (0° E and 180° E) but (b) the percentage of the surface area that is hollowed shows no regular variation.**

I found that hollows are considerably rarer on plains substrates: only ~ 7% of the hollowed area occurs on high-reflectance plains (HRP) and ~ 8% on low-reflectance blue plains (LBP). Where hollows occur on regional HRP, low-reflectance material is almost always present at the surface locally (37 out of 38 cases). Local low-reflectance material is also present in 25 out of 33 cases where hollows occur on regional LBP.

The preference for hollow formation in low-reflectance material rather than high-reflectance plains is particularly clear where an impact crater straddles a contact between these two regional substrates: Figure 2-11 shows an 80 km diameter crater that intersects the LRM rim of Rembrandt basin and its HRP fill. The north and south halves of the younger crater reflect the spectral properties of these substrates, and hollow formation is only seen in the low-

reflectance substrate. This association supports the theory that the hollow-forming volatiles are derived from a constituent of low-reflectance material.

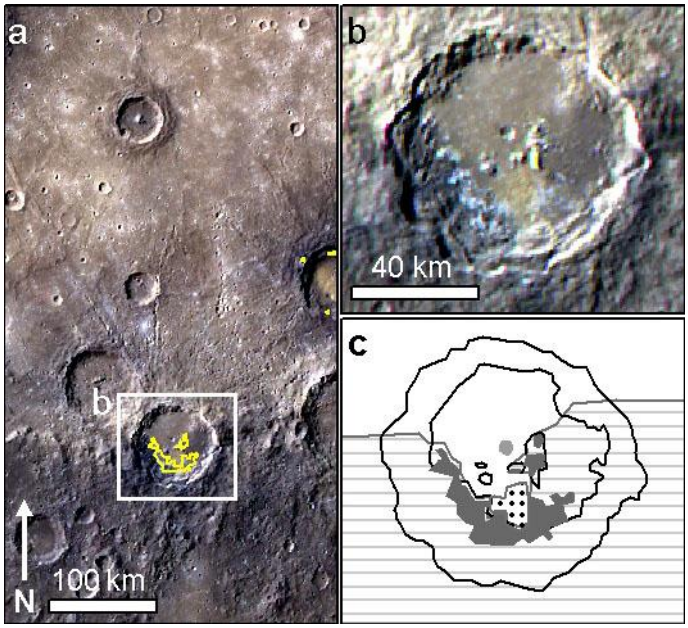


**Figure 2-11 Mansurian age crater straddling the southern rim of Rembrandt basin. Hollows (outlined in yellow) occur in the southern part of the crater, which has a low-reflectance substrate, and not in the high-reflectance northern part. (a) Location of the crater at the southern margin of Rembrandt basin (excerpt from global colour composite, centred at 88.1° E, -37.3° N). (b) The relation of hollows, a small pit and a pitted red area to the two substrates (colour composite based on EW0221673142G). (c) Sketch map of the area in b, black outlines: crater terraces and peak structures, dark grey: hollowed area, light grey: pit; dotted fill: pitted red area, hatched: LRM surfaces.**

## 2.5 Discussion

The results presented in this study have implications for the mechanisms that form hollows and bring hollow-forming volatiles to the surface, and provide clues to the origin of these volatiles.

### 2.5.1 Hollow formation mechanisms

#### *2.5.1.1 Exogenic processes*

Previous studies have suggested that hollows may form by sublimation or by space weathering processes (*Blewett et al.*, 2011), such as photon-stimulated desorption or sputtering by the solar wind.

Sublimation could form hollows if a moderately-volatile substance that is unstable at the temperatures and pressures at the surface of Mercury becomes exposed. It would then transition from solid to gas and be lost to space via the exosphere, leaving a depression. One reason why this is thought to be a viable mechanism is the morphological similarity between hollows and 'Swiss cheese' terrain in the south polar region of Mars. 'Swiss cheese' terrain is believed to form by scarp retreat as $CO_2$ ice sublimes (*Byrne and Ingersoll*, 2003a). The depth of sublimation may be limited by the thickness of the subliming layer: the $CO_2$ ice overlies a water ice layer that is more stable. This may also apply for hollow formation, though unless the volatile component of hollow-forming material is 100%, accumulation of a residual lag is likely to limit hollow depth (*Blewett et al.*, 2013).

'Swiss cheese' terrain is not a perfect analogue for hollows. The floors of the depressions in 'Swiss cheese' terrain are smooth and their outlines are more regular and cuspate. The cuspate outlines are believed to result from the consistency of the solar incidence angle through the day in polar regions (*Thomas et al.*, 2000; *Byrne and Ingersoll*, 2003b). As most of the hollows I have observed are closer to the equator, it is perhaps not surprising that hollows have more irregular margins if sublimation is responsible for their formation. The uneven floors of hollows compared to Swiss cheese terrain suggest that unlike sublimation of $CO_2$ ice, the formation of hollows leaves an appreciable lag fraction, and is perhaps brought to a halt when the surface lag has reached a critical thickness.

If hollows form by sublimation, it is probable that their occurrence would be correlated with local and regional variations in insolation. My results are consistent with this. Though few hollow groups show preferential formation on slopes of a particular orientation, when they

do so there is a strong preference for the sun-facing slope (Figure 2-5). The longitudinal variation in hollowing also supports a correlation with insolation intensity: when the effect of substrate is removed from a plot of the variation in the extent of hollowing at equatorial latitudes (Figure 2-3b), it varies broadly with variations in the intensity of insolation. If surface temperature controls hollowing, one would expect to see a greater reduction in the extent of hollowing with increased latitude than at different longitudes because the difference in maximum surface temperature between the equator and poles is larger than between points on the equator (*Peplowski et al.*, 2014). My data show such a pattern, but observational biases and differences in substrate mean this is not a robust result.

Thus I find that hollow formation appears to be correlated with insolation intensity, but not strongly. In most cases hollows form on flat surfaces, or else hollows within a group occur on slopes with a variety of aspects. This may suggest that the threshold above which insolation causes hollow formation is commonly met on the surface of Mercury.

A correlation of hollow location with insolation intensity does not uniquely point to sublimation as the formation mechanism. High insolation also means a higher photon flux, promoting photon-stimulated desorption (PSD). In this process, UV photons strike the planetary surface and excite atoms, which are then desorbed and can be lost to the exosphere. This process is intensified by high temperatures, possibly due to enhanced diffusion to the topmost surface (Yakshinskiy and Madey, 2004), and PSD fluxes contributing to the exosphere are up to three times higher from equatorial surfaces at perihelion than at aphelion (Lammer et al., 2003). This is consistent with the disparity of my results at different equatorial longitudes. However, PSD is a phenomenon of the extreme surface, affecting the topmost layer of atoms. Unless the volatile elements that are susceptible to loss by this mechanism can be very efficiently delivered to the surface through any lag components, or unless churning of the regolith by impact gardening exposes fresh materials very efficiently, it is not probable that it plays a major part in hollow formation.

Another possibility is that hollow formation is enhanced by, rather than caused by, high daytime insolation, because this leads to greater diurnal temperature variation. The varying

temperature in the top few tens of cm of the surface (*Vasavada et al.*, 1999) could set up a circulation system that could concentrate volatiles sufficiently to allow hollow formation by one or more of the processes suggested here.

In light of the extreme conditions at Mercury, at an average of 0.387 AU from the Sun, the solar wind must be considered as a possible agent to produce hollows. When solar ions strike the planet's surface, they may remove material through momentum transfer in a process known as physical sputtering. The importance of this process is potentially testable by looking at latitudinal variations in hollow formation: under normal solar wind conditions, the maximum precipitation flux of solar wind ions onto Mercury's surface is expected at high latitudes due to their direction along open magnetic field lines (*Sarantos et al.*, 2007), while other areas of the planet's surface as subject to ion bombardment only during relatively short-lived conditions of higher dynamic pressure (*Siscoe and Christopher*, 1975; *Kabin et al.*, 2000; *Slavin et al.*, 2010). This may mean the effects of physical sputtering are more pronounced at high latitudes than low latitudes. One would also expect a stronger effect on areas under the sun at perihelion than at aphelion, as the flux through open field lines is modelled to vary by a factor of four and the area open to the solar wind by a factor of two between these orbital points (*Sarantos et al.*, 2007). However, given the observational difficulties that hamper identification of hollows at polar and high southern latitudes and the presence of a plains substrate at high northern latitudes that appears to preclude hollow formation on compositional grounds, my current data does not allow me to confidently compare the extent of hollow formation at high vs. low latitudes. I do not rule out solar wind sputtering playing a part in hollow formation, though the stronger evidence for a correlation with insolation intensity at lower latitudes suggests that surface temperature plays a strong role and that sublimation is probably the dominant mechanism.

#### *2.5.1.2 Endogenic processes*

The strong correlation of pyroclastic pits and areas of spectrally red pitted ground with hollows (Section 2.4.5) suggests that endogenic heat sources may contribute to the heat necessary to release the volatiles within hollow-forming substrates. If magmatic activity was

contemporaneous with hollow formation at these sites, the heat of subsurface magma may have mobilized the volatile component of the host rock. This component may either ascend to the surface, condense and later be removed by sublimation, possibly aided by heat from below, or ascend as a gas and cause hollows to form by collapse of surface material due to volume loss in the underlying substrate.

The first hypothesis best fits the evidence, as hollows around pits have the same morphology as those on crater surfaces. Though it is possible that hollows and pits are found together only because they both occur in the same substrates for independent reasons, it is revealing that the areal extent of hollowing is on average higher around pyroclastic pits than elsewhere. Additionally, at locations where there is less insolation and so initiation of hollows would be relatively more strongly affected by any endogenic component to volatile mobilization, a higher proportion of hollow groups occur near pits. This suggests that proximity to pyroclastic pits leads to more hollow formation. Also, the percentage of the total hollowed area within each longitudinal band that is near pits is not strongly correlated to variations in the intensity of insolation (Figure 2-10b), suggesting that conditions in the vicinity of particular pits exert a stronger control on the extent of hollowing than do variations in mean insolation.

The second hypothesis, that hollows form by surface collapse when hollow-forming volatiles are lost, may be a more suitable explanation for the shallow areas of pitted ground with red deposits. These areas look similar to hollows but are deeper, more uneven, have a less crisp morphology and in all cases have hollows in their vicinity. They are also all found on smooth substrates, in most cases crater floors. This juxtaposition is seen clearly at Rachmaninoff basin (Figure 2-12). Here, hollows form in the low-reflectance material of the crater's peak ring and walls, and on the younger volcanic crater fill (*Marchi et al.*, 2011) around areas of spectrally red pitted ground. The presence of low-reflectance material on the crater's peak ring and walls suggests this material also forms the substrate to the volcanic infill. The lava may have heated the substrate and released its volatile component. Before the lava fully solidified, disruption of its surface by escaping volatiles and collapse due to volume loss in the

substrate may have given it a pitted morphology. This can be seen as broadly analogous to the process by which pitted terrain is suggested to form by the release of volatiles through impact melt on Mars (*Boyce et al.*, 2012) and Vesta (*Denevi et al.*, 2012). The spectrally-red deposits may indicate that magmatic volatiles and entrained juvenile material also escaped to the surface along the same pathways as the hollow-forming volatiles.

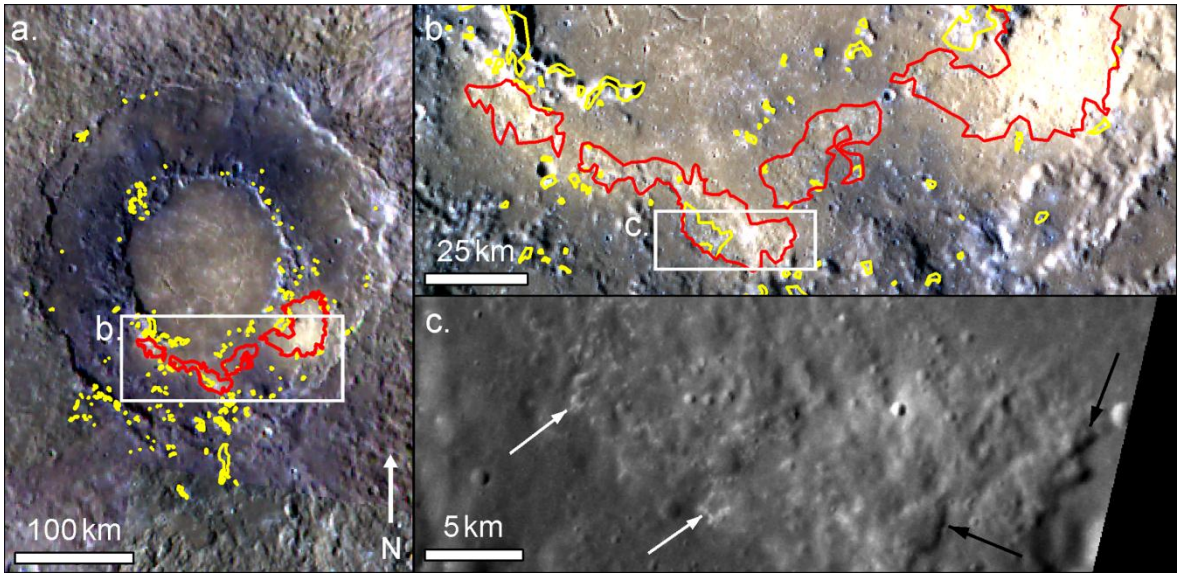


**Figure 2-12 Hollows, LRM and spectrally red pitted ground in Rachmaninoff basin (a). Hollows (outlined in yellow) form in low-reflectance material in the peak ring and walls of Rachmaninoff basin (3.6 Ga old (*Marchi et al.*, 2011), 57.4° E, 27.6° N) and around bright, relatively-red areas (outlined in red) south of a breach in its peak ring (excerpt from global colour mosaic). (b) The area south of the breach in the peak ring, where the bright spectrally-red areas are seen to be areas of pitted ground with hollows near their margins (composite of EW0254942264G, EW0254942268F and EW0254942272I). (c) Close-up of an area of pitted ground with steep margins at some points (black arrows) and hollow formation near its margins (white arrows) (EN0219350311M).**

Such a process may also explain the morphology of hollowed areas on crater floors over buried peaks rings, such as Sousa crater (Figure 2-13). The morphology of these areas is similar to that of those areas of spectrally red pitted ground that lack margins, but they have no associated red deposits. Here the crater fill (either impact melt or a later volcanic infill) may have volatilized a component of the buried low-reflectance peak ring, and released this material to the surface at the point where the fill is thinnest. This led to collapse of the surface

and some formation of crisper hollows where escaped material condensed on the surface before losing its volatile component via sublimation. This hypothesis is an extension of that of *Blewett et al.* (2013) that hollows may form through concentration of hollow-forming volatiles by contact heating.

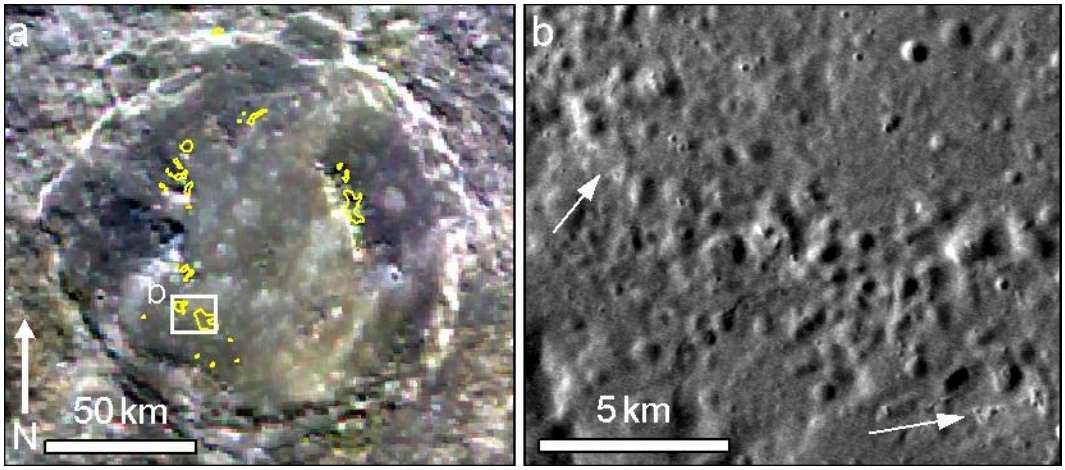


**Figure 2-13 Hollows (outlined in yellow) on the LRM peak ring and the crater fill where this overlies the peak ring in Sousa crater (Mansurian age, 0.5° E, 46.8° N). (a) Locations of hollows within the crater (outlined in yellow) (excerpt from global colour mosaic). (b) Close-up showing the majority of the hollowed region in the crater fill is pitted ground, with some small crisp hollows (white arrows) (mosaic of EN0251054159M and EN0251054171M).**

The global distribution of hollows does not simply mirror variations in insolation, and many hollows occur at a distance from pits and potential pyroclastic activity and without contact with crater fills. A further factor plays a stronger controlling role on the formation of hollows: substrate. This determines the quantity of hollow-forming volatiles at and near the surface, and the ability of volatiles to ascend to the surface. I explore this aspect below.

### 2.5.2 Means of transfer of hollow-forming volatiles to the surface

#### *2.5.2.1 Exhumation and exposure by impacts*

The strong correlation of hollows with craters suggests a genetic link. The vast majority of hollows lie within impact craters and their proximal ejecta. Hollows do not form on volcanic plains except where these have been breached by later impacts, and most of the small hollow clusters that occur outside impact craters appear to form in impact ejecta. For these reasons,

it has previously been suggested that hollows form in material exposed and exhumed by large impacts (*Blewett et al.*, 2011). Larger impacts sample the crust to greater depths compared to smaller impacts, exposing the strata underlying the impacted surface in their walls and ejecta, and uplifting material from depth in their central structures. The evidence supports this hypothesis. Hollows occur in low-reflectance material within impact craters, particularly on peak rings, which are the part of a crater that is exhumed from the greatest depth (Figure 2-14). The surface distribution of this low-reflectance material is consistent with the substrate into which the crater incised (Figure 2-11) as expected if it is exhumed material.

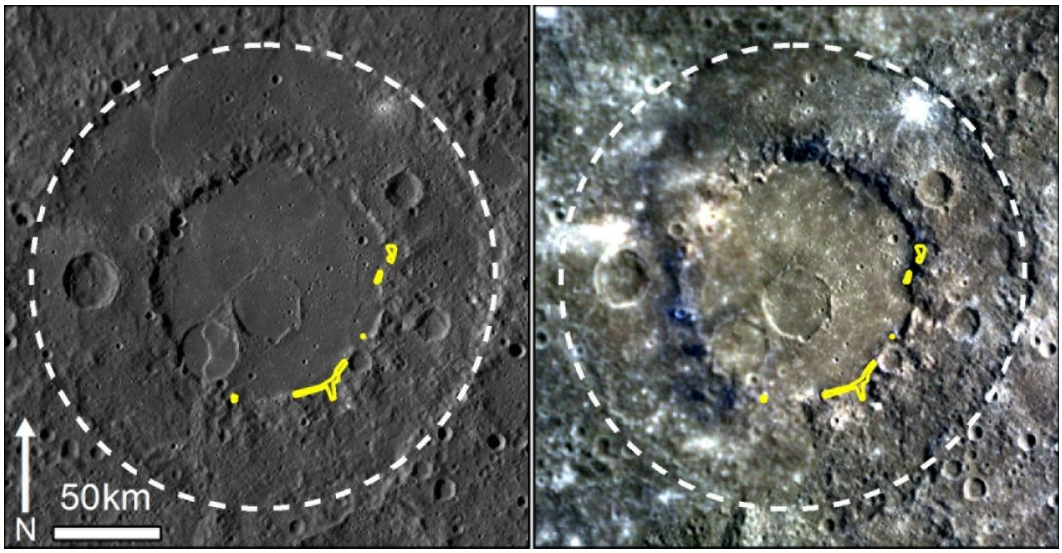


**Figure 2-14 Localization of hollows (outlined in yellow) and low-reflectance deposits in the peak ring of Renoir basin (Tolstojan age, -51.8° E, -18.3° N). Dashed white line shows the outer rim of the basin, where no low-reflectance material or hollows are observed. Left: excerpt from global monochrome mosaic; right: mosaic of colour composites based on EW0253851174G, EW0253851412G and EW0241374406G.**

The lack of correlation between increasing crater age and extent of hollows (Figure 2-7) could be seen as weakening this hypothesis: if hollowing begins at the time of crater formation, older craters should have a larger extent of hollows. However, firstly, the small scale of hollows means they may become obscured by later overlying ejecta over time and the areal extent of hollows visible in older craters may not be indicative of the true cumulative amount of hollow formation there. Secondly, if the quantity of material that can form hollows

is limited, hollow formation will eventually cease. This explains the drop-off in observed hollowed extent in craters of Calorian age (degradation state 3) and older (Figure 2-7).

Estimates of potential burial rates at Mercury's surface vary: regolith formation has been estimated at 5–10 m in the last 3–4 Ga (*Langevin*, 1997), while burial of polar ice deposits has been modelled to occur at a rate of 0.43 cm/Myr (*Crider and Killen*, 2005). The former rate would be sufficient to obscure the morphology of hollows and the latter to completely bury them in the estimated 3.9 Ga (*Neukum et al.*, 2001)) since the Calorian period.

It has alternatively been suggested (*Vaughan et al.*, 2012) that hollows form in material differentiated out of impact melt during crater formation. I find this to be an unconvincing explanation: hollows are found in small ejecta deposits distal from their host craters (Figure 2-8) and on a variety of steep surfaces. While differentiation is viable in pooled melt, it is difficult to envision in settings such as these.

#### *2.5.2.2 Post-impact exposure*

The presence of hollows in even very old craters (Figure 2-7) indicates that in these cases a process is operating that replenishes hollow-forming material at the surface of craters long after crater formation. My observation that hollows in older craters are found in the walls of younger craters and on thrust faults (Figure 2-6d) suggests that these are the agents of this late exposure. If hollow-forming material was exposed to surface conditions during the formation of the original crater, hollow formation may have ceased prior to its depletion in the near-surface due to deposition of a lag or burial by ejecta. Small new craters, crater-crossing thrust faults and fractures at fault-bend folds may have later exposed it to surface conditions, at which time fresh hollows formed.

Such processes may operate on a regional scale to produce the western broad area of distributed hollowing outside the Caloris basin (Figure 2-9a). The low-reflectance deposits here are close enough to Caloris to have been deposited as ejecta from that impact, and may have originally been as volatile-rich as the extensively-hollowed, very dark LRM deposits that are exhumed by younger impacts into the Caloris fill. The heavily-cratered appearance of the

hollowed surfaces suggests they are old and that any initial hollow formation in them would have long ceased, but smaller impacts and possibly mass wasting may continue to expose new volatile-bearing material to surface conditions and initiate new hollows.

The association of hollows with pyroclastic pits within craters could indicate that the structures associated with this volcanism aided the release of hollow-forming volatiles from depth. Pyroclastic pits occur primarily in parts of impact craters that are underlain by planes of weakness such as wall terraces and central structures. This suggests that crater-related faults act as conduits for the release of volatiles or volatile-bearing magma towards the surface, possibly aided by on-going fault movement in response to global contraction (*Klimczak et al.*, 2013). The same may be true for hollow-forming volatiles. The evidence does not, however, allow a definite identification of this phenomenon. For example, Figure 2-15 shows hollows around a pyroclastic pit in the north-west rim of a younger crater that intersects the wall of an older crater, and also hollows in small areas to its south. This could be explained by the migration of hollow-forming volatiles up the same crater-wall faults as were exploited by the probable pyroclastic volcanism. However, exhumation is a viable alternative explanation: hollow-forming volatiles may have been present in the deeply-excavated wall material of the older crater and then been exposed by the younger crater. The small cluster of distal hollows may be located in the ejecta from this impact. In this scenario, the association of hollows with pyroclastic volcanism may be partly due to the spatial coincidence of deep fractures that are conducive to magma ascent with volatile-bearing wall rocks, and possibly, if hollow formation and volcanism were contemporaneous, partly due to increased heat flow in this area enhancing upward diffusion of volatiles or hollow formation by sublimation (Section 2.5.1).

#### *2.5.2.3 Exposure outside craters*

A non-impact-related process is necessary to explain the exposure of hollow-forming material to produce the broad area of distributed hollowing along a curvilinear unit of HRP to the northwest of Caloris. These hollows form in LBP and on LRM outcrops standing above the plains. I propose that the HRP unit is a lava flow, and that contact heating by this material

caused concentration of volatiles from within the LBP and LRM substrates at the surface (in a process similar to that suggested for other incidences of hollowing by *Blewett et al.* (2013)), after which hollows formed by sublimation.

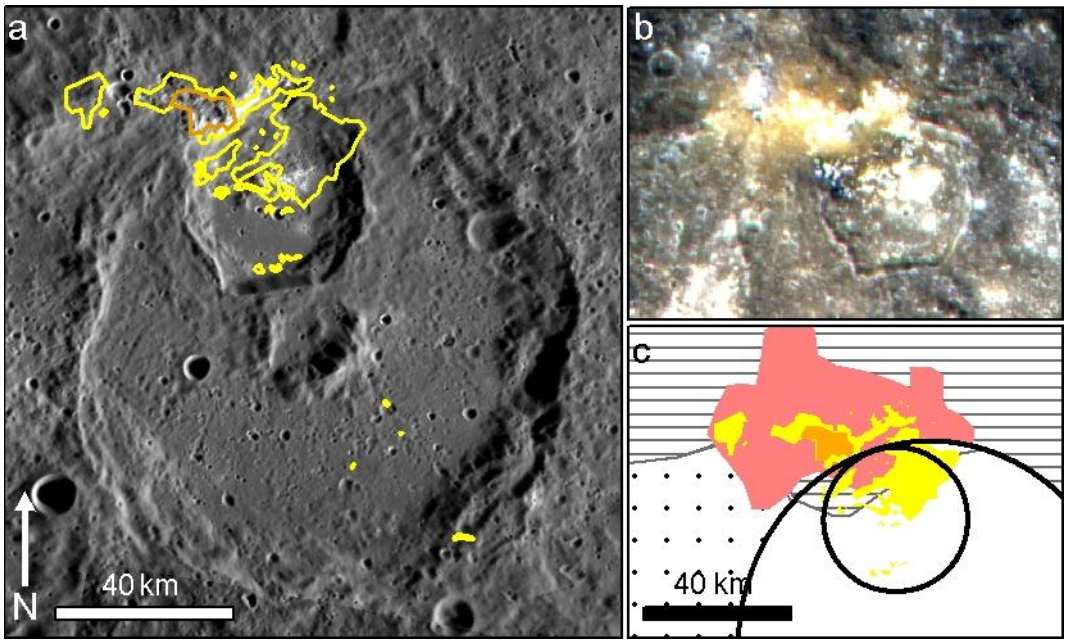


**Figure 2-15 Hollows and a pyroclastic pit at the rim and wall of an impact crater. (a) Hollows (outlined in yellow) occur at the north-west edge of a Calorian age crater at -3.6°E, 25.6°N, around a pyroclastic pit (outlined in orange) and scattered towards the south. This may be due to explosive escape of hollow-forming volatiles up the same conduits as used by the pyroclastic volcanism, or, if the two phenomena were contemporaneous, hollow formation in crater deposits and ejecta intensified in the region of volcanism by endogenic heat flow (MESSENGER global monochrome mosaic). (b) Colour composite of the superposed crater in the north (based on EW0225312562G). (c) Sketch map of (b): hatched area: low-reflectance material; dotted area: bright ejecta; pink area: bright 'red' deposits; orange area: pit; yellow area: hollowed area; black outline: crater walls.**

The formation of hollows in small 'dark spots' at the far northwest of this grouping (Figure 2-9d) is more enigmatic. These 'dark spots' occur on a non-plains substrate in which lower elevation areas appear anomalously smooth, adjacent to broad, smooth-floored channels and to pits that have been suggested as the source of voluminous lavas that carved those channels (*Byrne et al.*, 2012; *Hurwitz et al.*, 2013). It is possible that surface here appears somewhat smoothed because it has been draped by a thin layer of lava. This may have covered a

volatile-bearing substrate to a shallow depth. Subsequently either a high regional heatflow connected to magmatic activity volatilized the underlying substrate or burial was sufficiently shallow (< 1 m (*Vasavada et al.*, 1999)) for penetration of solar heating do so. Pressure built up and finally volatiles were released through fractures in the overlying material. This is consistent with the hypothesis that 'dark spots' form during intense outgassing during hollow formation (*Xiao et al.*, 2013). This process may have directly produced hollows in the manner of fumerolic vents, or through deposition of the volatile-rich dark material on the surface followed by its sublimation.

### 2.5.3 Nature of the hollow-forming material

Hollows are commonly found in low-reflectance material. Conversely, they are found in high-reflectance smooth plains only where low-reflectance material is locally present such as where younger impact craters exhume it from beneath the volcanic fill of the Caloris basin.

This strongly suggests that the volatile material responsible for hollow formation is not present in high-reflectance flood lavas, but is a component of low-reflectance material. The nature of low-reflectance deposits on Mercury is not yet established, although it has been suggested that the regional LRM unit could be primary crust (*Rothery et al.*, 2010) or a cumulate darkened by Fe- or Ti-bearing or other opaque oxides (*Denevi et al.*, 2009; *Riner et al.*, 2009). Space weathering complicates the determination of the composition of LRM on the basis of reflectance: the creation of nanophase iron during space weathering leads to more darkening of rock types initially richer in iron, so the albedo of any rock is the product of its composition and mineralogy, its exposure time and its susceptibility to space weathering (*Riner and Lucey*, 2012).

The presence of low-reflectance material in some craters of a particular diameter (and thus excavation depth) and absence in others shows that low-reflectance material is not present globally at a specific depth, so variations in the igneous and/or tectonic history of different parts of Mercury's crust appear to play a role in its occurrence. For example, the formation of

the Caloris impact basin may have exhumed large amounts of this material, providing the substrate for the broad regions of dispersed hollow formation to its northwest.

The relatively lower reflectance of some localized deposits around hollows (*Xiao et al.*, 2013) may suggest that before LRM has been hollowed it contains an additional darkening agent, and that this is the hollow-forming volatile. This may explain the presence of bright material in haloes around hollows and on their floors, which could be a brighter residue formed by the removal of a spectrally dark component (*Blewett et al.*, 2013). Alternatively, the high reflectivity of these deposits may be due to an unusual texture or small grain size (*Blewett et al.*, 2013). The diffuse margins of the haloes suggest two possible emplacement mechanisms for the bright material: a) ballistic ejection of a bright component as a result of high-energy escape of the hollow-forming volatiles, or b) diffusive alteration of hollow wall rock as a result of chemical reactions during hollow formation. In both cases, either the compositional or physical characteristics of these bright deposits could potentially be the cause of their high reflectance.

The composition of the darker, volatile component is as yet unknown, but will perhaps be resolved when BepiColombo with its higher-resolution visible-NIR, thermal infrared and X-ray spectrometers (*Rothery et al.*, 2010) arrives at Mercury in the coming decade.

## 2.6 Conclusions

1. In a global survey of the surface of Mercury, I found that the shallow rimless depressions know as hollows cover ~57,400 $km^2$, which is 0.08% of the total surface imaged at better than 180 m/pixel.
2. A weak overall correlation was found between hollow occurrence and insolation, as well as a possible correlation with subsurface heat sources. Both suggest a thermal control on hollow formation, thus supporting sublimation as the primary hollow-forming mechanism.
3. In most cases it appears probable that material containing hollow-forming volatiles was exposed and exhumed from depth by large impacts.

4. Some small impact craters and thrust faults within older craters also have hollows, hence these structures may expose subsurface hollow-forming material or facilitate the migration of volatiles to the surface. This suggests that some volatiles remain in the near-subsurface even after hollow formation has ceased at the surface.
5. Hollows do not occur in volcanic plains but are found mostly in low-reflectance material. This suggests that this low-reflectance material has a volatile component, and that hollows are formed by loss of that component. The widespread occurrence of hollows suggests that this material is similarly widespread within the crust of Mercury.

## 2.7 Epilogue: new data and additional statistical tests

Since the publication of the paper that makes up this chapter, new images (released by NASA's Planetary Data System up to 6th March 2015) have become available that have increased the number of recognizable hollows (Table A-1). Where these have affected the values quoted in this chapter, the changes are listed in Table 2-2.

There is only one regard in which these new results qualitatively affect the published findings: the proportion of the non-plains surface shows a less pronounced increase towards the 'hot pole' at 180° E (Figure 2-16) than previously indicated (Figure 2-3). However, the overall trend of more hollowing near the 'hot poles' is still supported. When the outlying result from the -60 to -40° E bin is removed, the percentage of each longitude bin that is hollowed, normalised to the non-plains area within that bin, correlates with relative insolation intensity with a Pearson Product-Moment Correlation Coefficient of 0.52, where 1 is total positive correlation.

**Table 2-2 Updates to published (*Thomas et al.*, 2014a) values in this chapter**

| Description | Published value | Updated value |
|---|---|---|
| Count of hollow groups | 445 | 481 |
| Count pit groups | 173 | 177 |
| Count of spectrally-red pitted ground | 24 | 28 |
| Total global area hollowed, km$^2$ (% of adequately-imaged surface) | 57,400 (0.08%) | 58,100 (0.08%) |
| Areal extent of group | | |
| Mean, km$^2$ (standard deviation) | 129 (475) | 121 (466) |
| Minimum value, km$^2$ | 0.07 | 0.07 |
| Maximum value, km$^2$ | 6771 | 7015 |
| Hollows within impact craters | | |
| Percentage of all hollow sites | 84.5% | 85.0% |
| Percentage of the total global hollowed area | 97.5% | 96.6% |
| Average area of hollowing in groups within impact craters, km$^2$ (standard deviation) | 148.6 (514.0) | 137.5 (495.0) |
| Hollows outside craters | | |
| Average area of hollowing in groups outside impact craters, km$^2$ (standard deviation) | 15.2 (38) | 11.6 (33.9) |
| Area of western grouping of Caloris-radial dispersed hollows, km$^2$ | 150 | 151 |
| Area of north-western grouping of Caloris-radial dispersed hollows, km$^2$ | 498 | 519 |
| Association with pyroclastic features | | |
| Endogenic pits with hollows within 50 km, % (and with associated spectrally-red deposits, %) | 74 (71) | 77 (75) |
| Pits within craters with hollows within 50 km, % | 77 | 54 |
| Pits outside craters with hollows within 50 km, % | 47 | 35 |
| Hollow groups associated with an endogenic pit or pitted spectrally red area, % (of which have associated bright red deposits, %) | 22 (93) | 22 (94) |
| Mean areal extent of hollows at groups that are associated with an endogenic pit or pitted spectrally red area, km$^2$ (standard deviation) | 307 (855) | 328 (911) |
| Mean areal extent of hollows at groups that are not associated with an endogenic pit or pitted spectrally red area, km$^2$ (standard deviation) | 129 (475) | 63 (174) |
| Percentage of total area hollowed that is associated with an endogenic pit or pitted spectrally red area | 52.5 | 59.3 |
| Association with regional substrates | | |
| Cases where LRM is present locally and the regional substrate is HRP | 37 out of 38 | 37 out of 42 |
| Cases where LRM is present locally and the regional substrate is LBP | 25 out of 33 | 26 out of 35 |

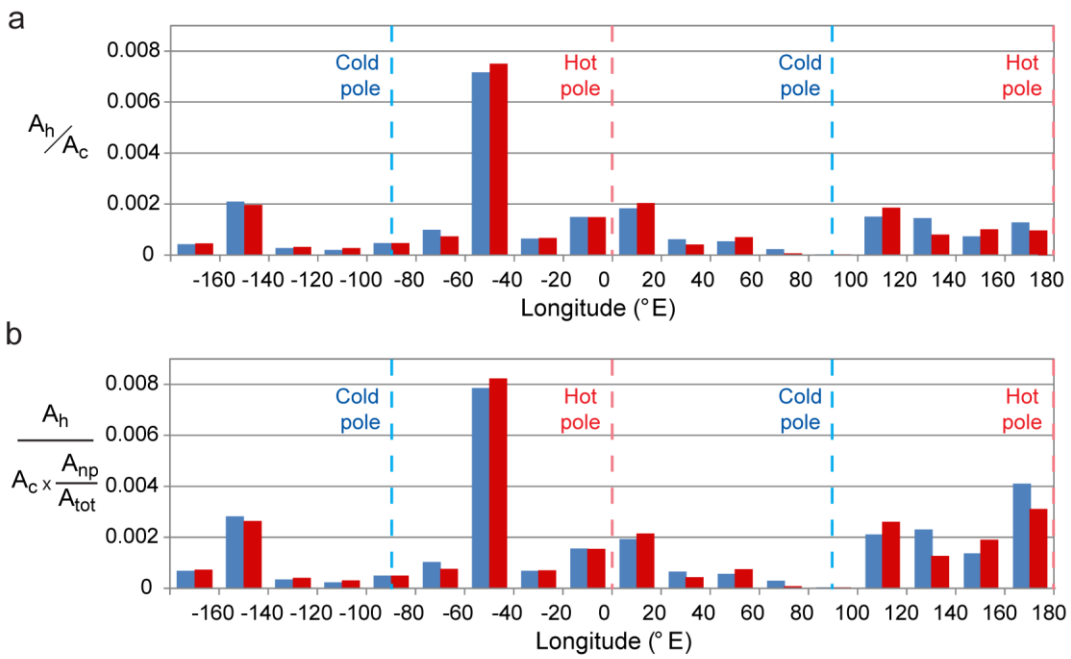


**Figure 2-16 Variation in the areal extent of hollows ($A_h$) by longitude bin in the region 30° S to 30° N (updated), normalized to (a) area imaged at < 180 m/pixel ($A_c$), and (b) $A_c$ × the fraction of the surface that is not smooth plains ($A_{np}/A_{tot}$). Blue: published values, red: updated values.**

In order to further validate the results presented in this chapter, I have compared the density of hollows observed to the resolution of the best available images. This tests the null hypothesis that the observed heterogeneous spatial distribution of hollows is a function of image resolution. Comparison of the areal coverage of hollows in 10 km × 10 km cells globally to the best image resolution available for that cell shows no systematic relationship (Figure 2-17). Thus the variability in density of observed hollows across Mercury is not solely a product of varying MESSENGER image resolution.

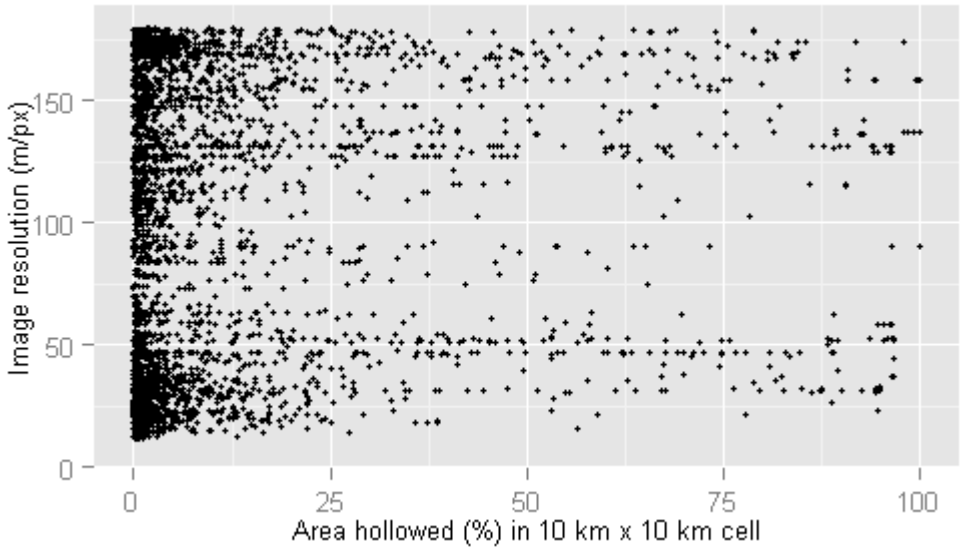


**Figure 2-17 Comparison of image resolution to hollow coverage in 10 km × 10 km cells.**

# Chapter 3. Constraining the nature of Mercury's volatile-rich surficial material through analysis of hollow floors

## 3.1 Introduction

The morphology of Mercury's hollows — steep walls, unbreached margins and flat floors — is most consistent with their formation by the loss of one or more relatively volatile substances present in high concentrations at the planet's surface (*Blewett et al.*, 2011). Their typical genesis within a low-reflectance substrate (regional LRM, localised LRM exposed by impacts or yet smaller 'dark spots') indicates that this substrate is the most common source of these volatiles. The nature of this volatile-rich material, which may be initially sourced from the planet's lower crust or upper mantle (*Ernst et al.*, 2015; *Murchie et al.*, 2015b), has implications for the planet's bulk composition (and thus its mode of formation) and for its geochemical evolution (e.g. *Vander Kaaden and McCubbin*, 2015). However, attempts to identify the volatile substance(s) involved in hollow-formation using MESSENGER data have, as yet, proved inconclusive. The kilometre scale of hollows precludes detection of variations in elemental composition in and around them by MESSENGER's X-Ray Spectrometer (XRS) (*Schlemm et al.*, 2007) and Gamma-Ray and Neutron Spectrometer (GRNS) (*Goldsten et al.*, 2007), which have, at best, resolutions of hundreds of kilometres per pixel. Analyses have therefore relied on spectral reflectance data at UV to visible wavelengths (250–750 nm) from the Mercury Dual Imaging System (MDIS) and Mercury Atmospheric and Surface Composition Spectrometer (MASCS) with pixel sizes ranging down to <100 m. However, the relatively featureless character of Mercury's surface spectra presents an obstacle to direct determination of composition: the absorption bands used to determine mineralogy on other planetary surfaces and in terrestrial laboratory experiments are very weakly developed (*Izenberg et al.*, 2014; *Murchie et al.*, 2015b). Studies have therefore focussed on broad spectral characteristics, in particular spectral slope (Figure 3-1) and overall reflectivity across the visible spectrum, which vary for different units on Mercury's surface. This has revealed that the bright material in and around hollows (referred to in this chapter as BCFD,

Bright Crater Floor Deposit, for convenience and for historical reasons (*Robinson et al.*, 2008), though it should be noted that these are not always on crater floors) has a lower spectral slope (is 'bluer') and is more reflective (is 'brighter') across the visible spectrum than any other unit barring fresh ejecta on Mercury's surface (*Blewett et al.*, 2009). The LRM within which hollows commonly form and the smoother Low-Reflectance Blue Plains (LBP) unit have a lower spectral slope than all other units barring BCFDs, but have the lowest reflectivity across the visible spectrum of the recognised regional unit types (*Murchie et al.*, 2015b). On this basis, it has been suggested that hollow-formation involves the loss of the 'darkening' agent within LRM (*Blewett et al.*, 2013), which may be spectrally neutral (making LRM relatively 'blue' by counteracting the 'redness' of other components) (*Blewett et al.*, 2009). Calcium or magnesium sulfides are most commonly-cited as candidates for both the darkening and relatively volatile substance, on the basis of the high concentration of sulfur detected at Mercury's surface (*Nittler et al.*, 2011; *Evans et al.*, 2012) and correlations between sulfur, calcium and magnesium abundance in some areas (*Weider et al.*, 2015). Laboratory spectral studies of magnesium, calcium and manganese sulfides do indicate that sulfides can be volatilized at the daytime temperatures experienced at Mercury's surface, and that extreme thermal cycling on the planet's surface could account for the lack of characteristic absorption bands (*Helbert et al.*, 2012, 2013), but have not provided a spectral match to BCFDs, LRM, or indeed any surface unit on Mercury (*Blewett et al.*, 2013; *Izenberg et al.*, 2014).

The approaches outlined above focus on BCFDs as the end-result of hollow-formation. However, higher-resolution Mercury Dual Imaging System (MDIS) Narrow Angle Camera (NAC) (*Hawkins et al.*, 2009) images obtained as MESSENGER made close approaches to the planet's surface in the latter part of its orbital mission (after Chapter 2 was published) suggest that this is not a valid assumption. These images indicate that BCFDs occur only on surfaces where hollows are actively forming, and that flat hollow floors have lower reflectivity (Figure 3-2). This raises the possibility that BCFDs are an intermediate product of hollow-formation, and that the ultimate result is material with lower reflectivity. It is

therefore necessary to investigate the spectral character of both BCFDs and these flat hollow floor areas to fully characterise changes in texture and composition during hollow-formation. In this chapter, I use multispectral data to compare the spectral character of seemingly inactive hollow floors to that of partially-developed hollows, BCFD halos and unhollowed substrates surrounding them. These comparisons allow me to investigate spectral changes over the course of hollow-formation, and thus provide constraints on the nature of the relatively volatile substance(s) lost in this process.

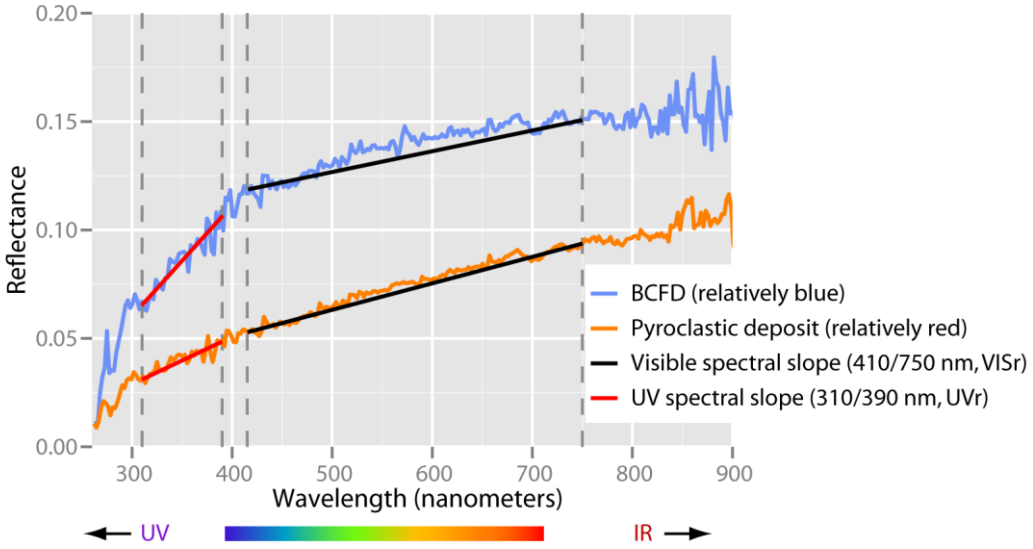


**Figure 3-1 Measures of visible (VISr) and UV (UVr) spectral slope. A steeper visible spectral slope results from greater reflectance at the red end of the spectrum than at the blue end. All spectra from Mercury are 'red-sloped' in this way, but some, such as BCFDs, are relatively 'blue-sloped' (the spectral slope is flatter). Sample data is from MASCS.**

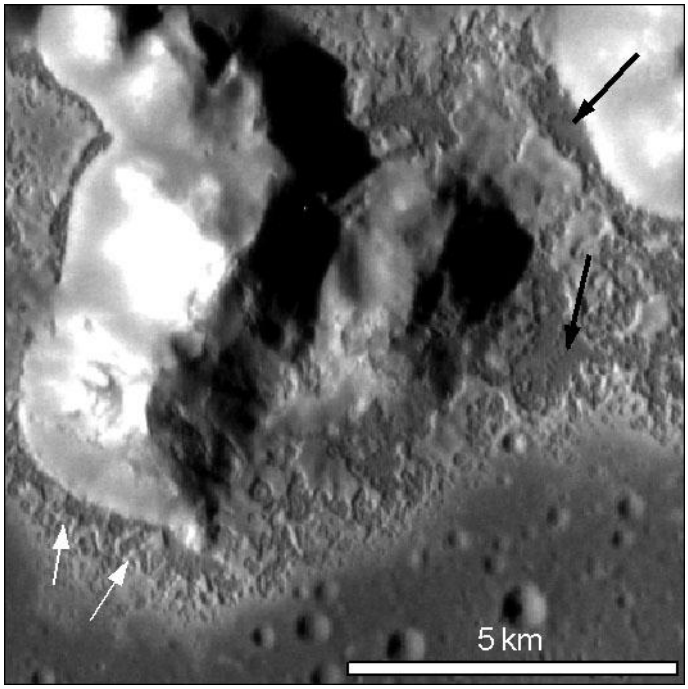


**Figure 3-2 High resolution MDIS NAC image EN0221282722M (25 m/pixel) shows that flat hollow floors (black arrows) have reflectivity comparable to that of the surrounding unhollowed unit, while upstanding knobs of material within hollows (white arrows) and the surrounding BCFD halo have relatively high reflectivity. Solar illumination from the left.**

## 3.2 Compositional analysis of hollows

To investigate changes in the character of surface materials over the course of hollow formation, I identified eight hollow groups in my global catalogue (Table A-1) where MDIS NAC images (which have a single medium-band filter centred on 750 nm) show parts of the hollow floor to be flat (lacking knobs of material) and for which MDIS Wide-Angle Camera (WAC) multispectral images are available with a pixel size smaller than that of the flat hollow floor area (Table 3-1). Hollow floors that appear dark in NAC images where solar incidence and emission angles are higher (Figure 3-3a) are brighter in images where both are lower (Figure 3-3b), indicating that lighting and viewing conditions affect reflectance at 750 nm.

**Table 3-1 Sites used to analyse the spectral character of hollow floors. Group ID is the catalogue number in Table A-1**

| Group ID | Latitude | Longitude | Regional substrate | Local substrate | Crater name | Multispectral image resolution (m/px) |
|---|---|---|---|---|---|---|
| 4030 | 38.5 | 175.6 | HRP | LRM | Balanchine | 188 |
| 6001 | 46.12 | 134.81 | IT | LRM | Pasch | 180 |
| 6040 | 41.27 | 123.93 | LBP | LRM | | 180 |
| 6054 | 10.72 | 114.38 | IT | LRM | Eminescu | 536 |
| 6070 | 27.32 | 146.14 | HRP | LRM,BE | Kertesz | 536 |
| 7020 | 40.43 | -138.08 | HRP | LRM | | 180 |
| 8001 | 30.54 | -33.35 | IT | LRM | | 204 |
| 8006 | 50.79 | -39.70 | IT | BE | | 180 |

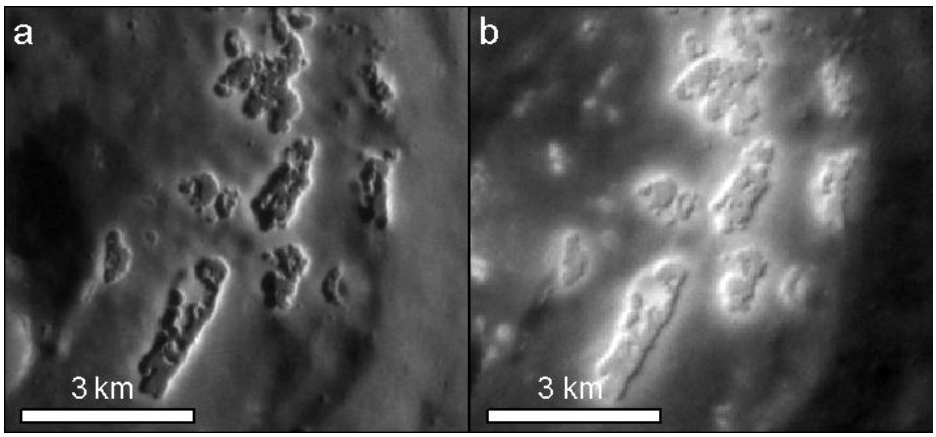


**Figure 3-3 Hollow floors in group 8001 have (a) low reflectance at 750 nm at solar incidence = 73°, emission angle = 32° (image EN0258515991M), and (b) higher reflectance at solar incidence = 45°, emission angle = 4° (image EN1017787684M).**

A 12-position filter wheel in the MDIS WAC is rotated to different positions for successive images, resulting in sets of largely-overlapping images taken under very similar lighting and spacecraft pointing conditions but capturing different parts of the spectrum. I selected the best resolution set of WAC images available for each site, and radiometrically and photometrically corrected and coregistered the 430 nm and 750 nm images using the ISIS3 image processing package of the USGS. I calculated spectral slope (VISr, the ratio of reflectance at 430 nm to that at 750 nm) by division of one image by the other. This measure of visible spectral slope is comparable with that used for VISr in MASCS data by *Izenberg et al.* (2014, 2015) (410 nm / 750 nm) (Figure 3-1). I took spot readings of VISr and reflectance at

750 nm (R750) at locations that visual comparison to higher-resolution NAC images (Figure 3-4) indicates are examples of specific unit types associated with hollows (Figure 3-5). These unit types are: 'hollow floor' — the centre of a flat hollow floor, 'BCFD halo' — an area of diffuse high-reflectance material at the margin of a hollow, 'partially-developed hollows' — an area where sub-pixel-scale hollows and upstanding knobs are seemingly draped by diffuse high-reflectance material (e.g. white arrows in Figure 3-2), 'crater wall/floor' — crater materials that are not clearly LRM on the basis of R750, and 'LRM' — low-reflectance surfaces outside hollows. As noted above, hollow floor reflectivity at 750 nm is higher in images at low emission angles (closer to nadir) and moderate solar incidence than under higher solar incidence and emission angles. The majority of WAC images used for this analysis have low emission angle and low-to-moderate (~45°) solar incidence, which can be expected to result in relatively high-reflectance hollow floors (Figure 3-6). The images used for Eminescu (group 6054) were taken at a low solar incidence angle (22°) but their high emission angle (57°) may result in lower R750 at this site.

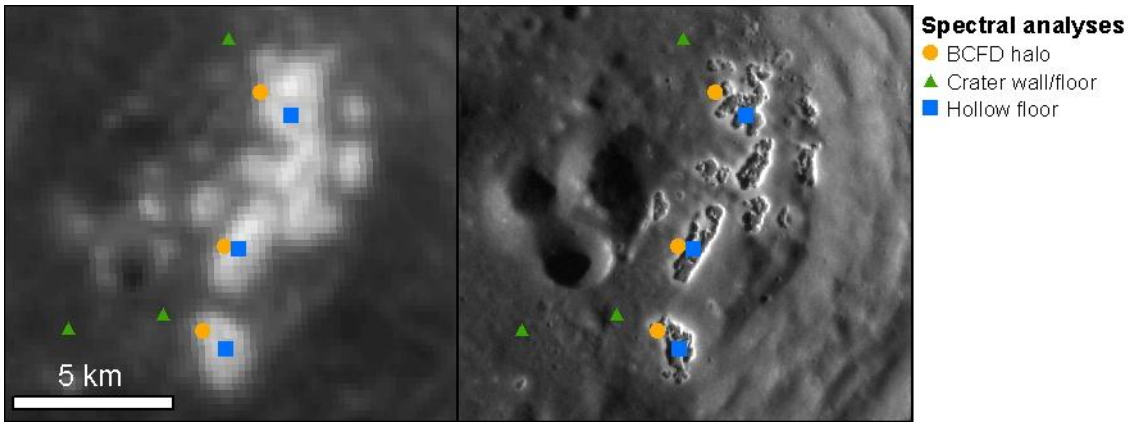


**Figure 3-4 Comparison of WAC (left, EW0210807816G) and NAC (right, EN0258515991M) images at location 8001, showing how higher-resolution NAC data provide morphological evidence for the unit type being probed at specific locations on the WAC image.**

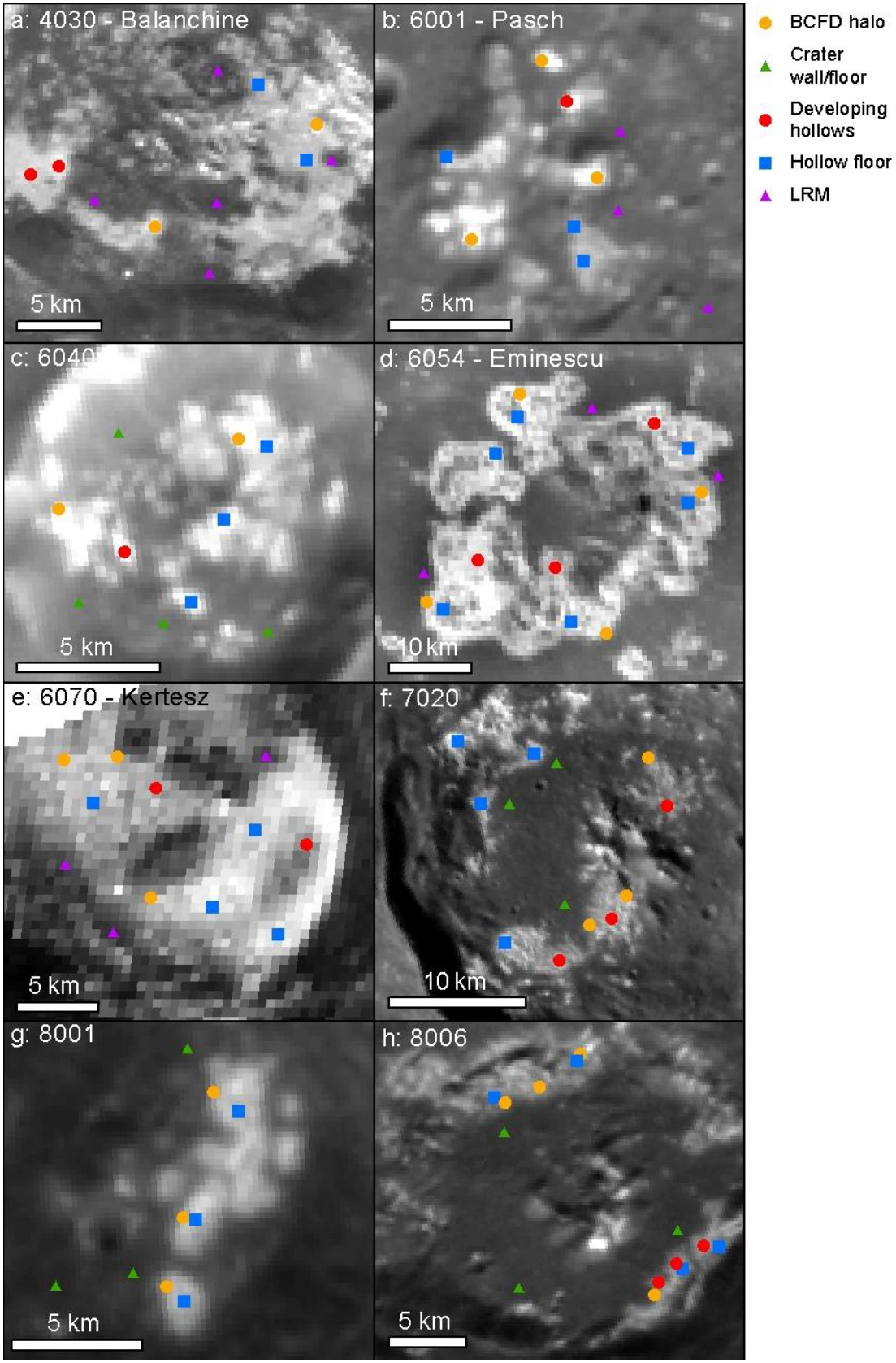


**Figure 3-5 Sites with flat-floored hollows. Headings correspond to the catalogue number of the hollow site. Dots indicate the location of point values plotted in Figure 3-7. Base: WAC images through the 750 nm filter.**

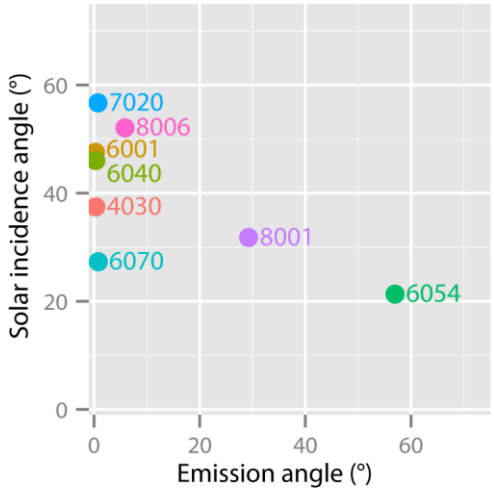


**Figure 3-6 Lighting and viewing angles of MDIS WAC images used to analyse hollow groups. Number indicates Group ID.**

Previous work on reflectance spectra from the Mercury Atmospheric and Surface Composition Spectrometer (MASCS) Visible and Infrared Spectrograph (VIRS) (*McClintock and Lankton*, 2007) indicates that spectral slope in the UV range at hollow sites is generally similar to that of surrounding substrates, raising a number of hypotheses about their composition and/or the correct interpretation of the spectral data (*Izenberg et al.*, 2015). However, the abovementioned study did not discriminate between BCFDs and hollow floors. In most cases, the footprint size of MASCS (which is, at best, 0.1 km cross-track and 3 km along-track) is insufficient to discriminate hollow floors, and could not be used in the present analysis. However at two of the selected sites, Kertesz and Eminescu, flat hollow floors are of broad enough extent to potentially be revealed by the detected spectrum. Because MASCS is non-imaging, there is no way to verify that the MASCS footprint is correctly located with respect to WAC data (global monochrome mosaic) and errors in spacecraft pointing parameters can result in a co-registration error. Therefore, I obtained spectral data for along-track footprints crossing an area of hollow floor rather than analysing individual footprints that appear to be collocated with hollow floors. This allowed analysis of how spectral slope in the UV range (UVr, 310 nm / 390 nm) varies with R750 and VISr across hollows, BCFDs and parental units (Figure 3-1).

## 3.3 Results: Spectral variation at hollow sites

Comparison of reflectivity and spectral slope at the eight sites indicates that flat hollow floors are the most 'blue' of the units sampled (VISr — 430 nm/750 nm — is relatively high) (Figure 3-7). Both BCFDs and hollow floors are 'bluer' than the surrounding substrate, even where this is LRM. At most sites, R750 of hollow floors is intermediate between that of BCFD halos/developing hollows and unhollowed surfaces, in the range 0.1–0.15. To some degree the difference in R750 between hollow floors and BCFD-dominated units is expected due to my use of unit type definitions in which BCFDs have high reflectivity. However, the unit type to which a point was ascribed was also determined on the basis of its spatial relationship with other units (BCFD halos are marginal to hollow floors) and morphology (developing hollows have knobs of material within them when viewed at NAC resolutions, while flat hollow floors do not). That point-selection was not dominated by assumed spectral characteristics is demonstrated by the finding that, though BCFD halos and developing hollows generally have the highest reflectance of the analysed units, in Kertesz crater (6070) and Group 7020 they have low reflectance relative to other sites and the same or lower reflectance than associated flat hollow floors. BCFDs may be thinner at these sites, allowing the spectral character of lower-reflectance underlying material to show through, or, in the case of Kertesz, for which the multispectral data resolution in >500 m/pixel, the reflectance of more than one unit type may be combined in the points analysed. Variations in the reflectance of hollow floors do not directly correlate with the solar incidence and emission angles at which the analysed images were taken, which may indicate variation in composition e.g. due to still-ongoing floor hollowing at some sites, or, as for BCFD halos, inclusion of surrounding substrates in the pixel analysed. At the resolution of the available data, it is not possible to be certain that a 'pure' hollow floor spectral signature has been obtained at all sites and spectral characterisation of hollow floors can be considered most robust at sites (e.g. Eminescu, Figure 3-8), where hollow floors cover a large area relative to the pixel size.

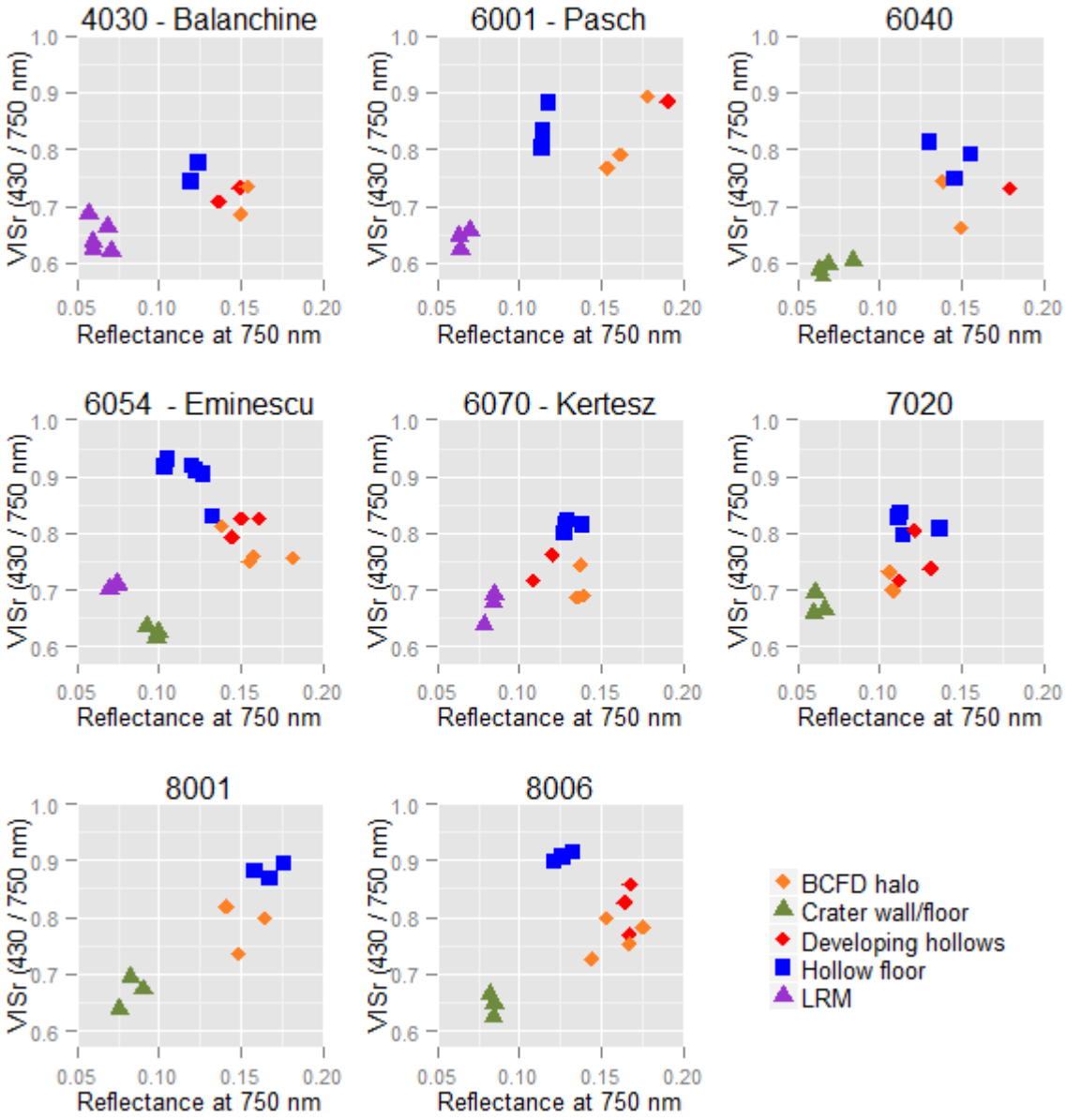


**Figure 3-7 Comparison of the spectral character of hollow floors and surrounding units. Hollow floors have the highest VISr (lowest spectral slope), whereas BCFD halos and partially-developed hollows can have the highest reflectance, though R750 of hollow floors relative to that of BCFD halos varies between sites. Error resulting from the bandwidth of WAC filters is in all cases < $1.4 \times 10^{-2}$ VISr, and < $4.1 \times 10^{-4}$ for R750.**

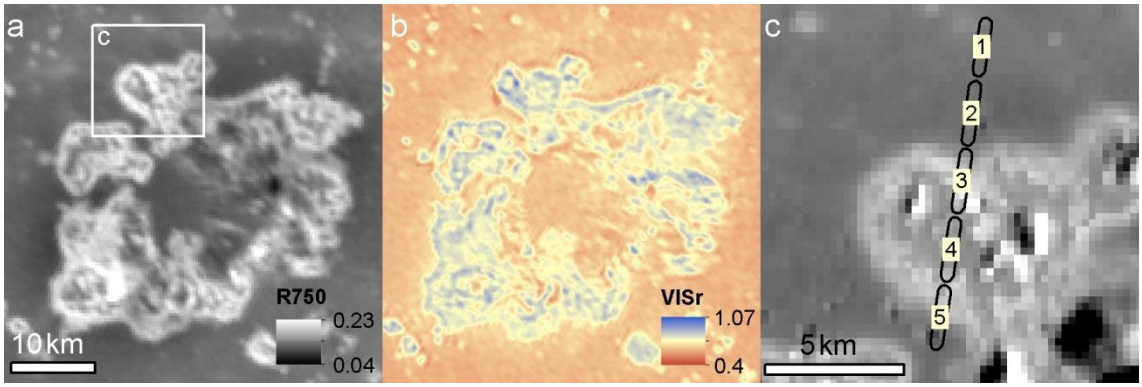


**Figure 3-8 The spectral character of hollows in Eminescu crater in MDIS data. (a) Reflectance at 750 nm (EW0249411920G). White outline: extent of (c). (b) Spectral slope at visible wavelengths (VISr, EW0249411904F/ EW0249411920G). (c) Excerpt from the global monochrome mosaic (v9) with black polygons indicating the approximate location of MASCS footprint sites plotted in Figure 3-9.**

Within MASCS footprints from Eminescu with high VISr and R750, and that appear to be spatially located in areas with hollow floor or hollow floor combined with BCFD, UVr is near the planetary average and similar to that of the wider crater floor, whereas the LRM immediately surrounding the hollowed area has very low UVr, similar to that observed in pyroclastic deposits and bright ejecta (*Izenberg et al.*, 2014) (Figure 3-9). Higher UVr correlates with higher VISr in the footprints crossing hollows. In Kertesz, all footprints analysed include both BCFD and flat hollow floors, so their spectrum should be viewed as a combination of these units (Figure 3-10). The UVr of these spectra is approximately at the planetary average (0.65–0.66).

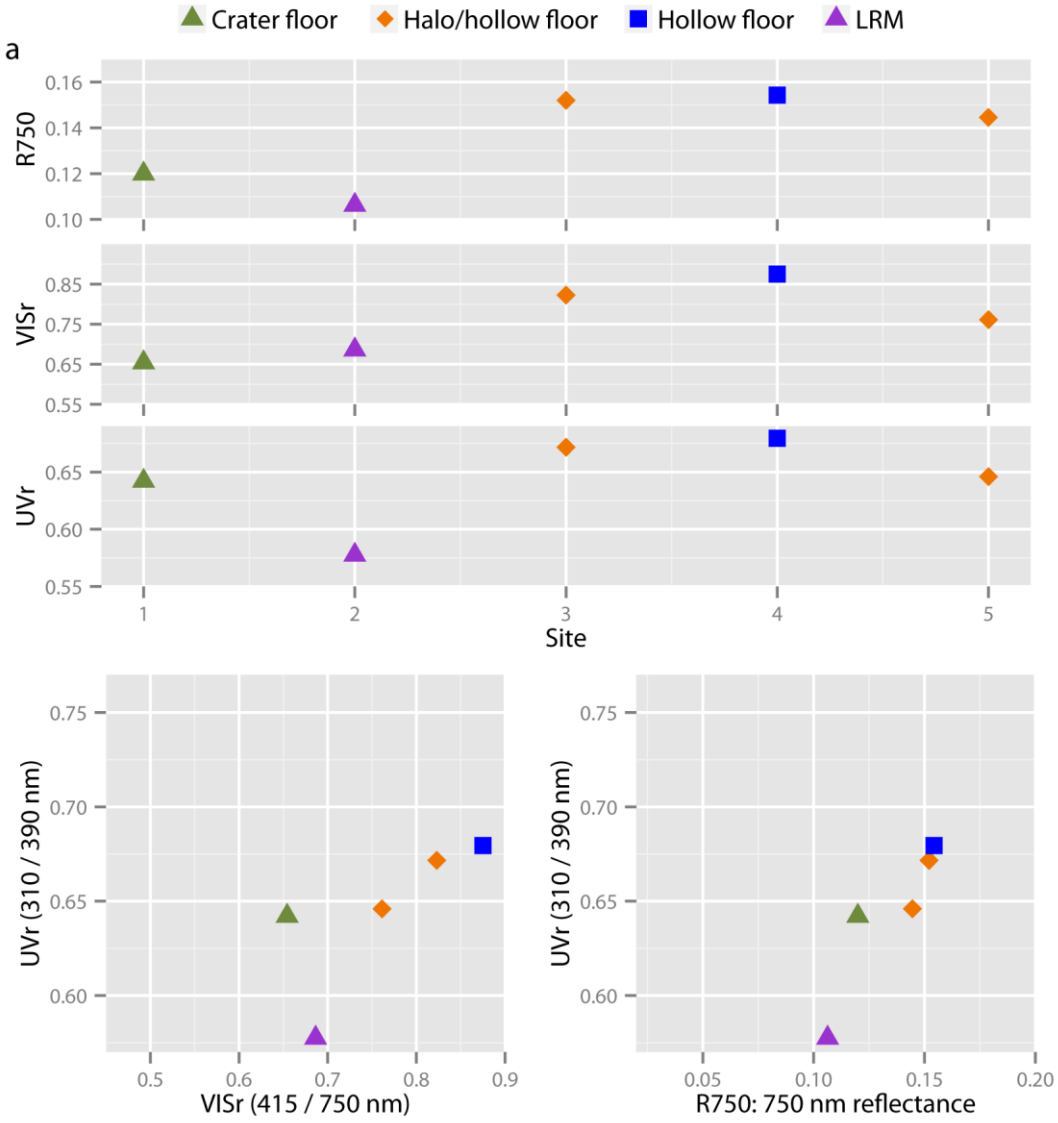


**Figure 3-9 The spectral character of hollows in Eminescu crater in MASCS data. Unit types are attributed on the basis of the unit overlain when plotted on the global monochrome mosaic v9, and the characteristic R750 and VISr signatures for these units indicated by MDIS data. (a) Plots of spectral metrics by site (Figure 3-8c). (b) Plots of UVr against visible spectral slope and reflectance at 750 nm.**

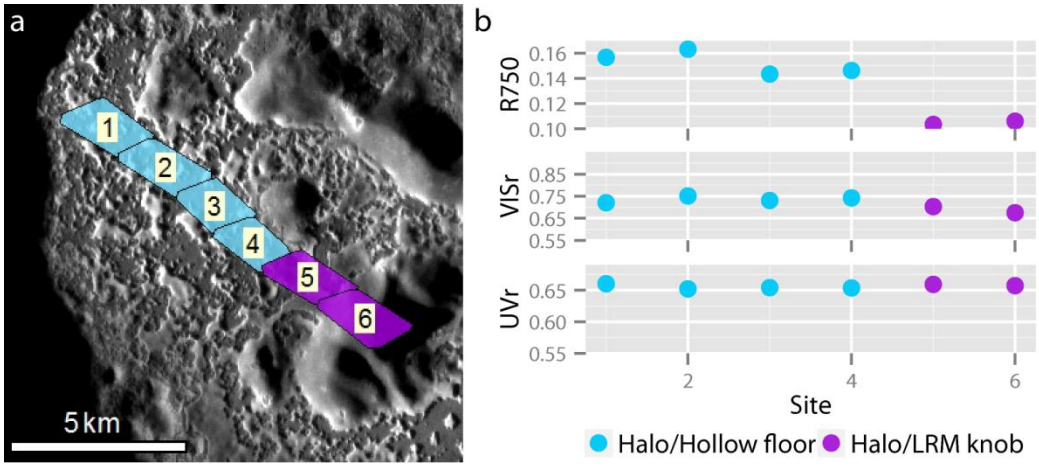


**Figure 3-10 MASCS footprints crossing Kertesz have a relatively consistent UVr, but each include more than one unit type. (a) The approximate locations of MASCS footprints for which spectral data is shown in (b). Base image: NAC images EN0250969325M and EN0250969334M. Solar illumination is from the left. (b) Plots of spectral metrics for sites numbered in (a).**

## 3.4 Discussion

The foregoing results imply that flat, lower reflectance, apparently inactive floors within hollows have a lower spectral slope at visible wavelengths than the bright material present during the process of hollow-formation. Both units have higher reflectance and a lower spectral slope at visible wavelengths than surrounding units, which are presumably formed of material similar to that lost in hollow-formation. Though data are scarce for reflectance at UV wavelengths, in two craters with LRM on their floors the UV spectral slope in hollowed areas is at Mercury's average. Spectral character in these broad terms is primarily controlled by maturity, composition and texture (e.g. grain size). Consideration of these factors suggests two possible explanations for the evidence.

### 3.4.1 Maturity: Hollows uncover immature exposures of their parental material

Hollow floors may simply represent less space weathered examples of their parent material. Under the high flux, high velocity micrometeoroid bombardment at Mercury's surface, any exposed surface is quickly darkened and reddened by the condensation of very fine-grained iron coatings onto mineral grains, and further darkened by the aggregation of these coatings into agglutinate glasses containing slightly larger sub-microscopic iron particles (*Lucey and*

*Riner*, 2011; *Riner and Lucey*, 2012). This means that any freshly-exposed surface is expected to be relatively bright and 'blue'. Thus, a fresh surface could be expected to have the spectral characteristics in the visible spectrum observed on hollow floors, and this may also explain the observation that the UV spectral slope at hollowed sites is commonly similar to that of the parent material (*Izenberg et al.*, 2015). If the spectrum of hollow floors is the result of immaturity alone, it cannot be used to identify the volatile substance(s) lost in hollow formation.

However, this hypothesis is inconsistent with the evidence presented in this chapter. The occurrence of BCFD preferentially around hollows and on upstanding knobs within them suggests that BCFD occurs where hollowing is active, whereas hollow floors have reached equilibrium and are older. If this interpretation is correct, hollow floors have been exposed to space weathering for longer than BCFD and so should be 'redder' as well as darker, while instead they are 'bluer'. Spectral slope at UV wavelengths at Eminescu is also inconsistent with that of immature parent material. Spectral studies of asteroids and laboratory and remote sensing data for lunar mare soil indicate that space weathering decreases UV spectral slope, particularly in the 300–400 nm range (*Hendrix and Vilas*, 2006). This means more space weathered materials will have higher UVr, and yet LRM surrounding hollows on the floor of Eminescu has much lower UVr than that of the hollow floors and BCFD halos, which are expected to be less mature. UVr is also affected by composition and texture: both higher transition metal content and, in basalts, larger grain size result in lower reflectance and higher UVr (*Cloutis et al.*, 2008). The spectrum of Eminescu hollow floors is thus consistent with concentration of non-volatile transition metal bearing minerals in a lag, and/or a lag with a larger average grain size than that of the surrounding LRM, but is not consistent with fresh exposure of parent material. The similarity in UVr of 'hollows' and their parent material at other sites (*Izenberg et al.*, 2015) could potentially result from detection of an average spectrum of BCFD and hollow floors in the analysed footprints: BCFDs appear to be fine-grained and so would be expected to decrease UVr, while hollow floors may contain more coarse-grained debris and non-volatile mafic minerals. Alternatively, LRM surrounding the

hollows in Eminescu may simply be an unusual case; it is noteworthy that its UVr is much lower than has been reported for LRM elsewhere on the planet (*Izenberg et al.*, 2015), and that the UVr of the wider crater floor is close to that of the BCFD halos and hollow floors. It will be necessary to obtain UV spectra at a high enough resolution to securely extract spectra of BCFDs and hollow floors at multiple locations on Mercury before a definite determination of the effects of hollow-formation on UV spectral slope can be made (Section 9.2.2).

The hypothesis that hollow floors are fresh exposures of parent material is also inconsistent with the morphology of hollows. For fresh parental material to be exposed at hollow floors, very little lag can be present. However, in the absence of a lag, hollow-formation should continue until all volatile material is lost. There is no evidence that hollows form within a thin volatile-bearing stratum of consistent thickness, and yet hollow floors are flat, and hollows have a characteristic depth of several tens of meters across the planet. If we instead propose that a relatively volatile substance (perhaps what we term BCFD) percolated through the parent material and entirely replaced it, the loss of this substance could leave a hole floored by parent material that has been churned but not otherwise affected. In that case, however, the morphology of hollows would be expected to indicate subsidence rather than scarp retreat. Such a process may be applicable to pitted ground (Section 2.5.1.2), where the loss of hollow-forming volatiles does create a morphology indicative of subsidence, but it is not a good model for hollow-formation.

### 3.4.2 Composition: Hollows are floored by the non-volatile component of the parent material

Given the morphology of hollows, the most probable model for their formation is that proposed by *Blewett et al.* (2013), in which a high proportion of the parent material is volatilised to form hollows, leaving behind a lag that ultimately prevents further deepening, while the high-relief hollow margins continue to degrade. The observed spectral slope of hollow floors fits well with this model: if partial loss of volatiles during hollow-formation leads to a relatively 'blue' spectral character for BCFDs, the even 'bluer' hollow floors represent its total removal. This indicates that the relatively volatile substance(s) lost in

hollow-formation is relatively red-sloped, consistent with laboratory spectra for (Ca,Mg) sulfides that have been thermally-cycled (*Helbert et al.*, 2013). Evidence for the reflectivity of the substance(s) lost is less certain: though the lower reflectivity commonly seen in hollow floors versus BCFDs and developing hollows could result from a greater fractional loss of a substance with relatively high reflectance, it could equally result from the greater maturity of hollow floors. Nevertheless, their relatively low reflectance is not consistent with the hypothesis that the loss of the volatile substance(s) has a 'brightening' effect (*Blewett et al.*, 2013), particularly given that the majority of the images analysed were taken under viewing conditions that render hollow floors brighter than otherwise (Figure 3-3, Figure 3-6). Indeed, as hollow floors are relatively young, they are expected to be brighter than surrounding older units even if they result from the loss of a higher-reflectance substance within those surrounding units. Thus, volatile-loss either has little effect or a darkening effect on the reflectivity of the parent material, suggesting that the substance responsible for the low reflectivity of LRM is non-volatile. This is consistent with the hypothesis that graphite is the darkening agent on Mercury (*Murchie et al.*, 2015a), and is intriguing in light of the twin hypotheses that graphite makes up Mercury's primary crust (*Vander Kaaden and McCubbin*, 2015) and that LRM is exhumed from the lower crust (*Ernst et al.*, 2015). However, until robust detections of the carbon content of Mercury's surface have been obtained, this must remain speculative (*Peplowski et al.*, 2015).

## 3.5 Conclusion

A spectral analysis of flat hollow floors clarifies the nature of the material remaining after hollow formation and thus the nature of relatively volatile substance(s) lost from the planet's surface. The morphological and spectral evidence is consistent with the presence of a non-volatile lag on hollow floors that has a lower spectral slope and, potentially, the same or lower reflectivity than the parental material. This indicates that the volatile substance lost in hollow-formation has a higher spectral slope and may be more reflective than the LRM substrate within which hollows commonly form. This is consistent with the volatilization of thermally processed sulfides at the surface of Mercury to form hollows, and with the

presence of a non-volatile, low-reflectance component within LRM that gives it its distinctive dark appearance.

Because this analysis depends on data from a small number of sites (eight), these results should be considered preliminary. It is possible that hollow floors display a greater range in spectral character than represented by this sample. Fortunately, the instrumental capabilities of the forthcoming BepiColombo mission are ideally suited to the detection of surface spectra at a spatial resolution necessary to discriminate hollow floors, so there is a good potential for such a wider analysis in the future (Section 9.2.2).

# Chapter 4. Long-lived explosive volcanism on Mercury

## 4.1 Introduction

Along with hollows, the products of explosive volcanism are our strongest landform evidence for volatile-release at Mercury's surface. An important issue regarding Hermean explosive volcanism is its longevity: if it occurred within the period when the planet has been in a state of global contraction, it will be necessary to determine what processes allowed magma ascent to the surface despite crustal compression. This chapter, a peer-reviewed paper published in *Geophysical Research Letters* (*Thomas et al.*, 2014b), sets out to determine the timescale over which explosive volcanism has occurred on Mercury.

## 4.2 Background

In order to constrain models for the composition, internal structure, and formation history of Mercury, it is necessary to assess the duration of volcanism. Model ages obtained for widespread plains-forming lava flows range from ~4.1 to 3.55 Ga (*Denevi et al.*, 2013; *Marchi et al.*, 2013), but little evidence has been found for lava emplacement after that period. It is possible that minor lava flows were emplaced up to 1 Ga (*Prockter et al.*, 2010; *Marchi et al.*, 2011), but this is currently debated (*Chapman et al.*, 2012).

Previous studies (*Head et al.*, 2009b; *Kerber et al.*, 2011) identified irregular pits on Mercury with surrounding deposits that are brighter and redder than the planetary average. On the basis of the anomalous spectral characteristics and diffuse margins of these deposits, plus the apparently endogenic nature of the pits, these are widely accepted as pyroclastic deposits formed by explosive volcanism (*Grott et al.*, 2011; *Byrne et al.*, 2013). This style of volcanism occurs through separation of volatiles from rising magma, so its occurrence challenges formation models for Mercury predicting a volatile-depleted bulk composition (*Cameron*, 1985; *Fegley and Cameron*, 1987; *Wetherill*, 1988; *Benz et al.*, 2007). Explosive vents within the Caloris basin clearly superpose the effusively-emplaced Caloris interior lava plains (*Head et al.*, 2009b; *Rothery et al.*, 2014), and it has been suggested that some explosive volcanism on Mercury in general may have occurred in the Mansurian Period (3.5–1 Ga) (*Goudge et al.*,

2014), which indicates that this type of volcanic activity is a potential indicator of the true duration of volcanic activity.

I use the presence of vents within young, morphologically-fresh impact craters and counts of superposed impact craters to demonstrate a long duration of explosive volcanism on Mercury, extending into the last billion years. I then highlight similarities and differences with the history of volcanic activity on the Moon.

## 4.3 Methods

### 4.3.1 Identification of sites of explosive volcanism

I have conducted a global survey for explosive volcanism on Mercury by examining images from the Mercury Dual Imaging System (MDIS) on board NASA's MErcury Surface, Space ENvironment, GEochemistry, and Ranging (MESSENGER) spacecraft. I examined all images at a resolution of 180 m/pixel and better taken prior to March 17, 2013, plus version 9 of the global colour and monochrome mosaics at 250 m/pixel produced by the MESSENGER team. In order to identify probable pyroclastic deposits, which are bright and red relative to Mercury's average spectral reflectance (*Kerber et al.*, 2011), I created colour composites by placing images taken through the 996 nm, 749 nm and 433 nm filters of the Wide Angle Camera (WAC) in the red, green, and blue bands, respectively.

This survey led to the identification of 150 locations where the association of irregular pits and relatively bright, red deposits indicates explosive volcanic activity (Figure 4-1), a considerable advance on the number of such locations previously documented (*Kerber et al.*, 2011; *Goudge et al.*, 2014). The majority (79%) of these are within impact craters. This provides a means of constraining the maximum age of the volcanism in each case, as these pits must post-date their host crater and any cross-cut intra-crater fills.

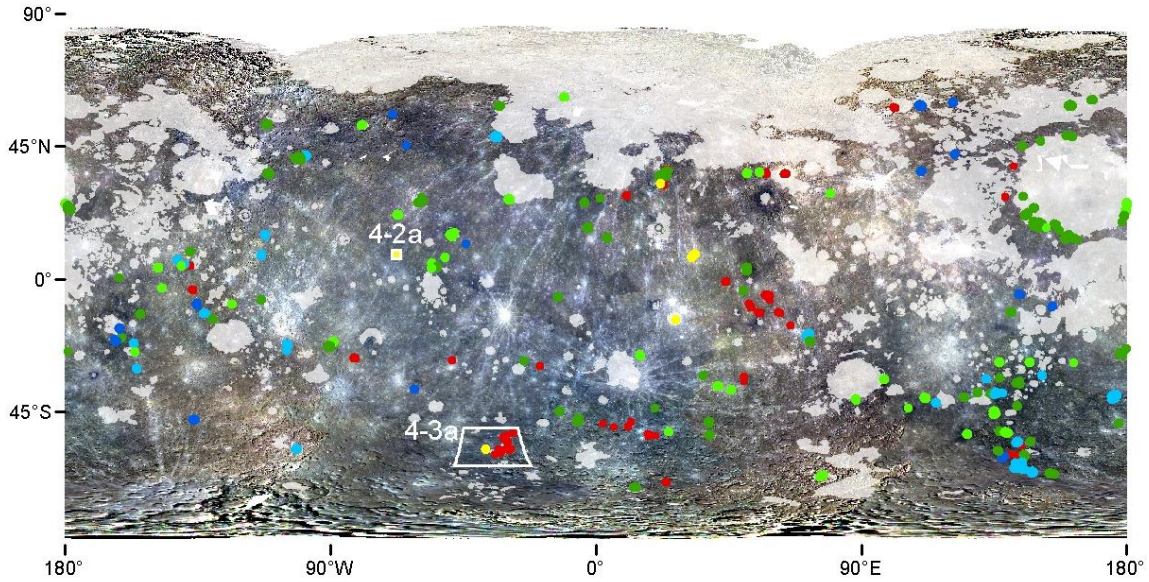


**Figure 4-1 Distribution of endogenic pits with a surrounding relatively bright, red spectral anomaly. Where the pit penetrates an impact crater, the degradation state of that crater is used to colour-code the site. This indicates the maximum age of pyroclastic activity. The relative freshness of the crater indicates an age (youngest to oldest) in the Kuiperian to late Mansurian (yellow), Mansurian (bright green), Calorian (dark green), Tolsojan (light blue) or pre Tolstojan (dark blue). Red dots: pits that are not superposed on an impact crater or where the crater degradation state is unclear. Locations of Figure 4-2a and Figure 4-3a indicated by white rectangles (base image: global colour mosaic v5).**

### 4.3.2 Assessing the ages of craters hosting explosive volcanism

Impact craters degrade over time as a result of subsequent impacts and the resulting regolith-forming processes, and hence the degree of degradation of the crater indicates its age (*Spudis and Guest*, 1988). This provides an essential tool for assessing the maximum age of pyroclastic deposits that overlie the impact crater. Where a pyroclastic deposit is small and thin (tens of $km^2$ and a few m thick), it is a poor candidate for dating by counting superposed impact craters, because it does not obscure underlying older craters and extends over an area smaller than desirable for the counting method at the resolution of the images available. Therefore, establishing the age of an impact crater in which a vent or pyroclastic deposit occurs is the most robust method of determining a maximum age for the volcanic activity.

Where vents and pyroclastic deposits occur within an impact crater or on its proximal ejecta, I have estimated the age of the host crater on the basis of its state of degradation. I use the scheme outlined by *Barnouin et al.* (2012) for Mercury (following *Spudis and Guest* (1988)), which assigns a crater a degradation state on the basis of attributes such as the preservation of its ejecta blanket, presence of superposed craters, and modification of its terraces.

### 4.3.3 Dating pyroclastic deposits

As discussed above, dating small-scale pyroclastic deposits on the basis of superposed impact craters is problematic. However, where deposits are thick and large (hundreds of $km^2$ and tens of m thick) it may be possible to determine their age using this method. I identified such deposits at five locations (Table 4-1) and counted superposed impact craters on the deposits and other surfaces in their vicinity using CraterTools in ArcGIS (*Kneissl et al.*, 2011). I recorded fractional counts where a crater intersects the counting area boundary to avoid overestimation of large craters straddling that boundary. I compared the crater size-frequency distribution to the established production and chronology function of *Neukum et al.* (2001) to derive model ages for the formation of these surfaces. I also explored the effect of using a different crater production function to assess the surface age by comparing these model ages with those indicated by the Model Production Function (MPF) of *Marchi et al.* (2009) at one location.

**Table 4-1 Locations and crater retention model ages for pyroclastic deposits on Mercury**

| Description | Longitude (° E) | Latitude (° N) | Pyroclastic deposit ages (Ga) | |
|---|---|---|---|---|
| | | | NPF | MPF |
| Annular pit (AP2) | -135.5 | -8.4 | 3.9 (+0.0/-0.1)<br>3.6 (+0.1/-0.1) | 3.7 (+0.0/-0.0) |
| NE Rachmaninoff | 64.1 | 36.1 | 3.7 (+0.0/-0.0) | |
| Picasso crater | 50.8 | 3.9 | 3.4 (+0.0/-0.1) | |
| RS-03 (within Caloris) | 146.2 | 22.4 | 3.4 (+0.1/-0.1) | |
| N Rachmaninoff | 57.4 | 36.0 | 3.3 (+0.1/-0.2) | |

I excluded craters from the analysis if I judged them to be secondaries on the basis of a chained or clustered arrangement or a non-circular shape. After removal of this fraction of the population, I performed a randomness analysis (*Michael et al.*, 2012) to statistically assess

the degree to which the remaining craters are clustered. Because secondary impact craters are not always distinguishable on the basis of clustering, and because of the high proportion of secondary craters on Mercury (*Strom et al.*, 2008), it is probable that I have not been able to exclude all secondaries. These will affect the model ages derived using the two production functions to different degrees. The Neukum Production Function (NPF) is a modification of the lunar production function, taking into account differences in the velocity of impactors and impact rate at Mercury versus the Moon (*Neukum et al.*, 2001). As the density of secondaries is thought to differ on Mercury and the Moon (*Strom et al.*, 2011; *Xiao et al.*, 2014), the NPF may not adequately account for non-obvious secondaries in its model age estimate, and because secondaries are spatially non-random, this may lead to an artificially high or low age estimate. On the other hand, the MPF is constructed by determining the crater population expected from the population of impactors at Mercury and then calibrating that to the lunar production function (*Marchi et al.*, 2009). It does not explicitly include secondaries, so if they are present in the counted population, they will lead to an overestimate of surface age. However, the presence of a large population of secondaries would alter the shape of the crater density plot versus that expected for Mercury. If plots lie along established Mercury isochrons, this is a good indication that secondaries do not dominate the counted population.

A pyroclastic deposit, even though sufficiently thick to produce the characteristic 'red' surface colour, might be too thin to hide the underlying craters. Therefore, where suitable images were available I produced stereo-derived digital elevation models (DEMs) of the pit and deposit using the Ames Stereo Pipeline (ASP) (*Moratto et al.*, 2010). Where the deposit lies on a surface that may reasonably be expected to have been originally flat, anomalous relief around the pit is potentially attributable to pyroclastic deposition. To calculate the maximum rim height of an older crater that would have been erased by a deposit observed in the DEM, I used *Pike's* (1988) equation for bowl-shaped craters on Mercury:

$$h = 0.052D^{0.930} \qquad (4\text{-}1)$$

where h = deposit thickness and D = crater diameter. If the maximum crater diameter upon which my model age determinations were based is less than D, it is reasonable to state that

the pyroclastic deposit is the surface being dated. Where topography was not available, I tested whether the model ages I derived dated the pyroclastic deposits or the background surface by also dating a surface at a distance from the pit and comparing this with the model age near the pit. If fewer craters per unit area superpose the pyroclastic deposit than the surface remote from the pit, either the pyroclastic deposit is significantly younger or its physical properties led to more rapid degradation of superposed craters.

## 4.4 Results

### 4.4.1 Evidence for recent explosive volcanism

I catalogue and illustrate the global distribution of all 150 groups of volcanic pits with associated bright, red deposits that I have identified on Mercury in Table B-1 and Figure 4-1. Of the 118 that occur within impact craters, the majority are within moderately degraded craters dating to the Calorian Period (3.9–3.5 Ga), but 28 are in only slightly degraded craters dating to the Mansurian Period (3.5–1 Ga) and four are in very fresh craters with bright ejecta that date to the late Mansurian (<c.1.7 Ga) or Kuiperian (<1 Ga) Period (using the criteria of *Spudis and Guest* (1988)). The age of the host crater provides a maximum age for the pyroclastic activity in each instance. Here I present two examples that provide the clearest evidence of recent (i.e. late Mansurian to Kuiperian) explosive volcanism on Mercury.

The first example is within a 21–km diameter crater at 67.9° W, 8.4° N (Figure 4-2). Explosive volcanic activity at this location is evident in the form of a large pit cutting the northern rim of the impact crater (white arrow, Figure 4-2b), as well as a relatively red deposit that is bright to a radius of 19 km around the largest pit, and fainter to a radius of 26 km. The deposit is centred on the pit, not on the crater, from which I conclude that it was sourced from the pit rather than exhumed during formation of the impact crater. The crisp rim and undegraded ejecta blanket show that the host crater is relatively young, and probably formed in the late Mansurian. Though its floor is superposed by numerous small impact craters, which would usually indicate a long duration of exposure, the colour image (Figure 4-2a) reveals that these are part of a bright ray of secondary craters from the Hokusai impact to the

northeast. The host crater therefore predates Hokusai, which is of Kuiperian age on the basis of its well-preserved bright rays (*Spudis and Guest*, 1988). The size and density of impact craters superposed on those parts of the ejecta blanket that appear relatively unaffected by Hokusai secondaries is low, supporting a young age (Figure 4-2c). Because of the small sampling area and uncertainties introduced by the higher proportion of secondaries at small crater diameters, I am cautious about ascribing an age to this impact crater on the basis of crater counting. However, the model age arrived at using the NPF, 1.7 Ga ± 0.3 (Figure 4-2), is consistent with the fresh morphology of the crater.

In the second example, the pit cuts the wall terraces within Kuniyoshi, a 26–km diameter crater at 37.4° W, 57.8° S (Figure 4-3). This crater's peak and walls have a crisp appearance and its ejecta blanket is undegraded and has a high albedo. Such a fresh morphology characterizes Kuiperian-aged (< 1 Ga) impact craters. Another important characteristic of Kuiperian-aged craters is the presence of rays. It is unclear whether these are present, but bright material surrounds the crater and there is a suggestion of alignments radial to the crater within this (Figure 4-3a). A slightly smaller crater 200 km northwest of Kuniyoshi crater has radial alignments that appear to be rays, and yet its morphology is less crisp than, or at most as fresh as, that of Kuniyoshi (Figure 4-3c). Its rays reach a distance from the crater that is less than the radius of the high-albedo material surrounding Kuniyoshi, so if present to that distance around Kuniyoshi, rays would not be visible against the bright material. A young age for Kuniyoshi is supported by the very low density of impact craters superposed on its ejecta blanket: only 15 craters, all <1 km diameter, are visible over an area 1581 $km^2$ (Figure 4-3b). Their morphology suggests that six of these are secondaries (red in Figure 4-3b) and given the high proportion of secondaries in the small crater population of Mercury relative to other planets, it is probable several of the remaining craters are as well. On the basis of this sparsity of superposed craters, the freshness of the host crater's morphology and the possible presence of rays, I date this crater to the Kuiperian, most probably to its earliest part. Two pits a few kilometres apart incise the crater's northern terraces and rim, and are surrounded by a relatively bright and red deposit. These indicate

that explosive volcanism occurred here after the crater's formation, and hence in the Kuiperian Period.

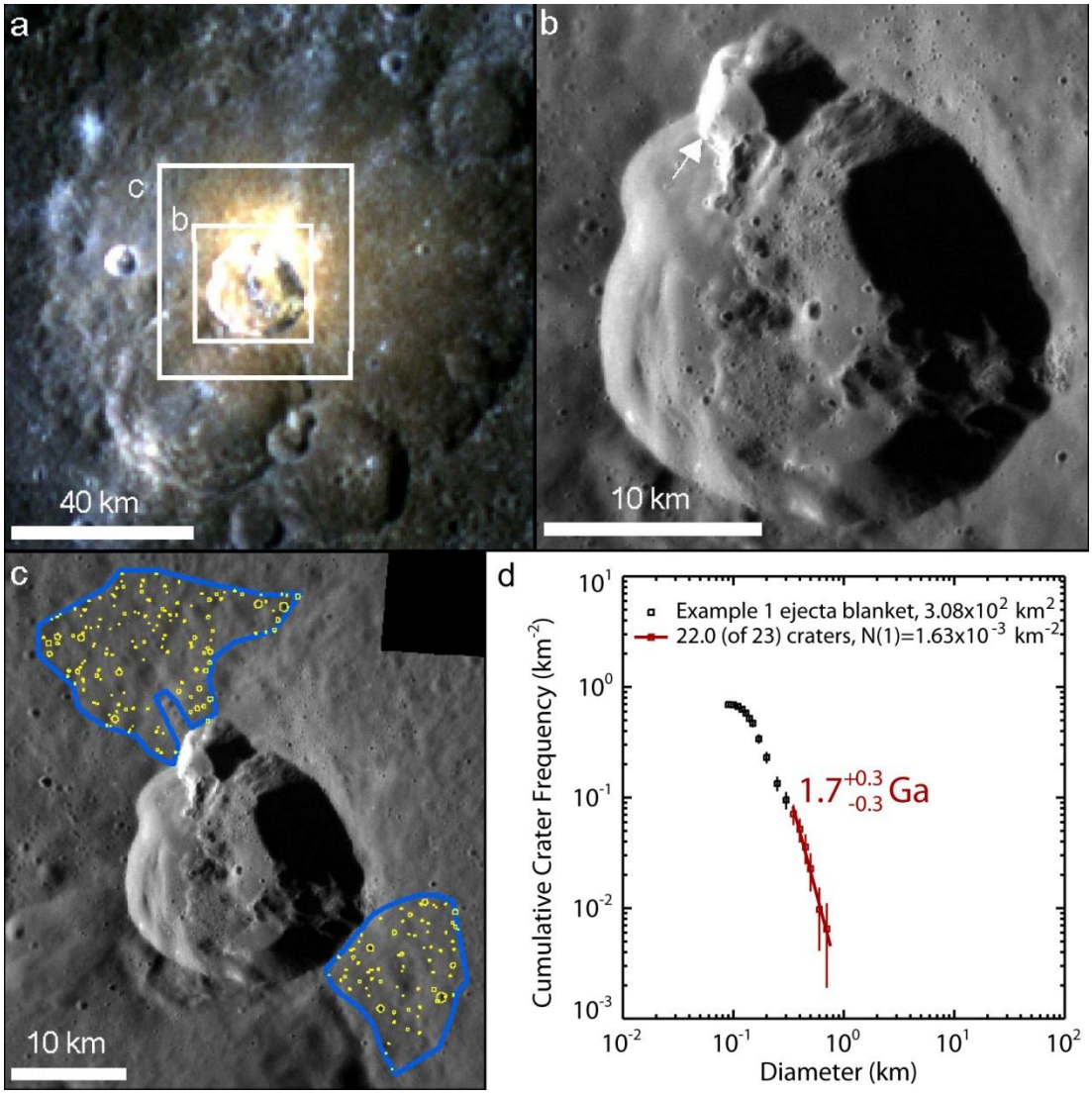


**Figure 4-2 A small, fresh late Mansurian crater with associated relatively bright and red deposits (67.9° W, 8.4° N). (a) Colour composite showing a surrounding spectral anomaly centred at the northern rim of the crater and superposition by a bright ray from Hokusai crater to the northeast (images EW0241501576I, EW0241501568G and EW0241501572F, with panchromatic sharpening using image EW0223917664G). (b) Higher-resolution monochrome image with white arrow indicating a large pit in the northern rim of the crater (image EN0239206510M). (c) Areas sampled to derive model ages through crater counting outlined in blue, superposed impact craters: yellow circles (image EN0239206510M and EN0239206492M). (d) Crater size-frequency distribution within the counting areas outlined in (c) indicating a maximum age for volcanic activity of ~1.7 Ga.**

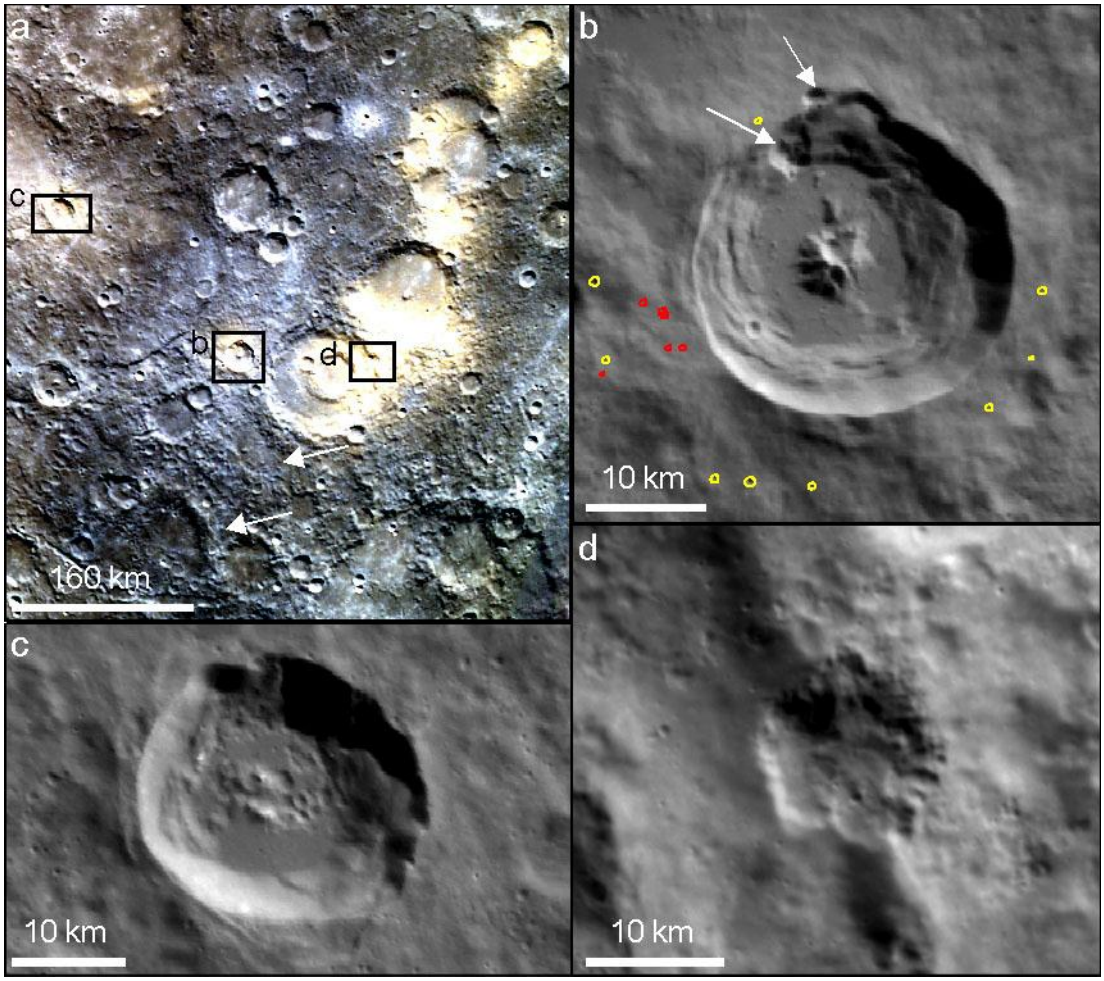


**Figure 4-3 Explosive volcanism at Kuniyoshi, a young (Kuiperian), fresh crater at 37.4° W, 57.8° S. (a) Colour composite image showing bright, red deposits at the northern rim of Kuniyoshi (located within box b) and a linear region with multiple centres of relatively bright and red deposits to its east and northeast, all indicative of explosive volcanism. White arrows: possible rays from Kuniyoshi; black rectangles: extents of (b), (c) and (d) (images EW1005108006I, EW1005108026G and EW1005108010F). (b) Monochrome image showing Kuniyoshi's crisp morphology and undegraded ejecta blanket and endogenic pits in its north wall (white arrows). Primary impact craters on its ejecta blanket circled in yellow, secondary impact craters circled in red (Image EN0239251642M). (c) A crater to the northwest of Kuniyoshi: its morphology is not as crisp as that of Kuniyoshi, but it appears to have visible rays in (a). (Image EN0239124609M). (d) Vent with crisp morphology in a crater to the east of Kuniyoshi.**

Interestingly, this crater lies adjacent to a 410–km–long region with numerous pits cross-cutting, and bright spectrally red-sloped deposits overlying, Tolstojan- (4.0–3.9 Ga (*Spudis and Guest*, 1988)) to Mansurian-age impact craters (Figure 4-3a). The morphology of these

pits is not appreciably more subdued than those within Kuniyoshi (Figure 4-3d), so explosive activity in this entire region may have been equally recent.

The above evidence indicates that explosive volcanic activity occurred on Mercury until the Kuiperian. While the evidence for a young age is most conclusive at these two locations, they are not unique: pyroclastic deposits occur in other young craters and the morphology of the associated pits in some older craters is distinctly more crisp than that of the host crater, indicating a considerably younger but, as yet, unquantifiable age. The freshest (least degraded) internal vent morphology yet documented is inside the four youngest vents within the RS-03 compound vent in the southwest of the Caloris basin (*Rothery et al.*, 2014).

### 4.4.2 Evidence for the duration of explosive volcanic activity

Additionally, I have found evidence for explosive volcanism as early as the Calorian Period (3.9–3.5 Ga). At five locations where pyroclastic deposits were sufficiently thick to be good candidates for dating in this way, I obtained model ages from 3.9 (±0.1) to 3.3 Ga (+0.1/-0.2) (Table 4-1). Below I present the evidence for the oldest and youngest of these ages in further detail.

#### *4.4.2.1 Pit annular to a crater central peak (AP2)*

At this location an endogenic pit (which apparently acted as a volcanic vent) has formed around the central structure of a very old, degraded impact crater (Figure 4-4). This pit is surrounded by deposits with the relatively bright and red spectrum characteristic of Mercury's pyroclastic deposits.

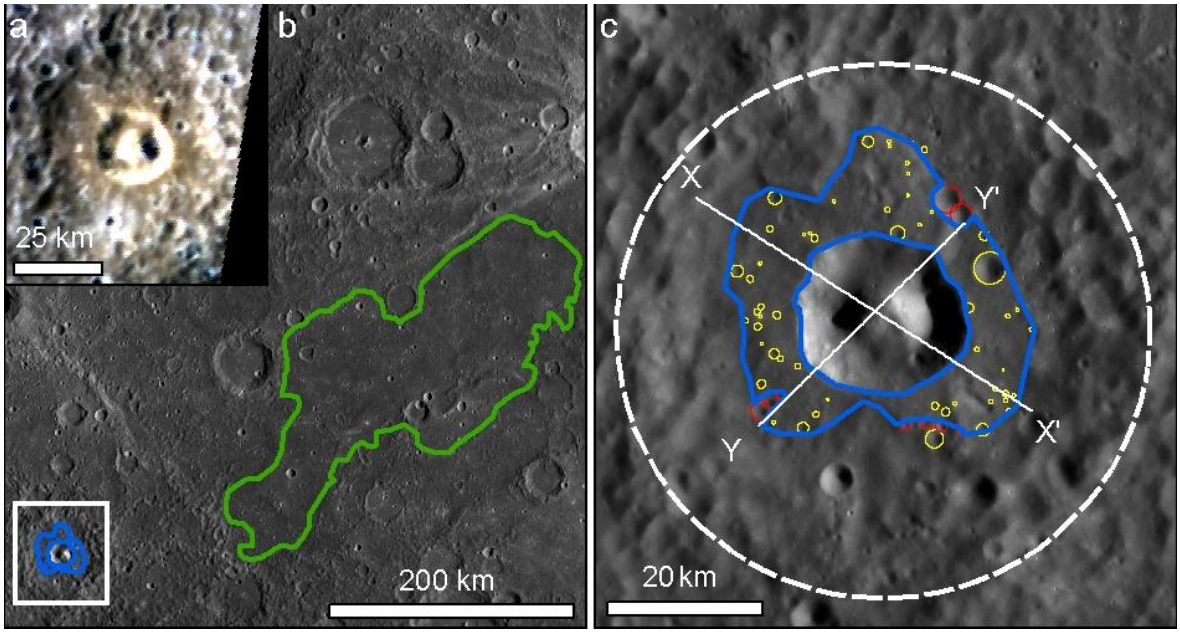


**Figure 4-4 Evidence for and dating of explosive volcanic activity at AP2 (-135.5° E, -8.4° N). (a) A pit around the central peak of an impact crater is surrounded by relatively bright and red deposits (colour composite combining images EW0262430050I, EW0262430070G and EW0262430054F with panchromatic sharpening using image EN0242378054M). (b) Areas sampled for crater-counting (blue: pyroclastic deposit, green: nearby smooth plains), white box: extent of (a) and (c), white lines: cross-sections in Figure 4-6 (image: global monochrome mosaic v.9). (c) High-resolution monochrome image showing a pit annular to the central peak of an old, degraded impact crater. White dashed outline: rim of host crater, blue outline: area used for counting superposed impact craters; yellow open circles: primary impact craters; red open circles: secondary impact craters (image EN0242378054M).**

Fitting an NPF isochron to the cumulative density plot of 1.2 to 2 km diameter craters around the pit gives a model age of 3.9 Ga (+0.0/-0.1) (Figure 4-5a). I interpret this as the age of the pyroclastic deposit rather than of the floor of the crater because the pyroclastic deposit appears to be up to 360 m thick here (Figure 4-6). This is sufficiently thick to erase the record of craters in the 1.2–2 km range. Fitting craters of all diameters to the MPF with a main belt asteroid (MBA) flux, and modelling the impacted surface as a cohesive soil with a strength of $1 \times 10^6$ dyne/cm$^2$, gives a model age of 3.7 Ga (±0.0) (Figure 4-5b). Because a resurfacing correction (*Michael and Neukum*, 2010) cannot be applied to the MPF, this fit includes a single large crater at the outer margin of the deposit. This crater may have formed prior to the pyroclastic activity, in which case its inclusion will have inflated the MPF age. I have obtained

very similar model ages for a smooth effusive volcanic plain 140 km to the east: a NPF model age of 3.8 Ga (±0.0), and a MPF model age of 3.6 Ga (±0.0) (using a cohesive soil scaling law, MBA-like flux, and a strength of $1 \times 10^6$ dyne/cm$^2$) (Figure 4-5). Thus, although the MPF gives a younger model age than the NPF, as noted elsewhere (*Massironi et al.*, 2009), both indicate that explosive volcanism was approximately contemporaneous with large-scale effusive volcanism in this region. An underabundance of smaller craters (<1.15 km diameter) causes a step in the cumulative crater density curve at small crater sizes, which may indicate more recent deposition of a thinner deposit (*Michael and Neukum*, 2010). This younger population of superposed craters is also apparent in a differential plot (Figure 4-7). This resurfacing event has a NPF model age of 3.6 Ga (±0.1), and the size range of the craters affected indicates the younger layer is 59–62 m thick.

#### *4.4.2.2 North of Rachmaninoff basin (N Rachmaninoff)*

This is a large (~33 km radius) pit 360 km north of the centre of the Rachmaninoff impact basin (Figure 4-8). The pit has an irregular outline and lacks an ejecta blanket or terraces, so I regard it as endogenic. It is surrounded by a deposit that clearly overlies impact craters on the continuous ejecta blanket of the Rachmaninoff basin (white arrows in Figure 4-8c), indicating that it post-dates Rachmaninoff. The deposit is thick to the south and west of the pit, obscuring the walls and floors of large craters, but appears thinner to the north of the pit (Figure 4-9). I interpret the deposit as pyroclastic on the basis of its association with the pit, the bright and red spectral signature of the surface and the diffuse margins of the overall spectral anomaly. The high relief in the south and west suggests deposition by flow here. In the absence of a nearby impact crater that could have generated this material by impact melting (Figure 4-8b), I suggest that this was clastogenic flow resulting from a high-flux pyroclastic eruption. The cumulative density of larger craters (1.2–2 km diameter) in the circum-pit area indicates a NPF model age of 3.6 Ga (±0.1), and a step in the cumulative plot at smaller crater sizes (0.6–1.1 km) suggests resurfacing dating to 3.3 Ga (+0.1/-0.2) by a layer 57–62 m thick (Figure 4-10). Because the larger craters occur in the north and east, where the deposits appear thinner, it is probable that the density of large craters indicates

the model age of the underlying surface, whereas the model age of 3.3 Ga dates the pyroclastic activity.

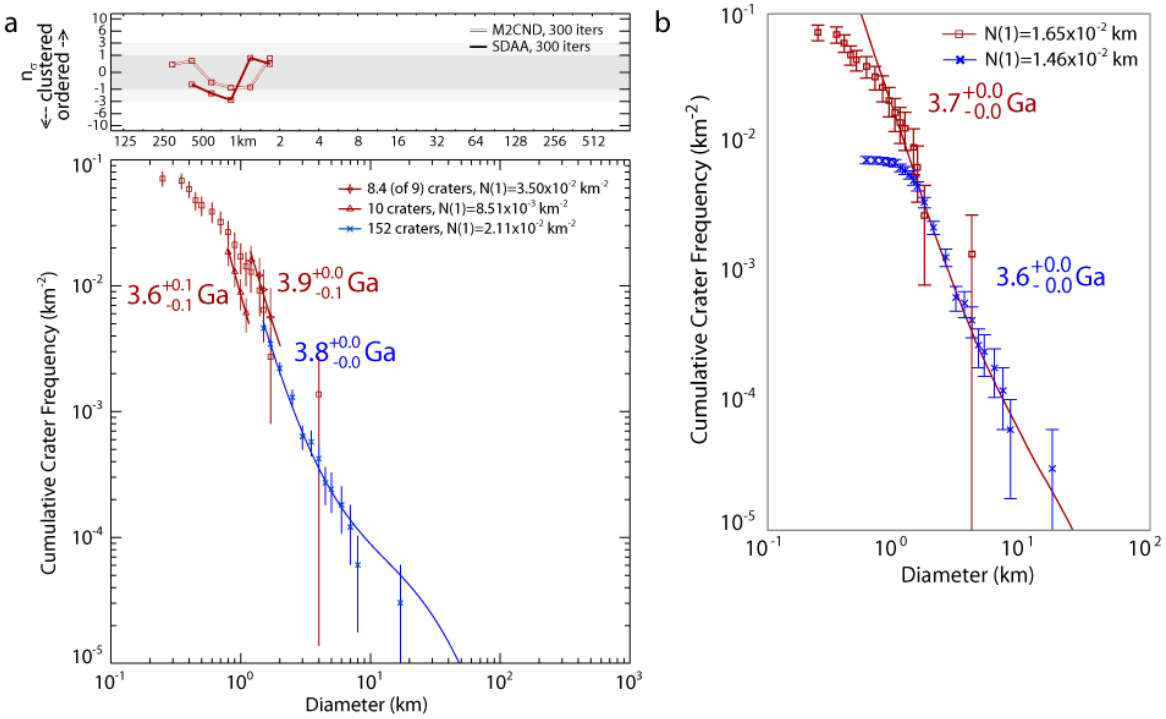


**Figure 4-5 Cumulative crater frequency plots showing that the model ages of explosive activity at AP2 and nearby effusive activity are very similar. Red points: crater counts for the surface of the AP2 deposit; red curved lines: fits to the AP2 deposit data; blue crosses: crater counts for the surface of the nearby smooth plains; blue curved line: fit to the smooth plains data; straight lines: error bars (AP2 deposit area: 7.27 × 102 km2; smooth plains area: 3.31 × 104 km2). (a) Fits to craters in the ranges 800 m–1.15 km diameter and 1.2–2 km diameter using the Neukum production and chronology function. A resurfacing correction was applied to account from the exclusion of larger craters in these fits. Results of randomness analysis (top) show that craters can be considered random for all diameters using a mean closest two neighbours distance (MC2ND) measure and for diameters > 1 km using the standard deviation of adjacent area (SDAA) measure. (b) Fits to the MPF.**

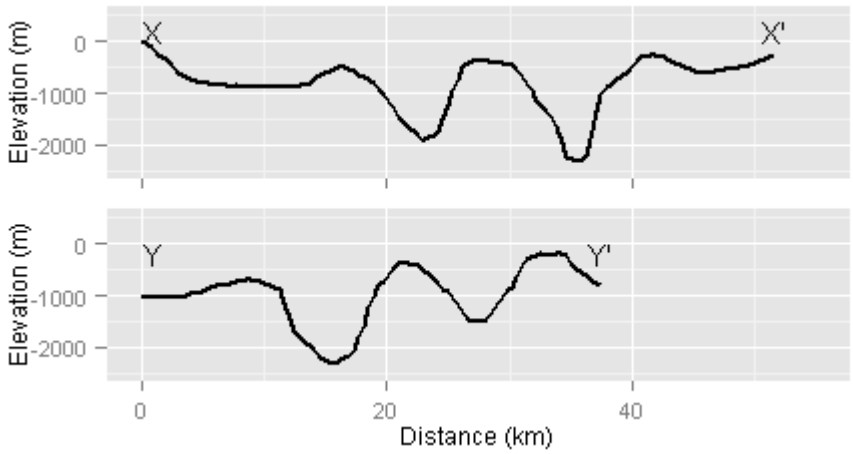


**Figure 4-6 DEM cross-sections across AP2 as indicated in Figure 4-4. Mounds of material up to > 360 m thick are observed around the pit margins. DEM derived from images EN0242378054M and EN0257763833M.**

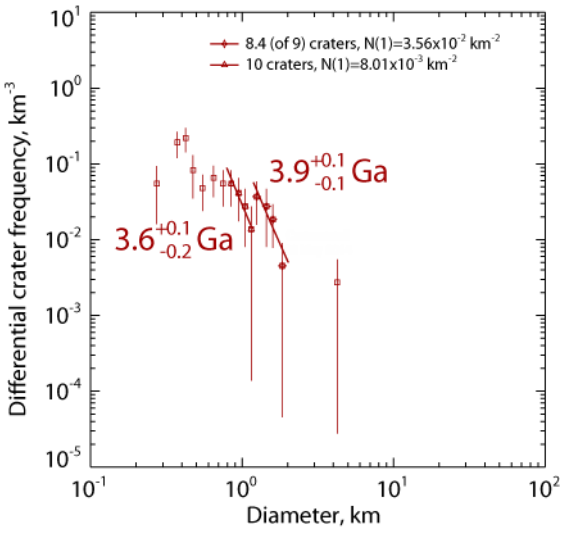


**Figure 4-7 Differential plot of crater frequency around AP2 showing two populations of craters (ranges as in Figure 4-5), indicative of a resurfacing event.**

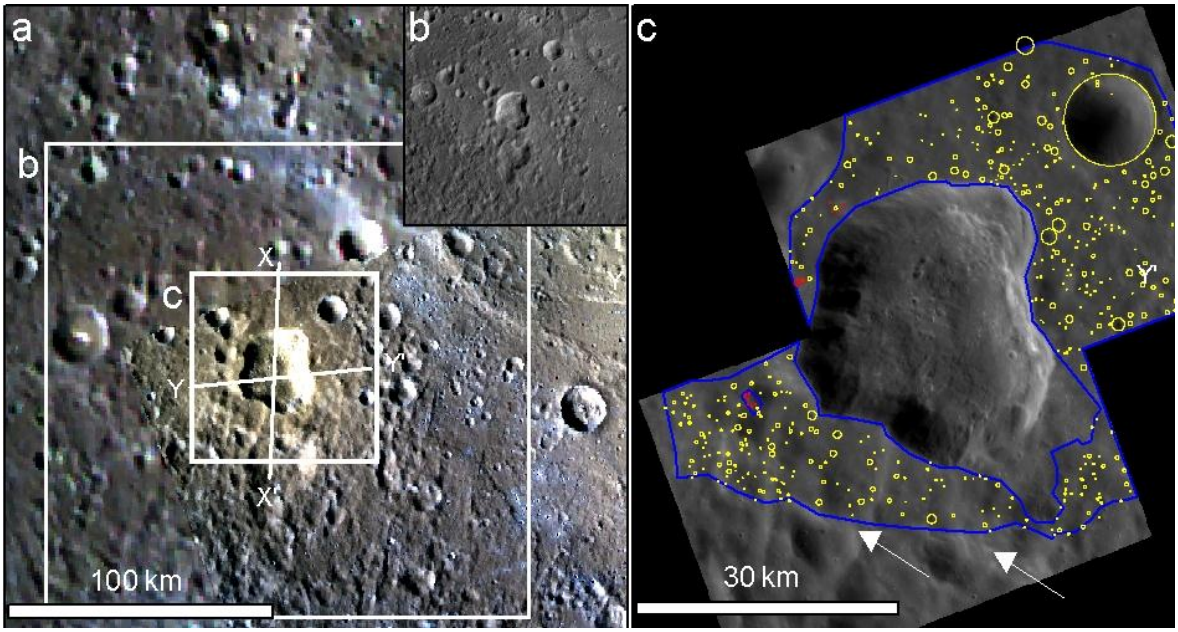


**Figure 4-8 Evidence for explosive volcanic activity north of the Rachmaninoff basin. (a) Colour composite showing a large endogenic pit surrounded by a relatively bright and red spectral anomaly and more spatially-limited thick, steep-edged deposits. White rectangles: extent of (b) and (c), white lines: cross-sections in Figure 4-9 (images EW0254942495I, EW0254942487G and EW0254942491F). (b) Monochrome image of the area around the pit, showing that the pit is the most probable source of the high-relief material to its south (excerpt from the global monochrome mosaic V9). (c) High-resolution monochrome mosaic of the pit. Deposits around it superpose craters on the continuous ejecta blanket of the Rachmaninoff basin (white arrows). Blue outlines: area sampled for crater-counting, yellow open circles: primary impact craters; red open circles: secondary impact craters (images EN0239539037M and EN0239539024M).**

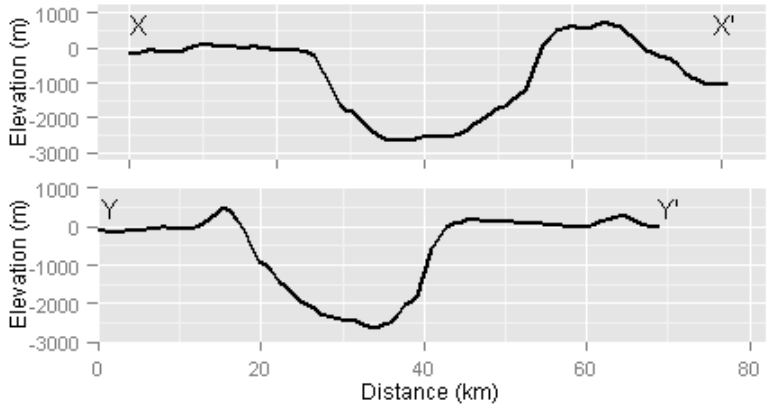


**Figure 4-9 DEM cross-sections across N Rachmaninoff pit as indicated in Figure 4-8a. Large mounds of material at its west and south margins, and more subdued relief to its north and east. DEM derived from images EW1003930329G and EW0254971314G.**

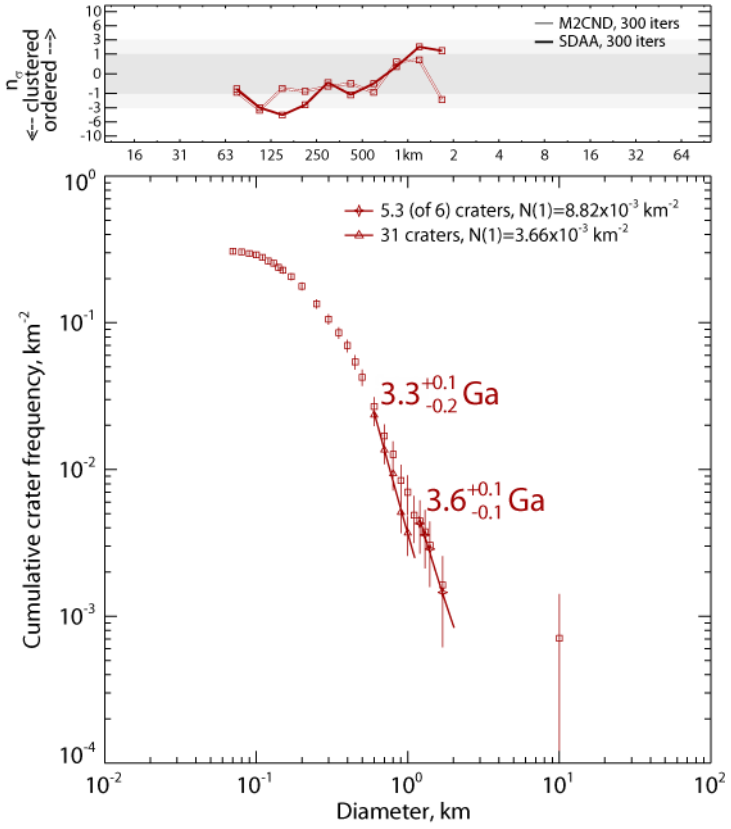


**Figure 4-10 Cumulative crater frequency plot showing resurfacing around N Rachmaninoff. 1.2–2 km diameter craters give a model age of 3.6 Ga (+0.1/-0.1) and an underabundance of craters 600 m–1.1 km diameter indicates later resurfacing (Deposit sample area: 1.41 × 103 km2). Randomness analysis (above) indicates that craters can be considered random for crater diameters between 120 m and 1 km using a mean closest two neighbours distance (MC2ND) measure and between 250 and 710 m using a standard deviation of adjacent area (SDAA) measure. This indicates that it is reasonable to consider the crater population used to obtain the younger model age statistically random.**

The evidence above demonstrates that thick, large-scale pyroclastic deposits were deposited on Mercury during and up to ~400 million years after the period of widespread plains-forming effusive volcanism. The evidence for two periods of activity at AP2 is consistent with earlier work (*Rothery et al.*, 2014), showing that explosive volcanic vents on Mercury can have a prolonged eruptive history.

## 4.5 Discussion

My results indicate a long history of volcanism on Mercury, with effusive volcanism from ~4.1 Ga (*Marchi et al.*, 2013) and explosive volcanism continuing until as little as a billion

years ago. This reinforces the necessity of incorporating long-lived volcanism into models of the thermo-chemical evolution of the planet *(e.g. Grott et al., 2011; Michel et al., 2013; Tosi et al.*, 2013), even if the age of possible young lava deposits (*Prockter et al.*, 2010) is revised upward. Because dating craters that predate pyroclastic vents and deposits gives only a maximum age for the volcanic activity, my results do not allow me to calculate the volume of late-stage explosive volcanism. However, I do find that pyroclastic activity continued until long after the period when voluminous lava eruption formed expansive volcanic plains. In addition to reflecting a decrease in melt production due to secular cooling, it is probable that this change in eruptive style was favoured by changes in the crust through time, e.g. due to the development of compressional stress, as indicated by pervasive fault-related landforms across the planet that date from shortly after 3.8 Ga (*Strom et al.*, 1975; *Watters et al.*, 2012), and thickening of the lithosphere due to planetary cooling. Both these conditions would impede magma ascent. Slow magma ascent allows exsolution of dissolved volatiles and coalescence of bubbles before eruption, promoting intermittent explosive strombolian eruption (*Wilson and Head*, 1981). Further, if magma rise is so inhibited that a dyke stalls below the surface, a magma chamber may form. Here, crystallization can lead to volatile oversaturation in the remaining melt (*Tait et al.*, 1989; *Parfitt et al.*, 1993), and these volatiles can exsolve in the low-pressure, near-surface environment. The resultant overpressure can trigger the propagation of dykes to the surface in an explosive eruption (*Head et al.*, 2002), particularly if, as is the case under impact craters on Mercury (Section 5.5.2), there are pre-existing fractures in the overlying crust. Thus it is to be expected that as magma ascent became impeded late in the planet's history, the volatile content in erupting magmas became elevated and the eruptions more explosive.

A further implication of my findings is that the longevity of volcanism on Mercury is similar to that on the Moon, but that the style of late volcanism differed on the two planets. On the Moon, lava surfaces have been dated to 1.2 Ga (*Hiesinger*, 2003) or even to 0.8 Ga (*Huang et al.*, 2011). Pyroclastic deposits have proved difficult to date by crater-counting because their unconsolidated nature leads to rapid degradation of small superposed impact craters

(*Lucchitta and Sanchez*, 1975). However, stratigraphic relationships in most cases indicate a maximum Late Imbrian (3.2 to 3.7 Ga) age (e.g. *Head and Wilson*, 1979; *Hiesinger et al.*, 2000; *Whitford-Stark and Head*, 2000) and young (< 1 Ga) explosive volcanism has only been proposed at one location on this basis (*Spudis*, 1989). Conversely, although I have shown that pyroclastic activity was very long-lived on Mercury, late effusive volcanism is as yet unproved. A young (~1 Ga) age proposed for smooth plains within Rachmaninoff basin (*Prockter et al.*, 2010) is currently being revised on the basis of the higher number of craters visible in higher resolution images (*Chapman et al.*, 2012) and no other lava surface has been dated to younger than 3.55 Ga.

Late effusive volcanism on the Moon is thought to have been enabled both by a concentration of heat-producing elements in the western nearside lunar crust (*Jolliff et al.*, 2000) and by extension at the margins of large impact basins due to flexural loading (*Head and Wilson*, 1992; *McGovern and Litherland*, 2011). As the loading is a result of the accumulation of thick, dense lavas in basins because the low density of the lunar primary crust prevented eruption in other regions with higher elevations and a greater crustal thickness, both of these factors are a result of compositional variations in the Moon's crust. Mercury's crust does not appear to have such extreme spatial variations in composition (*Nittler et al.*, 2011), so neither the stress-regime nor crustal heating would be expected to facilitate effusive volcanism to such a degree on Mercury late in its history. If the two bodies had a similar duration of volcanism despite their different composition, internal structure and geological history, this may indicate that similar mechanisms, such as insulation by a megaregolith (*Ziethe et al.*, 2009; *Grott et al.*, 2011), allowed a long duration of magma production, but that differing physical conditions in their respective crusts led to differing styles of late volcanism.

Compositional differences in the magma may also have led to greater explosivity on Mercury. In particular, it is possible that Mercury's magma had a higher volatile content than lunar magma. This would explain the large size of pyroclastic deposits on Mercury relative to those on the Moon (*Kerber et al.*, 2011) even without concentration of volatiles at shallow depths before eruption. Lacking, as we do, samples of the products of Hermean volcanism, this

possibility is difficult to assess. However, future spectral analyses using data gathered by MESSENGER and the forthcoming BepiColombo mission (*Benkhoff et al.*, 2010) may lead to valuable insights into the composition of both effusive and pyroclastic deposits on Mercury.

## 4.6 Epilogue: new data

Since the publication of the paper that makes up the majority of this chapter, new images (released by NASA's Planetary Data System up to 6th March 2015) have become available revealing 11 additional sites at which endogenic pits have a surrounding relatively bright and red spectral anomaly. This increases the proportion of such sites that occur within impact craters from 79% to 80% (129 out of 161). Six of these new sites occur in craters with a level of degradation consistent with a Mansurian age, giving a total of 34 sites of putative explosive volcanism within Mansurian-aged craters. These additional sites are included in Table B-1.

# Chapter 5. Mechanisms of explosive volcanism on Mercury: implications from its global distribution and morphology

## 5.1 Introduction

While conducting the global investigation of hollows presented in Chapter 2, I additionally noted any endogenic depressions that were not hollows. This allowed me to compile a more comprehensive catalogue of landforms potentially connected with explosive volcanism than had yet been published, and to use this to better constrain the mechanisms by which this volcanism may have occurred. This work makes up this chapter, and was published as a peer-reviewed paper in the *Journal of Geophysical Research: Planets* (*Thomas et al.*, 2014c).

## 5.2 Background

Traditional models of Mercury's formation predict a volatile-depleted bulk composition (*Cameron*, 1985; *Fegley and Cameron*, 1987; *Wetherill*, 1988; *Benz et al.*, 2007). Therefore, evidence for widespread explosive, volatile-driven volcanism on the innermost planet in the Solar System was not anticipated prior to the arrival of the MErcury Surface, Space ENvironment, GEochemistry, and Ranging (MESSENGER) spacecraft. However, images from MESSENGER flybys showed irregular, apparently endogenic pits surrounded by deposits that are spectrally bright and red relative to the Hermean average. The anomalous spectral character of the deposits, their association with a central depression, and their diffuse outer margins all support their emplacement by explosive volcanism (*Head et al.*, 2008; *Kerber et al.*, 2009). Under the airless conditions at Mercury's surface, this emplacement would have occurred by ejection of pyroclasts along ballistic trajectories. *Kerber et al.* (2009, 2011) and *Goudge et al.* (2014) used MESSENGER flyby and orbital images to produce a catalogue of 51 pyroclastic deposits. The current study increases this number, finding 150 sites, at many of which there are multiple pits and deposits. The spatial extent of the deposits has been used to calculate that their formation by steady fire-fountaining would require a high magma volatile

content (*Kerber et al.*, 2011), further challenging the expectation that Mercury is volatile-depleted. However, to infer the magma volatile content powering an explosive eruption, it is necessary to determine the mechanisms by which eruption occurred: if magma rise were slow or stalled below the surface, volatiles could become concentrated prior to an eruption and so they would not reflect the volatile content of the magma at source. To understand the intrinsic volatile content of Hermean magmas and of the planet as a whole, it is therefore important to constrain the mechanisms by which explosive eruptions occurred on Mercury.

A further surprising feature of Mercury's explosive volcanism is its global longevity. I showed in Chapter 4 that explosive volcanic eruptions occurred over a long period from 3.8 Ga to as recently as 1 Ga. Large-scale thrust faults attest to considerable crustal shortening at the beginning of this period (*Strom et al.*, 1975), and thrust faults that crosscut young craters show that this state of compression has persisted until geologically recently (and may still prevail today) (*Banks et al.*, 2014). This stress regime would tend to impede dyke propagation and so inhibit eruption of magma at the surface. Additionally, if Mercury initially contained the same proportion of heat-producing elements as larger terrestrial planets like Earth, it would have cooled, and its lithosphere thickened, more quickly due to its higher surface-area-to-volume ratio. Both of these conditions mean that volcanism should be hampered late in the planet's history, in conflict with the observations. Hence, further investigation is required to elucidate the mechanisms that permit late-stage Hermean volcanism.

Previous studies have identified sites of explosive volcanism on Mercury by searching for spectrally-distinct, relatively bright and red surface deposits, and then noting whether a vent occurs within those deposits (*Kerber et al.*, 2011; *Goudge et al.*, 2014). Here, I take a different approach by examining MESSENGER images first for probable endogenic pits and then for bright, red surrounding deposits. This method allows me to increase three-fold the number of published candidate sites for explosive volcanism, and thus to better understand their overall distribution. With the aid of stereo-derived digital elevation models (DEMs) and Mercury Laser Altimeter (MLA) data, I investigate the 3D topography of the pits and deposits, and I

combine this with their spatial distribution to better constrain the eruption mechanisms responsible for Mercury's widespread, long-lived explosive volcanism.

## 5.3 Methods

### 5.3.1 Identifying sites of explosive volcanism

To identify endogenic pits and surrounding deposits, I examined images taken by MESSENGER's Mercury Dual Imaging System (MDIS) (*Hawkins et al.*, 2007) prior to March 17th, 2013. I first identified pits in monochrome images, and then examined colour images to determine whether those pits were surrounded by spectrally-distinctive (i.e. bright and red) deposits.

#### *5.3.1.1 Pits*

As part of the study resulting in Chapter 2, I surveyed all MESSENGER Narrow Angle Camera (NAC) and Wide Angle Camera (WAC) images at a resolution of 180 m/pixel or better, noting all endogenic depressions. These depressions were numbered using an arbitrary scheme, with numbers ranging from 1000 to 8999. I distinguished such depressions from impact craters (exogenic depressions) on the basis of their departure from planform circularity and the absence of the characteristic ejecta deposits, terraces, raised rim, and central uplifts of impact craters. I applied radiometric and photometric corrections to these images using ISIS3 image processing software produced by the U.S. Geological Survey. I also examined the PDS-hosted 250 m/pixel global monochrome mosaic (March 2013 release) to ensure that no large-scale depressions, not otherwise visible with individual NAC and WAC frames, had been missed.

I classified all subsequently identified depressions as pits, hollows, or pitted ground (Figure 5-1). Pits are the deepest type of depression and generally have sloping floors. Any surrounding spectral anomaly is redder than the Hermean average. Hollows can individually be as little as tens of meters across, are shallow and flat-floored, and have steep margins (*Blewett et al.*, 2011). They are floored and haloed by relatively bright and blue deposits and probably form largely by sublimation or some other non-explosive process (Section 2.5.1),

and so are not considered further in this study. Pitted ground is morphologically intermediate between pits and hollows: it consists of an area of the surface with an uneven, pitted appearance of a similar to somewhat greater depth than hollows but with a more rounded texture. In some cases pitted ground is surrounded by a steep margin. Where floored and surrounded by spectrally bright and red deposits it is probable that, like pits, this type of depression has a volcanic genesis. In Section 2.5.1.2, I suggested that pitted ground forms when volatile escape disturbs an overlying stratum such as cooling lava, rather than by vent-centred explosive volcanism. On that basis, pitted ground has also been excluded from further investigation in this study.

I digitized the margin of each pit on the global monochrome mosaic using ArcGIS software and noted its location and geodetic areal extent using Tools for Graphics and Shapes software (*Jenness*, 2011). Where a pit lay within an impact crater or its proximal ejecta blanket, I noted its specific location in the crater (i.e. crater wall, peak structure, smooth or rough floor, proximal ejecta). Where several pits were identified within an impact crater or clustered within 50 km of each other (an arbitrarily-defined distance), they were grouped into a single site. Where a pit lies within 20 km of a lobate scarp or wrinkle ridge, or incises a crater that is affected by or overlies such tectonic structures, I noted this association. The surface traces of these tectonic structures were identified by reference to the 1:2,000,000 scale global fault map of *Byrne et al.* (2014), complemented by examination of high-resolution NAC data and my topographic products (see Section 5.3.2.1).

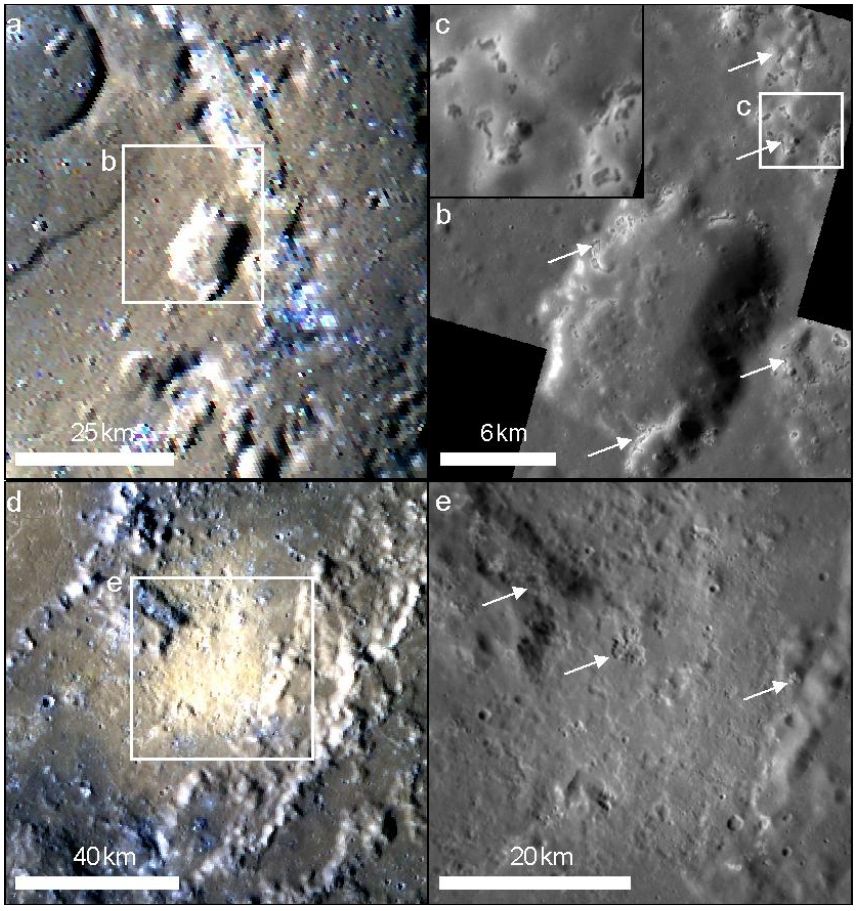


**Figure 5-1 Types of depression on Mercury: pits, pitted ground and hollows. (a) Peak ring area of Praxiteles crater (-59.1° E, 26.9° N) with both a pit with surrounding bright, red deposits and hollows with bright, blue deposits. White rectangle: extent of (b) (colour composite of frames EW0253964972I, EW0253964964G and EW0253964968F). (b) Close-up of the pit and surrounding hollows. The pit is larger and has a rounded floor, while the hollows are smaller, have flat floors and occur in clusters. Rectangle: extent of (c). Arrows: Clusters of hollows (images EN0223701867M and EN0223701860M). (c) Close-up of hollows showing their fresh morphology, steep margins and flat floors (Image EN0223701860M). (d) Pitted ground: a bright, red deposit on the floor of Rachmaninoff crater (59.6° E, 26.1° N) with bright, blue deposits (hollows) on the peak-ring and terraces around it. Rectangle: extent of (e) (composite of EW0254942272I, EW0254942264G and EW0254942268F). (e) Close-up showing the uneven, subtly pitted surface of the bright, red area (pitted ground), and hollows (white arrows) superposing and around it (image EN0224338598M).**

#### *5.3.1.2 Deposits and substrates*

To identify spectrally-distinct deposits around pits, I constructed colour images by combining images from 996 nm, 749 nm and 433 nm WAC filters in the red, blue, and green channels, respectively. This combination of wavelengths was chosen because such images allow for robust identification of spectral variations on Mercury's surface despite its generally red-sloped reflectance spectrum (*Denevi et al.*, 2009). I created and examined colour composites for all images at a resolution of 1000 m/pixel or better, and also examined the PDS-hosted 1000 m/pixel global colour mosaic (March 2014 release).

I digitized the extent of each identified spectral anomaly and calculated its area as for pits. This areal value should be viewed as a minimum because the margins of these anomalies are diffuse and I took a conservative approach to judging their limit, excluding the more tenuous outer fringe. Additionally, it is likely that the present visible area of a given deposit is less than its original extent due to averaging of the observed surface spectrum by impact gardening and, depending on composition, by space weathering. Modification of spectra by these effects will become more pronounced over time.

### 5.3.2 Investigating topography

#### *5.3.2.1 Data acquisition*

Where available I used Mercury Laser Altimeter (MLA) (*Cavanaugh et al.*, 2007) data to characterize the topography of the pits and deposits. The along-track spacing of data points is ~400 m at all latitudes, but the horizontal footprint and between-track spacing are both at a minimum at periapsis (~60° N). No MLA data are available for the region south of ~5° S.

Where a MLA track directly crosses a pit or its deposits, I constructed a topographical cross-section along it. Where many tracks are available in close proximity to the pit, I constructed a digital elevation model (DEM) using Natural Neighbour interpolation using ArcGIS, in a sinusoidal projection centred on the pit.

For those pits not crossed by multiple MLA tracks, I used stereo images (NAC or the WAC frames using the 750 nm filter) to create high-resolution DEMs by photogrammetry using the Ames Stereo Pipeline (ASP) (*Moratto et al.*, 2010). Where possible, I used MLA points to vertically control the DEM. Because it is difficult for ASP to identify single pixel correspondences between two images, point data were averaged on a 3×3 block of pixels, giving the DEM a resolution 3 times lower than the images from which is was derived. The resulting DEMs range in resolution from 215 to 880 m/pixel. In some cases, the stereo-derived DEMs had a monotonic slope across the scene. For stereo-derived DEMs without MLA control this slope may be an artefact of stereo correlation. In other cases, however, such a slope is a geological reality, as where regional tilting due to long-wavelength warping has been observed at numerous sites across Mercury (*Zuber et al.*, 2012; *Byrne et al.*, 2014). If a tilt was judged to be an artefact, or interpreted as real on the basis of its regional context but to have occurred after pit formation, I applied a linear detrending to the DEM using ArcGIS. Where the pit lay within a flat-floored impact crater, the dip of that floor (which can be assumed to have been originally horizontal) was used to judge the trend. In other cases, the dip of the entire DEM was used for this purpose.

Where possible, I calculated pit volume from a DEM by interpolating an additional surface above the pit in a buffer beyond its rim and calculating the volume difference between these two surfaces using the Cut Fill tool in ArcGIS. Where the unevenness of the surrounding surface or anomalous values in shadowed areas of the DEM made this approach impractical, I calculated pit volume by determining pit depth from my topographic data, measuring length and width in planform in a sinusoidal projection centred on the pit, and then calculating the volume by approximating it to a hemiellipsoid, cone or trench, depending on the pit morphology. To calculate the slopes of circum-pit deposits and of pit walls, I calculated the gradient between the DEM pixel values or MLA points at the slope top and base.

#### *5.3.2.2 Data accuracy and error*

The potential for horizontal and vertical error varies between the data types. MLA data have a vertical accuracy with respect to Mercury's centre of mass of < 20 m and a range precision

of < 1 m under nadir-viewing conditions. The horizontal accuracy of MLA data depends on the accuracy of the spacecraft pointing data, but can be approximated as being of the order of the footprint size, which varies from 15 to 100m, peaking at apoapsis.

The error in stereo-derived DEMs produced using ASP is more difficult to quantify. To explore this issue, I constructed a DEM with and without MLA control at five sites. Both DEMs were detrended, and the mean elevation difference and the difference in horizontal scale were calculated. I found that horizontal differences are negligible (<1%), but vertical differences are considerable: the standard deviation in relative elevation difference ranges from 42 to 79 m.

I calculated the error on my slope measurements by obtaining the slope of a best-fit line through MLA points and through raster pixels in the MLA-controlled and uncontrolled DEMs along cross-sections at ten locations across the five test cases. The mean slope difference between MLA-controlled DEMs and MLA profiles is 3%, whereas it is 13% between uncontrolled DEMs and MLA data.

#### *5.3.2.3 Identification of deposits*

Because both tectonic and impact processes can produce substantial topography, care was taken to interpret all anomalous topography near endogenic pits on the basis of planform imagery, and to attribute it to volcanic deposition only where no other explanation was viable. Where a pit covers a large proportion of an impact crater floor, topography resulting from pyroclastic deposition cannot be distinguished from that of the impact crater's original terrace/wall, and where pits occur outside an impact crater on rough terrain, only thick deposits with clear circum-pit topographic expression can be identified other than by colour. Therefore topography owing to volcanic deposition may not have been recognized at all locations where it is present, and I have most commonly identified such topography on the otherwise smooth, flat floors of impact craters.

## 5.4 Results

### 5.4.1 Occurrence of endogenic pits and deposits

I identified 174 candidate endogenic pit sites, at 150 of which a bright and red spectral anomaly is visible (Figure 5-2, Table C-2). There are multiple pits at 64 of these sites, with a total of 327 pits overall (Table C-1). Previous to this work, the largest number of putative pyroclastic deposits identified on Mercury was 137 (*Kerber et al.*, 2014), of which 51 had been identified in earlier published studies (*Kerber et al.*, 2011; *Goudge et al.*, 2014). My study finds 57 additional deposit locations not identified in *Kerber et al.* (2014). I do not observe an endogenic pit with an associated deposit at 40 of their candidate locations, but I do identify spectrally-red pitted ground at 15 of those 40 locations, and an endogenic pit lacking a surrounding deposit at two.

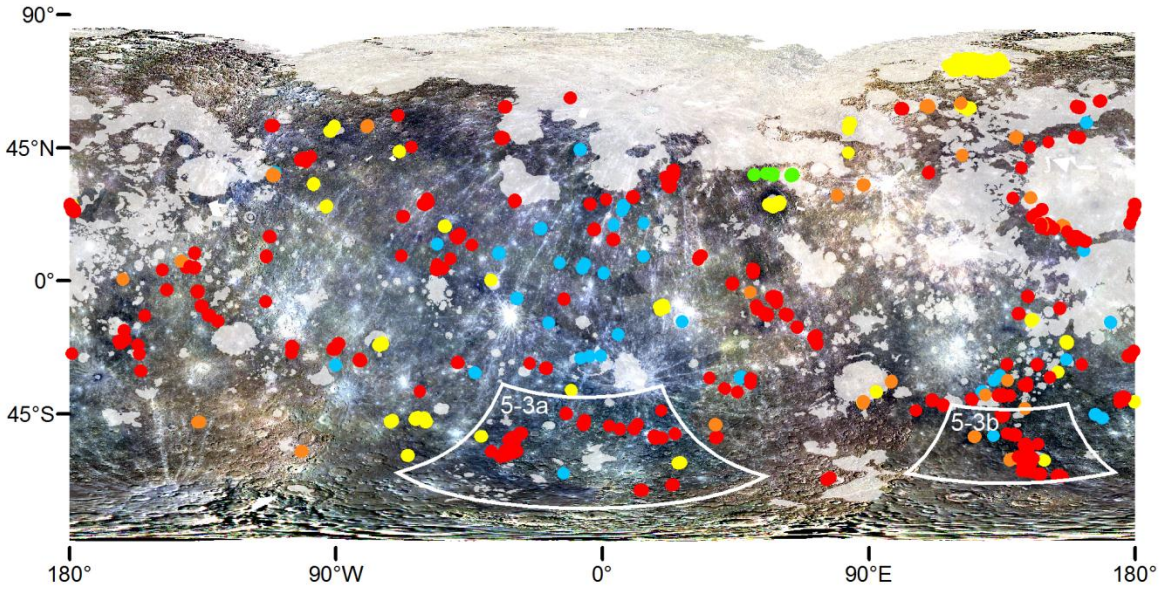


**Figure 5-2 Distribution of endogenic pits and areas of spectrally red pitted ground. Red dots: Endogenic pits with an associated bright, red spectral anomaly. Orange dots: Endogenic pits without a visible spectral anomaly. Yellow dots: Spectrally red pitted ground. Blue dots: Sites where pits or deposits indicate possible (but not definitive) explosive volcanism. Green dots: Aligned endogenic pits between Rachmaninoff basin and smooth plains. White boxes: Locations of Figure 5-3. White areas: Mapped smooth volcanic plains (*Denevi et al.*, 2013). (Base image: global colour MDIS mosaic version 5).**

#### *5.4.1.1 Global and regional distribution*

Endogenic pits are widespread on Mercury, although they are rare (only 5 of the 327 individual pits) on thick high-reflectance volcanic plains such as those at high northern latitudes and inward of the margins of the fill within the Caloris impact basin (Figure 5-2). Pits are not randomly distributed: the 327 individual pits have an average Nearest Neighbour ratio of 0.402, indicating that they are on average separated by less than half the distance expected in a random distribution. Additionally, pits have a Moran's Index of 0.148 based on their areal extent, a result indicating that those with a similar planform area are clustered. This statistic measures correlation in a value between different locations (*Moran*, 1950); a value of -0.003 indicates no spatial correlation between pits of a similar size. For both statistics, the z-value indicates a likelihood of less than 1% that this clustering is the result of random chance.

Clustering of pits is especially apparent at the margins of large impact basins. As previously noted (*Head et al.*, 2008; *Goudge et al.*, 2014; *Rothery et al.*, 2014), many endogenic pits and deposits occur around the marginal fill and rim of the Caloris basin. My study also finds conspicuous alignments of pits with spectrally-distinct deposits around a proposed ancient impact basin, listed as "b54" by *Fassett et al.* (2012), located in the southern hemisphere at approx. -2° E, -59° N (Figure 5-3a). The pits form alignments at the north and west of a relatively smooth unit that may correspond to volcanic infill within the basin. The region is surrounded by contractional tectonic structures (*Byrne et al.*, 2014), many of which bound high-standing terrain just outside the zone where the pits occur. Although this putative basin is heavily degraded and therefore very old, some of the pits surrounding it are much more recent: for example, the westernmost pit in this area incises the 27–km diameter Kuniyoshi crater, which appears to be Kuiperian (< 1 Ga) or at least Late Mansurian (1.7–1 Ga) (Section 4.4.1).

There is also evidence that pits occur along regional tectonic trends that appear unrelated to basin structures. For example, in another area in the southern hemisphere at137° E, -46° N (Figure 5-3b), endogenic pits with and without bright, red deposits occur in a relatively high-

standing, extensively-faulted region. These pits have the same general trend as, but are not collocated with, the largest faults.

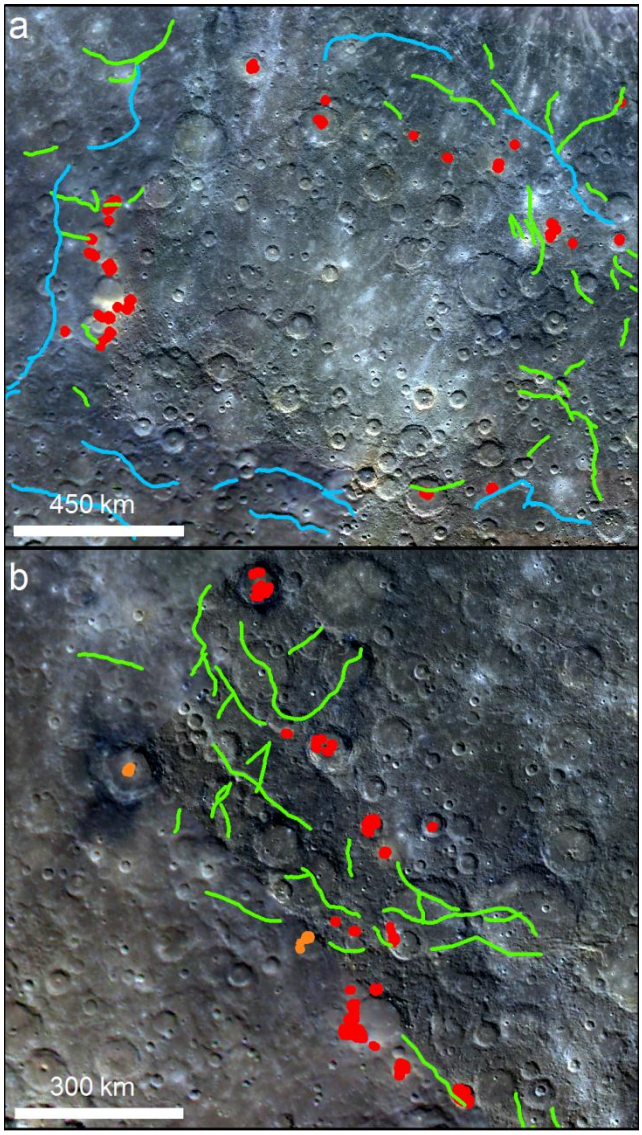


**Figure 5-3 Regional alignments of endogenic pits and their association with tectonic structures. (a) Alignments of pits with a surrounding bright, red spectral anomaly at the margins of a sub-circular area bounded by faulting. Red dots: Pits with spectrally bright, red deposits. Blue lines and green lines: high-terrain-bounding structures and cratered plains structures (after *Byrne et al.* (2014)) (global MDIS colour mosaic v5, Lambert equal area projection centred on -6° E, -57° N). (b) Alignment of endogenic pits with and without (red and orange dots, respectively) a surrounding spectral anomaly that lie along a faulted, heavily-cratered region. The coloured lines are as for (a) and base map image as for (a), with projection centred on 137° E, -46° N.**

#### *5.4.1.2 Local associations*

At 81% of the candidate pit sites, and 79% of those with a bright, red spectral anomaly, pits occur within an impact crater. The pits tend to occur at sites within the crater where there may be a structural control on their formation, such as at or around central uplift structures and along wall terraces. As noted above, pits also occur in association with tectonic structures: at 46% of pit sites and 47% of those with bright, red deposits they occur in close proximity to one or more surface fault traces. These tectonic structures are in all cases lobate scarps or wrinkle ridges, which are thought to be the surface expressions of thrust faults (*Schultz*, 2000; *Watters et al.*, 2009). In total, pits occur either in association with the surface trace of a thrust fault or within an impact crater at 92% of pit sites where there are associated bright, red deposits. Additionally, at some sites pit alignment suggests a subsurface structural control, such as where pits occur radial to the centre of Caloris (*Rothery et al.*, 2014) or where four pits form a 550 km–long line between the Rachmaninoff basin and the southern edge of the northern plains (at 50–67° E, 36° N; green dots in Figure 5-2).

Although endogenic pits are rare or absent in the central part of volcanic plains, where plains thickness is expected to be greatest, evidence for explosive volcanism is frequently present at locations where it is probable that effusive volcanism preceded it: 30% of endogenic pits with a surrounding spectral anomaly occur within probable lavas. For example, pits incise the floors of impact craters that are of a diameter where a central uplift feature would be expected (*Pike*, 1988), but where an uplift feature is not observed or is anomalously small. This suggests that the crater was infilled by volcanic material that covered its peak structure prior to formation of the pit.

Although there is a clear spatial correlation between endogenic pits and hollows (Section 2.4.5), I find no correlation between pit or deposit area and either proximity to hollows or the areal extent of nearby hollows.

### 5.4.2 Extent and morphology of pits and deposits

#### *5.4.2.1 Pits*

Endogenic pits vary widely in size. The 327 individual pits at the 174 pit sites range in surface area from 1.2 to 900 $km^2$, with a median value of 38 $km^2$. The 57 pits for which I have obtained topographic data (Table C-3) have calculated volumes of 1.3–1300 $km^3$, with a median of 40 $km^3$. These pits have depths of between 200 m and 4 km, with a median depth of 900 m.

The cross-sectional shape of pits varies. Many, especially those circumferential to the central peak of an impact crater (e.g. Figure 5-4b), have a V- to U-shaped cross-section. Some have steep margins and relatively flat floors (e.g. Figure 5-4d), whereas others have morphologies intermediate between these end-members (e.g. Figure 5-4f). In large pits, the floor is often multi-levelled. This may be the result of post-formational deposition of material at pit wall bases due to mass wasting, or it may be a primary feature of the pits themselves. It is probable that any pit with originally steep walls has been modified by mass wasting to some degree, so I am cautious about drawing conclusions about the mode of pit formation from the present cross-sectional shape.

In many cases, pit planform shapes are elongated along anticipated planes of weakness in impact craters, particularly around central peaks or along peak-rings. At some sites, several pits occur in close proximity to, or conjoined with, each other (Figure 5.5). Where these pits appear similarly pristine, they may have formed at the same time. However, where there are cross-cutting relationships and/or different degrees of softening of internal texture, discrete pit-formation events are indicated.

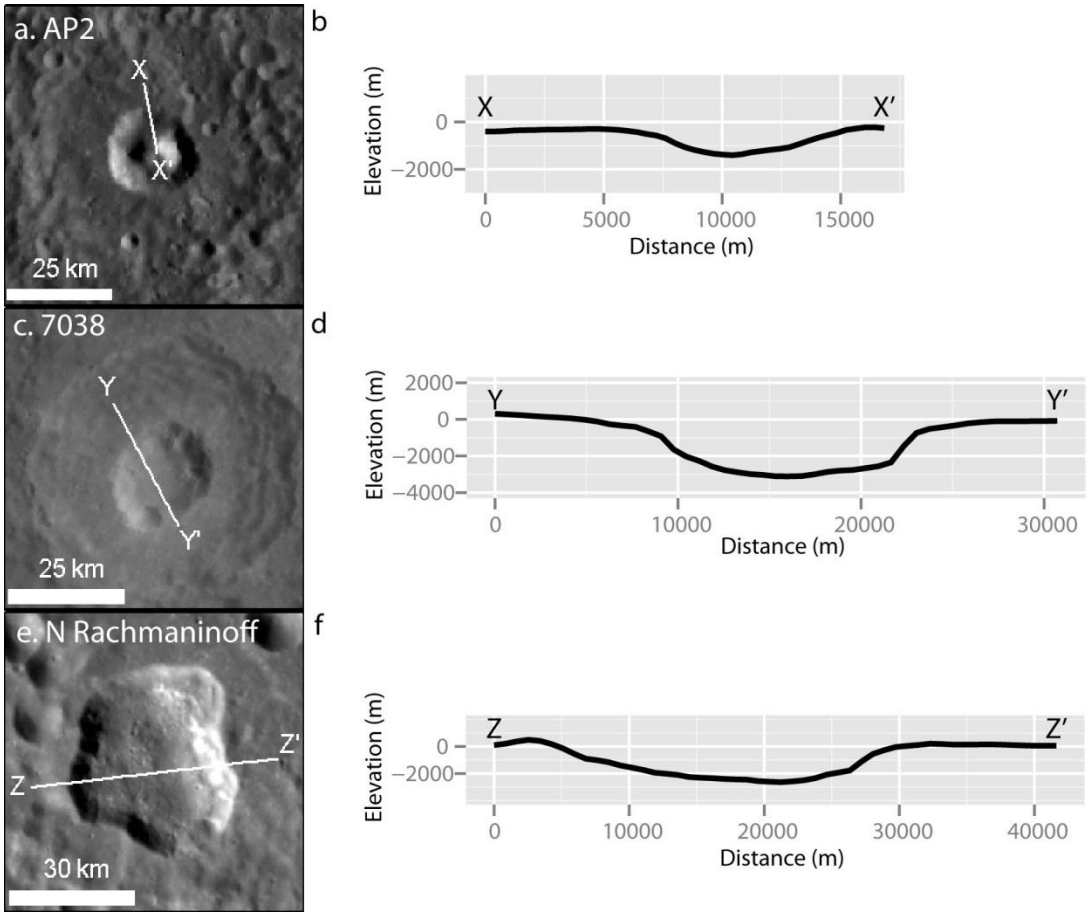


**Figure 5-4 The variety in cross-sectional shape of endogenic pits (no vertical exaggeration). Left images show the pit and the location of the DEM cross-section on the right side (white line). Stereo images are listed in Table C-3. (a),(b) V- to U-shaped profile in a pit circumferential to an impact crater central peak (AP2, -135.5° E, -8.4° N). (c),(d) Flat floor and steep walls of a pit at the centre of an impact crater (7038, -89.3° E, -21.1° N). (e),(f) Steep upper scarp in the east and smoothly-dipping floor of a large pit outside any impact crater (N Rachmaninoff, 57.4° E, 36.0° N).**

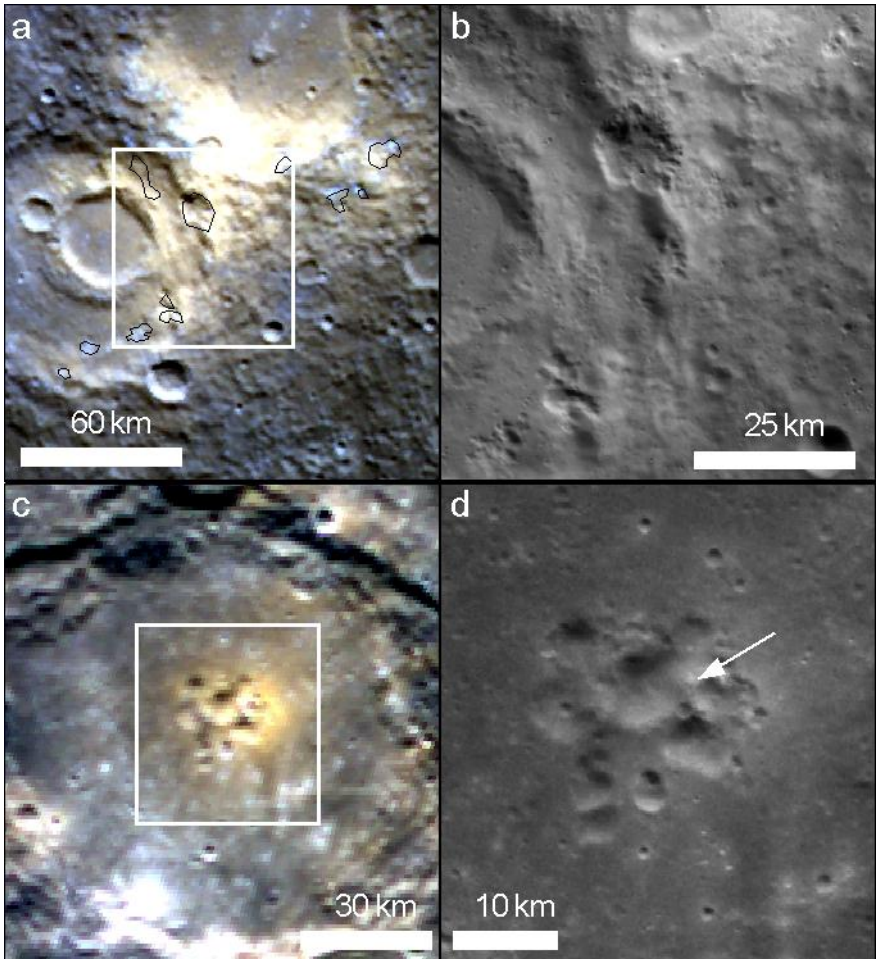


**Figure 5-5 Examples of multiple pits at a single location surrounded by relatively bright, red deposits indicating a complex history of volcanism. The white rectangle in the top images indicates the extent of the bottom images. (a) Many pits (outlined in black) occur over an area within and between two craters (-31.9° E, -58.1° N) and are surrounded by a bright, red spectral anomaly. Activity may have occurred concurrently or sequentially from different vents (composite of frames EW1005108006I, EW1005108026G and EW1005108010F). (b) Close-up showing that some of the pits in (a) are similarly pristine (image EN0239040293M). (c) Multiple small pits around the centre of an impact crater at -6.5° E, -48.4° N. The spectral anomaly is brightest around the northeast pits (composite of EW0222840754I, EW0222840774G and EW0222840758F). (d) Close-up of (c) showing that the pits at the centre of the brightest deposits have the freshest morphology and incise into the margins of the pits to their north (white arrow) and west, indicating that they post-date them (image EN0253479661M).**

### *5.4.2.2 Circum-pit deposits*

The areal extent of continuous spectrally bright and red deposits around pits varies from $1.06\times10^{1}$ to $3.86\times10^{4}$ km$^2$ (median $5.60\times10^{2}$ km$^2$). They can extend to a great distance from the pit: the largest deposit, NE of the Rachmaninoff basin, has a maximum radius of 130 km. This is greater than the previously-reported radius of 71 km for this deposit (*Kerber et al.*, 2011) because higher-resolution colour images obtained during MESSENGER's orbital campaign show that the spectral anomaly extends to greater distances. Assuming a circular deposit, the median areal extent of all the documented deposits indicates a median radius of 13.3 km.

In confirmation of earlier work (*Kerber et al.*, 2011), I find that the average area of a pyroclastic deposit on Mercury is greater than that of similar lunar deposits catalogued by *Gaddis et al.* (2003) (Figure 5-6). Although additional candidate lunar deposits have recently been detected, these are at the low end of the range of deposit sizes on the Moon (*Gustafson et al.*, 2012; *Gaddis et al.*, 2013).

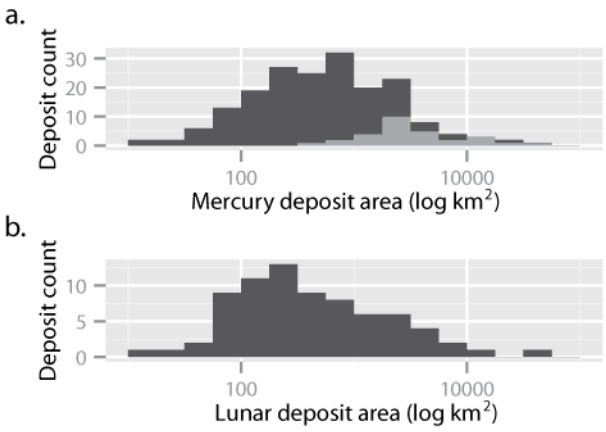


**Figure 5-6 Comparison of the size of pyroclastic deposits on (a) Mercury (light grey: documented by *Kerber et al.* (2011), dark grey: this study) with (b) those on the Moon (*Gaddis et al.*, 2003).**

Where the terrain surrounding a pit is relatively flat (e.g. an impact crater floor), a relatively bright and red spectral anomaly is visible, and there is no evidence that faulting or subsequent impacts have substantially modified that topography, I attribute positive relief

around the pit margins to deposition of material that originated from that pit. My topographic data indicate such a pre-existing level surface at 20 sites. Morphometric data at these sites are given in Table C-3, with stereo image or MLA track product IDs indicated. Where I produced a stereo DEM, I used this to orthorectify the left image, and used this as the monochrome image in figures in this section.

At six of these sites, there is little (≤ 1°) or no relief around the pit (Figure 5-7; Table C-4, Table C-5 (a–f)). At all of these sites the pit is surrounded by a relatively bright and red spectral anomaly, so it appears that deposits are present but they do not form thick accumulations close to the vents. At 12 of the remaining 14 sites, I have detected a rise around the pit (Figure 5-8, Table C-5 (g–r)). The outer flank slope is usually very low: the mean of 24 measurements is 2.9 ± 0.1° (standard deviation: 2.0), although the steepest is 8.3 ± 1.1°. The maximum elevation ranges from 29 ± 61 m to 567 ± 194 m above the surrounding topographic datum. In each case, the rise is proximal to the vent, with a mean distance from the pit margin to the slope base of 5.7 km (standard deviation: 2.8 km). The radius of the annulus of elevated terrain is usually a fraction of the entire radius of the spectral anomaly associated with the vent: the ratio between the radius of the elevated region and the radius of the spectral anomaly has a median value of 0.3. However, at two sites the relief extends as far as or even farther than the spectral anomaly. In these cases, the spectral anomaly is less pronounced than at other pit sites. At the remaining two sites, relief takes the form of a broad swell adjacent to a pit that is in turn circumferential to the centre of an impact crater. The swell has a relatively bright and red spectral signature and a rough pitted surface. The swells associated with Pits 6120 and 6123 have a maximum thickness of 128 ± 61 m and 98 ± 61 m and have radii of 14 km and 8 km, respectively (Table C-5 (s–t)). The bright-red, rough material adjacent to Pit 6120 overlies relatively smooth, low-reflectance material (LRM), indicating that its rough surface is not the result of exposure to the normal flux of impact craters after its formation but is instead primary to the deposit.

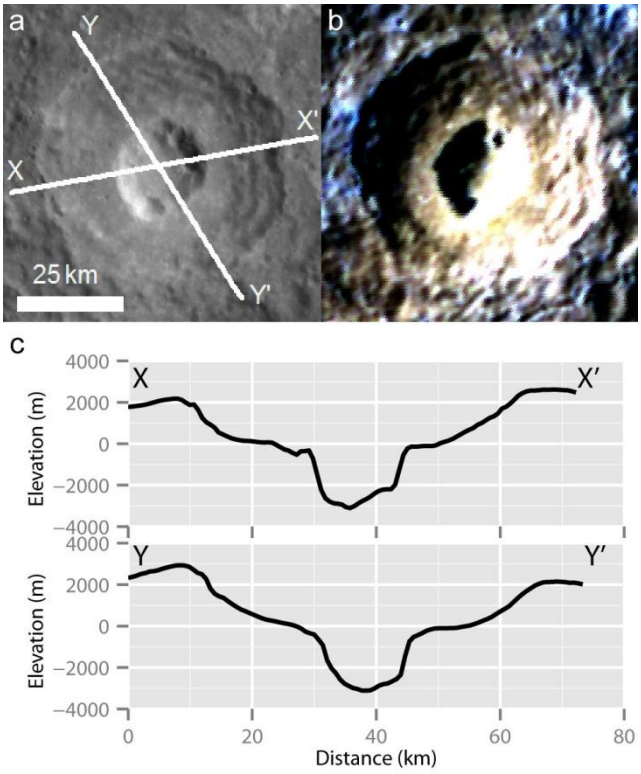


**Figure 5-7 Pit 7038 (located at -89.3° E, -21.1° N) lies at the centre of an impact crater and is surrounded by relatively bright, red deposits with little appreciable relief. (a) White lines indicate the locations of cross-sections in (c)). (b) A bright, red, diffuse-margined spectral anomaly is centred on the pit (composite of EW0259266820I, EW0259266840G and EW0259266824F). (c) West-east and northwest-southeast cross-sections from the DEM across the pit and crater show no pit-centred anomalous relief.**

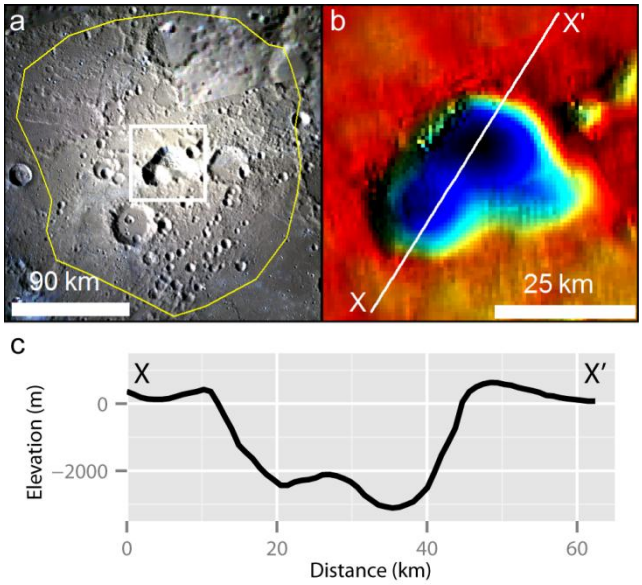


**Figure 5-8 A large pit NE of the Rachmaninoff basin with a relatively bright and red anomaly surrounding it to considerably greater distances than those to which circum-pit relief is detected. (a) A spectral anomaly (outlined in yellow) surrounds a central pit to a radius of 130 km. (b) Hillshade of the DEM in the circum-pit area. White line: The southwest-northeast cross-section shown in (c), illustrating the outward-sloping topography at the pit rim. This pit is located at63.9° E, 35.8° N. (The image in (a) is a mosaic of colour composites from frames EW0239664251I, EW0239664247G, EW0239664243F and EW0254913717I, EW0254913709G, EW0254913713F.)**

### *5.4.2.3 Correlation of pit and deposit dimensions*

The area covered by spectrally-red deposits generally scales with the pit area. Pits and deposits have a log–log relationship with a Pearson's product-moment correlation (*Pearson*, 1985) of 0.64 (where 1 is total positive correlation) (Figure 5-9). At the 13 sites where I have detected appreciable deposit topography, I found no statistically-significant correlation between the extent or volume of pits and deposits and the deposit's maximum outer flank slope.

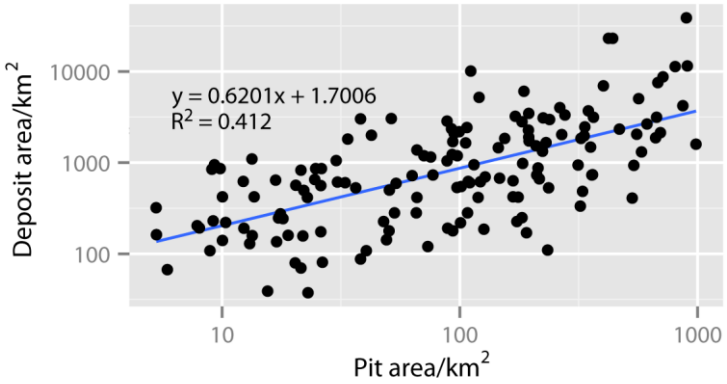


**Figure 5-9 The positive linear correlation between pit area and deposit area.**

## 5.5 Discussion

My evidence is consistent with the prevailing interpretation that the pits I catalogue here are the surface expression of volcanic vents, formed through explosive pyroclastic volcanism. Therefore, in the following discussion I will use the terms "pit" and "vent" synonymously. My results allow me to make inferences about the style of these explosive volcanic eruptions, the physical conditions controlling them, and the mechanisms by which they form.

### 5.5.1 Eruptive style

On Earth, explosive volcanism occurs in a number of styles: it can be steady or intermittent, and it can take a number of forms depending on the ratio of juvenile magma to external water (such as seawater or groundwater) (*Wohletz and Sheridan*, 1983). The style of eruption in turn affects the morphology of its products, so volcanic products are a window on the form(s) that explosive volcanism has taken on Mercury. As on Earth, a range of styles is to be expected, both over time at a single vent and between sites of eruption.

Morphologically, Mercury's pits and deposits are most similar to maars on Earth. Maars are pits incised into bedrock that are surrounded by low-relief deposits and are underlain by a rock-filled fracture (often termed a diatreme) (*White and Ross*, 2011). Two principle models have been advanced for maar–diatreme formation: fluidization of pyroclasts due to depressurization of a gas-rich magma (e.g. *Wilson and Head*, 2007) or phreatomagmatism (eruptions involving interaction between magma and non-magmatic water) (*Lorenz*, 1975). A

fluidization model has been applied to explain widely-dispersed glass beads on the Moon's surface, hypothesizing that the formation of a gas-rich foam at dyke tips at great depths could drive short, steady eruptions (*Wilson and Head*, 2003). It is possible such a process occurred on Mercury, although as deposits are, on average, larger on Mercury than on the Moon it does not necessarily follow that a similar eruption style was responsible for their formation. The hypothesis that Mercury's pits and deposits formed by a process comparable to phreatomagmatism is intriguing in light of growing evidence for near-surface volatiles on Mercury. In particular, the formation of hollows in the LRM substrate, probably primarily by sublimation, indicates that this substrate is (or was) volatile-rich (*Blewett et al.*, 2013; Section 2.5.3). Because phreatomagmatic eruptions are explosive due to the addition of external volatiles, the magma need not have had a high volatile content at depth. However, I find no correlation between the proximity or extent of nearby hollows and the scale of pyroclastic pits and deposits. Therefore, although I cannot exclude the possibility of a non-magmatic source for some of the volatiles that drove explosive eruptions, the evidence does not at present support their playing a major part.

It is an oversimplification to draw direct comparisons between my observations of Mercury and styles of volcanism on Earth on the basis of similar deposit morphology alone. For example, Earth's atmosphere allows non-ballistic transport mechanisms such as convection in an eruption column and pyroclastic flow, whereas its higher gravity reduces the ballistic range of similar-sized particles (*McGetchin et al.*, 1974). The same can be said for comparing pyroclastic landforms on Mercury with those on Mars, where air resistance reduces the ballistic range of pyroclasts of a given size, despite the planet's similar gravity (*McGetchin et al.*, 1974). This means formation of steep-sided pyroclastic cones such as those reported in Mars' Tharsis region (*Brož and Hauber*, 2012) is not favoured on Mercury, particularly at the high eruption velocities implied by my data (Section 5.5.3), at which the effect of atmospheric drag is proportionally greater.

The Moon is the terrestrial body that is most closely analogous to Mercury in terms of atmospheric pressure and gravity, so models of the dynamics of lunar explosive eruption are

potentially more appropriate for understanding those processes on Mercury. For those pyroclastic deposits on Mercury that have no topographic expression, little can be inferred about the precise style of eruption: it appears that the eruption was of low volume and/or short duration, such that no discernible topography resulted from differences in the size of particles deposited at different distances (*Wilson and Head*, 1981). However, the finding that, where there is topographic relief, it is greatest close to the pit and usually lies within a more extensive thin deposit is more revealing. Modelling of lunar pyroclastic eruptions suggests that this pattern of topography cannot occur through steady eruption of fine material, but instead requires extreme particle-size sorting in Strombolian eruption, or high flux steady eruption where the majority of the erupted mass forms large (10 mm–1m) particles (*Wilson and Head*, 1981). One or both of these eruption styles may thus have been responsible for the areally-extensive pyroclastic deposits on Mercury.

The processes forming a broad rise with a pitted surface adjacent to arcuate pits 6120 and 6123 (Table C-5 (s,t)) may differ from those discussed above. This non-axisymmetric relief may have formed by effusive or clastogenic flow, or by non-vertical explosive eruption. Alternatively or additionally, the pitted texture of the deposit may indicate a more complex genesis: this texture has some similarity to spectrally-red pitted ground (Figure 5-1e), which may have formed by disruption of the surface by escaping gases (Section 2.5.1.2). Given this similarity it is interesting to note that the deposit at pit 6120 overlies LRM, which is thought to be volatile-bearing. Therefore, the unusual surface texture of these pits' deposits may be due to modification of the surface by escaping gases, which might also be responsible for their broad, raised morphologies.

Whatever the style of eruption, my findings support the occurrence of multiple phases of activity at sites of pyroclastic volcanism on Mercury. Where there are multiple or coalesced pits at one location and a clear age relationship is observed (e.g. Figure 5-5d, *Rothery et al.*, (2014)), the locus of eruption appears to have shifted over time. Additionally, at site AP2 an underabundance of small superposed impact craters indicates resurfacing of the initial

deposit by a second, thin layer after up to 300 Ma (on the basis of model ages) (Section 4.4.2.1).

The morphology of pyroclastic deposits and the styles of eruption they imply do not have a simple relationship with the size of the pit or deposits. Whereas the three largest deposits, around NE Rachmaninoff (Figure 5-8), N Rachmaninoff (Table C-5 (l)), and, potentially, AP1 (Chapter 7), have thick deposits close to the vent indicating high-volume, high-energy eruption, the fifth-largest deposit, at Pit 7038 (Figure 5-7), has no appreciable topographic expression, indicating that the flux and total erupted volume were not enough for edifice-building. The vents are large in all four cases (among the twenty largest on the planet), but their flux and duration of activity appear to have differed substantially. Considering the wide range of eruptive styles documented at volcanoes on Earth and other planets, this should not be surprising.

The large scale of pits on Mercury, and their parallel with maar-diatreme volcanoes on Earth, raise the question of whether pyroclastic deposits on Mercury are primarily juvenile or non-juvenile material: in maars, juvenile (magmatic) material often makes up a small proportion of the erupted mass, which is mainly material stripped from the vent walls. A recent investigation of the NE Rachmaninoff deposit indicates that its chemical composition differs from that of the surrounding surface only by a relative depletion of sulfur (*Nittler et al.*, 2014). This may indicate that the cause of the deposit's spectral character is primarily volatile loss, rather than a difference in composition from the surrounding substrate. If vent-formation occurred by erosion of initially sulfur-rich country rock by a high-velocity gas, the sulfur may have been volatilized and lost or remobilized during the eruption, resulting in a deposit that is sulfur-poor but nevertheless non-juvenile. At twelve sites (indicated in Table C-1) where small pits with uneven floors occur within the ejecta blanket, rim or wall of an impact crater, there is the additional possibility that the pits and surrounding deposits were not formed by pyroclastic volcanism at all, but resulted from volatilization of the substrate below hotly-emplaced ejecta during impact crater formation (Figure 5-10). The dynamics by which this process could form the observed pits and deposits are untested, however, so the

degree to which impact-induced volatilization could be responsible for the sites currently interpreted as the result of explosive volcanism remains unknown. Compositional data at higher spatial resolutions than currently available, to be acquired as MESSENGER's orbit descends to lower altitudes and from the forthcoming BepiColombo mission (*Fraser et al.*, 2010; *Rothery et al.*, 2010), may further constrain the composition of Mercury's bright, red deposits and allow distinctions to be drawn between deposits formed by different processes.

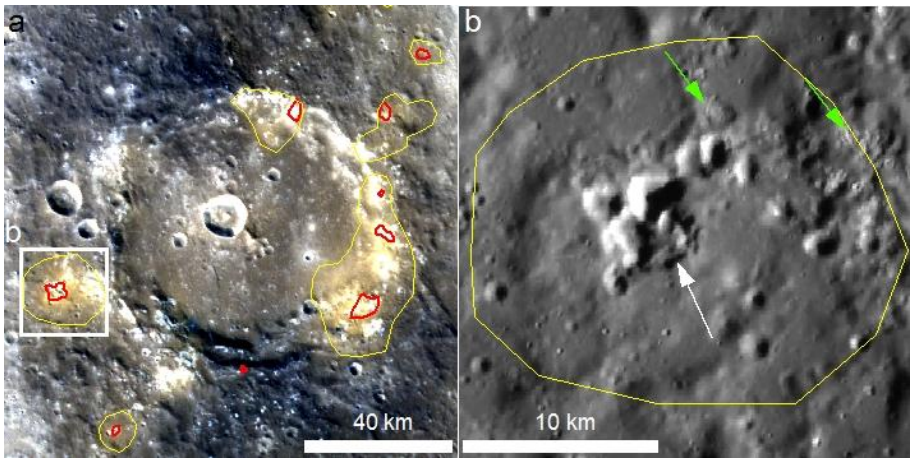


**Figure 5-10 Small pits, possibly formed by post-impact degassing, in the rim and continuous ejecta of an unnamed crater (22.8$^0$ E, 35.5$^0$ N). (a) Relatively bright and red deposits (outlined in yellow) surround small pits (outlined in red). White rectangle: extent of (b) (composite of EW0225101261I, EW0225101257G and EW0225101253F). (b) Close-up of the southwest pit (indicated by a white arrow), showing its uneven floor and irregular margin. Green arrows indicate nearby hollows (image EN0220115477M).**

### 5.5.2 Structural controls on eruption

The siting of 92% of vents with pyroclastic deposits close to thrust faults and zones of weakness in impact craters strongly suggests that such structures favour the occurrence of explosive volcanism. In the context of a state of global contraction persisting over much of Mercury's history that likely inhibited magma ascent, tectonic and impact structures represent the paths of least resistance to the surface, so these zones of weakness may act as conduits.

The occurrence of explosive volcanism within impact craters and concentrated around the rim of large impact basins raises the possibility that this volcanism was triggered by the impact process, as has been suggested for the widespread smooth plains emplaced during and shortly after the Late Heavy Bombardment period of Mercury (*Marchi et al.*, 2013). However, impact-induced volcanism is controversial (*Ivanov and Melosh*, 2003; *Roberts and Barnouin*, 2012), and in any case this process has been suggested only for the largest basin-forming impacts (*Elkins-Tanton et al.*, 2004). The smallest crater that hosts a vent is 7.6 km in diameter, and the total population (121) of craters hosting vents has a median diameter of 67 km. For this scale of crater, impact-induced volcanism is improbable. Additionally, the timing of explosive volcanism around basins is not consistent with the basin-forming event triggering that volcanism. The vents around the Caloris basin post-date the basin fill, which appears to be significantly younger than the basin itself (*Fassett et al.*, 2012). Moreover, the incision of pits into relatively young, well-preserved craters around the putative ancient basin "b54" indicates that explosive volcanism in that region occurred long after the basin formed. However, it is feasible that crater-formation facilitated ascent of magma by 'resetting' the compressive stress in the overlying rock. Kuniyoshi, the youngest crater that hosts pyroclastic volcanism identified in my survey, may illustrate this process: it lies within a cluster of volcanic vents at the west of basin "b54", where the structures delineating the basin and its constituent rings may well have permitted magma ascent from depth. Future work to constrain the relative ages of craters and basins and the explosive volcanic vents incising them will allow us to characterize this process.

If paths of crustal weakness acted as conduits for magma ascent and eruption, then the ease of access to the surface through these pathways presumably affects the volcanic style. My results support this inference. Eleven of the 14 sites at which the build-up of detectable deposits implies relatively long-lived eruption are spatially associated with likely deep-seated structures. Four pits with circum-pit relief lie at the centre of impact craters, and one overlies the expected location of the buried peak ring within Lermontov basin. In these cases, fractures associated with uplifted central peaks and peak rings could have facilitated magma

ascent. RS-03 (in SW Caloris) and other nearby vents incise a network of wrinkle ridges and, additionally, lie along a line radial to the centre of the Caloris basin. The formation of the vents, as well as where they formed, may have been structurally-controlled (*Rothery et al.*, 2014).

### 5.5.3 Mechanisms of eruption

The eruption styles indicated by variations in pyroclastic deposit morphology, the evidence for a tectonic control on eruption, and the large scale of some such deposits together shed light on the mechanisms that have resulted in explosive volcanic eruptions on Mercury for much of its geological history despite a thickening lithosphere in a state of net contraction.

The collocation of clusters of explosive volcanic vents along the major fold and thrust belts mapped by *Byrne et al.* (2014) and around large impact basins suggests that the presence of deep-seated faults and fractures facilitates magma rise from depth. At smaller scales, near-surface faults and fractures may have allowed eruption from shallow magma sources.

Magma storage at shallow levels is implied by three strands of evidence: the horizontal scale of the deposits, the eruption style suggested by the deposit morphology, and the occurrence of repeated eruption at the same location. The horizontal scale of the deposits is controlled by the kinetic energy of particle ejection, which in turn is approximately proportional to the volatile mass fraction in the released magma (*Wilson*, 1980). Mercury's pyroclastic deposits are, on average, larger than those on the Moon, despite the higher gravitational acceleration on Mercury, and so a higher volatile content is required to distribute particles to a given distance. This indicates a higher average volatile concentration in pyroclastic eruptions on Mercury than on the Moon. The maximum distance, X, to which particles can be ejected on an airless body can be related to the initial ejection velocity, *v*, by:

$$X = \frac{v^2}{g} \sin 2\theta \quad , \qquad (5\text{-}1)$$

where $g$ is gravitational acceleration (3.7 m/s$^2$ on Mercury) and $\theta$ is the angle at which dispersal is greatest (45°). This relationship indicates that for the largest deposit, NE

Rachmaninoff, the farthermost particles (those 130 km from the vent) were ejected at a minimum velocity of ~690 m/s. If I follow the method of *Wilson et al.* (2014) and make the simplifying assumptions that the gas expands adiabatically and that the pyroclasts acquire all of the gas speed, I can determine the released magmatic volatile gas fraction, *n* by:

$$n = \frac{(\mathrm{v}^2\, m(\gamma - 1))}{2QT\gamma}, \qquad (5\text{-}2)$$

where *m* is the molecular mass of the gas, γ is the ratio of the heat capacity of the gas at constant pressure and at constant volume, *Q* is the universal gas constant, and *T* is the magmatic temperature. Using a magmatic temperature of 1750 K as used by *Wilson et al.* (2014), where γ for CO is 1.302 (*Hilsenrath*, 1955), Equation 5-2 indicates that the emplacement of pyroclasts to radial distances of130 km from the vent requires over 10 wt% CO if this were the sole volatile species. In fact this may be an overestimate of magmatic temperature, which lies in the range 1275–1575 K (1000–1300° C) for terrestrial basaltic melts (*Spera*, 2000). At lower temperatures, a higher gas fraction is required to ejecta particles at the same velocity, so that CO content would need to be 15 wt% at 1275 K and 12 wt% at 1575 K (using values of γ from *Hilsenrath* (1955)) to produce a deposit of this scale. The value for $CO_2$ is 15 wt% at 1275 K and 12 wt% at 1500 K, and, for $H_2O$, 7 wt% at 1600 K (using the value of γ used by *Wilson et al.* (2014)). For comparison, melt inclusions indicate that basaltic magmas on Earth have up to 0.7 wt% $CO_2$ and 1.2–6 wt% $H_2O$ (*Metrich and Wallace*, 2008). The highest $H_2O$ contents are in subduction settings, where processes occur that are unlikely to be comparable to those on Mercury. In non-arc settings, the $H_2O$ content is considerably lower. At Kilauea in Hawaii, for example, magmatic gas contents responsible for fire-fountaining eruptions have been calculated as 0.3 wt% $H_2O$, 0.3 wt% $CO_2$, and 0.1 wt% S (*Greenland et al.*, 1985). These values are substantially lower than those required to emplace pyroclasts around the NE Rachmaninoff vent, but are closer to values needed to form pyroclastic deposits of the median radius on Mercury, 13.3 km: 1.2 wt% CO at 1575 K, 1.2 wt% $CO_2$ at 1500 K, or 0.7 wt% $H_2O$ at 1600 K. In reality, a combination of more reduced species is to be expected in Mercury's magmas. Chemical equilibrium models suggest that $N_2$,

CO, $S_2$, $CS_2$, $S_2Cl$, Cl, $Cl_2$, and COS could be the most abundant volatiles in Hermean melts (*Zolotov*, 2011), and the finding that the NE Rachmaninoff deposit is low in sulfur supports the involvement of one or more sulfur-bearing species (*Nittler et al.*, 2014). All of these volatiles have a higher molecular mass than CO, and so unless γ at magmatic temperatures is substantially lower than that of CO, a concentration greater than 10 wt% is required to deposit pyroclasts up to 130 km from a vent. As I do not find support for an external source of these species (Section 5.5.1), a high volatile fraction suggests either a high intrinsic volatile content in the magma or concentration of volatiles prior to eruption.

The formation of hollows by sublimation (*Blewett et al.*, 2013; Section 2.5.3), and the detection of volatile elements on Mercury's surface (*Nittler et al.*, 2011; *Peplowski et al.*, 2011), imply that the planet has a higher bulk volatile content than previously thought (e.g. *Cameron*, 1985). In order to attain a volatile content in excess of that present in basalts on Earth, however, further concentration of volatiles prior to eruption is probably required. On Earth, it is observed that volatile oversaturation occurs through fractional crystallization in magmas stored at shallow crustal levels (*Tait et al.*, 1989; *Fowler and Spera*, 2008). Indeed, it has been suggested that the build-up of overpressure through this process is a necessary condition for eruption from such a chamber (*Tait et al.*, 1989). Notably the occurrence of several pits at one location is also consistent with shallow subsurface storage. Although it is possible these pits were formed by magmas erupting from the tips of multiple dykes that propagated from considerable depth, the close spatial relationships of these depressions is more consistent with having originated from a single location in the shallow subsurface.

The styles of explosive volcanism I infer for the majority of the sites where I have topographic data are also consistent with shallow magma storage. If, as predicted by models for lunar explosive volcanism (*Wilson and Head*, 1981), the deposits with circum-pit relief on Mercury formed by Strombolian eruption, or steady eruption of predominantly large particles, this is indicative of bubble coalescence prior to eruption. Bubbles coalesce when magma rise is slow relative to bubble rise velocity, as when ascending magma slows or stalls. At those other sites where pyroclastic deposits have little topographic expression, a low volume, short-duration

eruption is probable. Although it has been suggested that such deposits can be due to volatile concentration in a dyke tip propagating from depth (*Wilson and Head*, 2003), overpressurization of a magma reservoir prior to failure could also lead to an eruption scenario that, because it is cyclical, is more consistent with the observed occurrence of several pits at a single site.

Where magma stalls at shallow crustal levels and accumulates volatiles, pre-existing near-surface faults and fractures can play a controlling role on eruption. Numerical modelling indicates that if large overlying subvertical fractures are present, dyke propagation may occur along these even if the distribution of stress due to neutral buoyancy would favour horizontal dyke propagation in their absence (*Parfitt et al.*, 1993). These fractures can act as valves: brittle failure occurs when magma exceeds the frictional strength of the faults, volatiles and/or magma is released, and then the fractures/faults seal again after the driving stress falls below that strength (*Sibson et al.*, 1988). If the magma chamber is a closed system, these processes will lead to repeated cycles of pressurization and eruption. This process accounts for the high volatile content and limited eruption volume I have inferred for many of Mercury's pyroclastic deposits, as well as the evidence for multiple eruptions at a single location.

Roof failure may occur above a magma reservoir even without the presence of pre-existing fractures, if the chamber is shallow enough and a sufficiently thick layer of low-density foam accumulates in its upper part (*Parfitt et al.*, 1993). Such a scenario may explain the occurrence of vents incised into effusive deposits within impact craters. Initial volcanism in these craters would have been facilitated by the presence of subsurface faults and fractures produced by crater formation, enabling sufficiently efficient magma rise for effusive eruption, or high-flux explosive eruption with clastogenic flow. When a resistant cap of lava had accumulated on the crater floor, magma ascent would have been inhibited, and volatiles would accumulate prior to eruption, so that later eruptions were more explosive. This progression in the ease of magma ascent may be responsible for pits clustered around the margins of the lava-filled Caloris basin.

The association of subsurface magma storage and explosive eruption due to volatile overpressure raises the possibility, originally noted by *Gillis-Davis et al.* (2009), that Mercury's pits form by collapse into magma reservoirs. Their model suggested magma withdrawal at depth, but at the 150 sites where pyroclastic deposits are observed, subsidence could alternatively have resulted from magma chamber drainage during eruption, as for the formation of large calderas during explosive volcanism on Earth. On Earth, the cross-sectional shape of a collapse caldera is the result of its eruptive history, the presence of pre-existing faults or the prevailing stress field, the dimensions of the magma chamber, and post-formational mass wasting. Nonetheless, the end-member morphologies observed on Earth encompass the range observed on Mercury (*Cole et al.*, 2005). Until more compositional data for Mercury's pyroclastic deposits are available, I cannot definitively assess the degree to which subsidence and the stripping of wall rock (Section 5.5.1) contribute to pit formation. In either case, however, it is probable that pre-existing faults such as those associated with impact crater central uplifts play some role in the siting and morphology of the resulting pit.

I therefore conclude that, for any location on the surface of Mercury, the potential for explosive volcanism and its scale and periodicity is strongly controlled by the presence or absence of both deep-seated and surficial faults and fractures. These zones of weakness assume such a key role on Mercury due to the planet being in a tectonic regime of net compression and the absence of other controlling conditions, such as the plate tectonics of Earth and the high loading stresses resulting from the density contrast between highlands and mare on the Moon (*Head and Wilson*, 1992; *McGovern and Litherland*, 2011).

## 5.6 Conclusions

I have identified 174 sites where endogenic pits occur on Mercury, at 150 of which they are surrounded by deposits that are likely pyroclastic in nature. There are multiple pits at 64 of these sites (with a total of 327 pits in all), suggesting multiple episodes and/or loci of eruption in close proximity to each other. The areal extent of pyroclastic deposits suggests a greater concentration of volatiles driving these eruptions than for lunar explosive volcanism, and similar to, or higher than, that associated with basaltic pyroclastic eruptions on Earth.

This unexpectedly high volatile content may in part be a result of concentration of magmatic volatiles in shallow magma chambers, and so the scale of the deposits does not necessarily correspond to the bulk volatile content of the planet. Nevertheless, the sizes and abundance of these deposits supports the growing viewpoint that Mercury's interior is far more enriched in volatile species than had been thought.

Pyroclastic landforms are, in general, widely distributed across the planet, but they are conspicuously absent in the thicker parts of smooth volcanic plains. I find strong support for the hypothesis that impact crater-related fractures and thrust faults control the occurrence of explosive volcanism, with deep-seated structures allowing magma ascent from depth and surficial faults and fractures controlling ascent, and possibly acting as valves for magma and/or volatile release, from shallow magma reservoirs. I therefore suggest that explosive eruption on Mercury represents an interaction between impact cratering, magma fractionation, and tectonic deformation that has allowed ascent and eruption of magma over a substantial part of the planet's geological history.

## 5.7 Epilogue: new data

Since the publication of the paper that makes up the majority of this chapter, new images (released by NASA's Planetary Data System up to 6th March 2015) have become available that have increased the number of recognizable pits and putative pyroclastic deposits (Table C-1). Where these have affected the values quoted in this chapter, the changes are listed in Table 5-1. None of these changes are sizable enough to impact the findings in this chapter.

**Table 5-1 Updates to published (*Thomas et al.*, 2014c) values in this chapter**

| Description | Published value | Updated value |
|---|---|---|
| Count of sites | 174 | 183 |
| Count where there is also a spectral anomaly | 150 | 161 |
| Sites where there are multiple pits | 64 | 70 |
| Total number of pits | 327 | 353 |
| New sites versus *Kerber et al.* (2014) | 57 | 66 |
| *Kerber et al.* (2014)-documented sites where I do not observe a pit and associated spectral anomaly | 40 | 81 |
| At which I observe spectrally-red pitted ground | 15 | 21 |
| At which I observe a pit but no spectral anomaly | 2 | 3 |
| Average nearest neighbour | 0.402 | 0.394 |
| Moran's index | 0.148 | 0.189 |
| **Local associations** | | |
| Sites within an impact crater, % | 81 | 82 |
| With a spectral anomaly and within an impact crater, % | 79 | 80 |
| Sites close to surface fault traces, % | 46 | 44 |
| Sites with a spectral anomaly close to surface fault traces, % | 47 | 45 |
| Sites with a spectral anomaly either in an impact crater or close to a surface fault trace, % | 92 | 90 |
| Sites with a spectral anomaly within probable lavas, % | 30 | 31 |
| **Extent and morphology of pits and deposits** | | |
| Median pit area ($km^2$) | 38 | 34 |
| Number of pits for which I have obtained topographic data | 57 | 74 |
| Volume range ($km^3$) | 1.3–1300 | 0.08–1300 |
| Median volume ($km^3$) | 40 | 17 |
| Depth range (km) | 0.2–4 | 0.1–4 |
| Median depth (km) | 0.9 | 0.6 |
| Median deposit area ($km^2$) | $5.6\times10^2$ | $5.2\times10^2$ |
| Median radius of deposit (calculated for a circular deposit of median areal extent), km | 13.3 | 12.8 |
| Pearson's product-moment correlation of pit area to deposit area | 0.64 | 0.67 |

# Chapter 6. Where have all the basins gone? Evidence from the distribution of explosive volcanism

## 6.1 Introduction

Comparison of the number of large impact basins (≥ 500 km diameter) on Mercury and the Moon indicates that there are surprisingly few such basins on Mercury (*Fassett et al.*, 2012). This suggests either a lower flux of large impactors at Mercury than at the Moon, or that geological processes have reduced the morphological expression of a significant population of large impact basins to such an extent that they are no longer visibly obvious. Thus, if morphologically-indistinct ancient basins could be detected by other means, this would constrain models of the rate and degree of topographic relaxation and/or volcanic activity, as these are the processes most likely to have resulted in obscuration of basins on Mercury. If no such basins are indicated, the alternative explanation, that the size-frequency distribution of impactors early in the planet's history differs from that at the Moon, is favoured.

In light of the observation that sites of putative explosive volcanism form concentric (*Head et al.*, 2012) and radial (*Rothery et al.*, 2014) alignments a short distance inwards of the wall zone of Caloris, the discovery of a concentric alignment of such sites inwards of a high-elevation, thrusted region (*Byrne et al.*, 2014) around the proposed ancient basin "b54" (*Fassett et al.*, 2012) (Figure 5-3a), and the finding that activity around "b54" persists long after basin formation (Section 5.4.1.1), the possibility arises that these alignments can provide evidence for the location of the rims of ancient impact basins that are no longer clearly visible morphologically. It is axiomatic that the human brain finds patterns even where they do not exist, and there are many examples of this in the literature of planetary observation (e.g. *Newcomb*, 1907). However, where other data sources point towards the presence of an impact basin, the occurrence of putative explosive volcanism in the region of the proposed rim is a valuable additional strand of evidence. In this chapter, I compare the distribution of sites of explosive volcanism that I have previously catalogued to several other datasets, including X-Ray Spectrometry, multispectral imaging, maps of tectonic features and

crustal thickness models, to identify sites where a very large ancient impact basin is probable or plausible.

## 6.2 Sources of evidence and methods of analysis

As MESSENGER approached Mercury at low altitudes in the latter part of its orbital mission, its instruments collected higher spatial resolution data than ever before. This resulted in several datasets that have relevance for the identification of ancient impact basins.

The first is a series of elemental ratio maps produced using data from MESSENGER's X-Ray Spectrometer (XRS) (*Schlemm et al.*, 2007). This instrument measured characteristic X-Ray fluorescence by atoms at the top 100 μm of Mercury's surface and was able to gather measures of Mg/Si and Al/Si during quiet Sun periods (resulting in global elemental ratio maps) and Ca/Si, Fe/Si and S/Si during solar flares (resulting in partial maps) (*Weider et al.*, 2015). The published maps have effective spatial resolutions of as little as 100 km/pixel, though resolutions are considerably worse at mid to low southern latitudes than near MESSENGER's periherm at ~ 60° N, and data are missing at high northern latitudes in the partial maps. These maps should be useful in identifying broad-scale compositional anomalies related to large impact basins (e.g. *Pieters et al.*, 1997) at low to mid-northern latitudes, so long as these are evident in the top 100 μm of the regolith.

If post-formation viscoelastic relaxation has not been totally efficient, impact basins are expected to be underlain by anomalously thin crust (*Mohit and Phillips*, 2006). By tracking MESSENGER's course as it orbited the planet, the NASA Deep Space Network (DSN) was able to determine Mercury's gravity field at ever-greater spatial resolution (*Smith et al.*, 2012; *Mazarico et al.*, 2013, 2014). In conjunction with a topographic model derived from Mercury Laser Altimeter (MLA) data (*Cavanaugh et al.*, 2007) and radio occultation measurements, gravity field measurements up to February 2014 have been used to model crustal thickness variations (*Mazarico et al.*, 2014; *James et al.*, 2015). As with the XRS data, MESSENGER's highly elliptical orbit resulted in crustal thickness models in which the spatial resolution is best near periherm and much lower at mid- to high southern latitudes, where gravity field

data have a lower resolution due to the high spacecraft altitude and only radio occultation data are available with which to model topography. A limitation to crustal thickness models, which may be particularly relevant for the identification of basins, is that they assume a uniform density contrast between the crust and mantle. Therefore if, for example, a region of the crust has an above-average density, this would result in the same gravity anomaly as thinner crust (*Frank et al.*, 2015).

A third strand of evidence for ancient impact basins is the presence of Low Reflectance Material (LRM) in their ejecta and on their floors. When LRM was first identified, variations in its occurrence in the ejecta of similar-sized impact craters was taken to indicate that its presence and/or depth beneath the planet's surface is spatially heterogeneous (*Denevi et al.*, 2009). However, more recent work, which notes a correlation between the depth of excavation of impact basins and the presence of LRM in their ejecta blankets and floors, suggests that it may form a common or ubiquitous part of the lower crust (*Ernst et al.*, 2015) or upper mantle (*Murchie et al.*, 2015b), which has reached the surface by excavation in basin-forming impacts, and has subsequently been redistributed by smaller impacts (*Rivera-Valentin and Barr*, 2014). This implies that any basin-forming impact would have excavated and/or melted LRM (if this reservoir were in existence at the time of impact) to a degree correlated with basin size. In order to map global LRM, I extracted the darkest 40% of pixels from the second principal component (PC2) band of the global enhanced colour mosaic produced by *Murchie et al.* (2015), in which low values represent relatively low ('blue') spectral slope, corresponding to LRM. Image-stacking to create this mosaic favours images taken under favourable illumination conditions (low solar incidence and emission angles) so it represents the best data available for spectral slope calculations at the time of its creation. However, refinements to the photometric correction of the constituent images are still underway at the time of writing, and it is to be expected that not all areas of the globe will have been imaged under optimal conditions, so the indicated distributions of surface LRM should be viewed as preliminary.

To test whether the distribution of explosive volcanism provides supplementary evidence for the presence of morphologically-obscure ancient basins, I overlay geospatial data for the sites of explosive volcanism catalogued in Table C-1 on visible-wavelength imagery (global monochrome mosaic v9 and PC2), MLA topography and maps of elemental ratio (*Weider et al.*, 2015), crustal thickness (*Mazarico et al.*, 2014), contractional tectonic landforms (*Byrne et al.*, 2014) and smooth volcanic plains (*Denevi et al.*, 2013). Where the combined evidence suggests an impact basin, I estimated the depth of excavation expected to produce the implied final diameter, to give an indication of the internal layers that should be present in its ejecta blanket. To do this I calculated the transient basin diameter as the average of three methods derived from lunar and terrestrial observations (*Croft*, 1985; *Melosh*, 1989; *Holsapple*, 1993) and experimental studies (*Holsapple*, 1993), as discussed by *Ernst et al.* (2010). For the *Croft* (1985) and *Holsapple* (1993) methods, it is necessary to stipulate the transition diameter from simple to complex impact craters; I used a figure of 10.3 ± 4 km as observed on Mercury by *Pike* (1988). I calculated the transient crater depth (and thus the depth of excavation), after *Ernst et al.* (2010), as one tenth of the transient basin diameter, though this may be an underestimate; other work uses the 1:3 diameter-depth ratio of a simple crater (*Grieve and Cintala*, 1982). If one were to use a 1:3 ratio to calculate the transient crater depth of the Caloris basin, the depth of excavation would be ~ 250 km versus the 73 km figure used by *Ernst et al.* (2010). Considering the prevalence of LRM on the floor of Caloris, this would imply that LRM makes up a large part of the mantle, which does not, at present, seem probable. In either case, the result of these calculations is expected to be very approximate, as the surviving evidence indicates only an approximate basin diameter and, at the scale of the proposed basins and at the supra-lunar average impact velocity of impacts at Mercury, methods of calculating excavation depth based on data from other planetary bodies are likely to need modification.

## 6.3 Possible ancient impact basins

This analysis indicated three locations, apart from the Caloris basin, where aligned sites of explosive volcanism, along with other strands of evidence, indicate the presence of a large ancient impact basin (Figure 6-1).

1. "B54", centred on -8° E, 61° S (Figure 6-2). As previously discussed in Section 5.4.1.1, this basin is identified on the basis of moderately smooth plains at its centre (*Fassett et al.*, 2012) and circumferential thrust faulting. Using a ring of 'high-terrain-bounding' thrust faults (*Byrne et al.*, 2014) as the site of the rim suggests the basin may have been ~1370 km in diameter. Additionally, the LRM map created for this analysis shows that the proposed basin is surrounded by a near-continuous region of LRM at its west, north and east margins. The material with the lowest spectral slope (indicating that surface materials are most dominated by LRM) is outwards of the proposed rim region, consistent with the expected location for its ejecta blanket. The estimated basin diameter implies a depth of excavation of ~ 70 km, greater than the average present-day crustal thickness, estimated at 40 km (*James et al.*, 2015). Therefore the LRM at its margin could be derived from either the lower crust or upper mantle. The modelled crustal thickness within the basin is lower (as little as 20 km) than in the proposed rim region (up to 60 km), though the resolution and precision of the model is low at such a high southern latitude (Figure 6-1). XRS data have very low spatial resolution and do not show any compositional variation in or around the proposed basin. As discussed in Section 5.4.1.1, the distribution of explosive volcanism, some of it very recent, around "b54" is supportive of its identification as an ancient impact basin. The most recent explosive volcanism recognised on the planet, within Kuniyoshi crater, and the line of proposed vents and deposits to the northwest of Kuniyoshi crater along the western part of the basin's proposed margin, is underlain by crust modelled to be thinner (~ 30 km) than elsewhere in the proposed rim region.

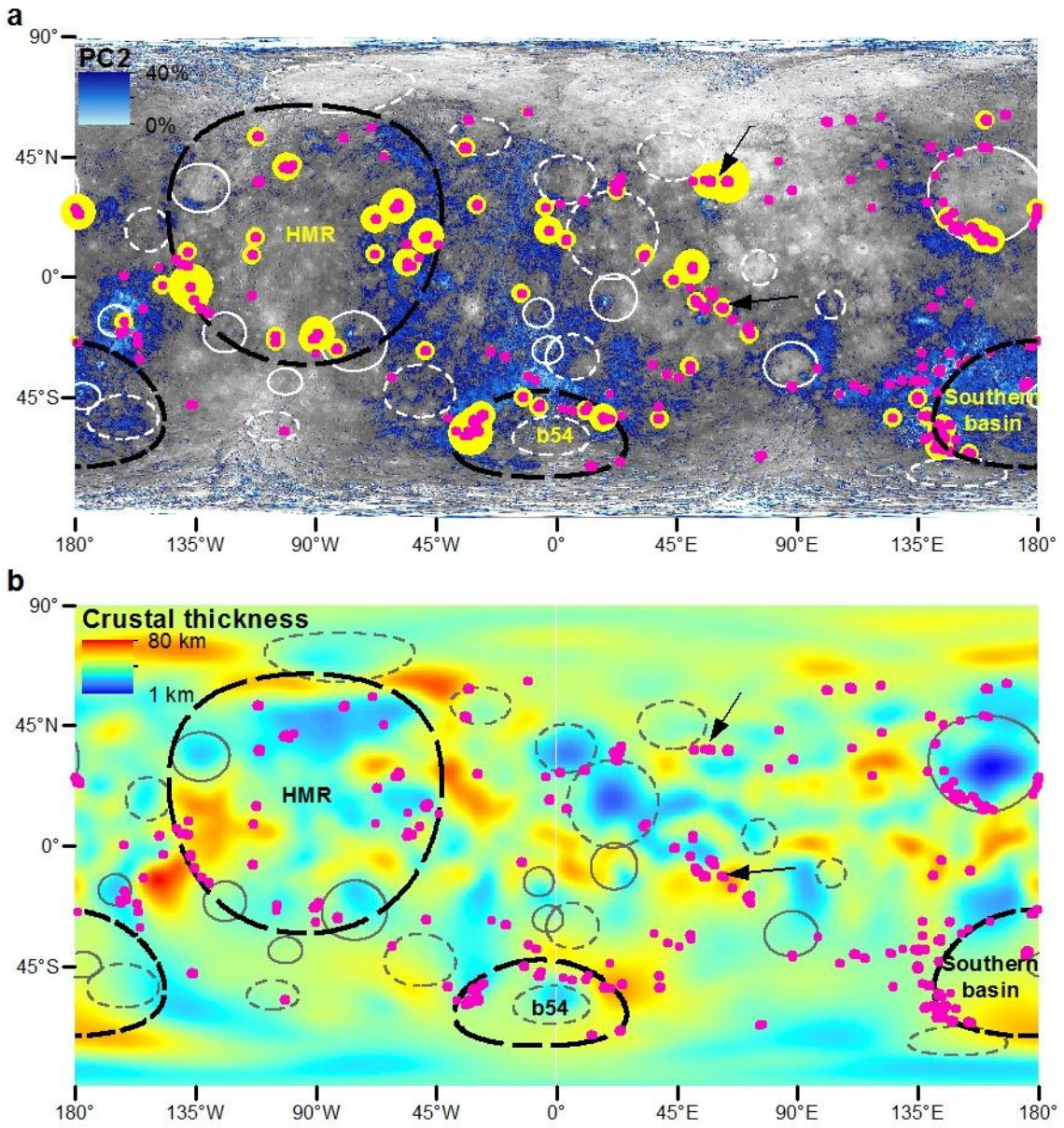


**Figure 6-1 Global distribution of sites of putative explosive volcanism and (a) impact basins and PC2 (low values indicate presence of LRM, see Section 6.2 for details) and (b) modelled crustal thickness. Black arrows: examples of aligned sites of putative explosive volcanism that do not appear to be associated with an impact basin. Pink dots: proposed volcanic vents (Table C-1). Ellipses outline basins: solid dashed outline = certain, dashed outline = possible; black = this study, white/grey = basins > 400 km diameter catalogued by *Fassett et al.* (2012). (a) Yellow circles indicate the presence of a putative pyroclastic deposit, scaled by deposit area. Base image: Global PC2 overlain by a map of the lowest 40% of PC2 values (brightest blue = 'bluest' substrate). (b) Base image: the crustal thickness model of *James et al.* (2015).**

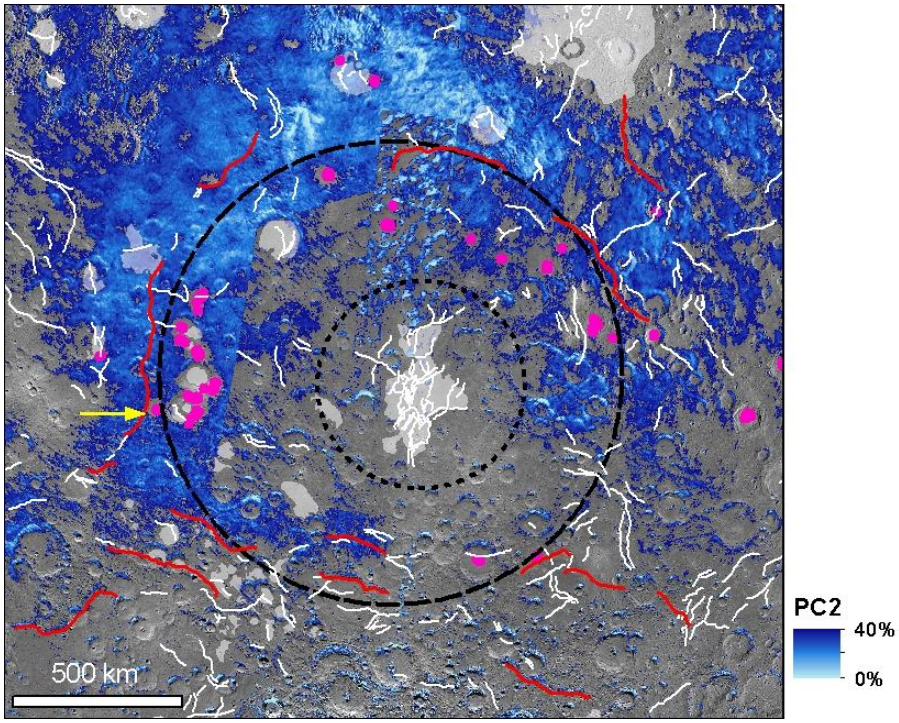


**Figure 6-2 Features suggesting an ancient basin ("b54") centred on -8° E, 58° S. Circles: proposed basin extent - long dashes, this study; dots, *Fassett et al.* (2012). Irregular lines: contractional features mapped by *Byrne et al.* (2014) — red: 'high-terrain-bounding structures', white: 'smooth plains' and 'cratered plains' structures. Grey polygons: smooth plains mapped by *Denevi et al.* (2013). Pink dots: proposed volcanic vents (Table C-1). Yellow arrow: Kuniyoshi crater. Base image: global monochrome mosaic (v9) overlain by a map of the lowest 40% of global PC2 values (brightest = 'bluest' substrate). Lambert equal area projection with a central meridian of -7° E and latitude of origin of 58° S.**

2. The High Magnesium Region (HMR), centred at -85° E, 15° N (Figure 6-3). This region was initially defined compositionally, on the basis of an anomalously high Mg/Si ratio (*Nittler et al.*, 2013). More recent XRS data show that Ca/Si, Fe/Si and S/Si are also above average, whereas Al/Si is low (*Weider et al.*, 2015), indicating an ultramafic composition consistent with over 50% partial melting of the mantle (*Charlier and Namur*, 2015). Two main hypotheses have been proposed to produce such a melt: that this region is underlain by a part of the mantle with an anomalously high concentration of heat-producing elements, resulting in effusive eruption of extraordinarily high-degree partial melts, or the inclusion of large quantities of mantle material in melt generated in a giant impact (*Weider et al.*, 2014). The finding that this region is relatively low-lying and has low modelled crustal thickness

supports the latter scenario, though potentially both may have played a part. The distribution of LRM provides some support for the basin hypothesis: it forms a broad band to the east of the HMR, from -70 to 0° E and 70° S-55° N, encompassing the -60 to -40° E latitude band identified in Section 2.4.1.1 as having an anomalously high (and otherwise unexplained) density of hollows. LRM is patchy in this region and has the lowest ('bluest') spectral slope where it has been exhumed by relatively fresh craters such as Lermontov. It is overlain by the northern volcanic plains in the north, indicating that it was emplaced prior to their formation, and originally extended further north. Both these pieces of evidence support its emplacement early in Mercury's geological history. However, as LRM does not form a clear circumferential deposit around the HMR, the observed deposit cannot be taken as strong supporting evidence for its identification as a basin.

There is a curvilinear alignment of sites of putative explosive volcanism along the south-west and south margins of the HMR compositional anomaly and a cluster at its eastern side, consistent with the basin hypothesis. If these occurred near the rim of a large impact basin, it would have had a diameter of approximately 4000 km, which implies an excavation depth of 190 km if scaling relationships for complex craters hold at this size. The presence of LRM at the location where an ejecta blanket would be expected (sourced from, at maximum, the excavation depth) and a mafic compositional signature inside the basin (where any exposed basin floor would be impact melt with a composition dominated by material from much greater depths (*Roberts and Barnouin*, 2012)) is consistent with this larger impact penetrating to greater depth below the LRM reservoir/s than the Caloris-forming impact, which has a strong LRM component in impact melt on its floor (*Ernst et al.*, 2015). I note, however, that there is no topographic high or concentric thrust faulting at the proposed basin rim.

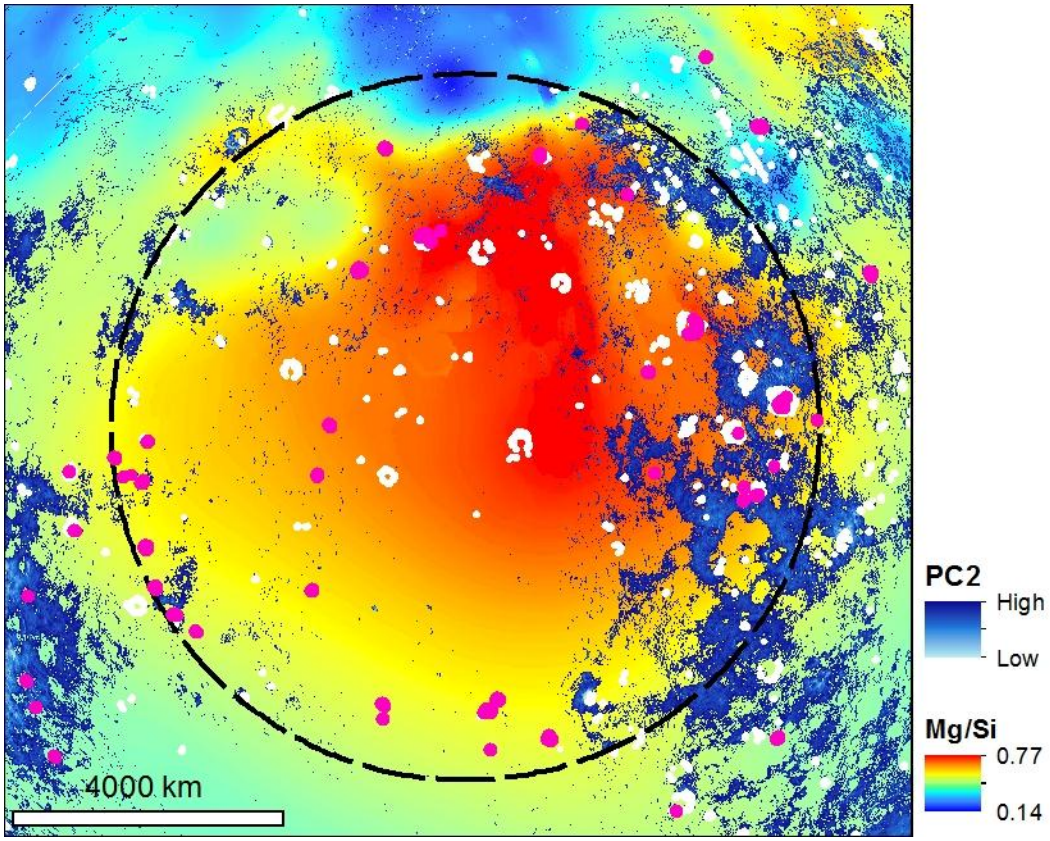


**Figure 6-3 The High Magnesium Region (HMR). Pink dots: proposed volcanic vents (Table C-1). White areas: hollows. Dashed circle: rim location of a possible impact basin if explosive volcanism is common just inwards of the rim as it is elsewhere. Base image: map of XRS-detected Mg/Si ratio (*Weider et al.*, 2015) overlain by a map of the lowest 40% of PC2 values (brightest blue = 'bluest' substrate). Lambert equal area projection with a central meridian of -91° E and latitude of origin of 14° N.**

3. Unnamed southern basin, centred on 178° E, 48° S. In Section 5.4.1.1, I noted a dense cluster of sites of putative explosive volcanism along a region of high-standing, extensively thrust-faulted terrain. Comparison of the location of this region with the PC2 map indicates that this coincides with the largest regional LRM unit on the planet (Figure 6-1), with a particularly low spectral slope in a curvilinear region along which the sites of explosive volcanism are aligned (Figure 6-4a). Additionally, I note the presence of a curvilinear thrust fault following this trend, with a morphology characteristic of tectonised basin fills seen elsewhere on the planet (*Rothery and Massironi*, 2013) (Figure 6-4b). Published elemental ratio data do not show a compositional anomaly here, though more recent, higher spatial resolution, data (Nittler, pers. comm.) show Mg/Si that is above the regional average at the

proposed basin location. The crustal thickness models of *Mazarico et al.* (2014) and *James et al.* (2015) indicate thickened crust in the southern quadrant of the proposed basin, but both models are very uncertain at this high southern latitude (70° S), so little weight should be put on this finding. Until a high-spatial resolution crustal thickness model that is better-constrained by southern hemisphere topographic data is produced during the BepiColombo mission (Chapter 9), the thickness of the crust here should be considered uncertain. The above observations may indicate the presence of a 2000 km diameter basin here, with an estimated excavation depth of ~ 100 km. However, many of the aligned sites of explosive volcanism occur in the region that the distribution of LRM and thrusted 'fill' suggest is the western rim, rather than on the basin floor inwards of that rim, as seen in Caloris and, potentially, "b54".

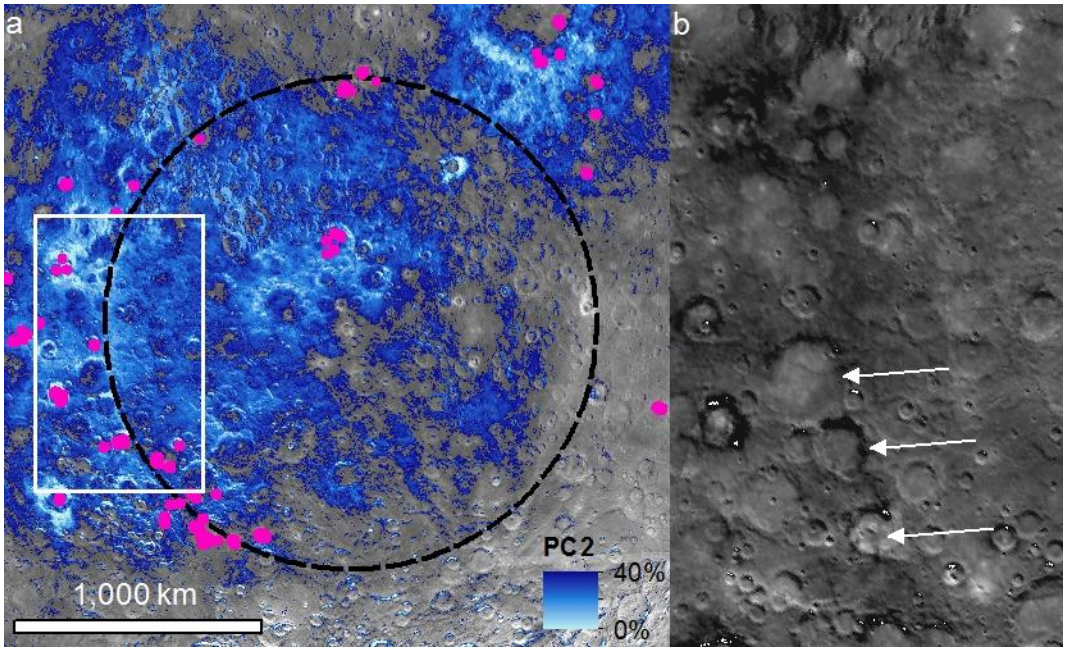


**Figure 6-4 A possible 2000 km diameter impact basin centred on 178° E, 48° S. (a) Black dashed line: proposed rim. Pink dots: proposed volcanic vents (Table C-1). Base image: Global PC2 overlain by a map of the lowest 40% of global PC2 values (brightest blue = 'bluest' substrate). White rectangle: extent of (b). (b) A thrust at the rim region of the proposed basin, which partially covers several impact craters (white arrows). Base image: Global PC2 (*Murchie et al.*, 2015b). (a) and (b) are in a Lambert equal area projection with a central meridian of -179.5° E and latitude of origin of 49° S.**

## 6.4 Discussion

Aligned sites of explosive volcanism combined with multiple other strands of evidence make a strong case for the presence of a basin at "b54". They are also consistent with the presence of an impact basin at the site of the High Magnesium Region, though this is less conclusive. The identification of a large southern hemisphere basin centred on 178° E, 48° S is more speculative, making this an interesting target for the greater capabilities and more southerly periherm of the BepiColombo MPO spacecraft (Section 9.3.4). If the evidence is found not to support the presence of the southern basin, an alternative explanation for the high density of sites of explosive volcanism and the exposures of LRM here must be proposed. The anomalously low modelled crustal thickness to its southwest (Figure 6-1b) could indicate an alternative basin location, though other evidence does not support this at this time.

Addition of these proposed basins to the catalogue of large (≥ 500 km diameter) basins on Mercury only slightly reduces the observed disparity with the number recognised on the Moon, increasing N(500) from 0.23 ± 0.05 to 0.24 ± 0.05 versus 0.37 ± 0.1 on the Moon (*Fassett et al.*, 2012). However, when basins with the rim diameters suggested here (1370 km, 2000 km, 4000 km) are created, material is excavated and deposited over sufficiently large areas to remove or obscure evidence for large basins present prior to their formation. Thus, infrequent, high-damage events may be a part of the reason for the low number of ≥ 500 km diameter basins on Mercury than the Moon. This could indicate a higher frequency of very large impactors at Mercury, but since such large impactors are rare, it is also possible that more impacted Mercury than the Moon by chance alone. Examination of the appearance of surface units comprising the proposed basins indicates subsequent morphological obscuration of the basins themselves by impacts and both relatively recent (smooth plains) and older (intercrater plains (*Whitten et al.*, 2014)) volcanic activity (Figure 6-5). As plains-forming mare lavas are commonly confined within basins on the Moon (due to a density contrast between mantle-derived magma and the anorthositic crust) this type of resurfacing can be expected to have been more efficient on Mercury than on the Moon. On this evidence,

it may not be necessary to postulate a smaller population of large impactors at Mercury than at the Moon.

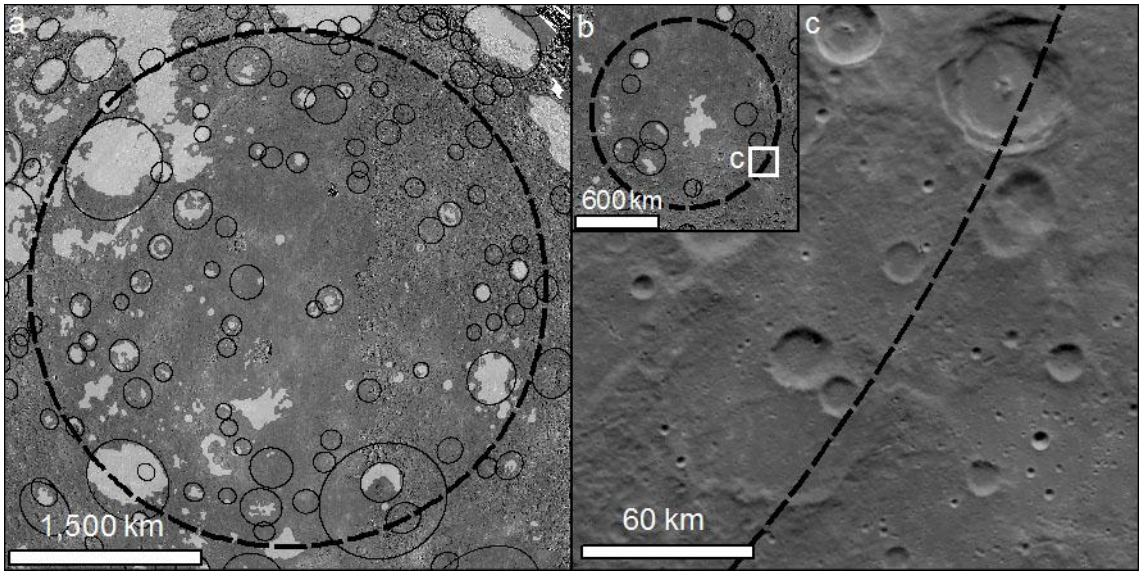


**Figure 6-5 Resurfacing of proposed basins (black dashed circles) by smooth plains (white polygons (*Denevi et al.*, 2013)) and > 120 km diameter impact craters (black ellipses (*Fassett et al.*, 2012)) in (a) the HMR and (b) "b54". (c) Impact craters on an otherwise relatively smooth substrate at the proposed rim region of "b54". Projections as in (a) Figure 6-3 and (b,c) Figure 6-2. Base image: global monochrome mosaic (v9).**

Inspection of the distribution of sites of explosive volcanism across the globe (Figure 6-1a) shows that they do not occur around every impact basin. This could be a result of basin size: Caloris and the proposed ancient basins are much larger than those basins where rim-region explosive volcanism is not seen. Also, sites of putative explosive volcanism form linear (rather than curvilinear) groupings at locations where they do not appear to be related to an impact basin, such as to the north of Rachmaninoff basin and in a NW-SE chain from 45° E, 3° N to 73° E, 22° S (black arrows in Figure 6-1). These observations suggest that processes other than those involved in basin-formation are equally capable of localising explosive volcanism.

This raises the question of whether the association of explosive volcanism with impact basins is genetic or associative. In Section 8.5.2, I raise the possibility that volcanism becomes explosive when magma rises through crustal material that is rich in volatiles, assimilating these volatiles during ascent and/or storage. As large basins commonly excavate LRM, which

appears to be volatile-rich, it may be the presence of this material near the surface at basin margins and floors that lends explosivity to volcanism occurring in that region, rather than any structural property of the basins themselves. However, on present evidence, the presence of LRM alone does not appear to be sufficient to favour explosive volcanism: neither the density of sites of explosive volcanism nor the scale of the associated deposit (and thus the energy of pyroclast ejection) strongly spatially correlate with surface exposures of LRM at non-basin-margin locations (Figure 6-1a).

Thus it appears probable that there is a genetic relationship between basins and explosive volcanism: the physical properties of impact basins favour explosive volcanism in their rim region. In Section 5.5.2 I emphasise the probable importance of sub-basin fractures for magma transfer to the surface under Mercury's compressional tectonic regime. It is also possible that thickened crust at basin margins plays an active role in melt generation. Impact basin formation is expected to result in an annulus of thickened crust in the rim region due to deposition of basin ejecta (*Neumann et al.*, 1996), and indeed, crustal thickness models indicate thickened crust around Caloris, the HMR and "b54". Additionally, the dense zone of thrust faulting seen at the rims of "b54" and the proposed southern basin, apparently localized by sub-basin structures, suggests that Mercury's global contraction can result in continued crustal thickening in the rim region long after a basin is emplaced. On Earth, crustal thickening during continental collision often results in melt-generation, either by crustal melting (attributed to processes such as basaltic underplating, heating of downthrust cool crustal material, or heating by the high concentration of heat-producing elements in thickened crust), or by pressure-release melting of the mantle and/or crustal melting after delamination of an eclogitised crustal root triggers mantle upwelling (*Gerdes et al.*, 2000; *Beck and Zandt*, 2002; *Zeng et al.*, 2011). Not all types of crustal melting proposed for Earth are necessarily applicable to Mercury: for example the mafic minerals expected to compose Mercury's crust may not be susceptible to melting under a raised geotherm in the absence of anomalously hot upwelling mantle (*Thompson and Connolly*, 1995). However, if lower crustal melting did occur on Mercury, and the lower crust is, as hypothesised, volatile-rich LRM, this

could explain the explosivity of these eruptions. Additionally, melting of either crust or mantle by these processes could provide a mechanism by which melt can be generated late in the planet's history without requiring long-lived mantle convection (*Tosi et al.*, 2013). The relatively thin crust modelled to underlie the part of the proposed rim region of "b54" where the most recent explosive volcanism occurs is more consistent with melt-generation by delamination than basal melting of thickened crust.

The above suggestions are, at present, speculative. Investigation of whether crustal thickness variations around basins were responsible for melt-generation must await compositional data for pyroclastic deposits, which may allow determination of whether there is a crustal component in erupted magma, and higher-resolution gravity data with which to better constrain crustal thickness. High-resolution gravity data from the GRAIL mission have been of great value in this respect for the Moon (e.g. *Andrews-Hanna*, 2013; *Melosh et al.*, 2013).

## 6.5 Conclusions

Comparison of the distribution of proposed sites of explosive volcanism to high-spatial resolution compositional, topographic and crustal thickness data from MESSENGER's low altitude campaign supports the hypothesis that the distribution of explosive volcanism can act as a marker for the location of ancient impact basins. This evidence indicates the presence of an impact basin ("b54") at -8° E, 61° S, supports the formation of the High Magnesium Region centred on -85° E, 15° N by a giant impact, and suggests a ~ 2000 km diameter southern hemisphere basin at 178° E, 48° S. If confirmed, these basins reduce the relative scarcity of basins ≥ 500 km in diameter on Mercury compared to the Moon. By resurfacing large parts of the planet, they additionally represent a means by which other, earlier, basins could have been obscured, thereby precluding detection. The association of explosive volcanism with basin margins appears to be genetic. The exact process by which basins favour explosive volcanism at their margins requires further study. Data from the BepiColombo mission have great potential for revealing whether thickened crust associated with basin rims could play a part in melt-generation.

# Chapter 7. A cone on Mercury: analysis of a residual central peak encircled by an explosive volcanic vent

## 7.1 Introduction

Though much of the proposed explosive volcanism on Mercury can be described as an irregular pit surrounded by a relatively bright and red spectral anomaly, some morphological peculiarities occur. The most eye-catching of these is the case where a spectral anomaly of this type surrounds a cone-shaped landform. This landform requires explanation, and the project by which I and my international collaborators have done so is presented in the peer-reviewed paper that makes up this chapter, published in *Planetary and Space Science* (*Thomas et al.*, 2015).

## 7.2 Background

Images acquired by the MErcury Surface, Space ENvironment, GEochemistry, and Ranging (MESSENGER) spacecraft since it went into orbit around Mercury in 2011 have revealed an unusual landform: a steep-sided cone that lies at the centre of a large diffuse-margined spectral anomaly that is bright and red-sloped compared to the Hermean average (Figure 7-1). Spectral anomalies of this type elsewhere on the planet have been attributed to pyroclastic deposition (e.g. *Kerber et al.*, 2009, 2011; *Goudge et al.*, 2014), so this association suggests a landform genesis involving explosive volcanism. Volcanism builds steep-sided edifices on Earth and Mars by deposition of ballistically-ejected particles (e.g. *Hasenaka and Carmichael*, 1985; *Brož and Hauber*, 2012) or by flow of viscous lava. However, on Mercury, the ballistic range of particles ejected at a particular velocity is greater than on Mars and Earth, due to a lack of air-resistance and weaker gravity. For this reason, edifices formed in this way would be expected to have relatively low relief (*McGetchin et al.*, 1974; *Brož et al.*, 2014). Additionally, compositional data do not at present support the presence of evolved lavas capable of building steep-sided edifices through effusion (*Nittler et al.*, 2011; *Weider et al.*, 2012; *Denevi et al.*, 2013). It would therefore be surprising to find that this cone is a volcanic construct. Indeed, studies of volcanic landforms on Mercury have thus far

documented very little relief, with lavas forming smooth plains (*Denevi et al.*, 2013) and deposition around vents attributed to explosive volcanism forming relief of only a few degrees (*Head et al.*, 2008; *Rothery et al.*, 2014; Section 5.4.2.2).

The specific morphology of the landform assemblage around the cone suggests an alternative hypothesis for its formation. The cone lies within an encircling trough, which is in turn encircled by a ridge. If the ridge is interpreted as the rim crest of a 43–km diameter impact crater, the cone occupies the location where a central uplift structure would be expected (*Pike*, 1988). In this scenario the bright, spectrally red-sloped deposit formed through explosive eruption from the trough, interpreted as a volcanic vent encircling the crater's central uplift. This would be consistent with the observation that pits associated with pyroclastic deposits on Mercury are co-located with regions of structural weakness in impact craters (*Gillis-Davis et al.*, 2009), and would support the hypothesis that such structures play a controlling role in explosive volcanic eruptions on Mercury (Section 5.5.2).

In order to assess the viability of this hypothesis, we have investigated the probable original morphology of an impact crater of this size on Mercury by (i) measuring topographic cross-sections across relatively similar-diameter fresh craters, and (ii) performing a hydrocode simulation of the impact. These methods are complementary: while real craters indicate the range of crater morphologies that may arise on Mercury, their variation results from both primary factors (e.g. target heterogeneity, variations in volume of impact melt) and secondary factors (e.g. degradation, volcanic infilling). The simulation results are an aid to distinguishing these elements. We have compared both of these strands of evidence to the present morphology of the cone and associated landform assemblage to assess our hypothesis and to make quantitative inferences. We have also considered other crater-centred explosive volcanic vents on Mercury to assess whether this hypothesis is consistent with a general model for common mechanisms of explosive volcanic eruption on the planet.

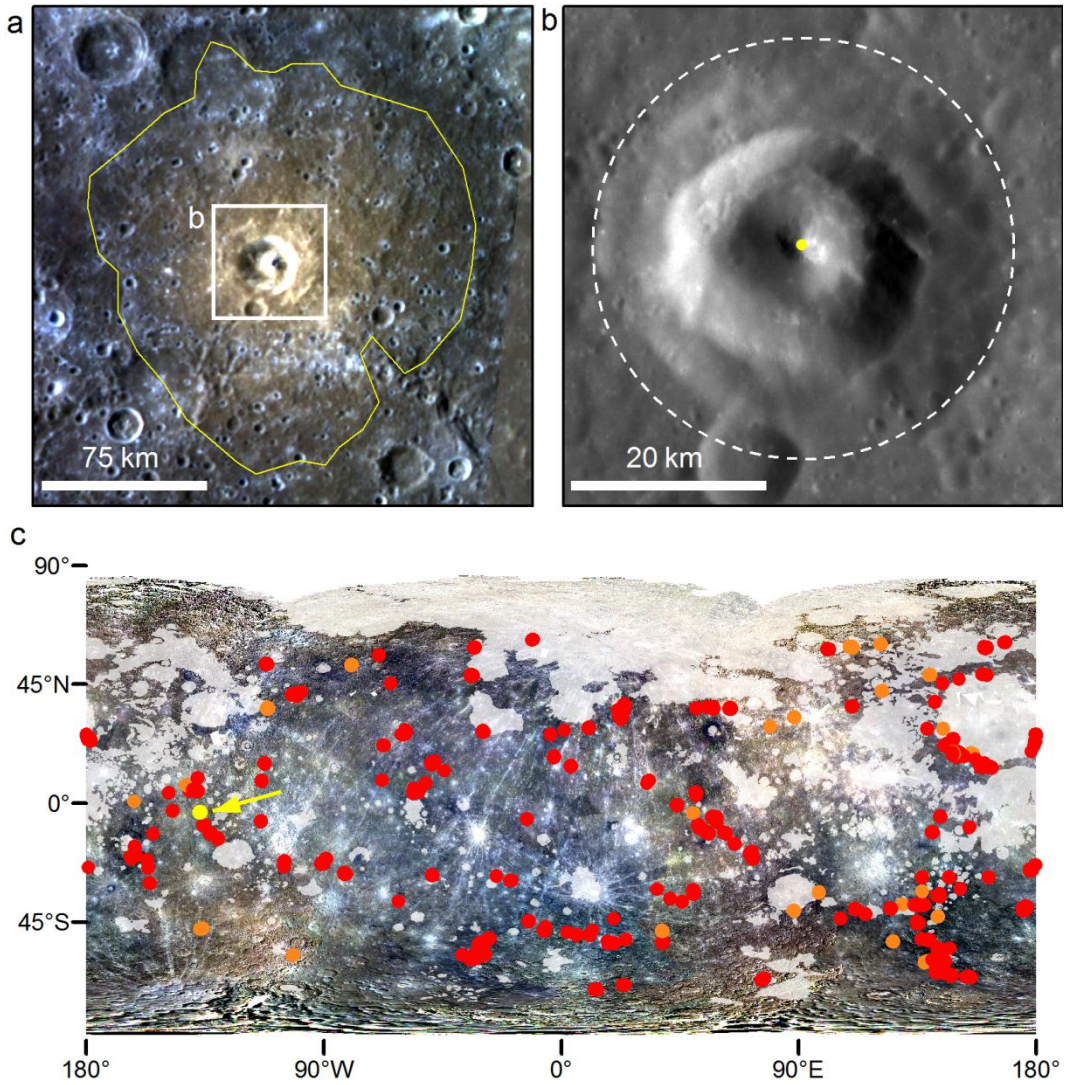


**Figure 7-1 A steep-sided cone associated with putative explosive volcanic products (-136.7° E, -3.5° N). (a) The cone lies at the centre of a widespread relatively bright and red-sloped spectral anomaly (yellow outline) characteristic of explosive volcanism. White rectangle: extent of (b). (Image: colour composite of images EW0262430050I, EW0262430054F and EW0262430070G) (b) Close-up showing that the cone lies within a pit, which is encircled by a ridge (dashed white line), interpreted as the rim-crest of an impact crater. Yellow dot: central point used for determining the median elevation profile in Figure 7-3 (Image EN0212284006M). (c) Global location of the cone (yellow dot, yellow arrow) relative to endogenic pits with (red dots) and without (orange dots) a surrounding relatively bright and red-sloped spectral anomaly. White areas indicate smooth volcanic plains (*Denevi et al.*, 2013). (Base image: MESSENGER global colour mosaic v5). Images in 1a and 1b were obtained by MESSENGER's Wide-Angle (10.5° field-of-view) and Narrow-Angle Camera (1.5° field-of-view) respectively.**

## 7.3 Landform description and proposed mode of formation

The steep-sided cone-like structure is surrounded by a 7 km–wide trench. This is in turn encircled by a topographic rise, which we interpret as the rim crest of a 43–km diameter impact crater (Figure 7-1b). This landform assemblage lies at the centre of a 23,000 $km^2$ spectral anomaly with the relatively bright, red-sloped character that is attributed elsewhere on Mercury to pyroclastic deposits (*Kerber et al.*, 2009; *Goudge et al.*, 2014), which is the second most areally-extensive such anomaly on the planet (Table C-2).

On Mercury, craters with a diameter greater than 12 km are expected to have a central uplift at the location where the cone occurs (*Pike*, 1988). We hypothesize that the first stage of formation of this landform assemblage was the creation of a 43–km diameter crater with a central uplift through an impact event (Figure 7-2a). After an unknown period, magma rose beneath the crater, either as a result of or independently of the impact crater formation (Figure 7-2b). This magma may have stalled in the low-density fractured zone beneath the crater, in a manner similar to that hypothesized to result in floor-fractured craters on the Moon (*Schultz*, 1976). During a period of sub-surface magma storage, crystallization of volatile-poor minerals may have enhanced the volatile content of the remaining melt. When either volatile overpressure or magma driving pressure favoured further dyke propagation, this occurred subvertically due to the presence of zones of weakness in the overlying crust (*Parfitt et al.*, 1993), particularly high-angle faults bounding the central uplift (*Scholz et al.*, 2002; *Senft and Stewart*, 2009; *Kenkmann et al.*, 2014). The resultant eruption of volatile-rich magma formed the trench, a vent that entirely encircles the central uplift, and emplaced pyroclastic deposits to form the surrounding spectral anomaly.

To test this hypothesis, we examine the morphology, dimensions and topography of the cone, pit, host crater and deposit, and we also compare the present-day topography with two estimates of the original host crater topography: the topography of fresh craters of a similar size that are not associated with pyroclastic deposits and hydrocode impact modelling. For brevity, we will refer to this crater as AP1 in this paper ('Annular Pit 1')

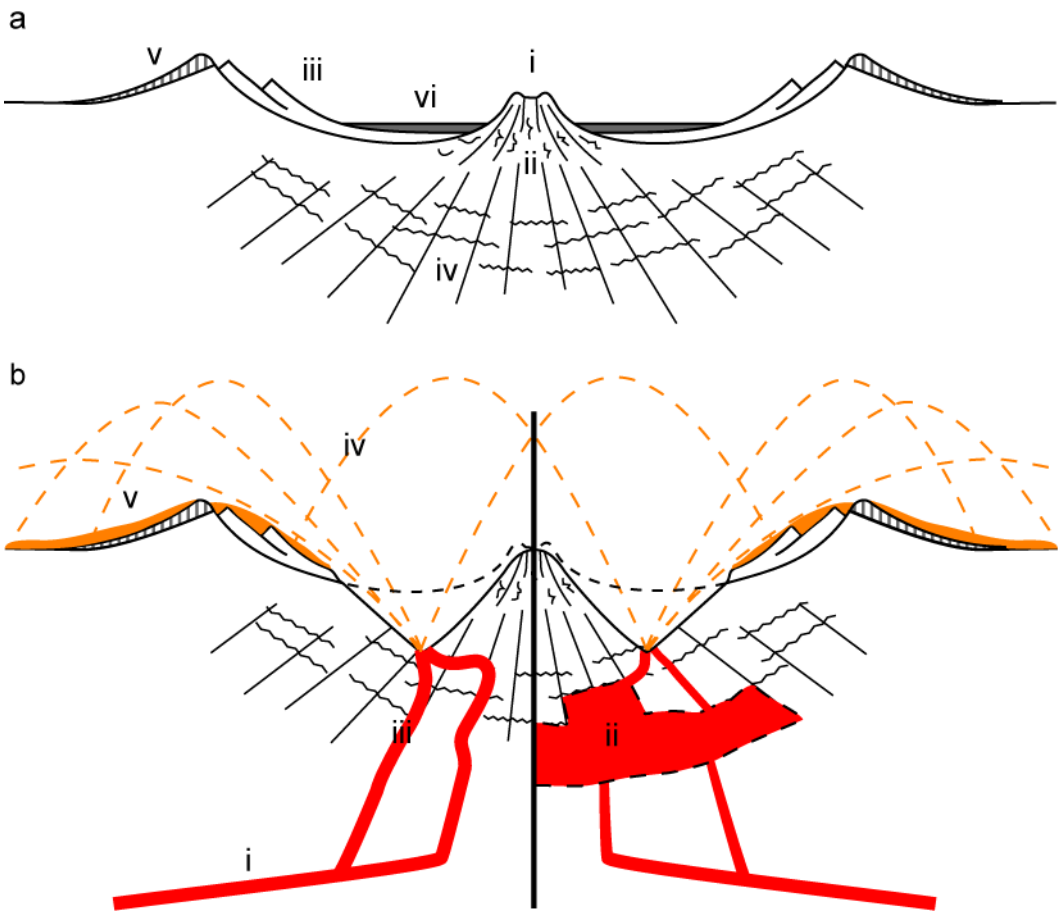


**Figure 7-2 Proposed model of formation of a crater-centred cone surrounded by pyroclastic deposits by vent formation around the central uplift of the impact crater. (a) Schematic of a complex impact crater with (i) a central uplift with (ii) internal steeply-dipping faults (*Scholz et al.*, 2002; *Senft and Stewart*, 2009), (iii) slump structures forming terraces, (iv) an underlying fracture zone (*Schultz*, 1976; *Kenkmann et al.*, 2014), (v) ejecta and (vi) impact melt deposits forming a flat floor. (b) Proposed morphology of the crater during explosive volcanic activity, with (left) or without (right) shallow magma storage. (i) Volatile-bearing magma rises from depth along a sill or dyke, possibly forming (ii) a shallow magma chamber or sill beneath the low density fractured zone (right; dashed outline indicates the margins may be gradational). (iii) Dyke propagation to the surface occurs along planes of crustal weakness, possibly aided by an increase in overpressure due to volatile exsolution. (iv) Volatiles within the magma expand at the surface and eject juvenile and vent-wall material. This falls along ballistic pathways to form (v) deposits with a relatively bright and red-sloped spectral character (dashed line indicates the original crater profile).**

## 7.4 Methods

### 7.4.1 Planform morphology

To investigate the planform morphology of the cone and associated deposits, we examined all images of the study location taken by the MDIS camera onboard MESSENGER with product creation times up to September 17, 2013. MDIS consists of a 1.5° field-of-view monochrome Narrow Angle Camera (NAC), and a 10.5° field-of-view multispectral Wide Angle Camera (WAC). We performed radiometric and photometric corrections on all images using the ISIS3 (Integrated System for Imagers and Spectrometers) software produced by the U.S. Geological Survey. Because the WAC takes repeated images of the same location through filters at different wavelengths, we were able to combine reflectance at 966 nm, 749 nm and 433 nm in the red, green and blue bands to produce colour images. This combination allows discrimination of relatively bright and spectrally red-sloped pyroclastic deposits (*Kerber et al.*, 2009; *Goudge et al.*, 2014) despite the generally subtle contrast in albedo and colour between regions of Mercury's surface (*Denevi et al.*, 2009).

We used Graphics and Shapes tools (*Jenness*, 2011) within ArcGIS software to make geodetic planform measurements of the dimensions of the cone, associated landforms and deposit.

### 7.4.2 Present-day topography

Due to MESSENGER's highly elliptical orbit around the planet, the Mercury Laser Altimeter (MLA) has not been able to obtain elevation data at the location of interest to this study. We therefore determined the present-day topography by creating a digital terrain model (DTM) using NAC stereo images EN0257648861M and EN0227259475M. Correlation of the images was performed using the area-based image matching software, Dense Matcher (*Re et al.*, 2012). The Ames Stereo Pipeline (*Moratto et al.*, 2010) was then used to triangulate from this data and produce a 215 m/pixel DTM (Figure 7-3). The DTM has approximately 1 pixel (215 m) horizontal accuracy and 100 m vertical accuracy.

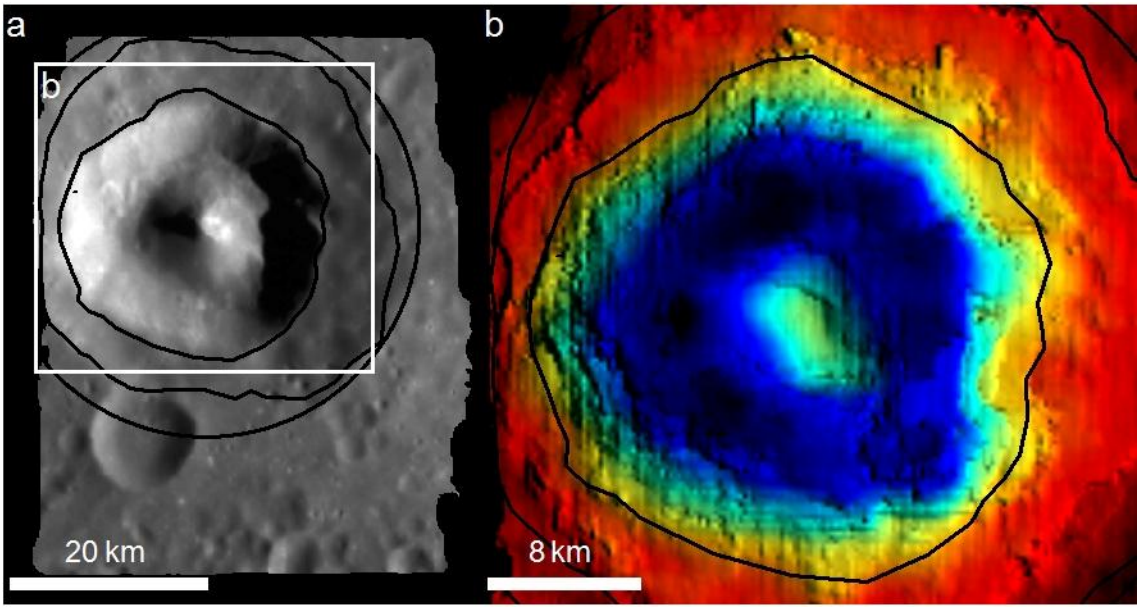


**Figure 7-3 Extent of the stereo-derived DTM of the cone and surrounding pit and crater (based on images EN0257648861M and EN0227259475M). (a) An orthorectified image showing the extent of the DTM. Black lines indicate the position of the pit and crater rims. White rectangle: extent of 3b. (b) Colourised shaded relief produced from the DTM (blue, green, red indicate increasing elevation) showing irregularities in the depth of the pit floor, probably mass wasted material.**

### 7.4.3 Original crater topography

To investigate the geological processes that formed the cone and estimate the volume of material involved, it is necessary to determine the probable morphology of the planet's surface at this location prior to its creation. As the cone lies at the centre of an impact crater, this can be approximated by estimating the original morphology of the host crater. We investigated this using two complementary methods, as follows.

#### *7.4.3.1 Topography of undegraded craters of a comparable size*

We identified three 42–47 km diameter impact craters where a MLA track crosses the central peak structure and approximately bisects the crater (Figure 7-4). These were used as a control on crater morphology and to assess the plausibility of the results of our simulations. We specifically chose impact craters with thick proximal ejecta blankets and little sign of terrace modification, indicating that they are relatively undegraded (Mansurian age, 3.5–1 Ga (*Spudis and Guest*, 1988)), and therefore approximate the morphology of the impact crater

being studied not long after its formation. We note with caution that the pyroclastic deposits obscure the original topography of AP1, so we cannot visually assess how degraded it was prior to the pyroclastic activity.

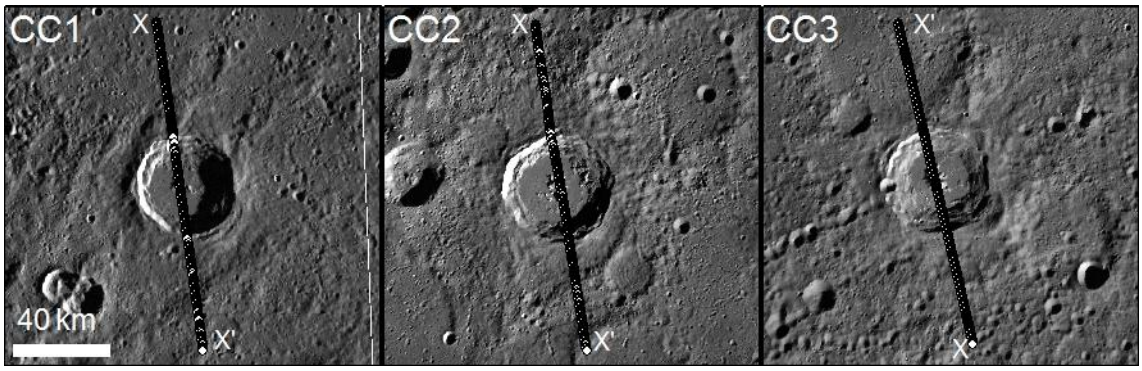


**Figure 7-4 ~ 43 km diameter morphologically fresh impact craters used as a control on the original crater shape and on the simulation. Outlined dots indicate MLA data points from X to X' used in Figure 7-6. CC1: 177.1° E, 50.9° N, MLA track MLASCIRDR1109231307 (orbit 380); CC2: -107.5° E, 49.2° N, MLA track MLASCIRDR1208272313 (orbit 1198); CC3: -122.1° E, 63.8° N, MLA track MLASCIRDR1203061631 (orbit 715). Only channel 1, high threshold, MLA pulse returns were used to avoid incorporating noise. All the panels have the same horizontal scale as that indicated for CC1 (Base image: MDIS global monochrome mosaic v9).**

#### *7.4.3.2 Impact crater numerical model*

We simulated the formation of the impact crater using the iSALE (Impact Simplified and Arbitrary Lagrangian Eulerian) hydrocode, one of several multirheology, multimaterial extensions of the SALE hydrocode (*Amsden et al.*, 1980). This has been specifically developed to model impact crater formation in its entirety (*Melosh et al.*, 1992; *Ivanov and Kostuchenko*, 1997; *Collins et al.*, 2004; *Wünnemann et al.*, 2006) and performs well in reproducing the results of laboratory experiments at high strain-rates (*Pierazzo et al.*, 2008).

The structure and composition of the projectile was simplified to spherical and homogeneous basalt impacting at an angle of 90°. Departure of the impact angle from the more statistically likely value of 45° is necessary due to the axisymmetric nature of the iSALE hydrocode. The only way to take the effect of different impact angles into account is to assume that the projectile has an average impact speed, but impacts at 45° impact angle. Therefore, the

impact speed used in the simulation is (v_average)×sin(45°), and we assume an impact velocity of 30 km/s, derived from an average impact velocity of 42 km/s (*Marchi et al.*, 2005). We estimated a porosity of 10%, derived from the average of meteorite types proposed by *Britt et al.* (2002). We estimated an impactor size of 2.4 km diameter by comparing profiles obtained in a series of runs at low resolution to the topographic profile of the present topography and cross-sections of the similar-sized control craters. We took an Eulerian approach, defining the number of computational cells per projectile radius (CPPR) as the resolution of our impact model. We used the Eulerian setup because of the inevitable extreme cell deformation that occurs with the alternative Lagrangian approach (*Pierazzo and Collins*, 2004). The crater was modelled on a computational mesh of 400×600 cells, with a cell size of 150 m and a projectile size of 8 CPPR. We used a spatially constant gravitational acceleration of 3.7 $m/s^2$.

We approximated the Hermean surface as a homogeneous layered half-space made up of a jointed 5 km basalt layer overlying an intact basalt layer. This depth was chosen on the basis of the thickness estimation of the fractured layer derived by *Schultz* (1993) and on the crater size frequency distributions predicted by the MPF (Model Production Function) for analogue smooth plains (*Marchi et al.*, 2011; *Giacomini et al.*, 2014). The material properties of these layers are summarized in Table 7-1.

The output morphology of the simulation is dependent on the equations of state and constitutive (material strength) models incorporated into the hydrocode. Therefore, the thermodynamic response for both the projectile and target in our simulations was approximated with an equation of state for basalt derived using the ANEOS model (*Thompson and Lauson*, 1974). The rock strength model employed in iSALE, which accounts for changes in material shear strength (*Collins et al.*, 2004), also includes a transient weakening mechanism called acoustic fluidization that allows the development of the central peaks and terraced walls through gravitational collapse (*Wünnemann and Ivanov*, 2003). iSALE adopts a simple mathematical approximation of Acoustic Fluidization (AF), known as the Block Model, which is controlled by two parameters: the kinematic viscosity of the fluidized region and the

decay time of the block vibrations. We performed simulations over a broad parameter space to determine the parameters producing the best fit to the dimensions of the crater being studied, and then selected between those produced at different kinematic viscosities on the basis that the final result should be consistent with the morphology of the crater being studied and the control craters.

**Table 7-1 Strength model parameters used in the simulation**

| Variable | Description | Jointed basalt | Intact basalt |
|---|---|---|---|
| $Y_0$ | Cohesion for intact material (MPa) | 10 | 10 |
| $Y_d$ | Cohesion for damaged material (MPa) | 1 | 0 |
| $Y_m$ | von Mises plastic limit (GPa) | 3.5 | 3.5 |
| $\mu_i$ | Coefficient of internal fiction | 1.2 | 1.2 |
| $\mu_d$ | Coefficient of friction (damaged material) | 0.6 | 0.6 |
| $T_m$ | Melt temperature (K) | 1500 | 1500 |

## 7.5 Results

### 7.5.1 Present-day morphology and deposit extent

The stereo-derived DTM reveals the topography of the cone, pit and all but the far western rim of the crater (Figure 7-3). The cone has a basal diameter of ~12.5 km. It stands up to 2.2 km above the floor of the pit surrounding it and its summit is 1.8 km below the rim crest of the host crater (Figure 7-5). It lacks a summit crater and has steeply-dipping flanks, averaging 26°. The pit margins are similarly steep, averaging 30°. The pit floor is shallower in some places than others, consistent with landsliding from the wall scarps (Figure 7-3b). This suggests that the original slope of the pit walls may have been greater prior to mass wasting. The crater's average diameter is 43.2 km. The area between the rim-crest (defined as the summit of the topographic rise around the pit) and the outer pit margin measures on average 8.5 km wide on the orthorectified image, has a smooth texture, and forms a 'step'. This may be a terrace formed by wall-slumping, draped by volcanic deposits. The surrounding bright, red-sloped spectral anomaly has a maximum extent of 92 km from the centreline of the pit.

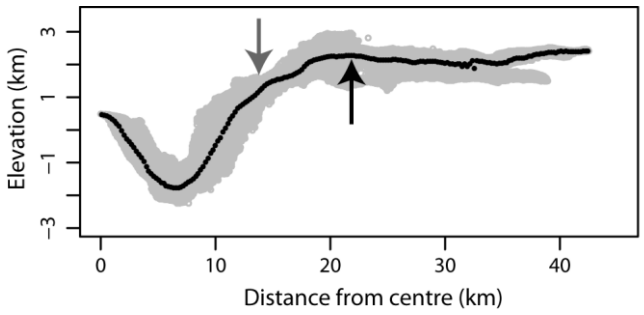


**Figure 7-5 Average present-day topography from the centre of the cone. Light grey circles mark the elevation of each pixel of the DTM against its distance from the cone centre. Black dots mark the median elevation within 215 m radial bins. Grey arrow: average location of the pit margin, black arrow: average location of the rim crest.**

### 7.5.2 Topography of the control craters

Craters CC1, CC2 and CC3 have diameters of 41.8 km, 46.7 km and 43.2 km, respectively. For comparison with the present-day topography of AP1, distances in the cross-sections were normalised to give a crater diameter of 43.2 km. Because a smaller impact crater would be expected to have a smaller ratio of rim-crest to floor depth, this necessitated a relatively minor adjustment to elevation values across CC1 and CC2. This was made by first calculating the expected rim crest to floor depth ($d$) of the crater on the basis of the relationship of this value to diameter ($D$) observed by *Pike* (1988) for complex craters on Mercury:

$$d = 0.353D^{0.496} \quad (7\text{-}1)$$

We calculated the ratio between the depth indicated by this method for the control crater and for a 43.2–km diameter crater and multiplied the MLA elevation values by this value.

To compare the morphology of the craters, we have plotted them so that distance along the cross-section is equal at the rim crest and elevation is equal at the base of the outer slope of the raised rim (known as the rim flank). The latter feature was chosen as the best point of reference because the topography beyond the craters (Figure 7-6a) is very uneven due to the presence of other impact craters, so it is impractical to identify a 'regional datum' at any greater distance. Because the elevation of the rim crest itself is particularly vulnerable to degradation processes, this too was judged an uncertain point of reference. The control craters have similar profiles, excepting that the floors of CC1 and CC2 are shallower (2.3 km

and 2.1 km) and the peak height above the floor is lower (0.4 km and 0.7 km) than those of CC3 (with a depth of 2.7 km and a peak height of 1.2 km) (Figure 7-6a). This suggests that the interiors of CC1 and CC2 have experienced more infilling than CC3, either by retention of a higher volume of impact melt during the modification stage of their formation, or by post-formation volcanic flooding.

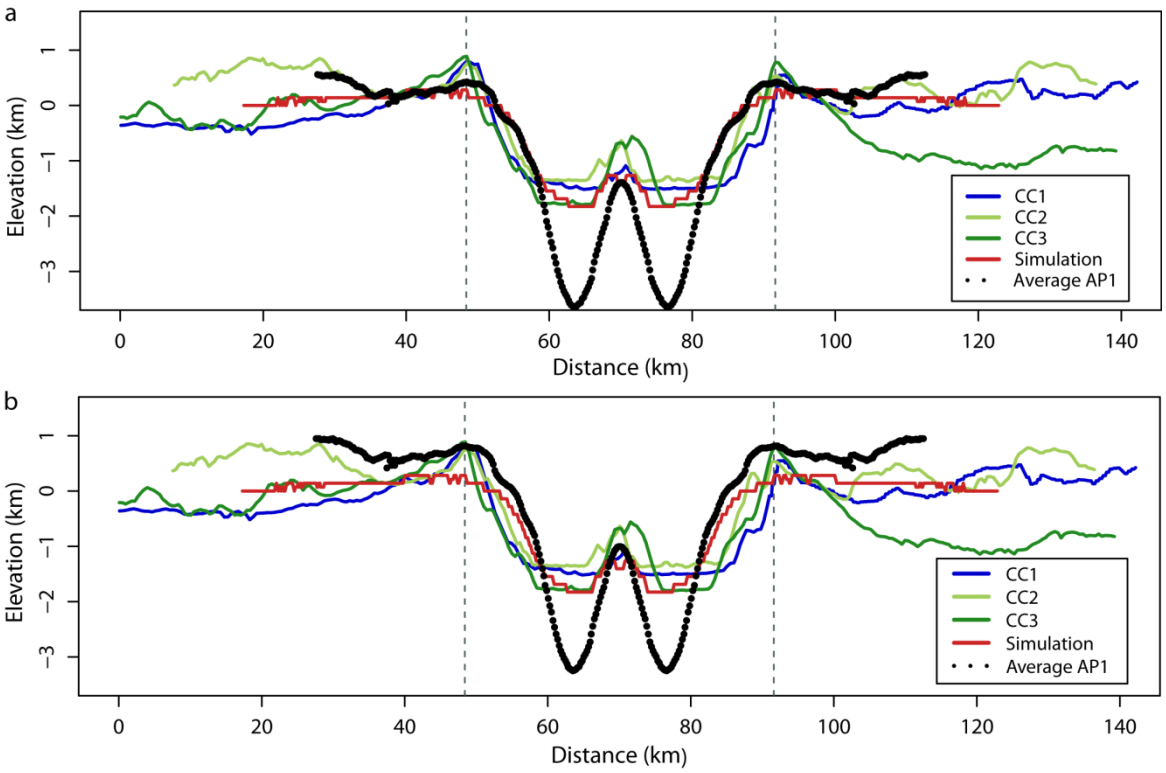


**Figure 7-6 Comparison between the average DTM elevations across the present-day landform, MLA cross-sections through the control craters, and the results of the hydrocode simulation, showing general agreement between complex crater morphology and the morphology of the cone in AP1. Vertical grey lines: the present-day rim of the 43.2 km diameter crater, AP1. (a) Values on the distance axis are equal at the leftmost rim crest, and elevations are equal at the base of the leftmost rim flank. (b) Horizontal location and elevations are matched as in (a), except that the DTM profile is placed so that the rim-crest elevation equals the average elevation of the leftmost rim crests of the control craters.**

### 7.5.3 Numerical simulation

A projectile with a diameter of 2.4 km, penetrating the target at 30 km/s (in accordance with *Marchi et al.* (2005)), generates a crater diameter in agreement with the DTM profile

considering that the final output of iSALE has a 4% radius uncertainty (a value found from code validation against laboratory experiments (*Pierazzo et al.*, 2008)) (Figure 7-6a). The simulation shows a best fit with the crater diameter and the interior morphology of the control craters with a decay time of 48 s and a kinematic viscosity of 120,000 $m/s^2$. As with the control craters, both horizontal and vertical values along the simulated cross-section were adjusted for comparison to a 43.2–km diameter crater.

Results from the simulation are in accordance with depth-diameter ratios observed in impact craters in large morphometric datasets for Mercury. *Pike* (1988) finds a best-fit to the depth-diameter values of 58 craters between 30 and 175 km diameter with the relationship given in Equation 7-1. Using this relationship, a 43.2 km wide crater would be expected to be 2.3 km deep; the simulated crater has a depth of 2.3 km (2.1 km after adjustment of its depth to take into account its greater diameter). *Baker and Head's* more recent study (2013) using MESSENGER data found a mean depth-diameter ratio of 0.034 ± 0.010 for complex craters greater than 50 km in diameter. If we apply this to the crater we are studying, it predicts a depth of 1–1.9 km: shallower than the simulated crater, but this may be a result of extrapolating their observed relationship to a sub–50 km diameter crater. Using a similar method of extrapolation for peak height data in the same work, the expected height of the central peak would be in the range of 0.3–0.9 km. The height of our simulated central peak above the crater floor is 600 m, or 570 m after adjustment for the greater crater diameter, and so is in agreement with this estimation. This indicates that though the simulated central peak is lower than those of the control craters, it lies within the range of observed values on Mercury. The simulated central peak width (8.7 km, or 7.8 km after adjustment for crater diameter) is somewhat narrower than the relationship

$$D_{cp} = 0.44D^{0.82}, \quad (7\text{-}2)$$

observed by *Pike* (1988) between crater diameter D and central peak width $D_{cp}$ in 138 craters: this predicts a width of 9.7 km.

When vertically matched with the control craters at the base of the rim flank, the elevation of the floor of the simulated crater almost exactly matches that of CC3, which we have previously identified (Section 7.4.3.1) as the least likely to have undergone significant infilling. However, the morphology of the simulation differs from that of the control craters in several aspects: the height of the rim crest relative to the base of the rim flank is much lower (140 m) versus an average of 780 m in the control craters, the walls are narrower, especially at high elevations, as a result of a broader (~4 km versus 1.6 km or less) shallowly-sloping region inwards of the rim crest, and there are no wall terraces. As the simulation indicates the crater morphology at the end of the modification stage of crater-formation, 1500 seconds after impact, these differences may result from an incomplete simulation of post-formational wall and rim modification resulting, for example, from long-timescale crustal response (*Kenkmann et al.*, 2014). These differences reinforce the value of looking at both strands of evidence to indicate the range of possible morphologies for AP1 during the period of volcanic activity.

### 7.5.4 Comparison of estimated original and present morphologies

We compare the present topography with the control craters and the simulated original topography using two possible vertical tie-points. The first plots all cross-sections so that the elevation at the base of the rim flank is equal (Figure 7-6a). This requires the assumption that there is not an appreciable thickness of pyroclastic material in this area, as this would increase the elevation of the original ground surface. The second comparison plots the topographic profile derived from the DTM such that its rim crest is at the average elevation of the rim crests of the control craters (Figure 7-6b). This would be a valid match if the original crater AP1 has undergone a similar amount of degradation as the control craters and if pyroclastic deposition has not increased the ground elevation at the rim crest. We judge that the first comparison leads to a better match between the interior and exterior morphology of AP1 and the morphology of the simulated and control craters, so we prefer to use this in the proceeding analysis.

The height of the cone (820 m above the expected floor height indicated by CC3 and the simulation, and 1.4 km below the rim crest) is consistent with that expected on the basis of the simulation and the control craters (Figure 7-6a) and with the relationship to crater diameter observed by *Baker and Head* (2013) in >50 km diameter craters on Mercury (which predicts a height of 0.3–0.9 km above the crater floor). The width of the cone at the elevation of the floors of the simulated crater and CC3 is 4.3 km, which is narrower than expected for the central peak of a crater of this size (9.7 km) (*Pike*, 1988). The wall-to-wall distance below the 'step' in the crater topography inwards of the rim crest is similar to that of the simulation, but narrower than in the control craters. There are three possible explanations of this. One is that this morphology is original to the crater, and results from the post-formational modification of AP1 being arrested at an earlier point than is normal. Such a phenomenon is not observed at other craters on Mercury, so we judge it improbable. The second is that the 'step' was created by wall slumping. This is very credible, as wall terraces resulting from slumping are seen in all three control craters and are characteristic of impact craters of this size on Mercury (*Pike*, 1988). The third is that the walls have been covered by a thick layer of pyroclastic material. There is some evidence for pyroclastic deposition in the region between the rim crest and the pit margin: it has the same smooth texture here and outside the rim, with no boundary between the two surfaces (Figure 7-1b). Pyroclastic deposits may thus contribute to the broad, high-elevation region inwards of the rim crest and the relative narrowness of the crater walls. However, it is not possible to distinguish relief resulting from pyroclastic deposition from that resulting from crater modification and degradation processes.

The pit represents a large loss of material: if the simulation and present-day DTM topography are vertically matched as in Figure 7-6a, the average pit floor is 1.4 km below the expected crater floor depth, and the volume difference (calculated using ArcGIS) is ~350 $km^3$. If a similar comparison is made to a DEM constructed with elevation plotted radially against distance from the crater centre to the northern rim of CC3, the volume of material missing within the trench and cone area of AP1 is ~300 $km^3$. These are approximate values for the

volume of material lost because shadows in the images used to construct the DTM do not allow us to calculate the volume loss in the eastern part of the pit, and because the vertical match is uncertain.

If the volume loss from the pit equals the volume of a pyroclastic deposit over the area indicated by the bright, red-sloped spectral signature, that deposit would average ~20 m thick using the volume change indicated by the hydrocode, or ~17 m thick using the volume difference from CC3, when scaled to take into account the different densities of basalt rock and pyroclastic fall (2760 kg $m^{-3}$ vs. 2000 kg $m^{-3}$ (*Wilson et al.*, 2014)). Elsewhere on Mercury, putative pyroclastic deposits ranging from 29 to 567 m thick have been identified in close (~6 km) proximity to vent margins (Section 5.4.2.2). Where such relief is observed, the surrounding relatively bright and red-sloped spectral anomaly extends to an average of three times as far from the vent margin, indicating the presence of an outer zone of thinner (and, at current resolutions, topographically undetectable) deposits. Because of the uncertainties of the vertical match between the original and present-day topography, we cannot determine whether deposits at AP1 are thicker near the vent than at greater distances, though if, as discussed above, the wide high-elevation area inwards of the rim crest and the narrowness of the crater walls are in some part the result of pyroclastic deposition, this deposition would have occurred within 9 km of the pit margin.

## 7.6 Discussion

### 7.6.1 Mode of formation of the landform assemblage

There is no evidence that the cone was constructed by volcanism: it lacks a summit caldera or vents, has no flow features on its flanks and has a similar slope to that of the outer scarps of the pit surrounding it. Conversely, its position, elevation, slope and morphology is consistent with a residual central peak of an impact crater, surrounded by an annular pit.

The occurrence of a pit associated with pyroclastic deposits at the centre of an impact crater is not unique to this location. In a global survey we identified 150 sites where endogenic pits are surrounded by a bright, red-sloped spectral anomaly interpreted as pyroclastic deposits

(Appendix C). 118 of these occur within impact craters, and 52 (excluding AP1) are at the crater centre (Table D-1). In some cases the pit is in place of an expected central peak or peak ring, but in 31 cases it is concentric to the peak or central region (Figure 7-7). In some cases small pits occur around the crater centre (Figure 7-7c), in others conjoined pits form arcs around the centre (Figure 7-7b), and in rare cases (e.g. Figure 7-7a) a pit or conjoined pits entirely encircle the crater centre, though not forming so distinctive a 'cone' as seen at AP1. These configurations form a continuum and may represent a time sequence in which, with continued or repeated eruptions, pits around a crater's central peak enlarge and conjoin until they form a continuous trench encircling the peak. This indicates that the cone and trench at AP1 are an extreme end-member of a characteristic landform association on Mercury.

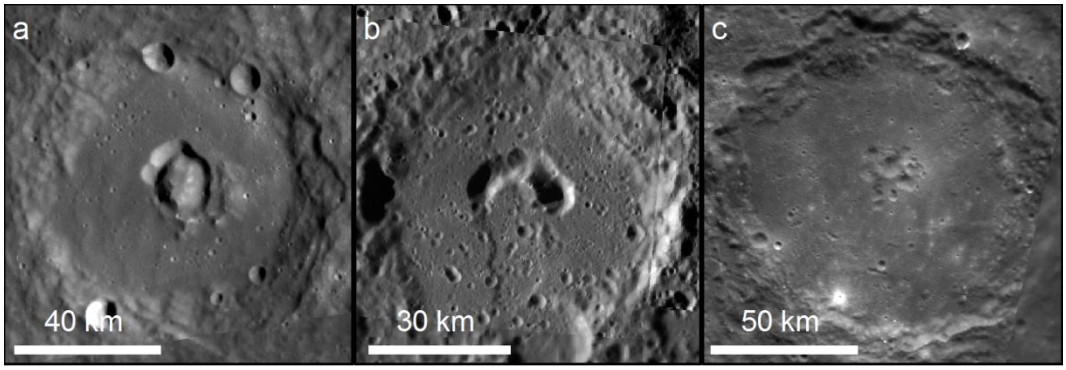


**Figure 7-7 Endogenic pits with surrounding putative pyroclastic deposits circumferential to the impact crater centre. (a) A pit entirely encircles the central uplift (72.4° E,-21.1° N). (b) Pits circumferential to the centre of an impact crater where the central peak is not visible, probably due to volcanic infill prior to pit formation (140.5° E, -11.1° N). (c) Multiple small pits occurring circumferential to the crater centre (6.5° E, -48.4° N).**

Terrestrial seismic surveys and numerical models give some indication of why vent-formation is localised in the vicinity of central peaks: they indicate that impact crater central uplifts are bounded by deeply-penetrating high-angle faults (*Scholz et al.*, 2002; *Senft and Stewart*, 2009; *Kenkmann et al.*, 2014). Mercury has been in a global state of compression for much of its history (*Strom et al.*, 1975), inhibiting the ascent of magma to the surface, so it is to be expected that any magma ascent that did occur would be localised in pre-existing zones of weakness such as these. It is interesting to note that, though, as has previously been stated

(*Gillis-Davis et al.*, 2009), endogenic pit formation appears to be structurally-controlled by host crater structures, our findings suggest that pits most commonly occur at the crater centre or along a peak ring, and less commonly at other fault-bounded structures such as the terraces or rim area. In contrast, on the Moon, volcanic vents within impact craters commonly occur at the margins of the crater floor (*Head and Wilson*, 1979; *Head et al.*, 2000; *Gaddis et al.*, 2013). This may indicate that either the mechanisms of magma ascent or the relative strengths of different parts of impact crater structures differ on the two bodies.

### 7.6.2 Mode of pit formation

A structural control on pit formation has been taken as evidence that Mercury's endogenic pits form by collapse along planes of weakness during magma withdrawal from a shallow magma chamber (*Gillis-Davis et al.*, 2009). It is possible that subsidence has occurred in our example: the summit of the cone is 1.4 km below the rim crest, versus an average depth of 1.6 km for the control craters, despite probable degradation of the rim crest area of AP1 by 400 m. However, given the wide range of observed peak heights within complex craters (*Baker and Head*, 2013), and the absence of a crater floor relative to which the peak can be measured, this low peak elevation cannot be conclusively attributed to post-formation modification.

The pit was clearly the locus of intense explosive volcanism, so it is probable that a significant amount of wall-rock erosion contributed to pit-formation (and possibly reduction in peak height and width). The maximum dispersal of pyroclasts ejected on ballistic trajectories in the airless conditions of Mercury, as discussed by *Kerber et al.* (2009), is $X = v^2 \sin 2\theta / g$. Taking $X$ as 92 km, the maximum horizontal radius of the deposit from the pit centreline, $g$ (gravity) as 3.7 m/s$^2$ and $\theta$ as the angle at which dispersal is greatest (45°), the minimum velocity at the vent is 580 m/s. On Earth, such velocities are typical of high-energy Plinian eruptions, in which significant vent-widening occurs (*Wilson et al.*, 1980). However, we do not know the volume of material ejected at this velocity, so it is not possible to quantify the kinetic energy available for wall erosion.

We await with interest higher-resolution compositional data, to be acquired by the forthcoming BepiColombo mission (*Fraser et al.*, 2010; *Rothery et al.*, 2010). This may allow us to constrain the proportions of juvenile and non-juvenile material in the pyroclastic deposits and thus determine the relative importance of magma chamber drainage versus wall-rock excavation for pit formation.

### 7.6.3 Evidence for magma storage prior to eruption

Our previous work (Section 5.5.1) has suggested that the horizontal scale of the largest pyroclastic deposits on Mercury (of which the 92 km radius AP1 deposit is the second-largest example) is consistent with their emplacement by either Strombolian eruption or by high flux steady eruption where the majority of the magma is disrupted into large particles, 10 mm to 1 m diameter (*Wilson and Head*, 1981). Both Strombolian eruption and eruption of predominantly large clasts indicate a slow magma rise speed, as a large particle size and intermittent, Strombolian eruption are both caused by bubble coalescence prior to eruption. This suggests that the magma may have been stored beneath the crater prior to eruption.

The extreme dispersal of the deposits indicates a high volatile content in the magma. If we follow the method of *Wilson et al.* (2014) to calculate the released gas fraction on the basis of the gas speed at the vent (as discussed in Section 5.5.3) we find that that ejection of pyroclasts to 92 km on Mercury requires 5.4 wt% $CO_2$ or 4.2 wt% $H_2O$ if each of these were the sole volatile. These are very high values: in non-subduction settings on Earth, melt inclusions indicate 0–0.25 ppm $CO_2$ and 0.2–0.8 wt% $H_2O$ in basaltic melts (*Metrich and Wallace*, 2008). Chemical equilibrium models suggest a combination of more reduced species such as $N_2$, CO, $S_2$, $CS_2$, $S_2Cl$, Cl, $Cl_2$, and COS would be present in Mercury's magmas (*Zolotov*, 2011). Due to their high molecular weights, a concentration greater than, or equal to, 7.6 wt% would be necessary to form the deposit if any of them were the sole volatile. As there is no reason to believe Mercury to be more volatile-rich than Earth, it is probable that such high volatile concentrations were reached by some process causing volatile enrichment in the erupted magma (Section 5.5.3). Slow magma rise and/or storage at shallow depths could achieve this, as this would allow accumulation of exsolved gas prior to eruption. We note,

however, that it is possible that some of the volatile enrichment may result from incorporation of volatile-bearing wall-rock, which could occur in steadily-rising magma that did not undergo a period of storage.

## 7.7 Conclusions

Our results confirm the hypothesis that a steep-sided cone surrounded by putative pyroclastic deposits on Mercury was formed by explosive volcanic eruption from a vent encircling a residual central peak of an impact crater. We find that the landform at this location likely represents the extreme end-member of a large class of volcanic vents circumferential to impact-crater central peak structures, indicating that crater-related faults control explosive volcanism at such locations. The scale of the pyroclastic deposit indicates that the magma had a high volatile content relative to basaltic eruptions on Earth, supporting the idea that it was stored for some time in the low-density fractured zone beneath the impact crater prior to eruption.

It is interesting to note that a similar process, where magma ascends to the fractured zone beneath an impact crater, stalls and, in some cases, erupts explosively due to pressure build-up resulting from volatile accumulation, is also hypothesised for the Moon (*Head and Wilson*, 1979). On the Moon, however, the crater floor becomes fractured by inflation of a sub-crater laccolith (*Schultz*, 1976; *Jozwiak et al.*, 2012) and dyke propagation to the surface is favoured by this fracturing, usually occurring from the crater floor adjacent to the walls. Additionally, surrounding putative pyroclastic deposits are, on average, less areally-extensive than those observed on Mercury (Figure 5-6). The observation that endogenic pits commonly occur at the centre, rather than at the margins, of impact craters on Mercury, and a lack of floor-fracturing, suggests a difference in the processes by which crater-hosted explosive volcanism occurs on the two small, airless bodies. Future comparative study may prove fruitful for our understanding of the processes at work on both the Moon and Mercury.

## 7.8 Epilogue: new data

Since the publication of the paper that makes up this chapter, new images (released by NASA's Planetary Data System up to 6th March 2015) have become available revealing eleven additional sites within an impact crater at which an endogenic pit is surrounded by a relatively bright and red spectral anomaly. Four of these occur at the centre or on the peak ring of the impact crater, providing further evidence that this is a common setting at which explosive volcanism occurs on Mercury.

# Chapter 8. Explosive volcanism in complex impact craters on Mercury and the Moon: influence of tectonic regime on depth of magmatic intrusion

## 8.1 Introduction

As noted in the conclusion of Chapter 7, the recognition that putative explosive volcanism commonly occurs from vents within impact craters on Mercury suggests that it may be revealing to compare this with similar yet contrasting evidence for explosive volcanism within impact craters on the Moon. To explore this, I have conducted a comparative analysis, which is presented in a paper that is in the final stages of peer-review (minor corrections to a revised manuscript) at *Earth and Planetary Science Letters* as of September 2015. That paper comprises this chapter.

## 8.2 Background

It has long been recognized that vents and deposits attributed to explosive volcanism frequently occur within complex impact craters on the Moon (e.g. *Schultz*, 1976; *Head and Wilson*, 1979; *Coombs and Hawke*, 1992; *Gaddis et al.*, 2013). More recently, data from the MErcury Surface, Space ENvironment, GEochemistry, and Ranging (MESSENGER) spacecraft have revealed that an association between putative explosive volcanism and impact craters also exists on Mercury (*Gillis-Davis et al.*, 2009; Chapter 5). Mercury and the Moon are similar in several respects: they are virtually airless, and have a surface geology that is dominated by a combination of impact cratering and volcanic resurfacing. The similar localization of explosive volcanic activity on both bodies, therefore, suggests the action of similar processes.

In the lunar case, it has been proposed that localization of explosive volcanism within impact craters results from density-trapping of magma in the brecciated zone below the crater (*Head and Wilson*, 1979). In this model, a vertically-propagating dyke encounters the low density, weak material of the breccia lens beneath the crater floor and is diverted to form a sill because the density and rigidity contrast favours lateral propagation rather than continued

vertical ascent (*Schultz*, 1976; *Wichman and Schultz*, 1995a). With continued recharge, this sill propagates horizontally until it encounters higher lithostatic pressures at the wall zone (*Thorey and Michaut*, 2014) and the intrusion begins to thicken, fracturing the floor above. Dyke propagation to the surface is commonly favoured along zones of extension at the intrusion margins (*Pollard and Johnson*, 1973) and results in either effusive volcanism, forming lava pools, or, if sufficient exsolved gas builds up prior to eruption, explosive volcanism (*Jozwiak et al.*, 2015). The products of both of these styles of volcanism are observed at circumferential fractures in floor-fractured craters (FFCs) on the Moon, so this appears to be a good explanatory model.

On Mercury, too, there is evidence for sub-crater magma storage prior to eruption. Endogenic pits surrounded by a spectrally-distinct deposit, interpreted as volcanic vents (*Kerber et al.*, 2009), often occur in groups within a single crater, indicating a shared proximal source for coeval and/or sequential eruptions. Moreover, the scale of vents and the scale and morphology of deposits are consistent with accumulation of volatiles in a subsurface magma chamber prior to eruption (Section 5.5.3). The occurrence of the majority (79%) of explosive volcanic vents surrounded by putative pyroclastic deposits within impact craters on Mercury also supports the hypothesis that the subsurface structure of craters plays a controlling role in the localization of explosive volcanism. However, the specific character of this volcanism differs from that on the Moon. Floor-fracturing is observed in only one impact crater on Mercury (*Head et al.*, 2009a), and this does not host a pyroclastic vent or deposit. Additionally, explosive volcanism commonly occurs at and around central uplifts in craters on Mercury, rather than at the outer margin of the floor (Section 7.6.1).

The contrasting character of volcanism and host-crater modification between the Moon and Mercury indicates that it cannot be assumed that magma rise beneath impact craters on terrestrial bodies will always result in the eruptive character familiar from the Moon. An investigation into probable controls on crater-localized magma rise, storage, and explosive eruption on each body has the potential to enhance our understanding of tectono-magmatic conditions on both bodies. To this end, I have investigated the dimensions and settings of pits

and deposits thought to result from explosive volcanism within complex impact craters on the Moon and Mercury. Using these data, I have characterized the energy of eruption and deformation of host craters and thereby placed constraints on the probable controls on intrusion and eruption. My findings suggest that the regional stress regime played an important role in the depth of magma intrusion on Mercury, and may also have done so on the Moon.

## 8.3 Data and methods

### 8.3.1 Site selection

I analysed 16 sites on Mercury and 15 on the Moon where an impact crater hosts candidate volcanic vents surrounded by a diffuse-margined spectral anomaly generally accepted to indicate a pyroclastic deposit (Table E-1). Only sites occurring within complex impact craters were selected (30–120 km diameter on Mercury (*Pike*, 1988) and 30–140 km on the Moon (*Pike*, 1980; *Bray et al.*, 2012)), so that subsurface crater-related structures could be considered broadly comparable across the sample set.

On both bodies, examples were drawn from previously identified sites where putative pyroclastic deposits appear to have been sourced from candidate vents within the crater structure, and where those vents are evident in topographic data. On this basis, and choosing examples only where the presence of a pyroclastic deposit is relatively uncontroversial, 15 lunar examples were drawn from 41 possible sites (*Wolfe and El-Baz*, 1976; *Head and Wilson*, 1979; *Coombs and Hawke*, 1992; *Gaddis et al.*, 2003; *Gustafson et al.*, 2012). A sample of 16 sites was drawn from 71 identified sites on Mercury (*Kerber et al.*, 2011; Appendix C). These selection criteria, choosing examples that are least-controversial and most amenable to analysis on each body, may mean that the samples do not reveal the full range of variation in pyroclastic activity within complex craters on either body.

### 8.3.2 Pyroclastic deposits

Identification of putative pyroclastic deposits on both Mercury and the Moon relies primarily, at present, on observation of a diffuse-margined spectral anomaly in orbital images. Deposits

believed to be pyroclastic on Mercury have higher reflectance and a steeper ("redder") slope of spectral reflectance versus wavelength than the planetary average. To identify them, I constructed composites combining reflectance data from the 996 nm, 749 nm and 433 nm filters in MESSENGER's 10.5° field-of-view Wide Angle Camera (WAC) in the red, green, and blue channels, respectively, in which they appear as a bright, orange spectral anomaly (Figure 8-1a). I constructed composites from all images created prior to October 17th, 2013 having a resolution of 1000 m/pixel or better, and also examined the PDS-hosted 1000 m/pixel global colour mosaic (March 2014 release).

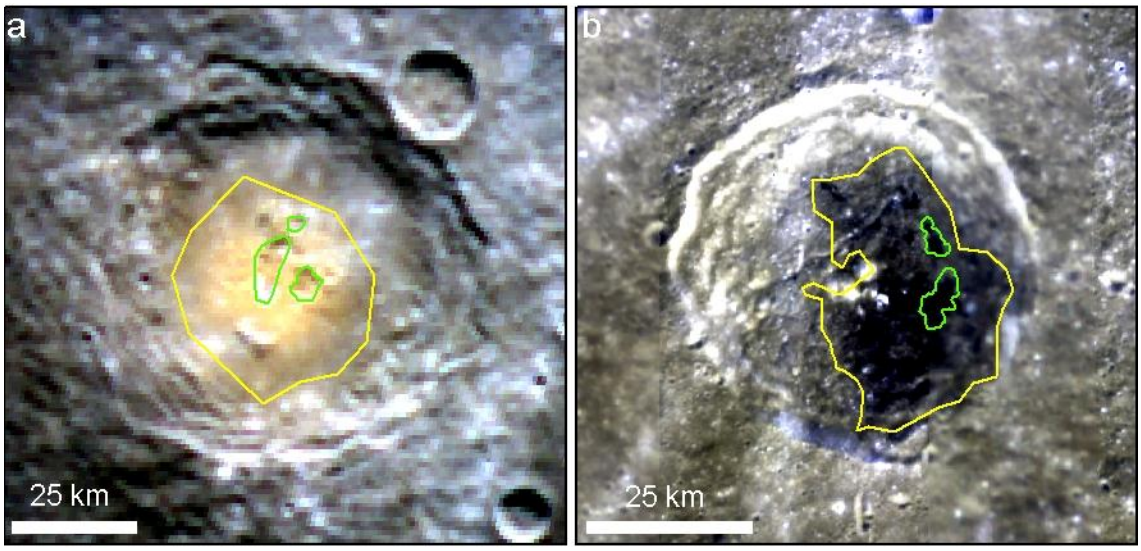


**Figure 8-1. Spectral anomalies with diffuse margins interpreted as pyroclastic deposits on (a) Mercury and (b) The Moon. Yellow outline: extent of the spectral anomaly, green outline: rim of candidate vent. (a) Rilke crater (pit group 8026). Colour composite of MDIS WAC images EW0222970395I (996 nm), EW0222970415G (749 nm), and EW0222970399F (433 nm) in the red, green and blue bands. (b) Franklin crater. Excerpt from the Clementine UVVIS global mosaic (*Eliason et al.*, 1999; *Hare et al.*, 2008) with reflectance at 1000 nm, 900 nm, and 415 nm and in the red, green and blue bands**

Lunar pyroclastic deposits are commonly identified by their low albedo relative to highlands material and a spectral character suggesting varying mixtures of highlands, basaltic and glass components (*Gaddis et al.*, 2003). I identified the extent of putative deposits on the basis of a low-albedo, diffuse-margined anomaly in the 1489 nm apparent reflectance mosaic from the Moon Mineralogy Mapper (M3) on the Chandrayaan-1 spacecraft, and in a colour composite

combining 1000 nm, 900 nm and 415 nm global mosaic reflectivity data from the Clementine spacecraft in the red, green and blue bands (Figure 8-1b).

For both bodies, I digitized the areal extent of the spectral anomaly, taking a conservative approach by excluding the tenuous outer fringe. This was further refined in lunar examples where the extent of the low albedo material is apparent as fine-grained material mantling the underlying terrain in high-resolution narrow-angle camera (NAC) images from the Lunar Reconnaissance Orbiter Camera (LROC). As a means of calculating the maximum specific energy with which particles were ejected from vents, I additionally measured the maximum distance between a candidate vent (Section 8.3.3) and the outer margin of its surrounding continuous deposit at each site. Because the available data types and the spectral character of deposits differ on the two bodies, the same level of error cannot be assumed in determination of the position of the outer boundary of the deposit. I estimated it as 2 pixels, but it may be higher, particularly on Mercury where there are no high-resolution images with which the position of this outer boundary can be refined. This introduces a bias in favour of larger detected deposits on the Moon. Comparisons of deposit areal extent on the two bodies are therefore made with caution.

### 8.3.3 Volcanic vents

On Mercury, irregular, rimless depressions lacking the characteristic ejecta blanket of impact craters (known as 'pits') are considered candidate volcanic vents (*Kerber et al.*, 2011). These are readily identifiable in monochrome orbital imagery taken by the NAC and WAC in MESSENGER's Mercury Dual Imaging System (MDIS) (Figure 8-2a-b). I obtained topographic data with which to determine the volume of these vents by using stereo images (NAC or WAC frames using the 750 nm filter) to create high-resolution DEMs by photogrammetry using the Ames Stereo Pipeline (*Moratto et al.*, 2010). Point data were averaged on a 3×3 block of pixels, giving the DEM a horizontal resolution 3 times larger than that of the stereo images used to create it. On the basis of error determinations made in Section 5.3.2.2, the vertical error is up to 80 m.

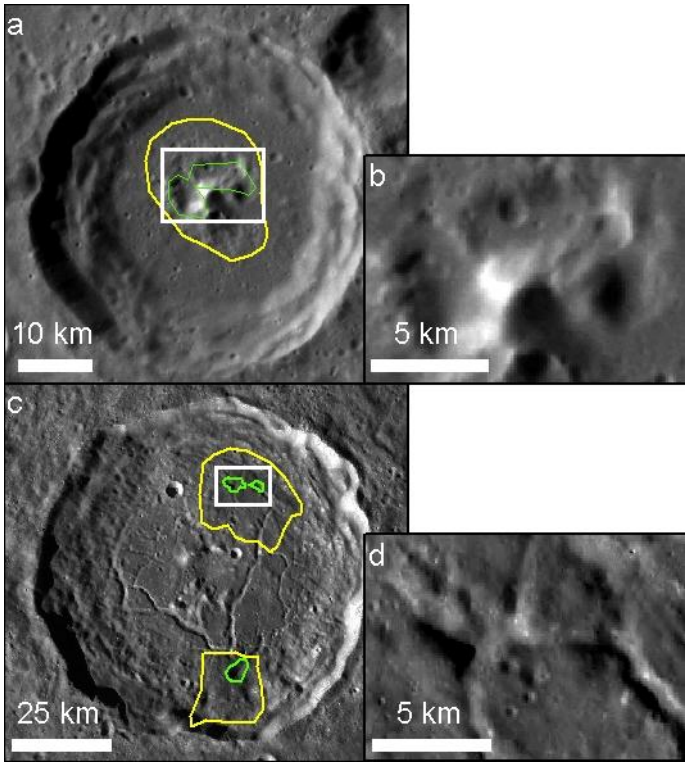


**Figure 8-2. Characteristic appearance of crater-hosted candidate explosive volcanic vents on (a,b) Mercury and (c,d) the Moon. Green outline = vent rim, yellow outline = extent of surrounding spectral anomaly. Close-ups (b) and (d) indicated by white rectangles. (a-b) Pit group ID 6083 (MDIS NAC image EN0251000097M). (c-d) Atlas crater (excerpt from the LRO WAC Global mosaic).**

I identified candidate lunar vents by reference to the LROC WAC Global mosaic at 100 m/pixel, higher-resolution NAC images, and the Lunar Orbiter Laser Altimeter 188 m/pixel DEM. Identification of vents within putative explosive volcanic deposits is less certain on the Moon than on Mercury because lunar examples commonly occur within floor-fractured craters. Relatively wide sub-circular regions of the crater-floor grabens, particularly where these occur within an intense part of the albedo anomaly, are interpreted as the probable source of the surrounding pyroclastic deposit (Figure 8-2c-d).

Volcanic vents commonly form by erosion of wall-rock during eruption and/or by collapse into an evacuated magma chamber. Therefore the volume of the vent can indicate the energy or volume of eruption. In order to calculate the volume of material that was lost to form the identified vents, I calculated their volume below a rim elevation determined with reference to orbital imagery and topographic products. On both bodies, though to a greater degree in

floor-fractured craters on the Moon, the original surface prior to vent-formation was uneven. To account for this when calculating the volume lost to form the vent, I used a Natural Neighbor technique within ArcGIS software to interpolate a surface at the vent rim level on the basis of the surrounding topography, and subtracted elevations on the vent floor from the elevation of that surface. Because this interpolation technique estimates elevation values on a local basis, any relief owing to a pre-existing graben crossing the vent is greatest at the margins of the interpolated area and reduces towards the interior. This means that the original graben volume is only partially accounted for, and the calculated volume of vents within grabens should be viewed as a maximum value.

### 8.3.4 Host crater dimensions

The intrusion of magma beneath impact craters on the Moon is proposed to result in a reduction in crater depth (*Schultz*, 1976). To explore this, I calculated the host crater depth for all sites in the two samples, defined as the vertical distance between the average rim crest elevation and the average floor elevation. In finding the average rim elevation, I excluded parts of the rim crest where major post-formation modification was evident. The average crater floor elevation was defined as the 100 m bin within which the highest number of DEM pixels in the interior of the crater fell. I compared the depth thus calculated to the depth calculated using depth-diameter relationships observed in large populations of mature complex craters (*Pike*, 1980, 1988). For craters on the Moon where floor-fracturing is observed, I used two methods to calculate the minimum effective thickness (Te) of overburden consistent with the observed uplift if this had been the result of sub-crater intrusion, using material constants as listed in *Thorey and Michaut* (2014) and *Jozwiak et al.* (2015), respectively. The method developed by *Thorey and Michaut* (2014) uses the finding that uplift will have a convex morphology if the flexural wavelength of the overburden is less than a quarter of the crater floor radius. If this uplift extends laterally to the wall zone, the crater floor radius can thus be used to calculate the minimum elastic thickness of the overburden. This method is appropriate for ten craters in my sample. Conversely, *Pollard and Johnson* (1973) calculate the effective thickness of the overburden based on the magmatic

driving pressure required to uplift overlying material to the observed uplift radius. Though this approach has been criticized (*Thorey and Michaut*, 2014), I include the results of this method as a basis for comparison with other studies (e.g. *Wichman and Schultz*, 1995a, 1995b; *Jozwiak et al.*, 2012, 2015). I noted any extensional or compressional tectonic structures within the crater, making reference to global datasets (*Jozwiak et al.*, 2012; *Byrne et al.*, 2014), and any evidence (such as burial of the central uplift) for post-crater-formation lava infilling.

### 8.3.5 Regional setting

To assess possible regional controls on the occurrence of explosive volcanism, I studied the geological setting of each site in detail. This included noting the proximity to and spatial relationship with extensive lava plains, association with specific substrates and types of tectonic structure, and proximity to other sites of explosive volcanism. For Mercury, I made reference to the global MESSENGER monochrome and colour mosaics, individual MDIS images, and published maps of smooth plains (*Denevi et al.*, 2013) and tectonic structures (*Byrne et al.*, 2014). For the Moon, I referred to published geological maps (*Wilhelms and McCauley*, 1971; *Scott, D. H., & McCauley*, 1977; *Wilhelms, D. E., and El-Baz*, 1977; *Lucchitta*, 1978; *Stuart-Alexander*, 1978) and the global LROC WAC mosaic.

## 8.4 Results

### 8.4.1 Vent and deposit scale

The average volume of an individual vent at sites on the Moon (0.54 ± 0.06 $km^3$) is significantly smaller than on Mercury (25.0 ± 2.1 $km^3$) (Figure 8-3a), despite the potential for overestimation of vent volume on the Moon (Section 8.3.3). The range in volume across the sample set is also lower: 0.002 ± 0.007 – 6.75 ± 1.96 $km^3$ on the Moon and 0.08 ± 0.08 – 454 ± 58.6 $km^3$ on Mercury. To investigate whether these differences are because of a more distributed style of volcanism on the Moon than on Mercury, I compared the total vent volume at each site on the two bodies and found that this, too, is significantly smaller on the Moon (average 1.9 ± 0.34 $km^3$) than on Mercury (average 47.0 ± 3.9 $km^3$) (Figure 8-3b).

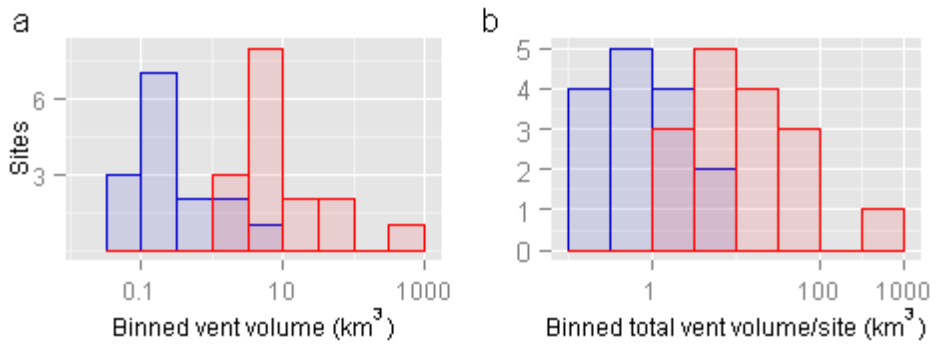


**Figure 8-3. Vent volumes on the Moon (blue) and Mercury (red). Both (a) the average volume and (b) total volume of vents at a site are significantly lower on the Moon than on Mercury (note the logarithmic scale for the x-axes).**

The maximum ballistic range measured for particles forming the observed deposit is generally higher on Mercury (median value of 18.6 ± 1.2 km, maximum of 50.3 ± 1.2 km) than on the Moon (median 10.7 ± 0.04 km, maximum 46.6 ± 0.04 km) despite the observational bias in favour of detection of pyroclastic material to greater distances on the Moon and despite higher gravity on Mercury, which means that particles ejected at equal velocity will have a smaller range than on the Moon. Because lunar vents commonly occur as a relatively subtle widening of a graben, it is probable that in some cases particle sources have been missed and the ballistic range overestimated. I therefore also compare the average geodetic area of deposits within the sample sets. This, too is larger for Mercury (median 1210 ± 53.2 km$^2$, maximum 6990 ± 138 km$^2$) than for the Moon (median 231 ± 5km$^2$, maximum 3949 ± 22 km$^2$), supporting the inference that particles were, on average, ejected to greater distances on Mercury. The maximum ballistic range ($X$) can be used to calculate the maximum speed ($v$) at which pyroclasts were ejected from a vent in a vacuum using the relationship:

$$X = \frac{v^2}{g} \sin 2\theta \quad , \qquad (8\text{-}1)$$

where $g$ is gravitational acceleration and $\theta$ is the angle at which dispersal is greatest (45°). This gives a value of 284 m s$^{-1}$ for the median and 468 m s$^{-1}$ for the greatest ballistic range observed in the Mercury sample set, and 143 m s$^{-1}$ for the median and 297 m s$^{-1}$ for the greatest ballistic range observed in the lunar sample set. As the specific energy of particle

ejection is approximately proportional to the volatile mass fraction in the released magma (*Wilson*, 1980), this indicates a higher concentration of volatiles in the eruptions on Mercury than on the Moon, for volatile species of similar molar mass. This is consistent with findings for the entire global populations (*Kerber et al.*, 2009; Section 5.4.2.2).

### 8.4.2 Tectonic modification of host craters

14 of the sites on the Moon lie within impact craters catalogued as floor-fractured (*Schultz*, 1976; *Jozwiak et al.*, 2012), and cover a range of documented FFC types (Table E-1). The anomalously shallow, fragmented floor of the crater Hell, which hosts the remaining site, suggests that this may also be an FFC. This high correlation to FFCs is also observed in the global population of putative pyroclastic deposits hosted by complex craters: 12 of the non-sampled 26 host craters are previously-catalogued FFCs, and 9 are flooded by mare lavas that would obscure any floor-fracturing, if present. One (Grimaldi F) is crossed by a graben of regional extent and vents in another (Messala) are aligned along grabens in the crater floor. Of the remaining three sites, I suspect that the 'pyroclastic deposits' at Lagrange C and Schluter A are spectrally-distinct impact ejecta, and, though Vitruvius has not previously been catalogued as a floor-fractured crater, its morphology is consistent with that of an FFC modified by volcanic deposition. Thus, it appears that floor-fracturing of craters hosting localized pyroclastic deposits on the Moon is almost ubiquitous. Candidate vents occur in concentric fractures adjacent to the crater wall at 10 of the sampled sites and adjacent to the crater central uplift at only two. The crater floor depth ranges from 38% to 83% of the expected depth of a crater of that diameter. Because the shallow depth of these craters does not appear to result from mare-infilling, and because of the fractures present on the crater floors, uplift by a sub-crater intrusion is the most probable explanation of their shallow rim-to-floor depths.

The calculated minimum effective thickness (Te) of crust overlying intrusions capable of producing the observed uplift ranges from 0.9 to 5.3 km for convex-floored craters using the method of *Thorey and Michaut* (2014), and 0.6 to 4.0 km over the whole sample set using the method of *Pollard and Johnson* (1973) (Figure 8-4). Where there is a piston-like uplift and the

crater is not large (e.g. Haldane, Kopff), intrusions are expected to be significantly shallower (*Thorey and Michaut*, 2014). Because Te is the thickness of a single layer with the observed flexural rigidity, and crater floor materials are heterogeneous and may contain some weaker layers, the true thickness of the overburden is expected to be considerably greater than Te. If, after *Wichman and Schultz* (1995a), we approximate it as 6 × Te for lunar FFCs, and if we approximate the transient crater depth as one third of the transient crater diameter ($D_{tr}$) (*Grieve and Cintala*, 1982) and calculate $D_{tr}$ as $D_t^{0.15}D^{0.85}$ after *Croft* (1985) where $D_t$ (the transition diameter between simple and complex impact craters on the Moon) is 17.5 km (*Pike*, 1980) and D is the observed rim–rim diameter, in all cases the approximated intrusion depth is equal to or less than that of the transient crater below the crater floor. This may indicate that intrusion occurred along the base of the fallback breccia zone but, given the uncertainty of the estimated values used in these calculations, this cannot be considered proven.

Extensional crater floor fractures are not observed at the sites on Mercury. Minor thrust faults cross two of the host craters. Otherwise, apart from central uplifts and relief proximal to candidate vents, the floors are flat, and there is no evidence of flexure over a larger region beyond the crater floor. Crater depths vary from 57% to 120% of the value predicted by the depth-diameter ratio of fresh craters observed by *Pike* (1988), and fall well within the range of depth-diameter ratios for complex craters observed by *Baker and Head* (2013) (Figure 8-5). Anomalously shallow craters have larger diameters, as has been observed for non-fresh impact craters on Mercury in general and attributed in large part to post-formational modification by infilling (*Barnouin et al.*, 2012). A smooth, shallow flat floor with only a small central peak projecting above it at six of the sampled sites indicates that this is a probable modification mechanism. Thus, my findings support post-formational shallowing of host craters, but there is no evidence that this occurred by tectonic uplift. At fourteen of the sixteen sites, vents occur at the crater centre.

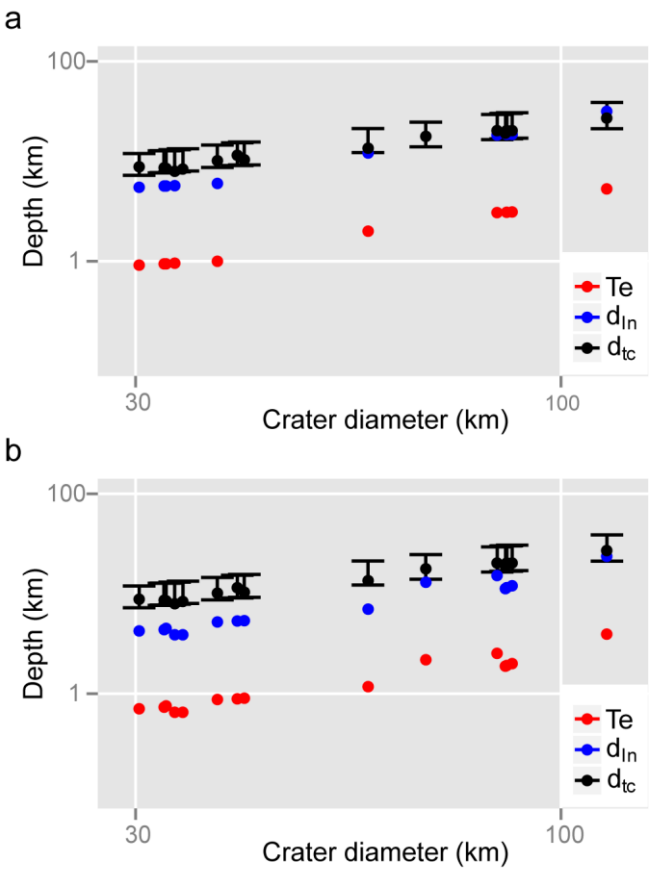


**Figure 8-4. Effective thickness (Te) of overburden consistent with (a) crater floor radius where there is convex uplift (*Thorey and Michaut* (2014) method) and (b) uplift radius (*Pollard and Johnson* (1973) method) within sampled lunar FFCs compared with the estimated depth of the transient crater below the present-day crater floor ($d_{tc}$). $d_{In}$ is 6 × Te, an estimate of intrusion depth.**

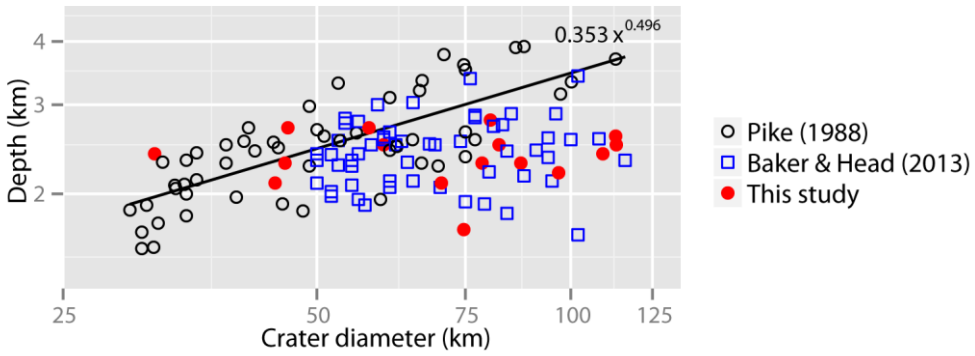


**Figure 8-5 Depth versus diameter of craters on Mercury, comparing those in this study with larger populations of complex craters measured by other authors. Black line indicates the d-D relationship observed by *Pike* (1988) for mature complex craters.**

### 8.4.3 Association with regional geological units and tectonic structures

Craters hosting pyroclastic deposits in the lunar sample set commonly superpose, are adjacent to, or are in areas annular to extensive basin-filling mare deposits. The distance to the edge of a major mare deposit ranges up to 340 km, with a mean distance of 90 km. Conversely, sites on Mercury are not commonly adjacent to morphologically young large-scale lava plains, which range from 90 to 1540 km distant, 800 km on average (Figure 8-6).

The sampled sites on Mercury are often in regions hosting many other sites of putative explosive volcanism. Seven sites overlie the relatively low-reflectance LRM substrate. This relationship is particularly apparent in an elevated, extensively thrust-faulted region centred on 136.8° E, 45.4° S, where four of the sampled craters lie within 350 km of each other, along with many other centres of putative pyroclastic volcanism (Figure 8-7). In this region, the lowest-reflectance surface material comprises the walls and proximal ejecta of large (> 80 km diameter) relatively fresh craters. The depth to which such craters excavate can be estimated as > 15 km (*Croft*, 1985), indicating that this substrate is present to considerable depth. At three of the sampled sites the crater also hosts hollows, which are rimless depressions thought to form by loss of a relatively volatile substance from the planet's surface (*Blewett et al.*, 2013; Chapter 2).

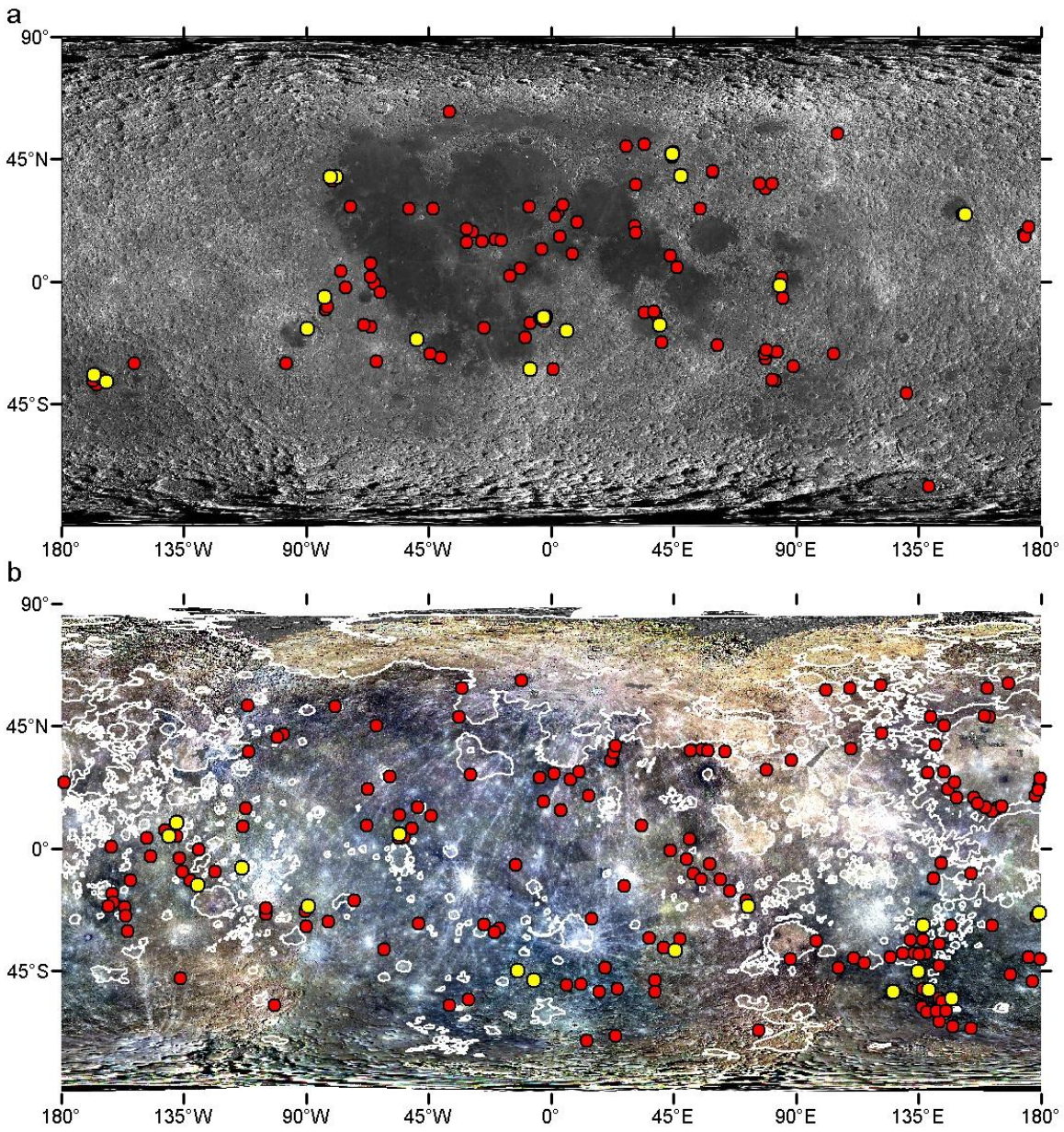


**Figure 8-6. Sampled (yellow circles) and all (red circles) sites with putative pyroclastic activity on a. the Moon and b. Mercury (white outline: extent of smooth volcanic plains (*Denevi et al.*, 2013)). Base images: LRO WAC global mosaic and MDIS global colour mosaic.**

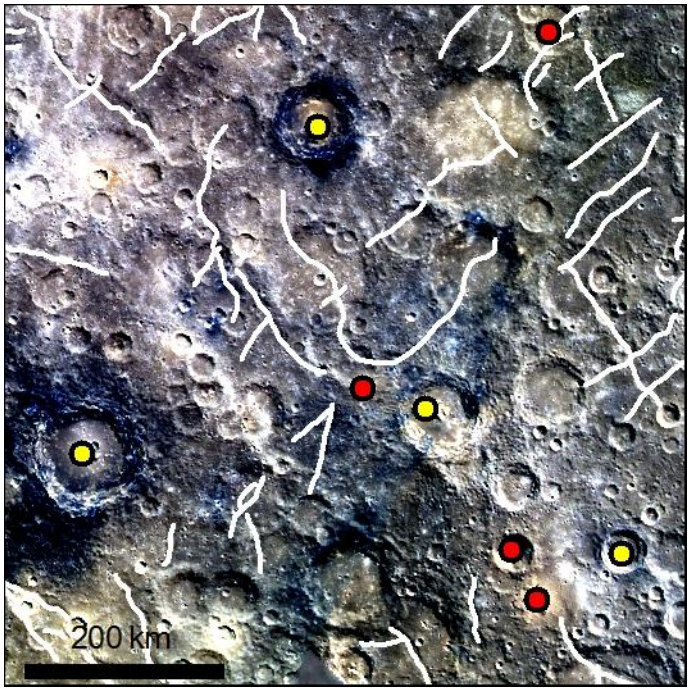


**Figure 8-7. A cluster of sites of explosive volcanism on LRM substrate on Mercury. Dots: yellow = sampled sites, red = not in sample set. White lines: contractional landforms (*Byrne et al.*, 2014) (mosaic of colour composites combining MDIS WAC images EW1012828676I, EW1012828668G and EW1012828664F, and EW0230923343I, EW0230923363G and EW0230923347F).**

## 8.5 Discussion

### 8.5.1 Scale and energy of eruption

Consistent with findings for the global population (*Kerber et al.*, 2011; Section 5.4.2.2), the maximum velocity at which pyroclasts were ejected at the sampled sites of explosive volcanism on Mercury is greater than at those on the Moon. Additionally, vents are larger on Mercury, though the higher gravity dictates that dykes should be narrower and mass fluxes lower (*Wilson and Parfitt*, 1989) than on the Moon. If the vents formed primarily through erosion of wall-rock during eruption, larger vents indicate higher eruption energy, consistent with the high ejection velocity. This in turn supports the inference, made on the basis of global dataset, of an on average higher volatile mass fraction in the released magma in explosive volcanism on Mercury than on the Moon (*Kerber et al.*, 2011; Section 5.5.3).

Volcanic vents can also form through collapse or subsidence into a magma chamber, and have been proposed to do so on Mercury (*Gillis-Davis et al.*, 2009). If this process contributed to vent-formation on both planets, the larger vent size on Mercury indicates higher volume eruption. Unfortunately, the low resolution of the topographic data on Mercury at present precludes calculation of the erupted volume; so, the importance of this process cannot be investigated. A further method by which a large vent can form is by sequential eruption at closely-spaced loci, forming a compound vent. There is evidence that this does occur on Mercury (*Rothery et al.*, 2014). If eruption were more localized at sites on Mercury, this process would lead to larger vents. However, as the summed vent volume at each site is significantly higher on Mercury than the Moon, overlapping vents on Mercury cannot be the prime explanation for the contrast in vent volume.

### 8.5.2 Implications for sub-crater magma storage on Mercury

The high incidence of floor-fracturing in complex craters hosting pyroclastic deposits on the Moon and its absence at such sites on Mercury requires explanation. Floor-fracturing on the Moon is proposed to occur due to sub-crater magmatic intrusion. An alternative hypothesis, that it occurs due to viscous relaxation (*Hall et al.*, 1981), has been found to be inconsistent with the geometry and spatial variability of most FFCs (*Wichman and Schultz*, 1995a; *Dombard and Gillis*, 2001; *Jozwiak et al.*, 2012). Therefore, an absence of floor-fracturing within complex impact craters on Mercury may simply indicate that dykes propagate directly to the surface without a period of near-surface magma storage. At sites where a small-scale pyroclastic deposit surrounds a single vent, I cannot preclude this possibility. However, there are multiple vents at five of the sampled sites, and at another there are two large vents close by in an overlapped crater (Figure 8-8). This suggests the presence of a magma reservoir in the shallow subsurface from which multiple eruptions were sourced, either in a coeval or a sequential manner. Additionally, unless Mercury's mantle is exceptionally enriched in volatiles, the high eruption velocities necessary to form the more extensive spectral anomalies by pyroclastic volcanism strongly suggest a period of storage prior to eruption, during which volatiles became concentrated through magmatic fractionation (Section 5.5.3). I

note that the maximum ballistic range indicated by the extent of putative pyroclastic deposits is not significantly larger at sites where the presence of multiple vents provides supporting evidence for pre-eruption crustal storage than at other sites. This may indicate that, as on the Moon, sub-crater storage occurs prior to eruption in all or most cases.

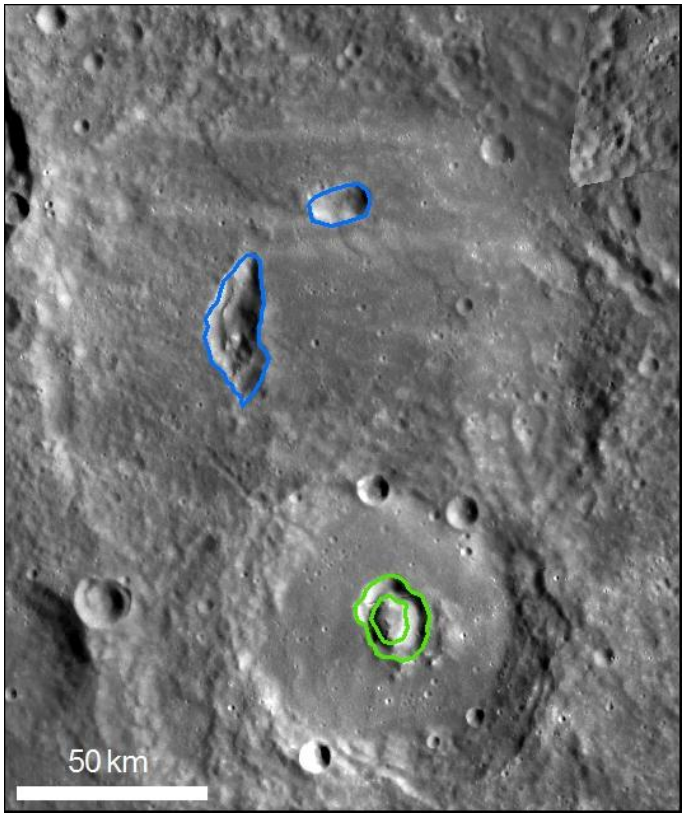


**Figure 8-8. Two intersecting craters hosting vents surrounded by putative pyroclastic deposits (-72.2° E, -19.6° N). Pit outlines: green = vent at sampled site 5023, blue = vents not within the sample set. Base image: mosaic of MDIS NAC images EN0219177174M and EN0219092124M.**

One possible contributing factor to a lack of surface deformation in response to a subsurface intrusion on Mercury is that the overburden is stronger than on the Moon. This could result from more voluminous impact melt (*Grieve and Cintala*, 1997) or less porosity (*Collins*, 2014) due to higher impact velocity and gravity, or from infilling by massive lavas prior to the proposed explosive volcanic activity. Numerical and physical modelling is necessary to determine the degree to which these factors could affect the bulk strength of sub-crater-floor materials, though the differences would need to be large if they were to account for the total lack of surface deformation seen in host craters on Mercury.

The major factor governing surface deformation above a magma body is the depth of intrusion. Deeper intrusion on Mercury would be consistent with the common localization of vents at the crater's central uplift, which are expected to be bounded by multiple high-angle, deep-going faults (*Scholz et al.*, 2002; *Senft and Stewart*, 2009; *Kenkmann et al.*, 2014). These are zones of weakness along which dyke propagation from relatively deep reservoirs to the surface would be favoured. On the basis of buoyancy alone, deeper intrusion on Mercury is not favoured. All other factors being equal, the higher gravity on Mercury means that a smaller thickness of overburden produces a given lithostatic pressure, leading to a shallower level of neutral buoyancy (LNB). Moreover, density contrasts between magmas and the crust also favour deeper intrusion on the Moon. Magmas forming picritic glasses believed to have been erupted in lunar pyroclastic eruptions are calculated to be denser (2850–3150 kg/m$^3$ (*Wieczorek et al.*, 2001; *Vander Kaaden et al.*, 2015)) than the highlands crust within which most of my sample occurs (Table E-1) (bulk density 2550 kg/m$^3$ (*Wieczorek et al.*, 2013)), rendering it necessary to invoke conditions such as excess pressure at the base of the crust (*Head and Wilson*, 1992) and superheating of the source magma (*Wieczorek et al.*, 2001) to explain the surface eruption of these magmas in the highlands. Conversely, elemental abundance data show a continuity of compositions between smooth volcanic plains and the heavily-cratered regions within which the sampled sites on Mercury occur (*Weider et al.*, 2015), supporting the inference from spectral data that these heavily-cratered surfaces may simply be ancient volcanic plains (*Murchie et al.*, 2015b). This suggests that, contrary to deeper magma storage being favoured, hot, volatile-bearing Hermean magmas are expected to be so buoyant that effusive eruption will occur without a period of sub-surface storage, except where the crust has anomalously low density. Thus in addition to the evidence presented here for deeper magma storage beneath impact craters on Mercury than on the Moon, the additional problem arises that the observed frequent occurrence of volcanic activity within impact craters (Section 5.4.1.2), where ascent should be *least* favoured (due to underlying low-density breccia), is the opposite of what is expected on the grounds of magma buoyancy.

However, the above applies only if an LNB is reached, whereas there is abundant evidence (e.g. *Takada*, 1989; *Vigneresse and Clemens*, 2000) that it is rarely reached in nature. The level of magma rise is commonly controlled by the presence of rheological or rigidity contrasts in the overburden (*Menand*, 2011); indeed the rigidity and density contrast at the base of the impact crater brecciated zone is proposed to account for the depth of sub-crater magma intrusion on the Moon. However, a deeper low-rigidity zone on Mercury does not appear to be supported. Modelling suggests that, due to higher average impact velocities, it will instead be shallower (*Cintala*, 1979; *Barnouin et al.*, 2011). Another important control on the depth of magma storage, and one that provides a good explanation for both volcanism within impact craters on Mercury and its depth relative to that on the Moon, is the regional stress field. This has been compressive on Mercury through much of the planet's history (*Strom et al.*, 1975), while compressive tectonics are observed only at a small scale and in the recent past on the Moon (*Watters et al.*, 2010). On Earth, upper-crustal magma storage is deeper in compressive than in extensional regimes (*Chaussard and Amelung*, 2014). Numerical simulations support this observation, showing that in a compressive regime, vertically-propagating dykes deflect to form a sill at greater depths than otherwise (*Maccaferri et al.*, 2011). The importance of the stress regime is greatest at the intermediate crustal levels considered here (below strength-limited very shallow levels < 3 km, and above the brittle-ductile transition). Under a compressive regime, magma chamber rupture tends to occur only where pre-existing structures are present in the overlying rock. Beneath an impact crater, the deep-going structures bounding the central uplift may act as preferential sites of chamber rupture should the magma become positively buoyant. These structures may explain why explosive volcanism occurs preferentially in impact craters on Mercury.

This begs the question of how the magma, once stalled, becomes positively buoyant, and how dykes are able to propagate to the surface despite the regional compressive stress. A major factor that enhances magma buoyancy is the presence of exsolved volatiles. As magma ascends from depth, volatiles are able to exsolve due to pressure-release. Additionally, if the magma is stored in the sub-surface, fractional crystallization of volatile-poor minerals leads

to concentration of volatiles in the remaining melt and more exsolution occurs (*Bower and Woods*, 1997; *Corsaro and Pompilio*, 2004), forming a progressively-thickening low-density foam layer at the roof of the chamber (*Parfitt et al.*, 1993). Both deeper magma storage and a compressive tectonic regime favour build-up of exsolved volatiles because they enable a magma chamber to remain stable up to a higher value of overpressure than it would under different conditions (*Currenti and Williams*, 2014).

However, because deeper storage (and thus higher pressure) inhibits the exsolution of volatiles, it may inhibit this process of exsolution, depending on the depth and volatile species involved. The evidence presented here suggests a second mode by which the volatile-content of magma can be enhanced during subsurface storage. Half of the sites sampled occur where LRM is visible at the surface. This substrate is proposed (on the basis of the apparent loss of a component of it to form hollows) to be volatile-rich (*Blewett et al.*, 2013; Section 2.5.3). The occurrence of LRM within the walls and central uplift of many impact craters on Mercury suggests that it is present at depth at many locations where it is not apparent at the surface. It is thus possible that it is the assimilation into the magma of volatiles from wall rock of this composition during subsurface magma storage that leads to an enhanced volatile concentration in the magma chamber and therefore higher eruption velocities in explosive eruptions on Mercury than on the Moon. In this model, when LRM is encountered by magma at depth, its volatile-content lends explosivity to volcanic eruptions, while when it is exposed at the surface, the volatiles are lost less dramatically to form hollows.

This hypothesis is potentially testable: if fractional crystallization plays a major role in concentration of volatiles in explosively-erupted magmas on Mercury, pyroclastic deposits will be fractionated relative to effusive lava compositions, while if the volatile-content is derived from country rock, pyroclastic deposits need not be so fractionated. Though the resolution of compositional data currently available is not sufficient to perform this test, this is expected to be remedied by the forthcoming BepiColombo mission, set to arrive at Mercury in 2024.

### 8.5.3 Implications for the Moon and other planetary bodies

The absence of floor-fracturing in complex impact craters hosting explosive volcanism on Mercury may have implications for the causes of the association of these phenomena on the Moon. As noted in Section 8.5.2, unlike Mercury, the Moon is not in a state of global compression to the degree occurring on Mercury. Thus, forces favouring deeper intrusion have not been present through most or all of the Moon's geological history and this alone may be sufficient for magmatic driving force to induce intrusion shallow enough to cause crater floor-fracturing (*Schultz*, 1976). Additionally, however, many of the sampled lunar sites hosting pyroclastic volcanism, and the majority of lunar FFCs in general, occur in the zone annular to mare-filled impact basins, which have a protracted history of flexural extension in response to the mare load. It has been proposed that this stress state has favoured magma ascent from depth in these regions (*Solomon and Head*, 1980; *McGovern et al.*, 2014). I suggest that it may additionally have favoured shallow intrusion beneath suitably-located impact craters. This would be consistent both with observations of shallow magma chambers in extensional regimes on Earth (*Chaussard and Amelung*, 2014), and with experimental results that show propagation of magma-filled cracks to higher levels than the magma's LNB where there is upwardly-increasing tensile stress (*Takada*, 1989). The calculated Te of crust overlying intrusions that could account for the deformation in the sampled lunar craters would allow magma storage within the fallback breccia lens rather than at its base. The occurrence of floor-fractured craters, as well as ancient mare pools (*Schultz and Spudis*, 1979), in the highlands far from mare basins indicates that stresses related to mare basin loading are not the only conditions capable of enabling the rise of basalts to the surface at supra-basin elevations. However, the high concentration of floor-fractured craters around basin margins is consistent with the hypothesis that these stresses favour their formation.

FFCs also occur on Mars, and are concentrated along the boundary between the southern highlands and northern plains (*Schultz and Glicken*, 1979; *Bamberg et al.*, 2014) where there is evidence for a history of extension (*Watters and McGovern*, 2006). While some of the fractures may form by fluvial processes (*Sato et al.*, 2010), others appear to have a magmatic

genesis similar to that proposed for FFCs on the Moon (*Schultz and Glicken*, 1979; *Bamberg et al.*, 2014). For example, the floor-fractured crater Lipany has abundant evidence for volcanic activity and none for fluvial activity and lies at the margin of the Isidis basin, a region with a long history of extensional tectonics (*Scott and Dohm*, 1990). This indicates that some Martian FFCs and associated volcanism may be attributable to flexural extension in a manner similar to those on the Moon.

## 8.6 Conclusions

A comparison of the scale of vents and surrounding deposits attributable to pyroclastic volcanism within complex impact craters on the Moon and Mercury indicates that eruptions had a significantly higher average energy on Mercury. On the Moon, this activity commonly occurs in craters with uplifted, fractured floors, but no such deformation is detected in host craters on Mercury. This evidence is most consistent with deeper magma storage prior to eruption on Mercury, in a magma chamber inhibited from upwards rupture by regional compression. Once stalled in such a reservoir, the eventual upward propagation of magma that results in a high-energy eruption is likely to have been promoted by concentration of volatiles by fractional crystallization and/or by incorporation of volatiles from wall rock.

The comparison with Mercury indicates that the absence of regional compressive stress was important in allowing shallow intrusions to form on the Moon. Further, because lunar FFCs are most common in circum-mare basin regions, which have been in flexural extension for much of their history due to the mare load, it is possible that it is not only the absence of compression but the action of extensional stresses that favoured shallow intrusion in these craters. The concentration of FFCs on Mars in zones that have undergone long-term regional extension is supportive of this hypothesis, and suggests that crustal extension may play a controlling role in the formation of floor-fractured craters on terrestrial bodies in general.

# Chapter 9. Looking forward: BepiColombo

## 9.1 Introduction

Observations made from the MESSENGER spacecraft have revolutionised our understanding of Mercury and have engendered numerous novel inferences presented in this thesis. Even during initial flybys of the planet, MESSENGER returned data for a larger proportion of the globe than ever seen before, and this was built-on at increasingly high spatial resolution during the twice-extended orbital mission. All of its instruments returned valuable information, giving an unexpectedly high scientific return during four Earth years in orbit. However, the budget and development timeframe for MESSENGER imposed limitations on the variety and sophistication of its instruments. Additionally, its highly elliptical orbit coupled with periherm at a high northerly latitude severely limited data coverage and resolution for the southern hemisphere. These limitations mean that many aspects of Mercury's surface composition, topography and morphology cannot be fully investigated with MESSENGER data, hindering a full understanding of the planet in general and the processes allowing volatile release at the surface in particular.

Fortunately, BepiColombo, currently in its final stages of preparation, has the potential to answer many outstanding questions (*Benkhoff et al.*, 2010). This is a joint ESA (European Space Agency) and JAXA (Japan Aerospace Exploration Agency) mission to send two spacecraft into orbit around Mercury. It is currently expected to launch in January 2017 and to begin science operations around Mercury in April or May 2024. The suites of instruments aboard the two spacecraft, the Mercury Planetary Orbiter (MPO) and Mercury Magnetospheric Orbiter (MMO), are focussed towards investigating the planet and its magnetosphere, respectively. Those on MPO are particularly suited to addressing the questions raised by this thesis. Some instruments, such as those that will obtain high-resolution images (SIMBIO-SYS HRIC), stereo images (SIMBIO-SYS STC) and visible-infrared (SIMBIO-SYS VIHI), X-ray (MIXS), gamma ray and neutron (MGNS) spectrometry, had counterparts on MESSENGER but are expected to have a greater spatial resolution, detection

resolution and range and/or coverage (Table 9-1). The thermal infrared imager, MERTIS (*Hiesinger and Helbert*, 2010), covers a part of the spectrum not detected by any instrument on MESSENGER and can provide information regarding the mineralogy and thermal properties of the surface that was previously lacking.

**Table 9-1 Comparison of the capabilities of MESSENGER and BepiColombo MPO instruments**

| Data type | MESSENGER | BepiColombo |
|---|---|---|
| Stereo imagery | Non-systematic and local, resulting in ≥ 200 m/px digital elevation models (DEMs) (*Hawkins et al.*, 2007). | Global panchromatic stereo plus colour for selected areas, 50–110 m/px resulting in ≥ 150 m/px DEMs (*Flamini et al.*, 2010). |
| High-resolution imagery | ≥ 5 m/px monochrome, ≥ 36 m/px multi-filter. Sparse coverage in 512-pixel-wide swaths at the highest resolutions. Typical values: 50 m/px NAC, 250 m/px WAC (*Hawkins et al.*, 2007). | 5–11 m/px at periapsis in 3 colours and 1 panchromatic band, ~20% of the surface in swaths 2048 pixels wide (*Flamini et al.*, 2010). |
| Altimetry | Footprint 15–100 m, 400 m along-track spacing, 30 cm precision. Northern hemisphere only (*Cavanaugh et al.*, 2007). | < 1 m vertical resolution, widespread coverage (*Thomas et al.*, 2007). |
| Visible and near-infrared spectrometry | Non-imaging, 115–600 nm and 200–1450 nm, footprint ≥ 0.1 × 3 km (*McClintock and Lankton*, 2007). | Imaging in 256 pixel-wide swaths, 400–2,000 nm. < 500 m/px globally, 100 m/px for ~10% of the surface (*Flamini et al.*, 2010). |
| Thermal infrared | Not covered. | Imaging, 7–14μm, 500 m/px globally, < 500 m/px for 5–10% of the planet. Radiometer: 7–40 μm at ≥ 280 m/px (*Hiesinger and Helbert*, 2010). |
| X-ray spectrometry | Mg, Al, Si, S, Ca and Fe. Spatial resolution as high as 100 km/px at high northern latitudes; up to ~ 500 km/px in the southern hemisphere (*Schlemm et al.*, 2007). | Also Na, P, Cl, Mn, K, Cr, Ni, O, possibly C. 70–270 km/px, with targeted imaging detections at < 10 km/px during solar flares (*Fraser et al.*, 2010; *Martindale et al.*, 2015). |
| Gamma ray and neutron spectrometry | Si, Ca, Fe, Al, Na, K, Th and U at ~ 1000 km/px. Cl in broad latitudinal bands. NS: polar volatiles. Effective in N hemisphere only. (*Goldsten et al.*, 2007; *Evans et al.*, 2015) | As for MESSENGER, at ~400 km/px. Both hemispheres (*Mitrofanov et al.*, 2010). |
| Gravity field detection | Radio science in conjunction with laser altimetry, to spherical harmonic degree and order 50 (higher resolution results not yet published) (*Mazarico et al.*, 2014). | Radio science in conjunction with laser altimetry and an Italian Spring Accelerometer to detect the non-gravitational component of MPO accelerations (*Benkhoff et al.*, 2010). |

The orbit of BepiColombo will also allow it to address the shortcomings of MESSENGER data coverage. MPO will initially reach a periherm of 480 km at 15° N, with an apoherm of 1,500 km. Current modelling suggests this will evolve considerably over the course of the mission, with periherm migrating ~28° southwards per Earth year, and periherm altitude falling to 250 km by the time it has migrated to the south pole (after about 4 years) (*Imperi et al.*, 2015). This will allow MPO to return high-resolution data from the southern hemisphere, something that MESSENGER, with its initial periherm at 60° N and apoherm of 15,200 km, was not able to provide. Low resolution at southern latitudes is a major problem when working with MESSENGER data, as it precludes direct comparisons of the prevalence of mesoscale landforms in the two hemispheres, hampers understanding of polar processes, and limits the detail in which intriguing southern hemisphere features such as tectonic structures and aligned sites of putative explosive volcanism (Chapter 6) can be investigated. Additionally, because MESSENGER's orbit precluded the use of its laser altimeter in the southern hemisphere, it is not possible to use this to constrain digital elevation models derived from stereo imagery, nor to constrain models of crustal thickness from gravity data.

In the preceding chapters, I pointed to several outstanding questions regarding volatile-release at the surface of Mercury that could potentially be addressed using data from BepiColombo. In this chapter I revisit these and other questions of interest and discuss the specific ways in which the instruments on-board BepiColombo can provide answers. In Appendix F, I provide a list of recommended targets by theme.

## 9.2 Hollows

### 9.2.1 Where (and thus how) do hollows form?

Because hollows are small-scale features, high spatial-resolution images are essential to identify them. Moreover, because they can be positively identified only where a depression, and not just a bright deposit, is visible, only images taken at a moderate solar incidence angle, in which the Sun casts moderate shadows, are suitable for their identification. As new areas were imaged at high resolution during the latter part of MESSENGER's orbital mission, the

catalogue of identifiable hollows grew, as shown in Section 2.7. Figure 9-1 shows the relation of identified hollows to MESSENGER image coverage at 180 m/pixel or better and moderate solar incidence (released by NASA's Planetary Data System up to 6th March 2015). Larger footprint size equates to lower spatial resolution, so it can be seen that imagery of mid- to high-southern latitudes is generally less favourable for the identification of hollows, and suitable images are relatively sparse in several regions of the northern hemisphere. The acquisition of high-resolution images over complementary parts of the globe by BepiColombo will potentially reveal more hollows. Where MESSENGER coverage at slightly over 180 m/pixel is relatively good, it is unlikely that large areas of hollows have been missed, and the detection of more hollows may not significantly affect the global trends observed in their occurrence. However, where it is not, considerable expanses of undocumented hollows could remain to be discovered.

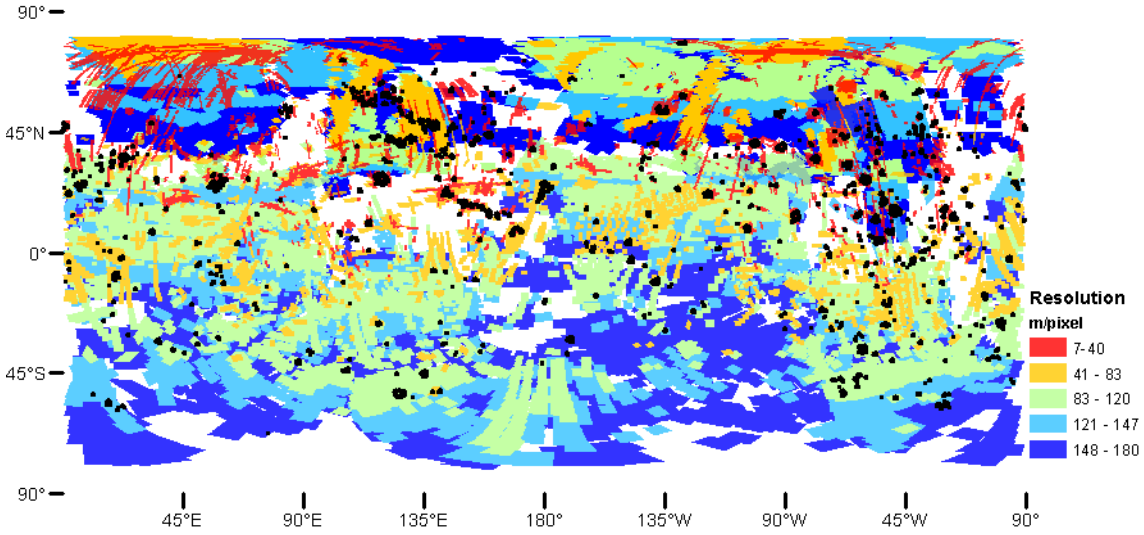


**Figure 9-1 Identified hollows in relation to MESSENGER MDIS image coverage at 180 m/pixel or better and moderate solar incidence (40–80 or 100–140°), showing gaps in the hollow distribution where there are gaps in image coverage. Black: hollows. Boxes: NAC and WAC 750 nm filter image footprints, coloured by spatial resolution.**

Identification of hollows at high-southern latitudes is particularly important for the determination of the mechanism that forms hollows. This is because some formation mechanisms can be expected to lead to latitudinal variation: if hollows form by sublimation, their spatial density is expected to decrease towards the poles, while if physical sputtering

plays a major role, this could enhance high-latitude hollow-formation (Section 2.5.1.1). The large proportion of HRP at high northern latitudes (a substrate in which hollows are not commonly found) complicates comparison of high and low latitude regions in the northern hemisphere, so knowledge of any latitudinal variation in hollow-distribution in the southern hemisphere is needed to resolve this question.

### 9.2.2 What volatile substance is lost in hollow-formation?

In Chapter 3, I characterised the visible spectrum of hollow floors, BCFDs and surrounding unhollowed surfaces at eight sites to investigate the compositional and textural changes that occur in the course of hollow-formation. Though my results are suggestive of the loss, during hollow formation, of a moderately volatile substance with higher visible spectral slope and reflectivity than the parent material, this cannot be considered conclusive with such a small sample. The sample size was restricted by necessity: these are the only sites for which MDIS WAC images are available with a high enough spatial resolution to discern the spectrum of flat hollow floors. Data from the higher-spectral-resolution MASCS could not be used at the vast majority of sites due to its large footprint size and incomplete coverage. The visible and near-infrared component of BepiColombo's SYMBIO-SYS (VIHI) and the MERTIS thermal-infrared spectrometer have the potential to fully address these issues. They cover a spectral range of 400–2000 nm and 7–14 μm, respectively, and will obtain global data at 500 m/pixel or better (up to 100 m/pixel for targeted VIHI observations). As both MERTIS and VIHI are imaging, unlike MASCS, it will also be easier to correlate morphological features with spectral data. The STC component of SYMBIO-SYS will provide additional global data at much better spatial resolutions (50 m/pixel), though a lower spectral resolution. Its 420 nm and 700 nm filters are broadly comparable to the 430 nm and 750 nm MDIS filters used to analyse spectral slope and reflectivity in Chapter 3.

As noted by *Blewett et al*. (2013), the spectral character of BCFDs could result from physical properties such as structure or grain size rather than (or in addition to) composition. Because thermal inertia is controlled by the thermophysical properties of the planetary surface (e.g. *Mellon et al.*, 2000), the radiometric component of MERTIS will be a valuable separate line of

evidence for the physical changes occurring during hollow-formation (though its > 500 m/pixel spatial resolution (*Helbert*, 2015) will limit its usefulness where hollow floor and BCFD units have small areal extent).

### 9.2.3 How does the depth of hollows vary?

Due to a lack of high-resolution topographic data and the high degree of error in shadow measurements on MDIS images, it has not yet been possible to make a rigorous comparison between the depth of hollows on different substrates, in surfaces of differing age and at different topographic locations. Such comparisons would be valuable to investigate the rate of, and propensity of different materials for, hollow-formation. For example, if there is a lower percentage of volatile material in one substrate compared to another, the lag fraction should be larger and hollow-formation should come to a halt at shallower depths. The better we understand the volatile content of a substrate, the better we can constrain the degree to which its spectrum is potentially affected by the presence of relatively volatile substances and so constrain the spectral character of those volatile substances. For small-scale landforms such as hollows, the best source of topographic data is stereo imagery. Global coverage at 50 m/pixel by STC, constrained by laser altimetry from a larger proportion of the planet than covered by MLA, should provide this information at most sites. Measuring shadow lengths on images at resolutions of up to 5 m/pixel from HRIC will allow more detailed analysis locally.

### 9.2.4 What is the relationship between pyroclastic deposits and hollows?

The common occurrence of hollows at sites of putative explosive volcanism could either result from spatial collocation due to a common generative cause (the presence of LRM near the surface (Section 8.5.2) or impact cratering (Section 2.5.2.2)), or could indicate that explosive volcanism or its deposits cause or favour hollow-formation (e.g. Section 2.5.1.2). MESSENGER images appear to indicate that the deposition of pyroclastic deposits hinders hollow development, potentially indicating that the volatile substance lost in hollow-formation is not present in pyroclastic deposits, and that it is necessary for hollow-forming volatiles to percolate through this deposit from volatile-bearing material beneath (Figure 9-2). However, this relationship is difficult to assess at the limited resolution of MESSENGER

colour images, on which the identification of pyroclastic deposits by their characteristic spectrum relies. BepiColombo's HRIC will obtain images in three colours at up to 5 m/pixel, which will be invaluable for resolving such stratigraphic relationships. As this instrument will image only 20% of the planet's surface in its primary mission, it will be important to target areas of interest. To this end, Table F-6 contains a list of high-interest targets.

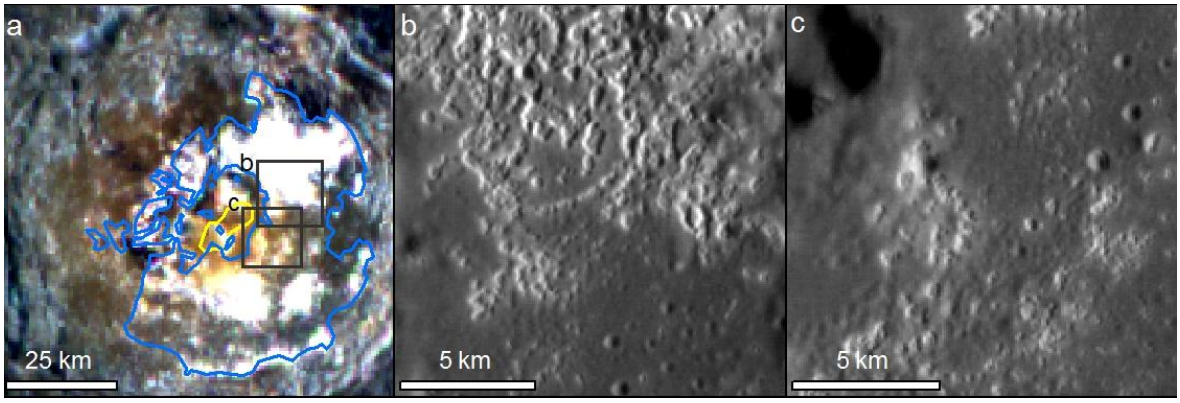


**Figure 9-2 Hollows and the putative pyroclastic deposit in Tyagaraja crater. (a) Relationship between the relatively 'red' putative pyroclastic deposit and the brighter deposits associated with hollows. (b) Hollows are dense and well-developed in the parts that lack a 'pyroclastic' spectral anomaly in MDIS, and (c) they are shallower, occurring in the rims of small impact craters, in the area where there is a relatively red spectral anomaly. Black rectangles in (a) indicate the extents of (b) and (c).**

## 9.3 Explosive volcanism

### 9.3.1 What is the composition of pyroclastic deposits and how does it vary?

The low resolution of XRS data and the difficulty of extracting compositional information from MESSENGER spectral data have hampered attempts to investigate the composition of putative pyroclastic deposits. Published elemental ratio maps derived from MESSENGER XRS data (*Weider et al.*, 2015) do not show a clear compositional anomaly across any putative pyroclastic deposit, nor can they be expected to, given the spatial resolution of this data relative to the size of putative pyroclastic deposits. For example, XRS map resolution is >1000 km/pixel across the second-largest such deposit on the planet, AP1 (Chapter 7), which has a radius of 92 km (Figure 9-3). Only higher-resolution, targeted observations at up to 180

km/pixel revealed the anomalous S/Si and Ca/S ratios at the 130–km radius NE Rachmaninoff deposit (*Nittler et al.*, 2014). Higher-resolution maps based on XRS data from MESSENGER's final year in orbit (*Frank et al.*, 2015) may, when published, provide additional compositional data for the largest putative pyroclastic deposits where these lie close to MESSENGER's periapsis and where the timing of solar flares was fortuitous. However, the near-equatorial initial periapsis of MPO, together with its generally less-elliptical orbit, will allow the Mercury Imaging X-Ray Spectrometer (MIXS) (*Fraser et al.*, 2010) to make elemental detections with a coverage and spatial resolution that was never possible for XRS. For example, AP1, which is at 3.5° S, is ideally-placed for low-altitude observation with the high-resolution imaging component, MIXS-T, near the beginning of the mission so long as a solar flare occurs as MPO traverses it. The greater spectral range of MIXS will allow detection of elements that XRS cannot, such as the volcanologically-important alkalis Na and K, and Cl, a candidate volatile to drive explosive volcanism (*Zolotov*, 2011). Its higher spectral resolution will allow it to detect iron in lower energy events than XRS is able to, and also low-abundance elements, potentially including carbon, though some spatial binning may be necessary to obtain statistically-significant results where count rates are very low (*Martindale et al.*, 2015).

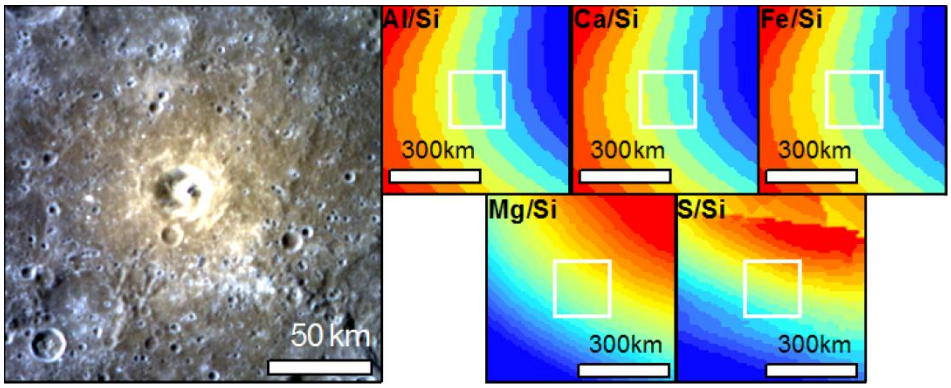


**Figure 9-3 XRS elemental ratio variations (*Weider et al.*, 2015) across the second-largest putative pyroclastic deposit on Mercury, AP1. White boxes in panels to the right indicate the extent of the image on the left.**

Together, MIXS data and spectral detections by MERTIS and SIMBIO-SYS have the potential to provide answers to major questions regarding the composition of pyroclastic deposits:

1. What proportion of a pyroclastic deposit is juvenile? It is important to answer this question before making inferences about parental magmas on the basis of compositional variability in putative pyroclastic deposits. Answering it will also help determine whether endogenic pits form primarily by erosion of the conduit, or by collapse or subsidence into the subsurface, which has implications for the style and energy of eruption and the volume of erupted material (Section 5.5.3). Spectrally, inter-deposit variability has been observed that could result from differences in the ratio of juvenile and non-juvenile material (*Goudge et al.*, 2014), as proposed for the Moon (*Gaddis et al.*, 2000). However spectra are affected not just by composition but by maturity and textural characteristics. Elemental data from MIXS, in conjunction with textural inferences based on data from the radiometric component of MERTIS, can provide constraints on spectral observations. If the spectral characteristics that are controlled by composition can be determined for these deposits, these can be compared to those characteristics in the spectra of surrounding and stratigraphically underlying substrates to determine the proportion of non-juvenile material in the deposit.

2. Do pyroclastic deposit compositions vary consistently on a regional basis? Because putative pyroclastic deposits are localised and have clear source vents, they give a better indication of the geospatial location of the source of the magma erupted than do large-scale lava plains. Any consistent difference between the composition of the juvenile component of pyroclastic deposits in, for example, the High Magnesium Region and the Caloris basin may support the hypothesis that there are chemically-isolated regions within Mercury's mantle (*Charlier et al.*, 2013), though alternative explanations, such as a varying lower-crustal component (Section 6.4), should also be considered.

3. Did magma composition vary through time? The occurrence of putative explosive volcanism within impact craters, the age of which can be inferred from their level of degradation, provides a method of assessing the maximum age of pyroclastic deposits (Section 4.3.2). Any clear temporal progression in composition globally could have implications for the secular thermal evolution of Mercury, due to the effect of high mantle temperature on the degree of partial melting possible. The line of putative pyroclastic

deposits at the south-west of the inferred ancient basin, "b54", which includes, and may be as recent as, explosive volcanic activity in Kuniyoshi crater (Section 4.4.1), would be a good location at which to investigate the composition of relatively young magmas. This is at a southern latitude where MESSENGER XRS data have very low spatial resolution, but where MIXS can potentially gather higher-resolution data. Locally, compositional changes through time could indicate geochemical evolution of a source region, for example in the Caloris basin, where putative pyroclastic deposits post-date large-scale lava plains, potentially derived from the same source.

4. Are pyroclastic deposits more fractionated than nearby effusive lavas? If magmas that are explosively erupted derive higher magmatic volatile concentrations than effusively-erupted magmas by fractionation during subsurface storage, the composition of pyroclastic deposits is expected to be more geochemically evolved than that of lava plains. A comparison of the composition of the juvenile component of pyroclastic deposits with that of nearby lavas can thus be used to test the hypothesis of subsurface (and, specifically, sub-impact crater) storage prior to explosive volcanic eruption on Mercury (Section 5.5.3).

5. Do all non-impact-excavated spectrally-red anomalies have a composition within the range of putative pyroclastic deposits? The answer to this will indicate whether spectrally-red pitted ground (Section 2.3.2.1) and uneven pits in ejecta blankets (Section 5.5.1) should be considered distinct geological phenomena, or understood within the paradigm of explosive volcanism.

### 9.3.2 How much material was ejected?

Imaging spectrometry from TIS in MERTIS and VIHI in SYMBIO-SYS will allow a robust determination of whether pyroclastic deposits are present at all sites where MASCS data are not available or have insufficient resolution to detect them, and where MDIS colour images do not show a spectral anomaly. This will resolve the question of whether endogenic pits are always associated with the ejection of material, or whether some formed purely by collapse into subsurface magma chambers (*Gillis-Davis et al.*, 2009).

As shown in Section 5.3.2, topographic data are not available with which to determine the thickness of putative pyroclastic deposits around endogenic pits at most sites. Stereo-derived DEMs based on MDIS images have large error margins and low spatial resolution, particularly when unconstrained by MLA data. Global stereo imagery at 50–200 m/pixel by STC will go a long way towards remedying this situation. Higher-resolution topographic data will not help in all cases: where pyroclastic deposits overlie an uneven surface, it will still be difficult to determine what portion of the relief was pre-existing and what results from pyroclastic deposition. However, on flat surfaces such as the impact crater floors on which such deposits commonly occur (e.g. Figure 5-7) it will be practical to determine deposit thickness and so, erupted volume. If the proportion of juvenile to non-juvenile material can be constrained using spectral and geochemical data, the deposit volume can be used to calculate erupted magma volume. This will, in turn, provide the grounds for a more nuanced consideration than hitherto possible of modes of magma production, transport and storage that can account for the high volatile concentrations implied by the deposit extent.

### 9.3.3 When did explosive volcanism occur?

Data from MESSENGER indicate that putative explosive volcanism occurred as recently as the Kuiperian period, and that it outlasted large-scale explosive volcanism (Chapter 4). This fits the picture of Mercury as a contracting planet in which propagation of magmatic dykes to the surface is increasingly inhibited in the absence of overpressure from volatiles. However, MESSENGER data are geographically incomplete and have a limited spatial resolution, rendering determination of the age relationship between explosive volcanism and other processes uncertain in many cases. High-resolution global and targeted observations from SYMBIO-SYS will be invaluable for exploring age relationships. In particular:

- Does putative explosive volcanism predate effusive volcanism at any site? This has not been observed so far, but this may be purely a result of the low resolution of the MESSENGER multispectral data, as pyroclastic deposits are not readily identified in higher-resolution monochrome MDIS NAC images. Global colour images at 50 – 200 m/pixel from STC are ideally suited to addressing this issue.

- What was the time interval between crater formation and putative explosive volcanism? Targeted three-colour observations at up to 5 m/pixel from HRIC may allow us to characterise the relative age of an impact crater and a volcanic vent within it by analysing their level of degradation relative to one another. This will indicate whether it is possible that the cratering event can trigger volcanism, or whether it is only the presence of subsurface crater-related structures that localises explosive volcanism within impact craters.

### 9.3.4 Is explosive volcanism correlated with variations in crustal thickness?

The occurrence of multiple sites of putative explosive volcanism at the thrust-faulted margins of proposed ancient impact basins raises the possibility that anomalously thick crust in these areas favours crustal melting, or mantle melting after delamination (Section 6.4). A thorough investigation of this, and of crustal thickness in other areas where putative explosive volcanism is common, requires the production of crustal thickness models at higher spatial resolutions than can be produced using MESSENGER data (*Smith et al.*, 2012; *Mazarico et al.*, 2013, 2014; *James et al.*, 2015). Higher-resolution global STC topographic data, and the higher-quality gravity data that can be obtained by combining the results of MPO's Italian Spring Accelerometer and Radio Science Experiment, should allow production of such models. These will be particularly useful for the southern hemisphere, where other evidence points to the presence of two large impact basins, but where existing models have very low spatial resolution. MESSENGER-derived crustal thickness models also indicate an area of anomalously thin crust near the south pole that is not associated with other evidence suggesting it is a basin (Figure 6-1). If confirmed by BepiColombo data, the thin crust here must be explained by either exogenic or endogenic processes.

## 9.4 The unexpected

MESSENGER delivered a host of surprising new results and it is very probable that BepiColombo will do the same. As we discovered when MESSENGER entered Mercury orbit and sent back images of hollows, higher resolution imagery does not only mean we can see

landforms we know about in more detail; it reveals the unexpected. It is probable that all of the instruments will return unforeseen results — there would be little reason to send the spacecraft if this were not so. The instrument with the highest potential for changing our understanding of Mercury is the thermal infrared spectrometer and radiometer, MERTIS, because this will gather an entirely new type of data from the planet. Variations in daytime and night-time temperature will give new insight into the physical properties of recognised units, and will reveal differences between areas that appear similar at visible wavelengths. The Thermal Emission Imaging System (THEMIS) on Mars Odyssey (*Christensen et al.*, 2004) provides an example of the potential usefulness of such an instrument: amongst a raft of other discoveries, it has revealed unexpected channels (*Mangold et al.*, 2004), expanses of bedrock (*Christensen et al.*, 2003), and south-polar water ice (*Titus et al.*, 2003) on Mars.

## 9.5 Conclusion

While MESSENGER's contribution to Hermean science has been immense, BepiColombo has the potential to take us as many steps forward again. Its less-elliptical, complementary orbit and the capabilities of its instruments are ideally-suited to addressing many of the outstanding questions that have been discussed in this thesis. The greatest anticipated advances are in our understanding of the composition of hollow-forming volatile(s) and the compositional variability through time and space of the products of explosive volcanism. Any further light that can be shed on these issues will have broad implications for the geochemical makeup and chemicophysical evolution of the planet as a whole.

# Chapter 10. Conclusions

This thesis has shown that landforms associated with the release of volatiles are widespread across the surface of Mercury. It has contributed a number of key advances in our understanding of these processes and their implications for global-scale issues such as the planet's thermal evolution and interior composition. The manner in which this work has addressed and met the aims set out in the Introduction is summarized below.

## 10.1 Global occurrence of hollows and putative explosive volcanism

I have documented 481 groups of hollows, and 183 groups of endogenic pits thought to be volcanic vents, 161 of which are surrounded by a spectral anomaly that suggests the presence of a pyroclastic deposit (Appendix A, Appendix C). Both types of landform occur globally, though they are rare in smooth volcanic plains, barring where sites of putative explosive volcanism occur at the margins of plains that infill impact basins (Sections 2.4.1 and 5.4.1.1). Locally, both hollows and putative volcanic vents most commonly occur within impact craters and are often seen in association with each other (Sections 2.4.4.1, 2.4.5 and 5.4.1.2).

The catalogues in Appendix A and Appendix C are the most complete yet produced for Mercury and are, at the time of writing, in use by other researchers internationally (e.g. *Ernst et al.*, 2015). While more hollows could potentially be discovered on the basis of MESSENGER images returned in the final months of spacecraft operation and released after September 2015, it is improbable that any undocumented hollow clusters of large areal extent remain in the parts of the globe that had previously been viewed at < 180 m/pixel. Putative vents and pyroclastic deposits are more amenable to further analysis: images obtained during that period may indicate that some of the documented endogenic pits do not result from explosive volcanism, and new spectral techniques and applications may reveal additional putative pyroclastic deposits or reclassify those documented here. Beyond this, new data with which to expand these catalogues will not be available until the commencement of BepiColombo's science operations at Mercury in 2024.

## 10.2 Hollows: the result of sublimation of lower-crustal sulfides?

### 10.2.1 Formation process

By showing a correlation between longitudinal variation in the density of hollows and mean insolation and, where mean insolation is lower, with the presence of sites of putative explosive volcanism, I have provided support for the hypothesis that hollows form primarily by sublimation of a moderately volatile substance from Mercury's surface (*Blewett et al.*, 2011) (Section 2.5.1.1).

### 10.2.2 The nature of the material lost

While the identity of the moderately volatile substance(s) lost in hollow-formation remains uncertain, I have contributed the additional constraint that its loss from materials undergoing hollow formation leads to a progressive reduction in the ratio of reflectivity across the visible spectrum, indicating that the substance lost has a steeper ('redder') spectral slope than that of the parental material (Section 3.4.2). My findings are not consistent with the loss of dark material, indicating that proposals that the low-reflectance component of Mercury's LRM regional unit is not volatile and could be e.g. graphite (*Vander Kaaden and McCubbin*, 2015), are potentially correct. Both the inferred spectral slope and overall reflectivity are consistent with loss of sulfides, which are a good candidate hollow-forming substance in light of Mercury's surface composition and inferred redox conditions (*Helbert et al.*, 2012).

### 10.2.3 The source of hollow-forming volatiles

I have shown that hollows almost always form in Low-Reflectance Material, LRM (96% of the hollowed area), either where it is the local or regional substrate (Section 2.4.6). This strongly indicates that this is the Hermean rock type that is most commonly volatile-bearing. By showing that 85% of hollow sites (96.6% of the total hollowed area) are within impact craters and their ejecta, and that the remaining sites are of small extent and are potentially within distal impact ejecta, I have provided strong support for the hypothesis that volatile-bearing material reaches the surface as a result of impact processes (*Blewett et al.*, 2011) (Section 2.5.2.1). In most cases, the specific setting of hollows suggests that LRM was

exhumed and exposed in deeply-penetrating impacts, and that continued hollow-formation was facilitated by exposure of near-surface volatile-bearing material by thrust faulting and subsequent small impacts. The recognition of a landform type not previously documented, spectrally-red pitted ground, and the presence of hollows on smooth plains superposing volatile-bearing substrates additionally support the hypothesis (*Blewett et al.*, 2013) that the hollow-forming volatile(s) is susceptible to mobilisation by hot lavas (Section 2.5.1.2).

It has been suggested that LRM forms a globally extensive part of Mercury's lower crust or lower mantle (*Ernst et al.*, 2015; *Murchie et al.*, 2015b). My findings support this by showing that some of the areas featuring the highest density of hollows could potentially be the ejecta blankets of very large ancient impact basins (Section 6.3), and by revealing dispersed hollows across a broad area where surface materials are expected to be dominated by Caloris basin ejecta (Section 2.4.4.2).

### 10.2.4 Implications

This investigation of hollows indicates the powerful effect the harsh environment in close proximity to a star can have on the geomorphology of a terrestrial planet. Moreover, the evidence presented has implications for the planet's internal composition, as it is consistent with the presence of a lower-crustal or upper mantle layer of sulfide-rich rock within Mercury. Crucially, it shows that the high concentrations of moderately volatile-substances required to form hollows occur almost exclusively in this one rock type, and so hollow-formation does not require that Mercury is, in bulk, volatile-rich. The process by which LRM formed, and how its volatile component was incorporated, is, as yet, very much open to question. Its formation by flotation during planetary differentiation (*Vander Kaaden and McCubbin*, 2015) or as a late-stage volatile-rich veneer (*Murchie et al.*, 2015b) could potentially accord with the evidence.

## 10.3 Explosive volcanism: long-lived and tectonically-controlled

### 10.3.1 The timing of explosive volcanism

I have shown compelling evidence that explosive volcanism continued until significantly later than the large-scale effusive volcanism that emplaced Mercury's smooth volcanic plains, potentially until as recently as one billion years ago (Section 4.4.1). While in some cases, stratigraphic relationships indicate explosive volcanism subsequent to effusive volcanism, the opposite relationship has not been observed. Thrust faulting and putative volcanic vents have varying cross-cutting relationships, indicating that explosive volcanism and tectonic shortening occurred contemporaneously (Section 5.4.1.2).

### 10.3.2 Processes dictating the spatial variability of explosive volcanism

The observation that sites of putative explosive volcanism cluster near both the margins of the Caloris impact basin and near the margins of other large impact basins proposed on the basis of other lines of evidence (Sections 5.4.1.1 and 6.3) suggests that basin structures play a role in the regional spatial variability of explosive volcanism. The reasons for this are, as yet, uncertain, though I have proposed magma ascent along impact-related structures (Section 5.5.2) and crustal thickening at basin margins (Section 6.4) as possible explanations.

I have shown that putative explosive volcanism very commonly (82% of cases) occurs within impact craters (Section 5.4.1.2), particularly at the crater centre (Section 7.6.1). Comparison with lunar explosive volcanism indicates that this specific localization may be favoured by magma storage at deeper levels than beneath impact craters on the Moon due to Mercury's long-lived state of crustal compression (Section 8.5.2).

### 10.3.3 Volcanic processes

The scale of the documented putative pyroclastic deposits indicate, on average, a slightly higher volatile content than erupting magmas in basaltic eruptions on Earth, and ranging up to much higher values (Section 5.5.3). I propose that these high volatile concentrations accumulate by fractional crystallisation and/or assimilation of volatiles from surrounding

volatile-bearing rocks during subsurface magma storage (Section 8.5.2), which occurs because deep-going impact-related fractures favour magma ascent and compressional forces inhibit it. These conditions, along with thickness variations in putative pyroclastic deposits (Section 5.5.1), are consistent with eruption of a mixture of large and very small particles in steady (Hawaiian) or (less probably) episodic (Strombolian) eruptions.

### 10.3.4 Implications

The longevity of explosive volcanism indicates that sufficient internal heat for melt-formation was present as recently as a billion years ago. This should be taken into account when constructing models of the planet's thermal evolution. However, the siting of the youngest-dated explosive volcanism at the margin of a proposed ancient impact basin may indicate that melt-generation was the result of crustal melting, or of mantle upwelling subsequent to delamination (Section 6.4). Thus, long-lived explosive volcanism may not require similarly long-lived mantle convection; Mercury's extant magnetic field is a stronger constraint on Mercury's interior rheology (*Hauck et al.*, 2015).

The interplay of impact cratering and tectonic compression appears to be essential to explosive volcanic activity on Mercury. Impact craters provide sub-surface conduits for the ascent of volatile-bearing magma until long after crater-formation, whereas crustal compression acts in opposition to its ascent. In so doing, however, it allows the accumulation of volatiles during subsurface magma storage, resulting, when failure occurs along crater-related fractures, in pyroclastic deposits of extraordinary extent. This indicates that, as with hollows, the concentrations of volatiles required to create the documented landforms should not be taken as evidence that Mercury's bulk composition is similarly volatile-enriched.

This work also has implications for other terrestrial bodies. I have shown that very shallow subcrater magma intrusions capable of fracturing the overlying crater floor are only possible in the absence of global contraction, and would be most favoured by crustal extension. This implies that tectonic regime may be a factor in the observed distribution of floor-fractured craters on the Moon and Mars (Section 8.5.3).

## 10.4 The big picture

To bring these findings into focus, I return to the overarching question posed at the beginning of this thesis:

> How has it been possible for concentrations of volatiles sufficient to result in hollows and pyroclastic volcanism to reach Mercury's surface over the course of its geological history, despite the absence of plate tectonics and in the state of crustal compression indicated by planet-wide thrust faulting?

It is clear on the basis of my findings that this activity does not occur simply because Mercury is so volatile enriched that volatile-driven activity at its surface is a foregone conclusion. Instead, impact cratering has introduced material to the surface from a particular volatile-bearing interior horizon of uncertain provenance, and has provided fractures up which magma has been able to ascend through the crust. Moreover, far from occurring *despite* global contraction, it appears that tectonic compression is, in large part, the *cause* of the high energy of explosive volcanism on Mercury, because it imposes a period of subsurface magma storage during which volatiles can accumulate prior to eruption. Without this condition, buoyancy would favour direct effusive eruptions such as those that formed the smooth plains (Section 8.5.2). Given Mercury's ongoing contraction (*Banks et al.*, 2012), it is thus not surprising that explosive volcanism significantly outlasted these less constricted eruptions.

## 10.5 The future

At discussed in detail in Chapter 9, the BepiColombo mission, set to begin science operations at Mercury in 2024, will bring a whole new suite of powerful instruments to bear on the outstanding questions regarding volatile-release on Mercury. I have made many specific suggestions of sites at which the scientific return will be high (Appendix F).

Beyond that, a lander (as initially planned as a third component of BepiColombo (*Grard and Balogh*, 2001)) is essential to ground-truth the remote-sensed data. Only through in-situ

observation and geochemical analysis can we convert many of the ‘may be’s and ‘could be’s that necessarily pervade the current literature into something more concrete.

# References


Amsden, A. A., H. M. Ruppel, and C. W. Hirt (1980), *SALE: A simplified ALE computer program for fluid flow at all speeds*, Los Alamos National Laboratory LA-8095, Los Alamos, NM.

Anderson, J. D., P. B. Esposito, E. L. Lau, G. B. Trager, and G. Colombo (1987), The mass, gravity field, and ephemeris of Mercury, *Icarus*, *349*(3), 337–349, doi:10.1016/0019-1035(87)90033-9.

Andrews-Hanna, J. C. (2013), The origin of the non-mare mascon gravity anomalies in lunar basins, *Icarus*, *222*(1), 159–168, doi:10.1016/j.icarus.2012.10.031.

Baker, D. M. H., and J. W. Head (2013), New morphometric measurements of craters and basins on Mercury and the Moon from MESSENGER and LRO altimetry and image data: An observational framework for evaluating models of peak-ring basin formation, *Planet. Space Sci.*, *86*, 91–116, doi:10.1016/j.pss.2013.07.003.

Bamberg, M., R. Jaumann, H. Asche, T. Kneissl, and G. G. Michael (2014), Floor-Fractured Craters on Mars – Observations and Origin, *Planet. Space Sci.*, *98*, 146–162, doi:10.1016/j.pss.2013.09.017.

Banks, M. E., T. R. Watters, R. G. Strom, S. C. Solomon, S. E. Braden, C. R. Chapman, N. G. Barlow, P. Studies, N. Air, S. Museum, S. Exploration, and H. Bombardment (2012), Stratigraphic Relationships Between Lobate Scarps and Young Impact Craters on Mercury: Implications for the Duration of Lobate Scarp Formation, *Lunar Planet. Sci. Conf.*, *43*, 2684.

Banks, M. E., C. Klimczak, Z. Xiao, T. R. Watters, R. G. Strom, S. E. Braden, C. R. Chapman, S. C. Solomon, and P. K. Byrne (2014), Duration of activity on lobate-scarp thrust faults on Mercury, *Lunar Planet. Sci. Conf.*, *45*, 2722.

Barnouin, O. S., C. E. Ernst, J. T. Heinick, S. Sugita, M. J. Cintala, D. A. Crawford, and T. Matsui (2011), Experimental results investigating the impact velocity effects on crater growth and the transient crater diameter-to-depth ratio, *Lunar Planet. Sci. Conf.*, *42*, 2258.

Barnouin, O. S., M. T. Zuber, D. E. Smith, G. A. Neumann, R. R. Herrick, J. E. Chappelow, S. L. Murchie, and L. M. Prockter (2012), The morphology of craters on Mercury: Results from MESSENGER flybys, *Icarus*, *219*(1), 414–427, doi:10.1016/j.icarus.2012.02.029.

Beck, S. L., and G. Zandt (2002), The nature of orogenic crust in the central Andes, *J. Geophys. Res.*, *107*(B10), 2230, doi:10.1029/2000JB000124.

Benkhoff, J., J. van Casteren, H. Hayakawa, M. Fujimoto, H. Laakso, M. Novara, P. Ferri, H. R. Middleton, and R. Ziethe (2010), BepiColombo—Comprehensive exploration of Mercury: Mission overview and science goals, *Planet. Space Sci.*, *58*(1-2), 2–20,

doi:10.1016/j.pss.2009.09.020.

Benz, W., W. L. Slattery, and A. G. W. Cameron (1988), Collisional stripping of Mercury's mantle, *Icarus*, *74*, 516–528, doi:10.1016/0019-1035(88)90118-2.

Benz, W., A. Anic, J. Horner, and J. A. Whitby (2007), The origin of Mercury, *Space Sci. Rev.*, *132*(2-4), 189–202, doi:10.1007/s11214-007-9284-1.

Blewett, D. T., M. S. Robinson, B. W. Denevi, J. J. Gillis-Davis, J. W. Head, S. C. Solomon, G. M. Holsclaw, and W. E. McClintock (2009), Multispectral images of Mercury from the first MESSENGER flyby: Analysis of global and regional color trends, *Earth Planet. Sci. Lett.*, *285*(3-4), 272–282, doi:10.1016/j.epsl.2009.02.021.

Blewett, D. T., N. L. Chabot, B. W. Denevi, C. M. Ernst, J. W. Head, N. R. Izenberg, S. L. Murchie, S. C. Solomon, L. R. Nittler, T. J. McCoy, Z. Xiao, D. M. H. Baker, C. I. Fassett, S. E. Braden, J. Oberst, F. Scholten, F. Preusker, and D. M. Hurwitz (2011), Hollows on Mercury: MESSENGER evidence for geologically recent volatile-related activity., *Science*, *333*(6051), 1856–9, doi:10.1126/science.1211681.

Blewett, D. T., N. L. Chabot, J. W. Head, and J. H. Johns (2012), Spectral and Morphological Studies of Mercury's Hollows, *Lunar Planet. Sci. Conf.*, *43*, 1329.

Blewett, D. T., W. M. Vaughan, Z. Xiao, N. L. Chabot, B. W. Denevi, C. M. Ernst, J. Helbert, M. D. Amore, A. Maturilli, J. W. Head, and S. C. Solomon (2013), Mercury's hollows: Constraints on formation and composition from analysis of geological setting and spectral reflectance, *J. Geophys. Res. Planets*, *118*(5), 1013–1032.

Bower, S. M., and A. W. Woods (1997), Control of magma volatile content and chamber depth on the mass erupted during explosive volcanic eruptions, *J. Geophys. Res.*, *102*(B5), 10273–10290.

Boyce, J. M., L. Wilson, P. J. Mouginis-Mark, C. W. Hamilton, and L. L. Tornabene (2012), Origin of small pits in martian impact craters, *Icarus*, *221*(1), 262–275, doi:10.1016/j.icarus.2012.07.027.

Bray, V. J., C. Atwood-Stone, and A. M. McEwen (2012), Investigating the transition from central peak to peak-ring basins using central feature volume measurements from the Global Lunar DTM 100 m, *Geophys. Res. Lett.*, *39*(21), doi:10.1029/2012GL053693.

Britt, D. T., D. K. Yeomans, K. R. Housen, and G. Consolmagno (2002), Asteroid density, porosity and structure, in *Asteroids III*, edited by W. Bottke, A. Cellino, P. Paolicchi, and R. Binzel, pp. 485–501, University of Arizona Press, Tucson.

Broadfoot, A. L., S. Kumar, M. J. S. Belton, and M. B. Mcelroy (1974), Mercury ' s Atmosphere from Mariner 10 : Preliminary Results Mercury, *Science*, *185*(4146), 166–169.

Brož, P., and E. Hauber (2012), A unique volcanic field in Tharsis, Mars: Pyroclastic cones as evidence for explosive eruptions, *Icarus*, *218*(1), 88–99, doi:10.1016/j.icarus.2011.11.030.

Brož, P., O. Čadek, E. Hauber, and A. P. Rossi (2014), Shape of scoria cones on Mars: Insights from numerical modeling of ballistic pathways, *Earth Planet. Sci. Lett.*, *406*, 14–23, doi:10.1016/j.epsl.2014.09.002.

Byrne, P. K., C. Klimczak, D. A. Williams, D. M. Hurwitz, S. C. Soloman, J. W. Head, F. Preusker, and J. Oberst (2012), An assemblage of lava flow features on Mercury, *J. Geophys. Res. Planets*, doi:10.1002/jgre.20052.

Byrne, P. K., C. Klimczak, D. A. Williams, D. M. Hurwitz, S. C. Solomon, J. W. Head, F. Preusker, and J. Oberst (2013), An assemblage of lava flow features on Mercury, *J. Geophys. Res. Planets*, *118*(6), 1303–1322, doi:10.1002/jgre.20052.

Byrne, P. K., C. Klimczak, A. M. C. Şengör, S. C. Solomon, T. R. Watters, and S. A. Hauck (2014), Mercury's global contraction much greater than earlier estimates, *Nat. Geosci.*, *7*(April), 301–307, doi:10.1038/NGEO2097.

Byrne, S., and A. P. Ingersoll (2003a), A sublimation model for martian south polar ice features., *Science*, *299*(5609), 1051–3, doi:10.1126/science.1080148.

Byrne, S., and A. P. Ingersoll (2003b), Martian climatic events on timescales of centuries: Evidence from feature morphology in the residual south polar ice cap, *Geophys. Res. Lett.*, *30*(13), 2–5, doi:10.1029/2003GL017597.

Cameron, A. G. W. (1985), The partial volatilization of Mercury, *Icarus*, *64*(2), 285–294, doi:10.1016/0019-1035(85)90204-0.

Cameron, A. G. W., B. Fegley Jr, W. Benz, and W. L. Slattery (1988), *The strange density of Mercury: Theoretical considerations*, edited by M. S. Matthews, C. Chapman, and F. Vilas, University of Arizona Press, Tucson, AZ.

Cavanaugh, J. F., J. C. Smith, X. Sun, A. E. Bartels, L. Ramos-Izquierdo, D. J. Krebs, J. F. McGarry, R. Trunzo, A. M. Novo-Gradac, J. L. Britt, J. Karsh, R. B. Katz, A. T. Lukemire, R. Szymkiewicz, D. L. Berry, J. P. Swinski, G. a. Neumann, M. T. Zuber, and D. E. Smith (2007), The Mercury Laser Altimeter instrument for the MESSENGER Mission, *Space Sci. Rev.*, *131*(1-4), 451–479, doi:10.1007/s11214-007-9273-4.

Chabot, N. L., C. Ernst, J. K. Harmon, S. L. Murchie, S. C. Solomon, D. T. Blewett, and B. W. Denevi (2013), Craters hosting radar-bright deposits in Mercury's north polar region: Areas of persistent shadow determined from MESSENGER images, *J. Geophys. Res. Planets*, *118*, 1–9, doi:10.1029/2012JE004172.

Chapman, C. R., W. J. Merline, S. Marchi, L. M. Prockter, C. I. Fassett, J. W. Head, S. C. Solomon, and Z. Xiao (2012), The young inner plains of Mercury's Rachmaninoff basin reconsidered, *Lunar Planet. Sci. Conf.*, *43*, 1607.

Charlier, B., and O. Namur (2015), Mantle sources and melting conditions for basalts on Mercury, in *MESSENGER-BepiColombo Joint Meeting*, p. 5, Berlin.

Charlier, B., T. L. Grove, and M. T. Zuber (2013), Phase equilibria of ultramafic compositions on Mercury and the origin of the compositional dichotomy, *Earth Planet. Sci. Lett.*, *363*, 50–60, doi:10.1016/j.epsl.2012.12.021.

Chase, S. C., E. D. Miner, D. Morrison, G. Münch, G. Neugebauer, and M. Schroeder (1974), Preliminary Infrared Radiometry of the Night Side of Mercury from Mariner 10, *Science*, *185*(4146), 142–145.

Chaussard, E., and F. Amelung (2014), Regional controls on magma ascent and storage in volcanic arcs, *Geochemistry, Geophys. Geosystems*, *15*(4), 1407–1418, doi:10.1002/2013GC005216.

Cheng, A. F., R. E. Johnson, S. M. Krimigis, and L. J. Lanzerotti (1987), Magnetosphere, exosphere, and surface of Mercury, *Icarus*, *71*, 430–440, doi:10.1016/0019-1035(87)90038-8.

Christensen, P. R., J. L. Bandfield, J. F. Bell, N. Gorelick, V. E. Hamilton, A. Ivanov, B. M. Jakosky, H. H. Kieffer, M. D. Lane, M. C. Malin, T. Mcconnochîe, A. S. Mcewen, H. Y. M. Jr, G. L. Mehall, J. E. Moersch, K. H. Nealson, J. W. R. Jr, M. I. Richardson, S. W. Ruff, et al. (2003), Morphology and composition of the surface of Mars: Mars Odyssey THEMIS results, *Science*, *300*(June), 2056–2062, doi: 10.1126/science.1080885.

Christensen, P. R., B. M. Jakosky, H. H. Kieffer, M. C. Malin, H. Y. McSween, K. Nealson, G. L. Mehall, S. H. Silverman, S. Ferry, M. Caplinger, and M. Ravine (2004), The Thermal Emission Imaging System (THEMIS) for the Mars 2001 Odyssey Mission, *Space Sci. Rev.*, *110*, 85–130, doi:10.1023/B:SPAC.0000021008.16305.94.

Cintala, M. J. (1979), Mercurian crater rim heights and some interplanetary comparisons, *Lunar Planet. Sci. Conf. Proc.*, *10*.

Cintala, M. J. (1992), Impact-induced thermal effects in the Lunar and Mercurian regoliths, *J. Geophys. Res. Planets*, *97*(E1), 947–973.

Cloutis, E. A., K. A. McCormack, J. F. Bell, A. R. Hendrix, D. T. Bailey, M. A. Craig, S. A. Mertzman, M. S. Robinson, and M. A. Riner (2008), Ultraviolet spectral reflectance properties of common planetary minerals, *Icarus*, *197*(1), 321–347, doi:10.1016/j.icarus.2008.04.018.

Cole, J., D. Milner, and K. Spinks (2005), Calderas and caldera structures: A review, *Earth-*

*Science Rev.*, *69*(1-2), 1–26, doi:10.1016/j.earscirev.2004.06.004.

Collins, G. S. (2014), Numerical simulations of impact crater formation with dilatancy, *J. Geophys. Res. Planets*, doi:10.1002/2014JE004708.

Collins, G. S., H. J. Melosh, and B. A. Ivanov (2004), Modeling damage and deformation in impact simulations, *Meteorit. Planet. Sci.*, *39*(2), 217–231, doi:10.1111/j.1945-5100.2004.tb00337.x.

Coombs, C. R., and B. R. Hawke (1992), Pyroclastic deposits on the western limb of the Moon, *Proc. Lunar Planet. Sci.*, *22*, 303–312.

Corsaro, R. A., and M. Pompilio (2004), Buoyancy-controlled eruption of magmas at Mt Etna, *Terra Nov.*, *16*(1), 16–22, doi:10.1046/j.1365-3121.2003.00520.x.

Crider, D., and R. M. Killen (2005), Burial rate of Mercury's polar volatile deposits, *Geophys. Res. Lett.*, *32*(12), L12201, doi:10.1029/2005GL022689.

Croft, S. K. (1985), The scaling of complex craters, *J. Geophys. Res. Solid Earth*, *90*(S02), C828–C842.

Currenti, G., and C. A. Williams (2014), Numerical modeling of deformation and stress fields around a magma chamber: Constraints on failure conditions and rheology, *Phys. Earth Planet. Inter.*, *226*, 14–27, doi:10.1016/j.pepi.2013.11.003.

Denevi, B. W., M. S. Robinson, S. C. Solomon, S. L. Murchie, D. T. Blewett, D. L. Domingue, T. J. McCoy, C. M. Ernst, J. W. Head, T. R. Watters, and N. L. Chabot (2009), The evolution of Mercury's crust: a global perspective from MESSENGER., *Science*, *324*(5927), 613–8, doi:10.1126/science.1172226.

Denevi, B. W., D. T. Blewett, D. L. Buczkowski, F. Capaccioni, M. T. Capria, M. C. De Sanctis, W. B. Garry, R. W. Gaskell, L. Le Corre, J.-Y. Li, S. Marchi, T. J. McCoy, a Nathues, D. P. O'Brien, N. E. Petro, C. M. Pieters, F. Preusker, C. a Raymond, V. Reddy, et al. (2012), Pitted terrain on Vesta and implications for the presence of volatiles., *Science*, *338*(6104), 246–9, doi:10.1126/science.1225374.

Denevi, B. W., C. M. Ernst, H. M. Meyer, M. S. Robinson, S. L. Murchie, J. L. Whitten, J. W. Head, T. R. Watters, S. C. Solomon, L. R. Ostrach, C. R. Chapman, P. K. Byrne, C. Klimczak, and P. N. Peplowski (2013), The distribution and origin of smooth plains on Mercury, *J. Geophys. Res. Planets*, *118*(5), 891–907, doi:10.1002/jgre.20075.

Dombard, A. J., and J. J. Gillis (2001), Testing the viability of topographic relaxation as a mechanism for the formation of lunar floor-fractured craters, *J. Geophys. Res.*, *106*(E11), 27901–27909.

Dzurisin, D. (1977), Mercurian bright patches: Evidence for physio-chemical alteration of

surface material?, *Geophys. Res. Lett.*, *4*(10), 383–386.

Eliason, E., C. Isbell, E. Lee, T. Becker, L. Gaddis, A. McEwen, and M. Robinson (1999), Mission to the Moon: The Clementine UVVIS Global Lunar Mosaic, PDS Volumes USA_NASA_PDS_CL_4001 through 4078, *US Geol. Surv.*

Elkins-Tanton, L. T., B. H. Hager, and T. L. Grove (2004), Magmatic effects of the lunar late heavy bombardment, *Earth Planet. Sci. Lett.*, *222*(1), 17–27, doi:10.1016/j.epsl.2004.02.017.

Ernst, C. M., S. L. Murchie, O. S. Barnouin, M. S. Robinson, B. W. Denevi, D. T. Blewett, J. W. Head, N. R. Izenberg, S. C. Solomon, and J. H. Roberts (2010), Exposure of spectrally distinct material by impact craters on Mercury: Implications for global stratigraphy, *Icarus*, *209*(1), 210–223, doi:10.1016/j.icarus.2010.05.022.

Ernst, C. M., B. W. Denevi, O. S. Barnouin, C. Klimczak, N. L. Chabot, J. W. Head, S. L. Murchie, G. a. Neumann, L. M. Prockter, M. S. Robinson, S. C. Solomon, and T. R. Watters (2015), Stratigraphy of the Caloris Basin: Implications for volcanic history and basin impact melt, *Icarus*, *250*, 413–429, doi:10.1016/j.icarus.2014.11.003.

Evans, L. G., P. N. Peplowski, E. a. Rhodes, D. J. Lawrence, T. J. McCoy, L. R. Nittler, S. C. Solomon, A. L. Sprague, K. R. Stockstill-Cahill, R. D. Starr, S. Z. Weider, W. V. Boynton, D. K. Hamara, and J. O. Goldsten (2012), Major-element abundances on the surface of Mercury: Results from the MESSENGER Gamma-Ray Spectrometer, *J. Geophys. Res.*, *117*, E00L07, doi:10.1029/2012JE004178.

Evans, L. G., P. N. Peplowski, D. S. Ebel, D. J. Lawrence, T. J. Mccoy, L. R. Nittler, R. D. Starr, S. Z. Weider, and S. C. Solomon (2014), Chlorine on the surface of Mercury: implications for Mercury's surface evolution, *Lunar Planet. Sci. Conf.*, *45*, 1794.

Evans, L. G., P. N. Peplowski, F. M. McCubbin, T. J. McCoy, L. R. Nittler, M. Y. Zolotov, D. S. Ebel, D. J. Lawrence, R. D. Starr, S. Z. Weider, and S. C. Solomon (2015), Chlorine on the Surface of Mercury: MESSENGER Gamma-Ray Measurements and Implications for the Planet's Formation and Evolution, *Icarus*, *257*, 417–427, doi:10.1016/j.icarus.2015.04.039.

Fassett, C. I., J. W. Head, D. T. Blewett, C. R. Chapman, J. L. Dickson, S. L. Murchie, S. C. Solomon, and T. R. Watters (2009), Caloris impact basin: Exterior geomorphology, stratigraphy, morphometry, radial sculpture, and smooth plains deposits, *Earth Planet. Sci. Lett.*, *285*(3-4), 297–308, doi:10.1016/j.epsl.2009.05.022.

Fassett, C. I., J. W. Head, D. M. H. Baker, M. T. Zuber, D. E. Smith, G. a. Neumann, S. C. Solomon, C. Klimczak, R. G. Strom, C. R. Chapman, L. M. Prockter, R. J. Phillips, J. Oberst, and F. Preusker (2012), Large impact basins on Mercury: Global distribution, characteristics, and modification history from MESSENGER orbital data, *J. Geophys. Res.*, *117*, E00L08,

doi:10.1029/2012JE004154.

Fegley, B., and A. G. W. Cameron (1987), A vaporization model for iron/silicate fractionation in the Mercury protoplanet, *Earth Planet. Sci. Lett.*, *82*, 207–222.

Flamini, E., F. Capaccioni, L. Colangeli, G. Cremonese, a. Doressoundiram, J. L. Josset, Y. Langevin, S. Debei, M. T. Capria, M. C. De Sanctis, L. Marinangeli, M. Massironi, E. Mazzotta Epifani, G. Naletto, P. Palumbo, P. Eng, J. F. Roig, a. Caporali, V. Da Deppo, et al. (2010), SIMBIO-SYS: The spectrometer and imagers integrated observatory system for the BepiColombo planetary orbiter, *Planet. Space Sci.*, *58*(1-2), 125–143, doi:10.1016/j.pss.2009.06.017.

Fowler, S. J., and F. J. Spera (2008), Phase equilibria trigger for explosive volcanic eruptions, *Geophys. Res. Lett.*, *35*(8), L08309, doi:10.1029/2008GL033665.

Frank, E. A., L. R. Nittler, A. H. Vorburger, S. Z. Weider, R. D. Starr, and S. C. Solomon (2015), High-resolution measurements of Mercury's surface composition with the MESSENGER X-Ray spectrometer, *Lunar Planet. Sci. Conf.*, *46*, 1949.

Fraser, G. W., J. D. Carpenter, D. a. Rothery, J. F. Pearson, A. Martindale, J. Huovelin, J. Treis, M. Anand, M. Anttila, M. Ashcroft, J. Benkoff, P. Bland, A. Bowyer, A. Bradley, J. Bridges, C. Brown, C. Bulloch, E. J. Bunce, U. Christensen, et al. (2010), The mercury imaging X-ray spectrometer (MIXS) on BepiColombo, *Planet. Space Sci.*, *58*(1-2), 79–95, doi:10.1016/j.pss.2009.05.004.

Gaddis, L. R., B. Ray, S. Robinson, and J. Herschel (2000), Compositional analyses of small lunar pyroclastic deposits using Clementine multispectral data, *J. Geophys. Res.*, *105*(1999), 4245–4262.

Gaddis, L. R., M. I. Staid, J. a Tyburczy, B. R. Hawke, and N. E. Petro (2003), Compositional analyses of lunar pyroclastic deposits, *Icarus*, *161*(2), 262–280, doi:10.1016/S0019-1035(02)00036-2.

Gaddis, L. R., L. Weller, J. Barrett, R. Kirk, M. Milazzo, J. Laura, B. R. Hawke, T. Giguere, B. Horgan, and K. Bennett (2013), "New" volcanic features in lunar, floor-fractured Oppenheimer crater, *Lunar Planet. Sci. Conf.*, *44*, 2262.

Gerdes, A., G. Worner, and A. Henk (2000), Post-collisional granite generation and HT – LP metamorphism by radiogenic heating: the Variscan South Bohemian Batholith, *J. Geol. Soc. London.*, *157*, 577–587.

Giacomini, L., M. Massironi, S. Marchi, C. I. Fassett, D. A. G., and G. Cremonese (2014), Dating a thrust system on Mercury: implications for the planet's thermal evolution, in *Volcanism and Tectonism Across the Inner Solar System*, edited by T. Platz, M. Massironi, P. K. Byrne, and H. Hiesinger, Geological Society, London, Special Publications, 269.

Gillis-Davis, J. J., D. T. Blewett, R. W. Gaskell, B. W. Denevi, M. S. Robinson, R. G. Strom, S. C. Solomon, and A. L. Sprague (2009), Pit-floor craters on Mercury: Evidence of near-surface igneous activity, *Earth Planet. Sci. Lett.*, *285*(3-4), 243–250, doi:10.1016/j.epsl.2009.05.023.

Goldsten, J. O., E. a. Rhodes, W. V. Boynton, W. C. Feldman, D. J. Lawrence, J. I. Trombka, D. M. Smith, L. G. Evans, J. White, N. W. Madden, P. C. Berg, G. a. Murphy, R. S. Gurnee, K. Strohbehn, B. D. Williams, E. D. Schaefer, C. a. Monaco, C. P. Cork, J. Del Eckels, et al. (2007), The MESSENGER Gamma-Ray and Neutron Spectrometer, *Space Sci. Rev.*, *131*(1-4), 339–391, doi:10.1007/s11214-007-9262-7.

Goudge, T. A., J. W. Head, L. Kerber, D. T. Blewett, B. W. Denevi, S. L. Murchie, N. R. Izenberg, E. Mcclintock, G. M. Holsclaw, D. L. Domingue, J. J. Gillis-Davis, Z. Xiao, R. G. Strom, S. C. Solomon, K. Gwinner, J. Helbert, R. L. Klima, W. E. McClintock, G. a. Neumann, et al. (2014), Global inventory and characterization of pyroclastic deposits on Mercury: New insights into pyroclastic activity from MESSENGER orbital data, *J. Geophys. Res. Planets*, *1325*, doi:10.1002/2013JE004480.

Grard, R., and A. Balogh (2001), Returns to Mercury: Science and mission objectives, *Planet. Space Sci.*, *49*(14-15), 1395–1407, doi:10.1016/S0032-0633(01)00081-2.

Greenland, L. P., W. I. Rose, and J. B. Stokes (1985), An estimate of gas emissions and magmatic gas content from Kilauea volcano, *Geochim. Cosmochim. Acta*, *49*(1), 125–129.

Grieve, R. A. F., and M. J. Cintala (1982), A method for estimating the initial impact conditions of terrestrial cratering events, exemplified by its application to Brent crater, Ontario, *Lunar Planet. Sci. Conf. Proc.*, *12*, 1607–1621.

Grieve, R. A. F., and M. J. Cintala (1997), Planetary differences in impact melting, *Adv. Sp. Res.*, *20*(8), 1551–1560, doi:10.1016/S0273-1177(97)00877-6.

Grott, M., D. Breuer, and M. Laneuville (2011), Thermo-chemical evolution and global contraction of mercury, *Earth Planet. Sci. Lett.*, *307*(1-2), 135–146, doi:10.1016/j.epsl.2011.04.040.

Gustafson, J. O., J. F. Bell, L. R. Gaddis, B. R. Hawke, and T. A. Giguere (2012), Characterization of previously unidentified lunar pyroclastic deposits using Lunar Reconnaissance Orbiter Camera data, *J. Geophys. Res. Planets*, *117*(E12), doi:10.1029/2011JE003893.

Hall, J. L., S. C. Solomon, and J. W. Head (1981), Lunar floor-fractured craters: Evidence for viscous relaxation of crater topography, *J. Geophys. Res.*, *86*(B10), 9537–9552.

Hare, T. M., B. A. Archinal, T. L. Becker, E. M. Gaddis, L. R., Lee, B. L. Redding, and M. R. Rosiek (2008), Clementine Mosaics Warped to ULCN 2005 Network, *Lunar Planet. Sci. Conf.*, *39*, 2337.

Hasenaka, T., and I. S. E. Carmichael (1985), The cinder cones of Michoacan-Guanajuato, Central Mexico: their age, volume and distribution, and magma discharge rate, *J. Volcanol. Geotherm. Res.*, *25*, 105–124.

Hauck, S. A., J.-L. Margot, S. C. Solomon, R. J. Phillips, C. L. Johnson, F. G. Lemoine, E. Mazarico, T. J. McCoy, S. Padovan, S. J. Peale, M. E. Perry, D. E. Smith, and M. T. Zuber (2013), The curious case of Mercury's internal structure, *J. Geophys. Res. Planets*, *118*(6), 1204–1220, doi:10.1002/jgre.20091.

Hauck, S. A., P. K. Byrne, C. L. Johnson, J.-L. Margo, E. Mazarico, S. J. Peale, R. J. Phillips, D. E. Smith, S. C. Solomon, and M. T. Zuber (2015), Mercury's interior: New views from MESSENGER, in *MESSENGER-BepiColombo Joint Meeting*, p. 44, Berlin.

Hawkins, S. E., J. D. Boldt, E. H. Darlington, R. Espiritu, R. E. Gold, B. Gotwols, M. P. Grey, C. D. Hash, J. R. Hayes, S. E. Jaskulek, C. J. Kardian, M. R. Keller, E. R. Malaret, S. L. Murchie, P. K. Murphy, K. Peacock, L. M. Prockter, R. A. Reiter, M. S. Robinson, et al. (2007), The Mercury Dual Imaging System on the MESSENGER spacecraft, *Space Sci. Rev.*, *131*(1-4), 247–338, doi:10.1007/s11214-007-9266-3.

Hawkins, S. E., S. L. Murchie, K. J. Becker, C. M. Selby, F. S. Turner, M. W. Noble, N. L. Chabot, T. H. Choo, E. H. Darlington, B. W. Denevi, D. L. Domingue, C. M. Ernst, G. M. HOLSCLAW, N. R. Laslo, W. E. McClintock, L. M. Prockter, M. S. Robinson, S. C. Solomon, and R. E. Sterner (2009), In-Flight Performance of MESSENGER's Mercury Dual Imaging System, *Proc. SPIE, Int. Soc. Opt. Eng.*, *SPIE7441*, doi:10.1117/12.826370.

Head, J. W. (1976), Lunar Volcanism in Space and Time, *Rev. Geophys. Sp. Phys.*, *14*(2), 265–300.

Head, J. W., and L. Wilson (1979), Alphonsus-type dark-halo craters: Morphology, morphometry and eruption conditions, *Lunar Planet. Sci. Conf. Proc.*, *10*, 2861–2897.

Head, J. W., and L. Wilson (1992), Lunar mare volcanism: Stratigraphy, eruption conditions, and the evolution of secondary crusts, *Geochim. Cosmochim. Acta*, *56*, 2155–2175.

Head, J. W., L. Wilson, and C. M. Weitz (2002), Dark ring in southwestern Orientale Basin: Origin as a single pyroclastic eruption, *J. Geophys. Res. Planets*, *107*(E1).

Head, J. W., S. L. Murchie, L. M. Prockter, M. S. Robinson, S. C. Solomon, R. G. Strom, C. R. Chapman, T. R. Watters, W. E. McClintock, D. T. Blewett, and J. J. Gillis-Davis (2008), Volcanism on Mercury: Evidence from the First MESSENGER flyby, *Science*, *321*, 69–72, doi:10.1126/science.1159256.

Head, J. W., S. L. Murchie, L. M. Prockter, S. C. Solomon, C. R. Chapman, R. G. Strom, T. R. Watters, D. T. Blewett, J. J. J. Gillis-Davis, C. I. Fassett, J. L. Dickson, G. a. Morgan, L. Kerber, D. M. Hurwitz, and L. R. Ostrach (2009a), Evidence for intrusive activity on Mercury

from the first MESSENGER flyby, *Earth Planet. Sci. Lett.*, *285*(3-4), 251–262, doi:10.1016/j.epsl.2009.03.007.

Head, J. W., S. L. Murchie, L. M. Prockter, S. C. Solomon, C. R. Chapman, R. G. Strom, T. R. Watters, D. T. Blewett, J. J. J. Gillis-Davis, C. I. Fassett, J. L. Dickson, G. a. Morgan, L. Kerber, D. M. Hurwitz, and L. R. Ostrach (2009b), Volcanism on Mercury: Evidence from the first MESSENGER flyby for extrusive and explosive activity and the volcanic origin of plains, *Earth Planet. Sci. Lett.*, *285*(3-4), 227–242, doi:10.1016/j.epsl.2009.03.007.

Head, J. W., S. C. Solomon, C. I. Fassett, S. L. Murchie, L. M. Prockter, M. S. Robinson, D. T. Blewett, B. W. Denevi, T. R. Watters, J. L. Whitten, T. A. Goudge, D. M. H. Baker, M. Debra, P. K. Byrne, C. Klimczak, and G. Sciences (2012), Effusive Volcanism on Mercury from MESSENGER Mission Data: Nature and Significance for Lithospheric Stress State and Mantle Convection, *Lunar Planet. Sci. Conf.*, *43*, 1451.

Head, J. W. I., L. Wilson, and C. M. Pieters (2000), Pyroclastic eruptions associated with the floor-fractured lunar farside crater Oppenheimer in the South Pole Aitken Basin, *Lunar Planet. Sci.*, (1280).

Helbert, J. (2015), Studying the surface of Mercury with BepiColombo, in *MESSENGER-BepiColombo Joint Meeting*, p. 55, Berlin.

Helbert, J., A. Maturilli, W. M. Vaughan, J. W. Head, R. L. Klima, T. David, and T. J. Mccoy (2012), Spectral Reflectance Measurements of Sulfides at the Planetary Emissivity Laboratory — Analogs for Hollow-Forming Material on Mercury?, *Lunar Planet. Sci. Conf.*, *43*, 1381.

Helbert, J., A. Maturilli, and M. D'Amore (2013), Visible and near-infrared reflectance spectra of thermally processed synthetic sulfides as a potential analog for the hollow forming materials on Mercury, *Earth Planet. Sci. Lett.*, *369-370*, 233–238, doi:10.1016/j.epsl.2013.03.045.

Hendrix, A. R., and F. Vilas (2006), The effects of space weathering at UV wavelengths: S-Class asteroids, *Astron. J.*, *132*(3), 1396–1404, doi:10.1086/506426.

Herrick, R. R., L. L. Curran, and A. T. Baer (2011), A Mariner/MESSENGER global catalog of mercurian craters, *Icarus*, *215*(1), 452–454, doi:10.1016/j.icarus.2011.06.021.

Hiesinger, H. (2003), Ages and stratigraphy of mare basalts in Oceanus Procellarum, Mare Nubium, Mare Cognitum, and Mare Insularum, *J. Geophys. Res.*, *108*(E7), 5065, doi:10.1029/2002JE001985.

Hiesinger, H., and J. Helbert (2010), The Mercury Radiometer and Thermal Infrared Spectrometer (MERTIS) for the BepiColombo mission, *Planet. Space Sci.*, *58*(1-2), 144–165, doi:10.1016/j.pss.2008.09.019.

Hiesinger, H., R. Jaumann, G. Neukum, and J. W. Head (2000), Ages of mare basalts on the lunar nearside, *J. Geophys. Res.*, *105*(E12), 29239–29275.

Hilsenrath, J. (1955), *Tables of thermal properties of gases: comprising tables of thermodynamic and transport properties of air, argon, carbon dioxide, carbon monoxide, hydrogen, nitrogen, oxygen, and steam*, U.S. Dept. of Commerce, National Bureau of Statistics, Washington.

Holsapple, K. A. (1993), The Scaling of Impact Processes in Planetary Sciences, *Annu. Rev. Earth Planet. Sci.*, *21*, 333–373.

Howard, H. T., G. L. Tyler, P. B. Esposito, J. D. Anderson, R. D. Reasenberg, I. I. Shapiro, G. Fjeldbo, a J. Kliore, G. S. Levy, D. L. Brunn, R. Dickinson, R. E. Edelson, W. L. Martin, R. B. Postal, B. Seidel, T. T. Sesplaukis, D. L. Shirley, C. T. Stelzried, D. N. Sweetnam, et al. (1974), Mercury: results on mass, radius, ionosphere, and atmosphere from mariner 10 dual-frequency radio signals., *Science*, *185*(4146), 179–180, doi:10.1126/science.185.4146.179.

Huang, J., L. Xiao, X. He, L. Qiao, J. Zhao, and H. Li. (2011), Geological characteristics and model ages of Marius Hills on the Moon, *J. Earth Sci.*, *22*, 601–609.

Hurwitz, D. M., J. W. Head, P. K. Byrne, Z. Xiao, S. C. Solomon, M. T. Zuber, D. E. Smith, and G. a. Neumann (2013), Investigating the origin of candidate lava channels on Mercury with MESSENGER data: Theory and observations, *J. Geophys. Res. Planets*, *118*(3), 471–486, doi:10.1029/2012JE004103.

Imperi, L., M. J. Mariani, and L. Iess (2015), Mercury Orbiter Radio Science Experiment (MORE): benefits from an extended mission, in *MESSENGER-BepiColombo Joint Meeting*, p. 47, Berlin.

Ivanov, B. A., and V. N. Kostuchenko (1997), Block oscillation model for impact crater collapse, *Lunar Planet. Sci.*, *28*, 1655.

Ivanov, B. A., and H. J. Melosh (2003), Impacts do not initiate volcanic eruptions: Eruptions close to the crater, *Geology*, *31*(10), 869, doi:10.1130/G19669.1.

Izenberg, N. R., R. L. Klima, S. L. Murchie, D. T. Blewett, G. M. Holsclaw, W. E. McClintock, E. Malaret, C. Mauceri, F. Vilas, A. L. Sprague, J. Helbert, D. L. Domingue, J. W. Head, T. A. Goudge, S. C. Solomon, C. A. Hibbitts, and M. D. Dyar (2014), The low-iron, reduced surface of Mercury as seen in spectral reflectance by MESSENGER, *Icarus*, *228*, 364–374, doi:10.1016/j.icarus.2013.10.023.

Izenberg, N. R., R. J. Thomas, D. T. Blewett, and L. R. Nittler (2015), Are there compositionally different types of hollows on Mercury?, *Lunar Planet. Sci. Conf.*, *46*, 1344.

James, P. B., M. T. Zuber, R. J. Phillips, and S. C. Solomon (2015), Support of long-wavelength topography on Mercury inferred from MESSENGER measurements of gravity and topography, *J. Geophys. Res. Planets*, doi:10.1002/2014JE004713.

Jenness, J. (2011), Tools for graphics and shapes: extension for ArcGIS, *Jenness Enterp.* Retrieved 26th Nov. 2012 from *http://www.jennessent.com/arcgis/shapes_graphics.htm.*

Jolliff, B. L., J. J. Gillis, L. A. Haskin, R. L. Korotev, and M. A. Wieczorek (2000), Major lunar crustal terranes: surface expression and crust-mantle origins, *J. Geophys. Res. Planets*, *105*(E2), 4197–4216.

Jozwiak, L. M., J. W. Head, M. T. Zuber, D. E. Smith, and G. A. Neumann (2012), Lunar floor-fractured craters: Classification, distribution, origin and implications for magmatism and shallow crustal structure, *J. Geophys. Res.*, *117*(E11), E11005, doi:10.1029/2012JE004134.

Jozwiak, L. M., J. W. Head, and L. Wilson (2015), Lunar floor-fractured craters as magmatic intrusions: Geometry, modes of emplacement, associated tectonic and volcanic features, and implications for gravity anomalies, *Icarus*, *248*, 424–447, doi:10.1016/j.icarus.2014.10.052.

Vander Kaaden, K. E., and F. M. McCubbin (2015), Exotic crust formation on Mercury: consequences of a shallow, FeO-poor mantle, *J. Geophys. Res. Planets*, doi:10.1002/2014JE004733.

Vander Kaaden, K. E., C. B. Agee, and F. M. McCubbin (2015), Density and compressibility of the molten lunar picritic glasses: Implications for the roles of Ti and Fe in the structures of silicate melts, *Geochim. Cosmochim. Acta*, *149*, 1–20, doi:10.1016/j.gca.2014.10.029.

Kabin, K., T. I. Gombosi, D. L. Dezeeuw, and K. G. Powell (2000), Interaction of Mercury with the Solar Wind, *Icarus*, *143*(2), 397–406, doi:10.1006/icar.1999.6252.

Kenkmann, T., M. H. Poelchau, and G. Wulf (2014), Structural geology of impact craters, *J. Struct. Geol.*, *62*, 156–182, doi:10.1016/j.jsg.2014.01.015.

Kerber, L., J. W. Head, S. C. Solomon, S. L. Murchie, D. T. Blewett, and L. Wilson (2009), Explosive volcanic eruptions on Mercury: Eruption conditions, magma volatile content, and implications for interior volatile abundances, *Earth Planet. Sci. Lett.*, *285*(3-4), 263–271, doi:10.1016/j.epsl.2009.04.037.

Kerber, L., J. W. Head, D. T. Blewett, S. C. Solomon, L. Wilson, S. L. Murchie, M. S. Robinson, B. W. Denevi, and D. L. Domingue (2011), The global distribution of pyroclastic deposits on Mercury: The view from MESSENGER flybys 1–3, *Planet. Space Sci.*, *59*(15), 1895–1909, doi:10.1016/j.pss.2011.03.020.

Kerber, L., S. Besse, J. W. Head, D. T. Blewett, T. A. Goudge, and P. Jussieu (2014), The global distribution of pyroclastic deposits on Mercury: the view from orbit, *Lunar Planet. Sci. Conf.*, *45*, 2862.

Killen, R., G. Cremonese, H. Lammer, S. Orsini, A. E. Potter, A. L. Sprague, P. Wurz, M. L. Khodachenko, H. I. M. Lichtenegger, A. Milillo, and A. Mura (2007), Processes that promote and deplete the exosphere of Mercury, *Space Sci. Rev.*, *132*(2-4), 433–509, doi:10.1007/s11214-007-9232-0.

Killen, R. M., M. Sarantos, and P. H. Reiff (2004), Space weather at Mercury, *Adv. Sp. Res.*, *33*(11), 1899–1904, doi:10.1016/j.asr.2003.02.020.

Klimczak, C., P. K. Byrne, S. C. Solomon, F. Nimmo, T. R. Watters, B. W. Denevi, C. M. Ernst, E. Maria, and L. E. Observatory (2013), The role of thrust faults as conduits for volatiles on Mercury, *Lunar Planet. Sci. Conf.*, *44*, 1390.

Kneissl, T., S. van Gasselt, and G. Neukum (2011), Map-projection-independent crater size-frequency determination in GIS environments - New software tool for ArcGIS, *Planet. Space Sci.*, *59*(11-12), 1243–1254, doi:10.1016/j.pss.2010.03.015.

Lammer, H., P. Wurz, M. R. Patel, R. Killen, C. Kolb, S. Massetti, S. Orsini, and A. Milillo (2003), The variability of Mercury's exosphere by particle and radiation induced surface release processes, *Icarus*, *166*(2), 238–247, doi:10.1016/j.icarus.2003.08.012.

Langevin, Y. (1997), The regolith of Mercury : present knowledge and implications for the Mercury Orbiter mission, *Planet. Space Sci.*, *45*(1), 31–37, doi:10.1016/S0032-0633(96)00098-0.

Lorenz, B. V. (1975), Formation of phreatomagmatic maar-diatreme volcanoes and its relevance to kimberlite diatremes, *Phys. Chem. Earth*, *9*, 17–27.

Lucchitta, B. K. (1978), *Geologic map of the north side of the Moon*, US Geological Survey, Reston.

Lucchitta, B. K., and A. G. Sanchez (1975), Crater studies in the Apollo 17 region, *Lunar Planet. Sci. Conf. Proc.*, *6*.

Lucey, P. G., and M. a. Riner (2011), The optical effects of small iron particles that darken but do not redden: Evidence of intense space weathering on Mercury, *Icarus*, *212*(2), 451–462, doi:10.1016/j.icarus.2011.01.022.

Maccaferri, F., M. Bonafede, and E. Rivalta (2011), A quantitative study of the mechanisms governing dike propagation, dike arrest and sill formation, *J. Volcanol. Geotherm. Res.*, *208*(1-2), 39–50, doi:10.1016/j.jvolgeores.2011.09.001.

Madey, T. E., B. V. Yakshinskiy, V. N. Ageev, and R. E. Johnson (1998), Desorption of alkali

atoms and ions from oxide surfaces : Relevance to origins of Na and K in atmospheres of Mercury and the Moon, *J. Geophys. Res.*, *103*(E3), 5873–5887.

Mangold, N., C. Quantin, V. Ansan, C. Delacourt, and P. Allemand (2004), Evidence for precipitation on Mars from dendritic valleys in the Valles Marineris area., *Science*, *305*(5680), 78–81, doi:10.1126/science.1097549.

Marchi, S., A. Morbidelli, and G. Cremonese (2005), Flux of meteoroid impacts on Mercury, *Astron. Astrophys.*, *431*, 1123–1127, doi:10.1051/0004-6361:20041800.

Marchi, S., S. Mottola, G. Cremonese, M. Massironi, and E. Martellato (2009), A new chronology for the Moon and Mercury, *Astron. J.*, *137*(6), 4936–4948, doi:10.1088/0004-6256/137/6/4936.

Marchi, S., M. Massironi, G. Cremonese, E. Martellato, L. Giacomini, and L. Prockter (2011), The effects of the target material properties and layering on the crater chronology: The case of Raditladi and Rachmaninoff basins on Mercury, *Planet. Space Sci.*, *59*(15), 1968–1980, doi:10.1016/j.pss.2011.06.007.

Marchi, S., C. R. Chapman, C. I. Fassett, J. W. Head, W. F. Bottke, and R. G. Strom (2013), Global resurfacing of Mercury 4.0–4.1 billion years ago by heavy bombardment and volcanism, *Nature*, *499*(7456), 59–61, doi:10.1038/nature12280.

Martindale, A., M. Alcacera, S. Aschauer, A. Balado, C. Bicknell, O. Blake, and Emma Bunce (2015), Future observations of Mercury with BepiColombo's Mercury Imaging X-ray Spectrometer (MIXS), in *MESSENGER-BepiColombo Joint Meeting*, p. 49, Berlin.

Massironi, M., G. Cremonese, S. Marchi, E. Martellato, S. Mottola, and R. J. Wagner (2009), Mercury's geochronology revised by applying Model Production Function to Mariner 10 data: Geological implications, *Geophys. Res. Lett.*, *36*(L21204), L21204, doi:10.1029/2009GL040353.

Mazarico, E., S. J. Goossens, F. G. Lemoine, D. E. Smith, M. T. Zuber, G. A. Neumann, M. H. Torrence, and S. C. Solomon (2013), The gravity field of Mercury derived from two years of MESSENGER data, *Lunar Planet. Sci. Conf.*, *44*, 2429.

Mazarico, E., A. Genova, S. Goossens, F. G. Lemoine, G. a. Neumann, M. T. Zuber, D. E. Smith, and S. C. Solomon (2014), The gravity field, orientation, and ephemeris of Mercury from MESSENGER observations after three years in orbit, *J. Geophys. Res. Planets*, *119*(12), 2417–2436, doi:10.1002/2014JE004675.

McClintock, W. E., and M. R. Lankton (2007), The Mercury Atmospheric and Surface Composition Spectrometer for the MESSENGER Mission, *Space Sci. Rev.*, *131*(1-4), 481–521, doi:10.1007/s11214-007-9264-5.

McGetchin, T. R., M. Settle, and B. A. Chouet (1974), Cinder cone growth modeled after Northeast Crater, Mount Etna, Sicily, *J. Geophys. Res.*, *79*(23), 3257–3272, doi:10.1029/JB079i023p03257.

McGovern, P. J., and M. M. Litherland (2011), Lithospheric stress and basaltic magma ascent on the Moon, with implications for large volcanic provinces and edifices, *Lunar Planet. Sci. Conf.*, *42*, 2587.

McGovern, P. J., W. S. Kiefer, Y. Kramer, M. T. Zuber, J. C. Andrews-Hanna, and J. W. H. III (2014), Magma ascent at lunar impact basins: effects of lithospheric tectonic stress gradients, brittle failure, and volatile generation, *Lunar Planet. Sci. Conf.*, *45*, 2771.

Mellon, M., B. M. Jackosky, H. H. Kieffer, and P. R. Christensen (2000), High-resolution thermal inertia mapping from the Mars Global Surveyor Thermal Emission Spectrometer, *Icarus*, *148*, 437–455, doi:10.1006/icar.2000.6503.

Melosh, H. J. (1989), *Impact Cratering: A Geologic Process*, Oxford University Press, New York.

Melosh, H. J., and W. B. McKinnon (1988), The Tectonics of Mercury, in *Mercury*, edited by F. Villas, C. R. Chapman, and M. S. Matthews, pp. 374–400, University of Arizona Press, Tucson, AZ.

Melosh, H. J., E. V. Ryan, and E. Asphaug (1992), Dynamic fragmentation in impacts: Hydrocode simulation of laboratory impacts, *J. Geophys. Res.*, *97*, 14735–14759.

Melosh, H. J., A. M. Freed, B. C. Johnson, D. M. Blair, S. C. Solomon, M. A. Wieczorek, and M. T. Zuber (2013), The origin of lunar mascon basins, *Science*, *340*(June), 1552–1556, doi:10.1126/science.1235768.

Menand, T. (2011), Physical controls and depth of emplacement of igneous bodies: A review, *Tectonophysics*, *500*(1-4), 11–19, doi:10.1016/j.tecto.2009.10.016.

Metrich, N., and P. J. Wallace (2008), Volatile abundances in basaltic magmas and their degassing paths tracked by melt inclusions, *Rev. Mineral. Geochemistry*, *69*(1), 363–402, doi:10.2138/rmg.2008.69.10.

Michael, G. G., and G. Neukum (2010), Planetary surface dating from crater size – frequency distribution measurements : Partial resurfacing events and statistical age uncertainty, *Earth Planet. Sci. Lett.*, *294*(3-4), 223–229, doi:10.1016/j.epsl.2009.12.041.

Michael, G. G., T. Platz, T. Kneissl, and N. Schmedemann (2012), Planetary surface dating from crater size–frequency distribution measurements: Spatial randomness and clustering, *Icarus*, *218*(1), 169–177, doi:10.1016/j.icarus.2011.11.033.

Michel, N. C., S. A. Hauck, S. C. Solomon, R. J. Phillips, J. H. Roberts, and M. T. Zuber (2013), Thermal evolution of Mercury as constrained by MESSENGER observations, *J. Geophys.*

*Res. Planets*, *118*(5), 1033–1044, doi:10.1002/jgre.20049.

Mitrofanov, I. G., a. S. Kozyrev, a. Konovalov, M. L. Litvak, a. a. Malakhov, M. I. Mokrousov, a. B. Sanin, V. I. Tret'ykov, a. V. Vostrukhin, Y. I. Bobrovnitskij, T. M. Tomilina, L. Gurvits, and a. Owens (2010), The Mercury Gamma and Neutron Spectrometer (MGNS) on board the Planetary Orbiter of the BepiColombo mission, *Planet. Space Sci.*, *58*, 116–124, doi:10.1016/j.pss.2009.01.005.

Mohit, P. S., and R. J. Phillips (2006), Viscoelastic evolution of lunar multiring basins, *J. Geophys. Res. E Planets*, *111*(12001), doi:10.1029/2005JE002654.

Moran, P. A. P. (1950), Notes on continuous stochastic phenomena, *Biometrika*, *37*(1-2), 17–23.

Moratto, S. Z. M., M. J. Broxton, R. A. Beyer, M. Lundy, and K. Husmann (2010), Ames Stereo Pipeline, NASA's open source automated stereogrammetry, *Lunar Planet. Sci. Conf.*, *41*, 2364.

Mura, A., P. Wurz, H. I. M. Lichtenegger, H. Schleicher, H. Lammer, D. Delcourt, A. Milillo, S. Orsini, S. Massetti, and M. L. Khodachenko (2009), The sodium exosphere of Mercury: Comparison between observations during Mercury's transit and model results, *Icarus*, *200*(1), 1–11, doi:10.1016/j.icarus.2008.11.014.

Murchie, S. L., R. L. Klima, B. W. Denevi, C. M. Ernst, M. R. Keller, D. L. Domingue, D. T. Blewett, N. L. Chabot, C. D. Hash, E. Malaret, N. R. Izenberg, F. Vilas, L. R. Nittler, J. J. Gillis-Davis, and J. W. Head (2015a), Orbital multispectral mapping of Mercury by MESSENGER: evidence for the origins of plains units and low-reflectance material, *Lunar Planet. Sci. Conf.*, *46*, 1606.

Murchie, S. L., R. L. Klima, B. W. Denevi, C. M. Ernst, M. R. Keller, D. L. Domingue, D. T. Blewett, N. L. Chabot, C. D. Hash, E. Malaret, N. R. Izenberg, F. Vilas, L. R. Nittler, J. J. Gillis-Davis, J. W. Head, and S. C. Solomon (2015b), Orbital multispectral mapping of Mercury with the MESSENGER Mercury Dual Imaging System: Evidence for the origins of plains units and low-reflectance material, *Icarus*, *254*, 287–305, doi:10.1016/j.icarus.2015.03.027.

Murray, B. C., R. G. Strom, N. J. Trask, and D. E. Gault (1975), Surface history of Mercury: Implications for terrestrial planets, *J. Geophys. Res.*, *80*(17), 2508–2514, doi:10.1029/JB080i017p02508.

Ness, N. F., K. W. Behannon, R. P. Lepping, Y. C. Whang, and K. H. Schatten (1974), Magnetic Field Observations near Mercury : Preliminary Results from Mariner 10, *Science*, *185*(4146), 151–160.

Neukum, G., J. Oberst, H. Ho, R. Wagner, and B. A. Ivanov (2001), Geologic evolution and cratering history of Mercury, *Planet. Space Sci.*, *49*, 1507–1521, doi:10.1016/S0032-

0633(01)00089-7.

Neumann, G. a., M. T. Zuber, D. E. Smith, and F. G. Lemoine (1996), The lunar crust: Global structure and signature of major basins, *J. Geophys. Res. Planets*, *101*(E7), 16841–16863, doi:10.1029/96JE01246.

Newcomb, S. (1907), The Optical and Psychological Principles Involved in the Interpretation of the So-Called Canals of Mars, *Astrophys. J.*, *26*, 1–17.

Nittler, L. R., R. D. Starr, S. Z. Weider, T. J. McCoy, W. V Boynton, D. S. Ebel, C. M. Ernst, L. G. Evans, J. O. Goldsten, D. K. Hamara, D. J. Lawrence, R. L. McNutt, C. E. Schlemm, S. C. Solomon, and A. L. Sprague (2011), The major-element composition of Mercury's surface from MESSENGER X-ray spectrometry, *Science*, *333*(6051), 1847–50, doi:10.1126/science.1211567.

Nittler, L. R., S. Z. Weider, R. D. Starr, E. J. Crapster-pregont, D. S. Ebel, and S. C. Solomon (2013), Mapping major element abundances on Mercury's surface with MESSENGER X-Ray Spectrometer data, *Lunar Planet. Sci. Conf.*, *44*, 2458.

Nittler, L. R., S. Z. Weider, R. D. Starr, B. W. Denevi, C. M. Ernst, T. A. Goudge, J. W. Head, J. Helbert, L. Rachel, T. J. Mccoy, and S. C. Solomon (2014), Sulfur-depleted composition of Mercury's largest pyroclastic deposit: implications for explosive volcanism and surface reflectance on the innermost planet, *Lunar Planet. Sci. Conf.*, *45*, 1391.

Parfitt, E. A., L. Wilson, and J. W. Head (1993), Basaltic magma reservoirs: Factors controlling their rupture characteristics and evolution, *J. Volcanol. Geotherm. Res.*, *55*(1-2), 1–14, doi:10.1016/0377-0273(93)90086-7.

Pearson, K. (1985), Notes on regression and inheritance in the case of two parents, *Proc. R. Soc. London*, *58*, 240–242.

Peplowski, P. N., L. G. Evans, S. a Hauck, T. J. McCoy, W. V Boynton, J. J. Gillis-Davis, D. S. Ebel, J. O. Goldsten, D. K. Hamara, D. J. Lawrence, R. L. McNutt, L. R. Nittler, S. C. Solomon, E. a Rhodes, A. L. Sprague, R. D. Starr, and K. R. Stockstill-Cahill (2011), Radioactive elements on Mercury's surface from MESSENGER: Implications for the planet's formation and evolution., *Science*, *333*, 1850–2, doi:10.1126/science.1211576.

Peplowski, P. N., D. J. Lawrence, E. a. Rhodes, A. L. Sprague, T. J. McCoy, B. W. Denevi, L. G. Evans, J. W. Head, L. R. Nittler, S. C. Solomon, K. R. Stockstill-Cahill, and S. Z. Weider (2012), Variations in the abundances of potassium and thorium on the surface of Mercury: Results from the MESSENGER Gamma-Ray Spectrometer, *J. Geophys. Res. Planets*, *117*(E00L04), doi:10.1029/2012JE004141.

Peplowski, P. N., L. G. Evans, K. R. Stockstill-Cahill, D. J. Lawrence, J. O. Goldsten, T. J. McCoy, L. R. Nittler, S. C. Solomon, A. L. Sprague, R. D. Starr, and S. Z. Weider (2014), Enhanced

sodium abundance in Mercury's north polar region revealed by the MESSENGER Gamma-Ray Spectrometer, *Icarus*, *228*, 86–95, doi:10.1016/j.icarus.2013.09.007.

Peplowski, P. N., D. J. Lawrence, L. G. Evans, R. L. Klima, D. T. Blewett, J. O. Goldsten, S. L. Murchie, T. J. McCoy, L. R. Nittler, S. C. Solomon, R. D. Starr, and S. Z. Weider (2015), Constraints on the abundance of carbon in near-surface materials on Mercury: Results from the MESSENGER Gamma-Ray Spectrometer, *Planet. Space Sci.*, *108*, 98–107, doi:10.1016/j.pss.2015.01.008.

Pierazzo, E., and G. Collins (2004), A brief introduction to hydrocode modeling of impact cratering, in *Cratering in Marine Environments and on Ice*, edited by H. Dypvik, M. J. Burchell, and P. Claeys, pp. 323–340, Springer, Berlin Heidelberg.

Pierazzo, E., N. Artemieva, E. Asphaug, E. C. Baldwin, J. Cazamias, R. Coker, G. S. Collins, D. a. Crawford, T. Davison, D. Elbeshausen, K. a. Holsapple, K. R. Housen, D. G. Korycansky, and K. Wünnemann (2008), Validation of numerical codes for impact and explosion cratering: Impacts on strengthless and metal targets, *Meteorit. Planet. Sci.*, *43*(12), 1917–1938, doi:10.1111/j.1945-5100.2008.tb00653.x.

Pieters, C. M., S. Tompkins, J. W. Head, and P. C. Hess (1997), Mineralogy of the mafic anomaly in the South Pole-Aitken Basin: Implications for excavation of the lunar mantle, *Geophys. Res. Lett.*, *24*(15), 1903–1906.

Pike, R. J. (1980), Geometric interpretation of lunar craters, *US Geol. Soc. Prof. Pap. 1046 -C*, C1–C77.

Pike, R. J. (1988), Geomorphology of impact craters on Mercury, in *Mercury*, edited by F. Vilas, C. R. Chapman, and M. S. Matthews, pp. 165–273, University of Arizona Press, Tucson, AZ.

Pollard, D. D., and A. M. Johnson (1973), Mechanics of growth of some laccolithic intrusions in the Henry Mountains, Utah, II. Bending and failure of overburden layers and sill formation, *Tectonophysics*, *18*, 311–354.

Potter, A. E. (1995), Chemical sputtering could produce solium vapor and ice on Mercury, *Geophys. Res. Lett.*, *22*(23), 3289–3292.

Prockter, L. M., C. M. Ernst, B. W. Denevi, C. R. Chapman, J. W. Head, C. I. Fassett, W. J. Merline, S. C. Solomon, T. R. Watters, R. G. Strom, G. Cremonese, S. Marchi, and M. Massironi (2010), Evidence for young volcanism on Mercury from the third MESSENGER flyby, *Science*, *329*(5992), 668–671, doi:10.1126/science.1188186.

Re, C., R. Roncella, G. Forlani, G. Cremonese, and G. Naletto (2012), Evaluation of area-based image matching applied to DTM generation with HIRISE images, *Int. Arch. Photogramm. Remote Sens. Spat. Inf. Sci.*, *39*(Part IV/7), 209–214.

Riner, M. A., and P. G. Lucey (2012), Spectral effects of space weathering on Mercury: The role of composition and environment, *Geophys. Res. Lett.*, *39*, L12201, doi:10.1029/2012GL052065.

Riner, M. A., P. G. Lucey, S. J. Desch, and F. M. McCubbin (2009), Nature of opaque components on Mercury: Insights into a Mercurian magma ocean, *Geophys. Res. Lett.*, *36*(L02201), doi:10.1029/2008GL036128.

Rivera-Valentin, E. G., and A. C. Barr (2014), Impact-induced compositional variations on Mercury, *Earth Planet. Sci. Lett.*, *391*, 234–242, doi:10.1016/j.epsl.2014.02.003.

Roberts, J. H., and O. S. Barnouin (2012), The effect of the Caloris impact on the mantle dynamics and volcanism of Mercury, *J. Geophys. Res.*, *117*(E2), 1–15, doi:10.1029/2011JE003876.

Robinson, M. S., S. L. Murchie, D. T. Blewett, D. L. Domingue, S. E. Hawkins, J. W. Head, G. M. Holsclaw, W. E. McClintock, T. J. McCoy, R. L. McNutt, L. M. Prockter, S. C. Solomon, and T. R. Watters (2008), Reflectance and color variations on Mercury: regolith processes and compositional heterogeneity., *Science*, *321*(5885), 66–9, doi:10.1126/science.1160080.

Rothery, D., L. Marinangeli, M. Anand, J. Carpenter, U. Christensen, I. a. Crawford, M. C. De Sanctis, E. M. Epifani, S. Erard, A. Frigeri, G. Fraser, E. Hauber, J. Helbert, H. Hiesinger, K. Joy, Y. Langevin, M. Massironi, A. Milillo, I. Mitrofanov, et al. (2010), Mercury's surface and composition to be studied by BepiColombo, *Planet. Space Sci.*, *58*(1-2), 21–39, doi:10.1016/j.pss.2008.09.001.

Rothery, D. A. (2015), *Planet Mercury: from pale pink dot to dynamic world*, Springer, Cham, Switzerland.

Rothery, D. A., and M. Massironi (2013), A spectrum of tectonised basin edges on Mercury, *Lunar Planet. Sci. Conf.*, *44*, 1175.

Rothery, D. A., R. J. Thomas, and L. Kerber (2014), Prolonged eruptive history of a compound volcano on Mercury: volcanic and tectonic implications, *Earth Planet. Sci. Lett.*, *385*, 59–67, doi:10.1016/j.epsl.2013.10.023.

Sandner, W. (1963), *The planet Mercury*, Faber and Faber, London.

Sarantos, M., R. M. Killen, and D. Kim (2007), Predicting the long-term solar wind ion-sputtering source at Mercury, *Planet. Space Sci.*, *55*(11), 1584–1595, doi:10.1016/j.pss.2006.10.011.

Sato, H., K. Kurita, and D. Baratoux (2010), The formation of floor-fractured craters in Xanthe Terra, *Icarus*, *207*(1), 248–264, doi:10.1016/j.icarus.2009.10.023.

Schlemm, C. E., R. D. Starr, G. C. Ho, K. E. Bechtold, S. a. Hamilton, J. D. Boldt, W. V. Boynton, W.

Bradley, M. E. Fraeman, R. E. Gold, J. O. Goldsten, J. R. Hayes, S. E. Jaskulek, E. Rossano, R. a. Rumpf, E. D. Schaefer, K. Strohbehn, R. G. Shelton, R. E. Thompson, et al. (2007), The X-Ray Spectrometer on the MESSENGER Spacecraft, *Space Sci. Rev.*, *131*(1-4), 393–415, doi:10.1007/s11214-007-9248-5.

Scholz, C. A., T. Karp, K. M. Brooks, P. Y. O. Milkereit, Bernd, Amoako, and J. A. Arko (2002), Pronounced central uplift identified in the Bosumtwi impact structure, Ghana, using multichannel seismic reflection data, *Geology*, *30*(10), 939–942.

Schultz, P. H. (1976), Floor-fractured lunar craters, *Moon*, *15*, 241–273, doi:10.1007/BF00562240.

Schultz, P. H., and H. Glicken (1979), Impact crater and basin control of igneous processes on Mars, *J. Geophys. Res.*, *84*(9), 8033–8047.

Schultz, P. H., and P. D. Spudis (1979), Evidence for ancient mare volcanism, *Proc. Lunar Planet. Sci. Conf.*, *10*, 2899–2918.

Schultz, R. A. (1993), Brittle Strength of Basaltic Rock Masses with Applications to Venus, *J. Geophys. Res.*, *98*(E6), 10883–10895, doi:10.1029/93JE00691.

Schultz, R. A. (2000), Localization of bedding plane slip and backthrust faults above blind thrust faults: Keys to wrinkle ridge structure, *J. Geophys. Res.*, *105*(E5), 12035–12052.

Scott, D. H., and J. M. Dohm (1990), Chronology and global distribution of fault and ridge systems on Mars, *Proc. 20th Lunar Planet. Sci. Conf.*, 487–501.

Scott, D. H., & McCauley, J. F. (1977), *I-1034 Geologic map of the west side of the Moon*, US Geological Survey, Reston.

Senft, L. E., and S. T. Stewart (2009), Dynamic fault weakening and the formation of large impact craters, *Earth Planet. Sci. Lett.*, *287*(3-4), 471–482, doi:10.1016/j.epsl.2009.08.033.

Sibson, R. H., F. Robert, and K. H. Poulsen (1988), High-angle reverse faults, fluid-pressure cycling, and mesothermal gold-quartz deposits, *Geology*, *16*, 551–555.

Siscoe, G., and L. Christopher (1975), Variations in the solar wind stand-off distance at Mercury, *Geophysical*, *2*(4), 158–160.

Slavin, J. A., B. J. Anderson, D. N. Baker, M. Benna, S. A. Boardsen, G. Gloeckler, R. E. Gold, G. C. Ho, H. Korth, S. M. Krimigis, R. L. McNutt, L. R. Nittler, J. M. Raines, M. Sarantos, D. Schriver, S. C. Solomon, R. D. Starr, P. M. Trávnícek, and T. H. Zurbuchen (2010), MESSENGER observations of extreme loading and unloading of Mercury's magnetic tail., *Science*, *329*(5992), 665–8, doi:10.1126/science.1188067.

Smith, D. E., M. T. Zuber, R. J. Phillips, S. C. Solomon, S. a Hauck, F. G. Lemoine, E. Mazarico, G.

A. Neumann, S. J. Peale, J.-L. Margot, C. L. Johnson, M. H. Torrence, M. E. Perry, D. D. Rowlands, S. Goossens, J. W. Head, and A. H. Taylor (2012), Gravity field and internal structure of Mercury from MESSENGER, *Science*, *336*(6078), 214–7, doi:10.1126/science.1218809.

Solomon, S. C., and J. W. Head (1980), Lunar Mascon Basins: Lava Filling, Tectonics, and Evolution of the Lithosphere, *Rev. Geophys. Sp. Phys.*, *18*(1), 107–141.

Spera, F. J. (2000), Physical properties of magma, in *he encyclopedia of volcanoes*, edited by H. Sigurdsson, B. Houghton, S. McNutt, H. Rymer, and J. Stix, pp. 171–190, Academic Press, New York.

Spudis, P. D. (1989), Young dark mantle deposits on the Moon, in *Workshop on Lunar Volcanic Glasses: Scientific and Resource Potential*, edited by J. W. D. and G. H. Heiken, p. 60, Lunar and Planetary Institute, Houston, TX.

Spudis, P. D., and J. E. Guest (1988), Stratigraphy and geologic history of Mercury, in *Mercury*, edited by F. Vilas, C. R. Chapman, and M. S. Matthews, pp. 118–164, Unversity of Arizona Press, Tucson, AZ.

Strom, R. G. (1987), *Mercury: The elusive planet*, Smithsonian Institution Press, Washington, DC.

Strom, R. G., and A. L. Sprague. (2003), *Exploring Mercury: the iron planet*, Springer Praxis Books / Space Exploration.

Strom, R. G., N. J. Trask, and J. E. Guest (1975), Tectonism and volcanism on Mercury, *J. Geophys. Res.*, *80*(17), 2478–2507, doi:10.1029/JB080i017p02478.

Strom, R. G., C. R. Chapman, W. J. Merline, S. C. Solomon, and J. W. Head (2008), Mercury cratering record viewed from MESSENGER's first flyby, *Science*, *321*(5885), 79–81, doi:10.1126/science.1159317.

Strom, R. G., M. E. Banks, C. R. Chapman, C. I. Fassett, J. A. Forde, J. W. Head, W. J. Merline, L. M. Prockter, and S. C. Solomon (2011), Mercury crater statistics from MESSENGER flybys: Implications for stratigraphy and resurfacing history, *Planet. Space Sci.*, *59*(15), 1960–1967, doi:10.1016/j.pss.2011.03.018.

Stuart-Alexander, D. E. (1978), *I-1047 Geologic map of the central far side of the Moon*, US Geological Survey, Reston.

Tait, S., C. Jaupart, and S. Vergniolle (1989), Pressure, gas content and eruption periodicity of a shallow, crystallising magma chamber, *Earth Planet. Sci. Lett.*, *92*, 107–123.

Takada, A. (1989), Magma transport and reservoir formation by a system of propagating cracks, *Bull. Volcanol.*, *52*(2), 118–126.

Thomas, N., T. Spohn, J. P. Barriot, W. Benz, G. Beutler, U. Christensen, V. Dehant, C. Fallnich, D. Giardini, O. Groussin, K. Gunderson, E. Hauber, M. Hilchenbach, L. Iess, P. Lamy, L. M. Lara, P. Lognonné, J. J. Lopez-Moreno, H. Michaelis, et al. (2007), The BepiColombo Laser Altimeter (BELA): Concept and baseline design, *Planet. Space Sci.*, *55*, 1398–1413, doi:10.1016/j.pss.2007.03.003.

Thomas, P. C., M. C. Malin, K. S. Edgett, M. H. Carr, W. K. Hartmann, A. P. Ingersoll, P. B. James, L. A. Soderblom, J. Veverka, and R. Sullivan (2000), North-south geological differences between the residual polar caps on Mars., *Nature*, *404*(6774), 161–4, doi:10.1038/35004528.

Thomas, R. J., D. A. Rothery, S. J. Conway, and M. Anand (2014a), Hollows on Mercury: Materials and mechanisms involved in their formation, *Icarus*, *229*, 221–235, doi:10.1016/j.icarus.2013.11.018.

Thomas, R. J., D. A. Rothery, S. J. Conway, and M. Anand (2014b), Long-lived explosive volcanism on Mercury, *Geophys. Res. Lett.*, *41*(17), 6084–6092, doi:10.1002/2014GL061224.

Thomas, R. J., D. A. Rothery, S. J. Conway, and M. Anand (2014c), Mechanisms of explosive volcanism on Mercury: implications from its global distribution and morphology, *J. Geophys. Res. Planets*, *119*, 2239–2254, doi:10.1002/2014JE004692.

Thomas, R. J., A. Lucchetti, G. Cremonese, D. A. Rothery, M. Massironi, C. Re, S. J. Conway, and M. Anand (2015), A cone on Mercury: Analysis of a residual central peak encircled by an explosive volcanic vent, *Planet. Space Sci.*, *108*, 108–116, doi:10.1016/j.pss.2015.01.005.

Thompson, A. B., and J. A. D. Connolly (1995), Melting of the continental crust: Some thermal and petrological constraints on anatexis in continental collision zones and other tectonic settings, *J. Geophys. Res.*, *100*(B8), 15,565–15,579.

Thompson, S. L., and H. S. Lauson (1974), Improvements in the Chart-D radiation hydrodynamic code III: revised analytic equations of state, *Tech. Rep. SC-RR-7107140714*.

Thorey, C., and C. Michaut (2014), A model for the dynamics of crater-centered intrusion: Application to lunar floor-fractured craters, *J. Geophys. Res. Planets*, *119*, 286–312, doi:10.1002/2013JE004467.

Titus, T. N., H. H. Kieffer, and P. R. Christensen (2003), Exposed water ice discovered near the south pole of Mars, *Science*, *299*(February), 1048–1051, doi: 10.1126/science.1080497.

Tosi, N., M. Grott, A.-C. Plesa, and D. Breuer (2013), Thermo-chemical evolution of Mercury's interior, *J. Geophys. Res. Planets*, doi:10.1002/jgre.20168.

Vasavada, A. R., D. A. Paige, and S. E. Wood (1999), Near-Surface Temperatures on Mercury and the Moon and the Stability of Polar Ice Deposits 1, *Icarus*, *141*, 179–193.

Vaughan, W. M., J. Helbert, D. T. Blewett, J. W. Head, S. L. Murchie, K. Gwinner, T. J. Mccoy, and C. Solomon, Sean (2012), Hollow-Forming Layers in Impact Craters on Mercury: Massive Sulfide or Chloride Deposits Formed by Impact Melt Differentiation?, *Lunar Planet. Sci. Conf.*, *43*, 1187.

Vigneresse, J. L., and J. D. Clemens (2000), Granitic magma ascent and emplacement: neither diapirism nor neutral buoyancy, *Geol. Soc. London, Spec. Publ.*, *174*(1), 1–19, doi:10.1144/GSL.SP.1999.174.01.01.

Vilas, F., C. R. Chapman, and M. S. Matthews (Eds.) (1988), *Mercury*, University of Arizona Press.

Watters, T. R., and P. J. McGovern (2006), Lithospheric flexure and the evolution of the dichotomy boundary on Mars, *Geophys. Res. Lett.*, *33*(8), doi:10.1029/2005GL024325.

Watters, T. R., S. C. Solomon, M. S. Robinson, J. W. Head, S. L. André, S. A. Hauck, and S. L. Murchie (2009), The tectonics of Mercury: The view after MESSENGER's first flyby, *Earth Planet. Sci. Lett.*, *285*(3-4), 283–296, doi:10.1016/j.epsl.2009.01.025.

Watters, T. R., M. S. Robinson, R. A. Beyer, M. E. Banks, J. F. B. Iii, M. E. Pritchard, H. Hiesinger, C. H. Van Der Bogert, P. C. Thomas, E. P. Turtle, and N. R. Williams (2010), Evidence of recent thrust faulting on the Moon revealed by the Lunar Reconnaissance Orbiter Camera, *Science*, *329*(5994), 936–940, doi: 10.1126/science.1189590.

Watters, T. R., S. C. Solomon, M. S. Robinson, J. W. Head, R. G. Strom, C. Klimczak, P. K. Byrne, A. C. Enns, C. M. Ernst, L. M. Prockter, S. L. Murchie, J. Oberst, F. Preusker, M. T. Zuber, S. a. Hauck II, and R. J. Phillips (2012), Tectonic features of Mercury: an orbital view with MESSENGER, *Lunar Planet. Sci. Conf.*, *43*, 2121.

Weidenschilling, S. J. (1978), Iron/silicate fractionation and the origin of Mercury, *Icarus*, *35*, 99–111.

Weider, S. Z., L. R. Nittler, R. D. Starr, T. J. McCoy, K. R. Stockstill-Cahill, P. K. Byrne, B. W. Denevi, J. W. Head, and S. C. Solomon (2012), Chemical heterogeneity on Mercury's surface revealed by the MESSENGER X-Ray Spectrometer, *J. Geophys. Res.*, *117*, 1–15, doi:10.1029/2012JE004153.

Weider, S. Z., L. R. Nittler, R. D. Starr, E. J. Crapster-Pregont, and S. C. Solomon (2014), Geochemical terranes on the innermost planet: possible origins of Mercury's high-magnesium region, *Lunar Planet. Sci. Conf.*, *45*, 1866.

Weider, S. Z., L. R. Nittler, R. D. Starr, E. J. Crapster-Pregont, P. N. Peplowski, B. W. Denevi, J. W.

Head, P. K. Byrne, S. a. Hauck, D. S. Ebel, and S. C. Solomon (2015), Evidence for geochemical terranes on Mercury: Global mapping of major elements with MESSENGER's X-Ray Spectrometer, *Earth Planet. Sci. Lett.*, *416*, 109–120, doi:10.1016/j.epsl.2015.01.023.

West, M. (1974), Martian volcanism - Additional observations and evidence for pyroclastic activity, *Icarus*, *21*, 1–11, doi:10.1016/0019-1035(74)90085-2.

Wetherill, G. W. (1988), Accumulation of Mercury from planetesimals, in *Mercury*, edited by F. Vilas, C. R. Chapman, and M. S. Matthews, pp. 670–691, University of Arizona Press, Tucson, AZ.

White, J. D. L., and P.-S. Ross (2011), Maar-diatreme volcanoes: A review, *J. Volcanol. Geotherm. Res.*, *201*(1-4), 1–29, doi:10.1016/j.jvolgeores.2011.01.010.

Whitford-Stark, J. L., and J. W. Head (2000), Stratigraphy of Oceanus Procellarum basalts: Sources and styles of emplacement, *J. Geophys. Res. Solid Earth*, *85*(B11), 6579–6609.

Whitten, J. L., J. W. Head, B. W. Denevi, and S. C. Solomon (2014), Formation of intercrater plains on Mercury, *Lunar Planet. Sci. Conf.*, *45*, 1219.

Wichman, R. W., and P. H. Schultz (1995a), Floor-fractured craters in Mare Smythii and west of Oceanus Procellarum: Implications of crater modification by viscous relaxation and igneous intrusion models, *J. Geophys. Res.*, *100*(E10), 21201–21218.

Wichman, R. W., and P. H. Schultz (1995b), Floor-fractured impact craters on Venus: Implications for igneous crater modification and local magmatism, *J. Geophys. Res.*, *100*(E2), 3233–3244.

Wieczorek, M. A., M. T. Zuber, and R. J. Phillips (2001), The role of magma buoyancy on the eruption of lunar basalts, *Earth Planet. Sci. Lett.*, *185*(1), 71–83, doi:10.1016/S0012-821X(00)00355-1.

Wieczorek, M. A., G. A. Neumann, F. Nimmo, W. S. Kiefer, G. J. Taylor, H. J. Melosh, R. J. Phillips, S. C. Solomon, J. C. Andrews-Hanna, S. W. Asmar, A. S. Konopliv, F. G. Lemoine, D. E. Smith, M. M. Watkins, J. G. Wiliams, and M. T. Zuber (2013), The crust of the Moon as seen by GRAIL, *Science*, *339*(6120), 671–675, doi:10.1126/science.1231530.

Wilhelms, D. E., and J. F. McCauley (1971), *I-703 Geologic map of the near side of the Moon*, U.S. Geological Survey, Reston.

Wilhelms, D. E., and El-Baz, F. (1977), *I-948 Geologic map of the east side of the Moon*, US Geological Survey, Reston.

Wilson, L. (1980), Relationships between pressure, volatile content and ejecta velocity in three types of volcanic explosion, *J. Volcanol. Geotherm. Res.*, *8*, 297–313.

Wilson, L., and J. W. Head (1981), Ascent and eruption of basaltic magma on the Earth and Moon, *J. Geophys. Res.*, *86*(B4), 2971–3001.

Wilson, L., and J. W. Head (2003), Deep generation of magmatic gas on the Moon and implications for pyroclastic eruptions, *Geophys. Res. Lett.*, *30*(12), 1605, doi:10.1029/2002GL016082.

Wilson, L., and J. W. Head (2007), An integrated model of kimberlite ascent and eruption, *Nature*, *447*(7140), 53–7, doi:10.1038/nature05692.

Wilson, L., and E. A. Parfitt (1989), The influence of gravity on planetary volcanic eruption rates: A reappraisal, *Lunar Planet. Sci. Conf.*, *20*, 1213.

Wilson, L., R. S. J. Sparks, and G. P. L. Walker (1980), Explosive volcanic eruptions—IV. The control of magma properties and conduit geometry on eruption column behaviour, *Geophys. J. R. Astron. Soc.*, 117–148.

Wilson, L., J. W. Head, and A. R. Tye (2014), Lunar regional pyroclastic deposits: evidence for eruption from dikes emplaced into the near-surface crust, *Lunar Planet. Sci. Conf.*, *45*, 1223.

Wohletz, K. H., and M. F. Sheridan (1983), Hydrovolcanic explosions II. Evolution of basaltic tuff rings and tuff cones, *Am. J. Sci.*, *283*, 385–413.

Wolfe, R. W., and F. El-Baz (1976), Photogeology of the multi-ringed crater Haldane in Mare Smythii, *Lunar Planet. Sci. Conf. Proc.*, *7*, 2903–2912.

Wünnemann, K., and B. a. Ivanov (2003), Numerical modelling of the impact crater depth-diameter dependence in an acoustically fluidized target, *Planet. Space Sci.*, *51*(13), 831–845, doi:10.1016/j.pss.2003.08.001.

Wünnemann, K., G. S. Collins, and H. J. Melosh (2006), A strain-based porosity model for use in hydrocode simulations of impacts and implications for transient crater growth in porous targets, *Icarus*, *180*(2), 514–527, doi:10.1016/j.icarus.2005.10.013.

Xiao, Z., R. G. Strom, D. T. Blewett, P. K. Byrne, S. C. Solomon, S. L. Murchie, A. L. Sprague, D. L. Domingue, and J. Helbert (2013), Dark spots on Mercury: A distinctive low-reflectance material and its relation to hollows, *J. Geophys. Res. Planets*, *118*, 1–14, doi:10.1002/jgre.20115.

Xiao, Z., R. G. Strom, C. R. Chapman, J. W. Head, C. Klimczak, L. R. Ostrach, J. Helbert, and P. D'Incecco (2014), Comparisons of fresh complex impact craters on Mercury and the Moon: Implications for controlling factors in impact excavation processes, *Icarus*, *228*, 260–275, doi:10.1016/j.icarus.2013.10.002.

Yakshinskiy, B. V., and T. E. Madey (2004), Photon-stimulated desorption of Na from a lunar

sample: temperature-dependent effects, *Icarus*, *168*(1), 53–59, doi:10.1016/j.icarus.2003.12.007.

Zeng, L., L. E. Gao, K. Xie, and J. Liu-Zeng (2011), Mid-Eocene high Sr/Y granites in the Northern Himalayan Gneiss Domes: Melting thickened lower continental crust, *Earth Planet. Sci. Lett.*, *303*(3-4), 251–266, doi:10.1016/j.epsl.2011.01.005.

Ziethe, R., K. Seiferlin, and H. Hiesinger (2009), Duration and extent of lunar volcanism: Comparison of 3D convection models to mare basalt ages, *Planet. Space Sci.*, *57*(7), 784–796, doi:10.1016/j.pss.2009.02.002.

Zolotov, M. Y. (2011), On the chemistry of mantle and magmatic volatiles on Mercury, *Icarus*, *212*(1), 24–41, doi:10.1016/j.icarus.2010.12.014.

Zuber, M. T., D. E. Smith, R. J. Phillips, S. C. Solomon, G. A. Neumann, S. A. H. Ii, S. J. Peale, O. S. Barnouin, J. W. Head, C. L. Johnson, F. G. Lemoine, E. Mazarico, X. Sun, M. H. Torrence, A. M. Freed, C. Klimczak, J. Margot, J. Oberst, M. E. Perry, et al. (2012), Topography of the Northern Hemisphere of Mercury from MESSENGER laser altimetry, *Science*, *336*, 217–220.

# Appendix A. Global catalogue of hollows

**Table A-1 Location of the geographic centroid of each group of hollows. This is a version of the Supplementary material published with (*Thomas et al.*, 2014a) with some values updated as a result of observations of MESSENGER images released by NASA's Planetary Data System between 16th September 2013 and 5th March 2015. * indicates newly-observed sites not included in the published work and changes to the central longitude or latitude (when rounded to one decimal place) resulting from the identification of new hollows in a group.**

| Group ID | Central longitude | Central latitude |
|---|---|---|
| 1000 | -54.9195 | 45.319 |
| 1001 | -55.2261 | 37.3513 |
| 1002 | -58.768 | 47.9426 |
| 1003 | -58.4983 | 43.8686 |
| 1005 | -58.6174 | 57.4265 |
| 1006 | -56.3331 | 50.7335 |
| 1007 | -55.6031 | 47.0348 |
| 1008 | -54.9368 | 45.9818 |
| 1009 | -54.6966 | 40.6227 |
| 1010 | -53.7977* | 29.9417* |
| 1011 | -53.1725 | 59.2433 |
| 1012 | -58.732 | 31.9572 |
| 1013 | -59.7997 | 26.9346 |
| 1014 | -53.9648 | 21.8748 |
| 1015 | -56.3439 | 12.212 |
| 1016 | -55.8066 | 5.38166 |
| 1017 | -54.2077 | 4.32664 |
| 1018 | -51.1755 | 7.5766 |
| 1019 | -50.0564 | 11.5738 |
| 1020 | -48.4305 | 15.4709 |
| 1021 | -53.8607 | 58.6423 |
| 1022 | -59.4837 | 51.5532 |
| 1024 | -56.1577 | 3.70723 |
| 1025 | -51.911 | -27.2375 |
| 1026 | -56.143 | -3.9504 |
| 1027 | -55.8726 | -12.5026 |
| 1029 | -56.3037 | -37.9943 |
| 1030 | -49.855 | -40.3735 |
| 1031 | -48.7517 | -54.3574 |
| 1032 | -47.827 | -2.5897 |
| 1035 | -53.1639 | -14.6949 |
| 1036 | -51.0773 | -19.0737 |
| 1037 | -49.3144 | -25.3485 |
| 1038 | -50.7228 | -22.2951 |
| 1039 | -62.9822 | -46.3912 |
| 1040 | -53.9434 | -53.7914 |
| 1044 | -53.2205 | 18.8771 |
| 1048 | -62.7638 | 14.0104 |
| 1053 | -61.2805 | -36.6282* |
| 1054 | -63.2094 | -18.4396 |
| 1055 | -61.9275 | 14.9904 |
| 1056 | -63.1364 | -49.9874 |
| 1058 | -62.4581 | -31.4623 |
| 1060 | -64.3108 | 25.3735 |
| 1061 | -62.4371 | 6.27545 |
| 1062 | -61.7465 | 4.50636 |
| 1063 | -59.6631 | -4.69543 |
| 1064 | -61.4979 | 53.894 |
| 1068 | -45.8391 | -4.39642 |
| 1069 | -56.0033 | 33.5049 |
| 1072 | -57.5827 | -8.07458 |
| 1073 | -63.1673 | 45.8371 |
| 1075 | -50.2359 | 23.067 |
| 1076 | -55.9538 | 42.3522 |
| 1077 | -48.2031 | 20.1773 |
| 1078 | -45.2349 | 35.8421* |
| 1079 | -48.7774 | 43.1494 |
| 1080* | -57.8706 | 5.89837 |

| Group ID | Central longitude | Central latitude |
|---|---|---|
| 1081* | -61.3 | 2.12174 |
| 1082* | -45.3536 | 37.5205 |
| 1083* | -44.9874 | 36.7994 |
| 2003 | -3.82083 | 25.8867 |
| 2004 | 5.07023 | 25.3024 |
| 2005 | 1.94452 | 22.0268 |
| 2008 | -2.26727 | 51.2479 |
| 2009 | 7.65961 | 25.947 |
| 2010 | 0.501477 | 24.1596 |
| 2011 | 1.98131 | -3.71815 |
| 2012 | 2.42827 | -6.22789 |
| 2013 | 6.39749 | 23.857 |
| 2018 | 4.2384 | 30.0885 |
| 2020 | -1.13128 | 26.9529 |
| 2024 | 1.48632 | 30.6511 |
| 2027 | 9.66989 | 28.3667 |
| 2028 | -1.11924 | 54.0843 |
| 2031 | -2.9992 | 17.5194 |
| 2032 | -6.10326 | -2.51634 |
| 2035 | 3.55431 | 28.6274 |
| 2036 | -9.14332 | -26.2449* |
| 2037 | 0.384908 | 46.7446 |
| 2038 | -8.91459 | 9.53117 |
| 2040 | -4.81318 | -48.1858 |
| 2042 | -4.79903 | -23.3813 |
| 2043 | 0.941334 | -10.99 |
| 2044 | -6.63138 | -38.1399 |
| 2047* | -6.13048 | 29.5823 |
| 2048* | -0.483525 | 12.1144 |
| 2049* | 3.5986 | 14.0847 |
| 2050* | 6.50002 | 30.5849 |
| 2051* | 5.73364 | 37.8985 |
| 2052* | 7.23439 | 34.7374 |
| 3001 | 81.2677 | 19.6252 |
| 3003 | 87.9351 | -41.1716* |
| 3004 | 83.448 | -5.18081 |
| 3007 | 83.0376 | 42.8754 |
| 3009 | 92.304 | -36.9538 |
| 3010 | 83.2804 | 53.3862 |

| Group ID | Central longitude | Central latitude |
|---|---|---|
| 3013 | 93.7086 | 15.8436 |
| 4002 | 178.911 | 20.5747 |
| 4003 | 166.772 | 25.6353 |
| 4004 | 163.124 | 30.5195 |
| 4005 | 160.376 | 59.0888 |
| 4006 | 164.946 | 14.8751 |
| 4007 | 168.099 | 60.8851 |
| 4008 | 172.259 | 71.4205 |
| 4009 | 169.395 | 8.09819 |
| 4011 | 162.383 | 13.7329 |
| 4012 | 177.273 | 18.8703 |
| 4022 | 166.872 | 36.5084 |
| 4023 | 178.238 | 21.6245 |
| 4024 | 179.533 | 25.4545 |
| 4026 | 179.346 | 23.1764 |
| 4028 | 179.453 | 21.3044 |
| 4030 | 175.492 | 38.5184 |
| 4032 | 165.801 | 59.6339 |
| 4033 | 166.926 | 13.9814 |
| 4034 | 162.666 | 12.5635 |
| 4035 | 178.987 | 21.5235 |
| 4036 | 160.871 | 48.2009 |
| 4046 | 167.483 | 29.4315 |
| 4047 | 178.881 | -41.332 |
| 5001 | 33.1683 | 7.77266 |
| 5002 | 19.5415 | -8.57847 |
| 5003 | 29.1698 | 17.9718 |
| 5004 | 35.132 | 27.2828 |
| 5005 | 21.9851 | -1.9738 |
| 5006 | 12.7945 | 3.54637 |
| 5007 | 16.17 | 25.1947 |
| 5008 | 22.7597* | 35.1275 |
| 5009 | 26.8509 | -13.6876 |
| 5011 | 23.3808 | 5.85207 |
| 5013 | 38.4559 | 16.227 |
| 5015 | 57.4332 | 25.4916 |
| 5017 | 24.2202 | 26.9448 |
| 5018 | 13.9134 | 19.3851 |
| 5019 | 15.3447 | 0.627028 |

| Group ID | Central longitude | Central latitude |
|---|---|---|
| 5021 | 18.7335 | -18.5406 |
| 5025 | 72.4 | 14.35 |
| 5027 | 79.249 | 28.9495 |
| 5028 | 69.2001 | 27.3668 |
| 5029 | 59.2202 | 15.1158 |
| 5033 | 50.4667 | -4.5912 |
| 5035 | 59.8896 | -11.5398 |
| 5036 | 44.7274 | 27.1954 |
| 5037 | 76.1904 | -12.8117 |
| 5038 | 72.3471 | -20.3455 |
| 5040 | 49.8401 | 3.75158 |
| 5042 | 58.3736 | -6.22035 |
| 5043 | 58.0236 | 17.1223 |
| 5044 | 65.2356 | 3.51944 |
| 5045 | 71.531 | -19.2259 |
| 5046 | 59.2504 | -8.85664 |
| 5048 | 56.0117 | -10.9729 |
| 5049 | 57.3844 | -8.22095 |
| 5050 | 55.0908 | -7.9036 |
| 5051 | 54.3812 | -3.22702 |
| 5052 | 47.9317 | -19.4445 |
| 5054 | 21.5936 | 32.4827 |
| 5056 | 24.7634 | 31.4207 |
| 5057 | 13.9844 | 33.0805 |
| 5058 | 18.2055 | 33.8152 |
| 5059 | 13.9806 | 35.6954 |
| 5060 | 12.3911 | 32.8519 |
| 5062 | 31.5663 | 36.7633 |
| 5064 | 43.424 | 65.9796 |
| 5065 | 23.6637 | 38.9554 |
| 5067 | 25.9396 | 39.4859 |
| 5068 | 57.9836 | -31.916 |
| 5069 | 45.3258 | -37.4421 |
| 5071 | 41.0881 | -36.472 |
| 5073 | 35.5897 | -33.1285 |
| 5074 | 24.3007 | -30.6677 |
| 5075 | 16.8843 | -55.8064 |
| 5076 | 18.4621 | -23.1298 |
| 5078 | 11.0107 | -52.851 |
| 5079 | 20.9707 | -58.0722 |
| 5080 | 50.0249 | -34.1332 |
| 5081 | 49.788 | -30.2082 |
| 5089 | 15.1714 | -25.5617 |
| 5099 | 55.3541 | 36.3533 |
| 5100 | 76.5156 | -67.5833 |
| 5101 | 17.1354 | -12.3188 |
| 5105 | 12.9677 | 19.5607 |
| 5106 | 13.5411 | 22.4503 |
| 5107 | 14.3183 | 30.8091 |
| 5108 | 17.529 | 0.511726 |
| 5109 | 18.1752 | 32.2018 |
| 5110 | 32.9717 | 48.1484 |
| 5111 | 18.7408 | 37.3578 |
| 5112 | 25.8483 | 35.372 |
| 5113 | 27.5056 | 36.8818 |
| 5114* | 63.9052 | 36.1533 |
| 6001 | 134.807 | 46.1195 |
| 6002 | 135.601 | 44.615 |
| 6003 | 159.269 | 43.5946 |
| 6004 | 154.543 | 42.3984 |
| 6005 | 157.418 | 53.8702 |
| 6006 | 152.905 | 40.3802 |
| 6008 | 145.78 | 47.3086 |
| 6009 | 139.007 | 67.3742 |
| 6010 | 153.484 | 66.5398 |
| 6011 | 145.148 | 35.9415 |
| 6012 | 142.587 | 37.0311 |
| 6013 | 139.725 | 36.4604 |
| 6015 | 141.533 | 38.2957 |
| 6017 | 118.965 | 63.1786 |
| 6018 | 109.013 | 57.762 |
| 6019 | 108.912 | 58.3924 |
| 6020 | 111.529 | 57.7891 |
| 6021 | 112.497 | 61.683 |
| 6022 | 125.807 | -53.0056 |
| 6023 | 113.532* | 55.1087 |
| 6024 | 116.696 | 57.0401 |
| 6025 | 120.219 | 55.4544 |

| Group ID | Central longitude | Central latitude |
|---|---|---|
| 6026 | 114.025 | 59.4322 |
| 6027 | 143.222 | 32.803 |
| 6028 | 142.71 | 38.6453 |
| 6029 | 125.844 | 39.6564 |
| 6030 | 121.273 | 43.2523 |
| 6031 | 121.08 | 41.6601 |
| 6032 | 127.655 | 40.7673 |
| 6033 | 122.932 | 41.6996 |
| 6034 | 123.973 | 57.4301 |
| 6035 | 125.039 | 56.9287 |
| 6036 | 125.9 | 57.1231 |
| 6037 | 125.988 | 56.274 |
| 6038 | 120.721 | 58.4141 |
| 6039 | 116.707 | 58.492 |
| 6040 | 123.937 | 41.2698 |
| 6041 | 120.124 | 59.5752 |
| 6042 | 126.744 | 60.2895 |
| 6043 | 104.323 | 71.7507 |
| 6045 | 139.67 | 48.5404 |
| 6046 | 123.038 | 57.7006 |
| 6047 | 134.455* | 48.6864 |
| 6048 | 123.392 | 61.0195 |
| 6050 | 128.408 | 41.8917 |
| 6051 | 116.514 | 43.0113 |
| 6052 | 156.783 | -35.0749 |
| 6053 | 117.906 | -26.523 |
| 6054 | 114.378 | 10.7202 |
| 6055 | 119.117 | 27.1292 |
| 6056 | 104.738 | -11.1749 |
| 6057 | 103.56 | 7.0953 |
| 6058 | 109.172 | 4.86234 |
| 6059 | 148.097 | 14.2176 |
| 6061 | 140.929 | -26.1054 |
| 6063 | 145.184 | 21.8494 |
| 6065 | 155.802 | 4.61892 |
| 6066 | 156.936 | 16.5319* |
| 6068 | 155.219* | 17.5085 |
| 6069 | 159.403 | 14.6511 |
| 6070 | 146.142 | 27.3168 |
| 6072 | 149.817 | 17.8884 |
| 6073 | 152.48 | 17.7966 |
| 6076 | 143.52 | 22.1785 |
| 6077 | 154.038 | -10.122 |
| 6079 | 142.881 | -7.05575 |
| 6081 | 145.413 | -12.8045 |
| 6082 | 143.379 | -29.8975 |
| 6085 | 140.359 | -51.9496 |
| 6088 | 140.206 | 27.8814 |
| 6089 | 105.692 | -44.0931 |
| 6091 | 142.338 | -34.0458 |
| 6092 | 146.84 | -37.7589 |
| 6095 | 135.125 | -45.6448 |
| 6097 | 107.001 | -39.8188 |
| 6098 | 124.784 | -45.2428 |
| 6101 | 157.605 | 51.9325 |
| 6103 | 145.173 | 60.7804 |
| 6105 | 144.39 | 45.3418 |
| 6106 | 133.222 | 64.324 |
| 6108 | 126.835 | 39.4216 |
| 6109 | 120.741 | 33.9549* |
| 6110 | 109.876 | 39.5987 |
| 6122 | 108.583 | 60.8244 |
| 6135 | 120.992 | -34.0461 |
| 6137 | 138.263 | -6.70542 |
| 6138 | 114.487 | 1.06095 |
| 6139 | 115.163 | 57.3292 |
| 6141 | 123.395 | 56.0378 |
| 6142 | 150.065* | 42.5659* |
| 6143 | 130.651 | -54.0353 |
| 6144 | 141.782* | 21.2626 |
| 6145 | 150.15 | -9.65257 |
| 6146 | 111.009 | 23.1172 |
| 6147 | 100.56 | 20.3101 |
| 6148 | 105.204 | 62.5955 |
| 6150 | 107.234 | -18.8437 |
| 6162* | 143.324 | 43.7177 |
| 6163* | 144.242 | 40.341 |
| 6164* | 148.496 | 50.6259 |

| Group ID | Central longitude | Central latitude |
|---|---|---|
| 6165* | 153.003 | 48.6488 |
| 6166* | 158.166 | 61.3495 |
| 6167* | 105.039 | 34.8553 |
| 7001 | -78.8641 | 52.0249 |
| 7002 | -98.0307* | 32.7195* |
| 7004 | -142.867 | 35.4338 |
| 7005 | -143.469 | 33.8929 |
| 7006 | -143.75 | 31.0893 |
| 7008 | -176.53 | 32.2057 |
| 7009 | -68.6364 | 43.5568 |
| 7010 | -78.0114 | 34.6464 |
| 7011 | -79.583 | 35.0536 |
| 7012 | -169.398 | 64.4776 |
| 7013 | -127.737 | 37.2401 |
| 7014 | -66.7883 | 32.626 |
| 7015 | -71.2944 | 45.1614 |
| 7016 | -92.5595 | 51.5072 |
| 7017 | -136.41 | 53.0516* |
| 7018 | -101.245 | 40.7085 |
| 7020 | -138.079 | 40.43 |
| 7021 | -140.355 | 40.8186 |
| 7022 | -151.087 | 65.889 |
| 7023 | -163.993 | 48.0895 |
| 7024 | -111.061 | 36.0582 |
| 7025 | -111.567* | 41.394* |
| 7027 | -72.7363 | 61.3041 |
| 7028 | -91.5347* | 39.1426 |
| 7029 | -107.83 | 38.9799 |
| 7030 | -140.116 | 48.4294 |
| 7032 | -127.988 | 58.1733 |
| 7033 | -80.2588 | 39.9763 |
| 7034 | -71.4881 | -47.6239 |
| 7035 | -68.7801 | -47.8862 |
| 7036 | -90.1352 | -28.4116 |
| 7040 | -170.32 | -32.6031 |
| 7053 | -140.771 | 14.2807 |
| 7059 | -84.5346 | 41.7515 |
| 7060 | -74.7746 | -21.9697 |
| 7061 | -138.663 | 9.71103 |
| 7062 | -138.985 | 27.0976 |
| 7063 | -142.396 | -23.5677 |
| 7064 | -141.025 | 35.3576 |
| 7066 | -128.386 | 78.0996 |
| 7068 | -115.775* | 36.3034* |
| 7069 | -171.388 | -37.9273 |
| 7070 | -73.1916 | -0.975579* |
| 7071 | -121.466 | -5.98978 |
| 7072 | -64.7949 | 23.5115 |
| 7073 | -118.745 | 21.9174 |
| 7085 | -138.533 | -10.7999 |
| 7089 | -141.649 | 15.0254 |
| 7091 | -148.51 | 3.71184 |
| 7093 | -177.53 | 24.1265 |
| 7095 | -147.673 | -2.80808 |
| 7099 | -157.4 | 4.97987 |
| 7100 | -160.682 | 11.1907 |
| 7101 | -164.249 | 16.8154 |
| 7102 | -161.793 | 1.96268 |
| 7103 | -162.168 | 0.715905 |
| 7105* | -160.807 | -16.0126 |
| 7108 | -155.572 | 0.436286 |
| 7112 | -103.195 | 23.0247 |
| 7113 | -113.342 | 26.3017 |
| 7116 | -132.951 | -12.6034 |
| 7117 | -130.263 | 23.7551 |
| 7118 | -142.587 | -4.88347 |
| 7119 | -105.977 | 25.3943 |
| 7120 | -104.43 | 9.32314 |
| 7121 | -115.338 | 1.45955 |
| 7122 | -102.68 | 17.431 |
| 7123 | -107.521 | 18.9632 |
| 7124 | -112.284 | 15.0901 |
| 7127 | -134.842 | -29.0236 |
| 7128 | -124.111 | -21.8515 |
| 7130 | -70.8066 | 16.3391 |
| 7131 | -86.1788 | 14.135 |
| 7133 | -76.5234 | -21.1443 |
| 7134 | -131.59 | 0.93363 |

| Group ID | Central longitude | Central latitude |
|---|---|---|
| 7135 | -120.493 | -19.5339 |
| 7136 | -107.774 | 10.7398 |
| 7137 | -95.3293 | 25.0718 |
| 7138 | -67.5835 | 22.2172 |
| 7139 | -75.048 | 21.5201 |
| 7140 | -72.6055 | -28.7213 |
| 7142 | -69.1926 | -26.9991* |
| 7143 | -80.3267 | -28.2541 |
| 7144 | -93.4427 | 25.0792 |
| 7147 | -67.816 | 8.47261 |
| 7148 | -92.0699 | 4.0325 |
| 7149 | -75.3614 | -24.0301 |
| 7150 | -72.3072 | -18.9943 |
| 7152 | -72.0717 | -17.9243 |
| 7153 | -74.5301 | 1.93294 |
| 7154 | -179.814 | -18.4324 |
| 7155 | -66.9197 | -7.31428 |
| 7156 | -72.0618 | 8.22372 |
| 7157 | -77.6366 | 18.1715 |
| 7159 | -91.1081* | -23.339* |
| 7161 | -68.4014 | -52.5317 |
| 7167* | -179.577 | 22.6557 |
| 7168* | -146.542 | 41.4561 |
| 7169* | -99.9201 | 16.4753 |
| 7170* | -70.7954 | 57.3624 |
| 8001 | -33.3541 | 30.5449 |
| 8002 | -19.085 | 38.2353 |
| 8003 | -38.8828 | 37.7058 |
| 8004 | -33.0558 | 58.8732 |
| 8005 | -40.0396 | 59.9165 |
| 8006 | -39.702 | 50.7857 |
| 8007 | -33.6949 | 48.4409 |
| 8009 | -41.552 | 46.5105 |
| 8010 | -38.7197 | 43.0087 |
| 8011 | -38.01 | 45.2713 |
| 8012 | -42.0524 | 36.6605 |
| 8013 | -27.1188 | -31.4642 |
| 8014 | -39.31 | -33.5509 |
| 8015 | -36.0793 | -47.788 |
| 8016 | -37.5636 | -48.5963 |
| 8017 | -30.1217 | -40.135 |
| 8018 | -40.076 | -52.7542 |
| 8019 | -32.0805 | -57.2353 |
| 8021 | -37.26 | 54.4666 |
| 8022 | -43.7031 | 44.4279 |
| 8032 | -29.7725 | -56.4222 |
| 8033 | -10.8221 | -36.7185 |
| 8035 | -39.173 | 42.2439 |
| 8036 | -40.6477 | 43.8734 |
| 8037 | -41.5242 | 44.6039 |
| 8038 | -15.4769 | 1.58775 |
| 8039 | -30.1524 | 10.2206 |
| 8040 | -31.6829 | 43.6373 |
| 8041 | -31.9243 | 45.5434 |
| 8042 | -37.7413 | 4.95978 |
| 8043 | -30.6382 | 13.45 |
| 8044 | -30.7482 | 9.03881 |
| 8045 | -23.9098 | 42.4771 |
| 8046 | -29.5225 | -53.0829 |
| 8047 | -43.582 | -4.60077 |
| 8048 | -24.6834 | 44.2295 |
| 8049 | -20.9572 | -30.7812 |
| 8052 | -42.1105 | -30.7501 |
| 8053 | -13.9664 | -39.9345 |
| 8054 | -38.4145 | -2.49618 |
| 8055 | -37.1408 | 24.3411 |
| 8056 | -28.9518 | 43.1523 |
| 8057 | -38.0982 | 0.75456 |
| 8058 | -20.3722 | 43.5032 |
| 8059 | -14.6805 | 13.1029 |
| 8060 | -21.1569 | 1.59045 |
| 8061 | -15.6329 | -6.75828 |
| 8062 | -34.2937 | 3.6187 |
| 8063 | -19.9678 | -37.2964 |
| 8064 | -18.1566 | 35.5265 |
| 8065 | -34.5495 | 35.5082 |
| 8161 | -23.7559 | -0.057647 |
| 8162 | -42.1459 | -3.04763 |

| Group ID | Central longitude | Central latitude |
|---|---|---|
| 8164 | -34.8355 | -1.7737 |
| 8165 | -15.2035 | -16.3052 |
| 8166 | -29.6746 | 26.9703 |
| 8168 | -36.341 | -18.2863 |
| 8169 | -22.7619* | 23.3049 |
| 8170 | -31.1371 | 22.1246 |
| 8171 | -24.809 | -27.6931 |
| 8173 | -31.1066 | -11.2643 |
| 8174 | -44.2646 | -5.61038 |
| 8176 | -38.1126 | -12.0916 |
| 8177 | -21.1362 | 17.7432 |
| 8179 | -37.5158 | 22.7759 |
| 8181 | -39.4893 | 0.192933 |
| 8182 | -36.4072 | 1.19162 |
| 8184 | -44.1845 | 12.2162 |
| 8185 | -15.7549 | -24.6388 |
| 8186 | -16.7908 | -27.3787 |
| 8187 | -43.0012 | 10.5646 |
| 8188 | -21.2846 | 10.5865 |
| 8189 | -19.0976 | 7.40985 |
| 8190 | -23.7572 | 6.44317 |
| 8191 | -25.7207 | 9.12461 |
| 8192 | -27.5901 | 12.8718 |
| 8193 | -25.9634 | 12.5171 |
| 8194 | -26.7362 | 14.4763 |
| 8195 | -30.082 | 16.2976 |
| 8196 | -25.3506 | 5.07382 |
| 8197 | -35.0335 | 9.47916 |
| 8200* | -36.2537 | 28.8571 |
| 8201* | -35.5795 | 12.4677 |
| 8202* | -26.2251 | -1.45432 |
| 8203* | -37.5412 | 35.9312 |
| 8204* | -24.9723 | 38.498 |

# Appendix B. Degradation states of impact craters hosting putative explosive volcanism

**Table B-1 Catalogue of endogenic pit groups with a surrounding spectral anomaly and the degradation state of their host impact crater. Central longitude and latitude indicates the centroid of the group in decimal degrees. Crater degradation classes: 1 = Pre-Tolsojan, 2 = Tolsojan, 3 = Calorian, 4 = Mansurian, 5 = Kuiperian to late Mansurian, 0 = cannot be determined, n/a = does not lie within a crater. This is an updated version of Table S1 in (*Thomas et al.*, 2014b). Where pits and/or deposits were newly-identified in MESSENGER images released by NASA's Planetary Data System between 7th March 2014 and 5th March 2015, or where the discovery of new pits led to a change in the central longitude or latitude of the group rounded to one decimal place, this is indicated with *.**

| Pit Group ID | Central latitude | Central longitude | Crater degradation class | Crater name |
|---|---|---|---|---|
| 1042 | 4.18208 | -54.0911 | 3 | Mistral |
| 1043 | 5.40528 | -55.7995 | 4 | |
| 1045 | 15.0162 | -49.001 | 4 | Lermontov |
| 1046 | 3.7557 | -56.085 | 4 | |
| 1047 | 26.6068 | -59.4069 | 3 | Praxiteles |
| 1052 | -37.2695 | -61.7383 | 1 | Chekhov |
| 1065 | 7.47479 | -51.3424 | 4 | |
| 1066 | -27.4952 | -48.94 | n/a | |
| 1067* | 12.4442 | -55.814 | 3 | Giotto |
| 1074 | 45.3868 | -64.5913 | 1 | |
| 2002 | 27.539 | 1.23683 | 3 | |
| 2006 | 17.4012 | -2.75865 | 3 | Hemingway |
| 2007 | 14.0051 | 3.65481 | 3 | |
| 2029 | 26.0056 | -4.09383 | 3 | |
| 2039 | -48.4294 | -6.51739 | 3 | |
| 2041 | -50.0023 | 5.80077 | n/a | |
| 2045 | -48.9564 | 2.26688 | n/a | |
| 2046 | -47.0739 | -6.04293 | 3 | |
| 2053* | -38.3493 | -7.77438 | 4 | |
| 3011* | 43.384 | 82.9909 | 4 | |
| 4001 | 21.5008 | 178.967 | 3 | Caloris |
| 4010 | 25.7479 | 179.98 | 4 | |
| 4013 | -39.7556 | 175.655 | 2 | Liang K'ai |

| Pit Group ID | Central latitude | Central longitude | Crater degradation class | Crater name |
|---|---|---|---|---|
| 4014 | 58.8284 | 160.717 | 3 | Navoi |
| 4015 | 13.7039 | 162.362 | 3 | Caloris |
| 4017 | 60.8055 | 168.064 | 3 | |
| 4037 | 48.4023 | 161.229 | 3 | Caloris |
| 4038 | 23.0499 | 179.461 | 4 | |
| 4040 | -28.1626 | 161.933 | 4 | |
| 4041 | -23.6502 | 179.97 | 3 | Hauptmann |
| 4044 | 19.497 | 178.073 | 3 | |
| 4048 | -25.2856 | 177.612 | 2 | |
| 5014 | 35.5111 | 23.1669 | 3 | |
| 5016 | 28.3662 | 10.2985 | n/a | |
| 5020 | -51.6599 | 24.4144 | 4 | |
| 5022 | -19.0753 | 71.579 | 2 | Kipling |
| 5023 | -21.0378 | 72.4513 | 3 | |
| 5024 | -15.563 | 65.7418 | n/a | |
| 5034 | -0.81852 | 43.8684 | n/a | |
| 5039 | 3.5413 | 50.9792 | 3 | Picasso |
| 5041 | -5.66971 | 58.1529 | n/a | |
| 5047 | -11.2567 | 55.2067 | n/a | |
| 5053 | 32.1638 | 22.7564 | n/a | |
| 5055 | 32.4413 | 21.8351 | 5 | |
| 5061 | 35.99 | 57.4322 | n/a | |
| 5063 | 37.3538 | 23.7992 | n/a | |
| 5066 | 36.3186 | 55.2953 | 4 | |
| 5070 | -37.4978 | 45.6366 | 4 | |
| 5072 | -32.6985 | 36.1268 | 3 | |
| 5077 | -11.4008 | 62.1781 | n/a | |
| 5082 | 35.7954 | 64.0003 | n/a | |
| 5083 | -33.2587 | 49.9551 | n/a | |
| 5084 | -52.8102 | 38.2961 | 3 | |
| 5085 | -49.8341 | 10.7517 | n/a | |
| 5086 | -9.15486 | 52.2909 | n/a | |
| 5087 | 35.9417 | 51.1418 | 4 | |
| 5090 | -70.6439 | 13.0063 | 3 | |
| 5091 | -68.8936 | 23.6707 | n/a | |
| 5092 | -52.7133 | 17.7142 | n/a | |
| 5094 | -36.2086 | 41.2941 | 4 | |
| 5095 | -43.7973 | 19.7504 | 3 | |
| 5096 | 8.13621 | 32.8684 | 5 | |

| Pit Group ID | Central latitude | Central longitude | Crater degradation class | Crater name |
|---|---|---|---|---|
| 5097 | -66.8024 | 76.2552 | 4 | Alver |
| 5103 | -48.3247 | 11.8058 | n/a | |
| 5104 | -53.0162 | 20.171 | n/a | |
| 6007 | 48.6929 | 159.48 | 3 | Caloris |
| 6014 | 38.2797 | 141.471 | n/a | |
| 6016 | 14.297 | 159.689 | 3 | Caloris |
| 6060 | -5.20355 | 143.593 | 1 | |
| 6062 | 22.0478 | 145.872 | 3 | Caloris |
| 6064 | -11.0137 | 140.58 | 3 | |
| 6067 | 16.3072 | 157.212 | 3 | Caloris |
| 6071 | 18.7473 | 149.655 | 3 | Caloris |
| 6074 | -28.2183 | 146.868 | 4 | |
| 6075* | -52.5569 | 125.647 | 4 | Neruda |
| 6078 | -9.21725 | 154.509 | 1 | |
| 6083 | -28.124 | 136.556 | 4 | |
| 6086 | -59.6059 | 141.492 | n/a | |
| 6087 | 28.0165 | 138.617 | n/a | |
| 6090 | -43.7408 | 105.786 | 4 | |
| 6096 | -59.8402 | 145.27 | 3 | |
| 6099 | 45.3181 | 144.352 | 3 | |
| 6100* | -60.6238 | 149.194 | n/a | |
| 6102* | 28.1036 | 144.639 | 3 | Caloris |
| 6111 | 24.2069 | 148.383 | 3 | Caloris |
| 6113 | 36.606 | 110.168 | 1 | |
| 6115 | 58.2096 | 101.077 | n/a | |
| 6117 | -55.2192 | 142.659 | 2 | |
| 6119 | -45.3429 | 135.107 | 4 | Sher Gil |
| 6120 | -40.3315 | 111.341 | 4 | Beckett |
| 6123 | -41.9587 | 115.121 | 2 | |
| 6124 | -51.5263 | 136.546 | 3 | |
| 6125 | -63.5287 | 142.665 | 2 | |
| 6126 | -65.2769 | 147.733 | 2 | |
| 6127 | -56.3414 | 143.904 | n/a | |
| 6129 | -65.885 | 154.312 | 3 | |
| 6130 | -38.6292 | 137.633 | 2 | |
| 6131 | -38.6423 | 133.703 | 3 | |
| 6132 | -38.7106 | 135.283 | 2 | |
| 6133 | -55.0409 | 147.151 | 3 | |
| 6134 | -40.0887 | 124.806 | 3 | |

| Pit Group ID | Central latitude | Central longitude | Crater degradation class | Crater name |
|---|---|---|---|---|
| 6136 | -51.9731 | 138.955 | 4 | |
| 6149 | -35.1335 | 142.659 | 3 | |
| 6151 | -32.5761 | 151.114 | 2 | |
| 6153 | 17.6497 | 152.572 | 4 | |
| 6155 | 18.6001 | 150.952 | 3 | Caloris |
| 6156 | 46.8633 | 150.557 | 3 | Caloris |
| 6157 | 17.3591 | 149.951 | 3 | Caloris |
| 6158* | -30.7095 | 153.901 | 2 | |
| 6161 | 18.535 | 148.147 | 3 | Caloris |
| 6168* | 26.2547 | 117.85 | 4 | Raditladi |
| 7019 | 41.1319 | -100.813 | 3 | Scarlatti |
| 7031 | 52.5553 | -111.651 | 3 | To Ngov Van |
| 7038 | -21.2169 | -89.1973 | 4 | |
| 7041 | 9.45622 | -137.764 | 3 | |
| 7042 | 4.42281 | -137.8 | n/a | |
| 7044 | -11.7315 | -154.646 | 3 | |
| 7045 | -21.6354 | -156.926 | 2 | Eitoku |
| 7046 | -30.3481 | -155.945 | 2 | |
| 7047 | 8.29851 | -113.526 | 2 | |
| 7049* | -28.3823 | -90.1199 | 4 | Lessing |
| 7051 | -22.0732 | -104.822 | 2 | |
| 7054 | -24.6265 | -156.461 | 4 | |
| 7055 | 42.0109 | -98.5088 | 2 | |
| 7057 | 21.797 | -67.3702 | 4 | |
| 7058 | -24.1195 | -105.021 | 2 | Rumi |
| 7074 | -3.54144 | -136.788 | 0 | |
| 7075 | -8.41716 | -135.495 | 1 | |
| 7090 | 3.80181 | -148.662 | 4 | Tyagaraya |
| 7092 | 24.2694 | -178.97 | 3 | Caloris |
| 7094 | -2.9716 | -147.242 | 4 | Zeami |
| 7096 | 4.58257 | -140.668 | 4 | |
| 7104 | -16.7501 | -161.611 | 1 | Tolstoj |
| 7107 | -19.8725 | -161.07 | 3 | |
| 7109 | -21.0552 | -162.851 | 1 | Tolstoj |
| 7110 | -6.93046 | -113.798 | 3 | |
| 7114 | -13.5333 | -129.994 | 3 | |
| 7115 | -11.6018 | -132.973 | 2 | |
| 7125 | 15.0115 | -112.377 | 2 | Glinka |
| 7141 | -26.7598 | -81.9273 | n/a | |

| Pit Group ID | Central latitude | Central longitude | Crater degradation class | Crater name |
|---|---|---|---|---|
| 7146 | 8.59485 | -67.9205 | 5 | |
| 7160 | -22.8582 | -90.5563 | 3 | |
| 7164 | 5.08245 | -139.488 | 2 | |
| 7165 | 55.9929 | -69.1463 | 1 | |
| 7166 | -20.2439 | -163.391 | 1 | Tolstoj |
| 8008 | 48.3288 | -33.9994 | 2 | |
| 8020 | -58.0857 | -31.6951 | n/a | |
| 8023 | -6.06093 | -13.0714 | 3 | |
| 8024 | 61.8274 | -10.9485 | 4 | Abedin |
| 8025 | 58.8416 | -32.8942 | 3 | |
| 8026 | -44.78 | -12.4139 | 3 | Rilke |
| 8027 | -57.6204 | -37.5289 | 5 | Kuniyoshi |
| 8029 | -29.4306 | -19.1131 | n/a | |
| 8031* | -52.5181 | -40.7896 | 2 | Africanus Norton |
| 8034* | -36.8202 | -10.6917 | 3 | Pigalle |
| 8167 | 27.0474 | -29.5918 | 4 | Geddes |
| 8172 | -27.7333 | -24.5524 | 3 | |
| 8178 | -51.5123 | -27.6924 | 4* | |
| 8183 | 12.1812 | -44.2048 | 1 | |
| 8198 | -55.0961 | -30.0106 | n/a | |
| 8199 | -53.6243 | -31.1497 | n/a | |

# Appendix C. Global catalogue and morphometry of landforms indicating putative explosive volcanism

**Table C-1 Catalogue of endogenic pits on Mercury. Central longitude and latitude indicates the centroid of the pit in decimal degrees. Presence of an associated relatively bright, relatively red-sloped spectral anomaly indicated with a '1' in the 'spectral anomaly' column. Where it is possible the pit was formed by degassing in an ejecta blanket rather than by volcanism, this is indicated with a '1' in the 'Degassing possible' column. This is an updated version of Table S1 in (*Thomas et al.*, 2014c) with sites where pits and/or deposits identified in MESSENGER images released by NASA's Planetary Data System between 5th September 2014 and 5th March 2015 indicated with *.**

| Pit Site ID | Central latitude | Central longitude | Area (km$^2$) | Spectral anomaly | Degassing possible |
|---|---|---|---|---|---|
| 1042 | 4.08837 | -54.382 | 18.86453 | 1 | 0 |
| 1042 | 4.20238 | -54.0281 | 87.06239 | 1 | 0 |
| 1043 | 5.40528 | -55.7995 | 88.20221 | 1 | 0 |
| 1045 | 14.902 | -49.1143 | 652.7852 | 1 | 0 |
| 1045 | 15.4959 | -49.0363 | 24.56669 | 1 | 0 |
| 1045 | 15.7751 | -48.0966 | 82.36618 | 1 | 0 |
| 1046 | 3.7557 | -56.085 | 100.8222 | 1 | 0 |
| 1047 | 25.9591 | -60.2719 | 276.568 | 1 | 0 |
| 1047 | 26.8298 | -59.1193 | 126.9174 | 1 | 0 |
| 1047 | 26.9035 | -59.0082 | 503.5902 | 1 | 0 |
| 1052 | -37.2695 | -61.7383 | 10.00959 | 1 | 0 |
| 1065 | 7.43454 | -51.3165 | 4.788897 | 1 | 1 |
| 1065 | 7.5187 | -51.3707 | 4.389824 | 1 | 1 |
| 1066 | -27.4952 | -48.94 | 254.2301 | 1 | 0 |
| 1067* | 12.4442 | -55.814 | 26.42131 | 1 | 1 |
| 1074 | 45.3868 | -64.5913 | 9.804905 | 1 | 0 |
| 2002 | 27.5251 | 1.19122 | 15.77439 | 1 | 0 |
| 2002* | 27.6079 | 1.46419 | 3.162097 | 1 | 0 |
| 2006 | 17.4012 | -2.75865 | 288.873 | 1 | 0 |
| 2007 | 14.0051 | 3.65481 | 268.8081 | 1 | 0 |
| 2029 | 26.0056 | -4.09383 | 81.00575 | 1 | 1 |
| 2039 | -48.5663 | -6.39417 | 19.10024 | 1 | 0 |
| 2039 | -48.4626 | -6.27948 | 18.04429 | 1 | 0 |
| 2039 | -48.341 | -6.38301 | 16.347 | 1 | 0 |

| Pit Site ID | Central latitude | Central longitude | Area (km$^2$) | Spectral anomaly | Degassing possible |
|---|---|---|---|---|---|
| 2039 | -48.2733 | -6.72796 | 12.59444 | 1 | 0 |
| 2039* | -48.4377 | -6.8116 | 21.08563 | 1 | 0 |
| 2041 | -50.0023 | 5.80077 | 24.79801 | 1 | 0 |
| 2045 | -48.9564 | 2.26688 | 10.0338 | 1 | 0 |
| 2046 | -47.0739 | -6.04293 | 17.60079 | 1 | 1 |
| 2053* | -38.3493 | -7.77438 | 81.61551 | 1 | 0 |
| 3005 | -41.2781 | 88.1545 | 2.998332 | 0 | 0 |
| 3005 | -40.7289 | 87.9334 | 21.37554 | 0 | 0 |
| 3005 | -40.7372 | 88.1522 | 30.37383 | 0 | 0 |
| 3011* | 43.3702 | 82.9767 | 15.06879 | 1 | 0 |
| 3011* | 43.4087 | 82.8831 | 3.765409 | 1 | 0 |
| 3011* | 43.4039 | 83.0984 | 5.752615 | 1 | 0 |
| 3012 | -33.9315 | 97.5767 | 89.14978 | 0 | 0 |
| 3014 | 32.4694 | 88.168 | 202.1485 | 0 | 0 |
| 4001 | 21.5008 | 178.967 | 13.06542 | 1 | 0 |
| 4010 | 25.3162 | -179.867 | 6.712012 | 1 | 0 |
| 4010 | 25.756 | 179.922 | 358.3691 | 1 | 0 |
| 4013 | -40.915 | 174.764 | 12.89715 | 1 | 0 |
| 4013 | -40.5492 | 175.688 | 20.04022 | 1 | 0 |
| 4013 | -39.6482 | 174.77 | 23.03889 | 1 | 0 |
| 4013 | -39.3194 | 176.546 | 32.0712 | 1 | 0 |
| 4013 | -39.0224 | 175.803 | 20.56985 | 1 | 0 |
| 4014 | 58.8284 | 160.717 | 612.0406 | 1 | 0 |
| 4015 | 13.3349 | 163.126 | 32.83073 | 1 | 0 |
| 4015 | 13.8421 | 162.075 | 87.48463 | 1 | 0 |
| 4017 | 60.8055 | 168.064 | 127.9828 | 1 | 0 |
| 4037 | 48.4023 | 161.229 | 20.26158 | 1 | 0 |
| 4038 | 22.9472 | 179.28 | 8.622837 | 1 | 1 |
| 4038 | 23.0891 | 179.668 | 11.11867 | 1 | 1 |
| 4038 | 23.2404 | 179.147 | 2.355275 | 1 | 1 |
| 4040 | -28.1626 | 161.933 | 9.27764 | 1 | 0 |
| 4041 | -24.4981 | -179.231 | 3.881642 | 0 | 0 |
| 4041 | -23.742 | 179.422 | 20.50696 | 1 | 0 |
| 4041 | -23.5484 | 179.508 | 51.06544 | 1 | 0 |
| 4044 | 19.497 | 178.073 | 15.54547 | 1 | 0 |
| 4048 | -25.3783 | 178.18 | 21.73149 | 1 | 0 |
| 4048 | -25.4268 | 177.418 | 78.25462 | 1 | 0 |
| 4048 | -25.0003 | 177.673 | 45.94012 | 1 | 0 |
| 5014 | 34.2655 | 21.77 | 3.014504 | 1 | 1 |

| Pit Site ID | Central latitude | Central longitude | Area (km$^2$) | Spectral anomaly | Degassing possible |
|---|---|---|---|---|---|
| 5014 | 34.6555 | 22.7531 | 1.742592 | 0 | 1 |
| 5014 | 35.0507 | 23.6991 | 30.82182 | 1 | 1 |
| 5014 | 35.1478 | 21.2977 | 17.93408 | 1 | 1 |
| 5014 | 35.5183 | 23.8613 | 9.915051 | 1 | 1 |
| 5014 | 35.7747 | 23.8377 | 1.228106 | 1 | 1 |
| 5014 | 36.2925 | 23.8774 | 9.86591 | 1 | 1 |
| 5014 | 36.3035 | 23.1698 | 11.90965 | 1 | 1 |
| 5014 | 36.6638 | 24.1828 | 6.885469 | 1 | 1 |
| 5016 | 28.3662 | 10.2985 | 314.669 | 1 | 0 |
| 5020 | -51.6599 | 24.4144 | 36.48487 | 1 | 0 |
| 5022 | -19.2551 | 71.4231 | 411.7752 | 1 | 0 |
| 5022 | -18.4914 | 72.0851 | 127.3829 | 1 | 0 |
| 5023 | -21.0378 | 72.4513 | 223.206 | 1 | 0 |
| 5024 | -15.563 | 65.7418 | 146.723 | 1 | 0 |
| 5026 | 28.9602 | 79.2201 | 17.43188 | 0 | 0 |
| 5032 | -3.82215 | 49.9521 | 36.39041 | 0 | 0 |
| 5034 | -0.81852 | 43.8684 | 334.1743 | 1 | 0 |
| 5039 | 3.5413 | 50.9792 | 680.9678 | 1 | 0 |
| 5041 | -7.1784 | 58.7613 | 61.95487 | 0 | 0 |
| 5041 | -6.22304 | 58.2056 | 196.176 | 1 | 0 |
| 5041 | -5.76336 | 58.7187 | 49.51615 | 0 | 0 |
| 5041 | -5.44101 | 58.4486 | 410.0778 | 1 | 0 |
| 5041 | -5.29445 | 57.1044 | 86.25308 | 1 | 0 |
| 5041 | -5.26688 | 57.6485 | 122.5933 | 0 | 0 |
| 5041 | -5.13329 | 57.3852 | 58.96042 | 1 | 0 |
| 5047 | -11.4275 | 55.7186 | 196.0192 | 1 | 0 |
| 5047 | -11.1568 | 54.9073 | 335.3389 | 1 | 0 |
| 5053 | 32.1638 | 22.7564 | 580.9162 | 1 | 0 |
| 5055 | 32.4413 | 21.8351 | 24.53773 | 1 | 1 |
| 5061 | 35.99 | 57.4322 | 716.898 | 1 | 0 |
| 5063 | 37.3144 | 23.6478 | 46.12064 | 1 | 1 |
| 5063 | 37.4611 | 24.2105 | 16.94412 | 1 | 1 |
| 5066 | 36.3186 | 55.2953 | 49.14134 | 1 | 0 |
| 5070 | -37.4978 | 45.6366 | 39.86552 | 1 | 0 |
| 5072 | -32.6985 | 36.1268 | 16.94377 | 1 | 0 |
| 5077 | -11.4984 | 62.3861 | 260.2929 | 1 | 0 |
| 5077 | -11.1304 | 61.6021 | 94.13974 | 1 | 0 |
| 5082 | 35.7954 | 64.0003 | 897.1118 | 1 | 0 |
| 5083 | -34.6046 | 50.0287 | 21.23691 | 1 | 0 |

| Pit Site ID | Central latitude | Central longitude | Area (km$^2$) | Spectral anomaly | Degassing possible |
|---|---|---|---|---|---|
| 5083 | -33.0912 | 49.9459 | 173.7564 | 1 | 0 |
| 5084 | -52.8462 | 38.2062 | 154.3876 | 1 | 0 |
| 5084 | -52.6713 | 38.643 | 40.15151 | 1 | 0 |
| 5085 | -49.8341 | 10.7517 | 99.38961 | 1 | 0 |
| 5086 | -9.36005 | 52.4081 | 441.4786 | 1 | 0 |
| 5086 | -8.35181 | 51.8322 | 113.1159 | 1 | 0 |
| 5087 | 35.9667 | 51.2982 | 24.68408 | 1 | 0 |
| 5087 | 35.9327 | 51.0856 | 68.76435 | 1 | 0 |
| 5090 | -70.6439 | 13.0063 | 97.24749 | 1 | 0 |
| 5091 | -68.8936 | 23.6707 | 107.6695 | 1 | 0 |
| 5092 | -53.0139 | 17.7136 | 83.02365 | 1 | 0 |
| 5092 | -52.5711 | 18.0513 | 32.5204 | 1 | 0 |
| 5092 | -52.3519 | 17.6191 | 30.3719 | 1 | 0 |
| 5092 | -52.3279 | 17.3939 | 25.22887 | 1 | 0 |
| 5093 | -48.4839 | 38.1499 | 156.5249 | 0 | 0 |
| 5094* | -36.1918 | 41.3495 | 20.5583 | 1 | 0 |
| 5094 | -36.353 | 41.4743 | 2.835779 | 1 | 0 |
| 5094 | -36.2014 | 41.1095 | 8.95201 | 0* | 0 |
| 5095 | -43.7973 | 19.7504 | 9.046562 | 1 | 0 |
| 5096 | 7.38428 | 32.3871 | 12.86678 | 1 | 1 |
| 5096 | 8.21225 | 32.63 | 12.31144 | 1 | 1 |
| 5096 | 8.63074 | 33.2101 | 4.932704 | 1 | 1 |
| 5096 | 8.63894 | 33.4632 | 12.47492 | 1 | 1 |
| 5097 | -66.4559 | 76.8972 | 10.20287 | 1 | 0 |
| 5097 | -66.5926 | 76.3692 | 2.558816 | 1 | 0 |
| 5097 | -66.7772 | 76.1853 | 4.877752 | 1 | 0 |
| 5097 | -67.0711 | 75.8393 | 15.24258 | 1 | 0 |
| 5103 | -48.3247 | 11.8058 | 21.51411 | 1 | 0 |
| 5104 | -53.0162 | 20.171 | 13.66595 | 1 | 0 |
| 6007 | 48.6929 | 159.48 | 53.10083 | 1 | 0 |
| 6014 | 38.2797 | 141.471 | 16.79028 | 1 | 0 |
| 6016 | 13.588 | 159.434 | 30.34253 | 1 | 0 |
| 6016 | 13.7878 | 158.753 | 6.447884 | 1 | 0 |
| 6016 | 14.0926 | 159.941 | 51.66013 | 1 | 0 |
| 6016 | 14.3359 | 159.497 | 12.77865 | 1 | 0 |
| 6016 | 14.3745 | 158.945 | 26.58155 | 1 | 0 |
| 6016 | 14.4919 | 160.792 | 19.83907 | 1 | 0 |
| 6016 | 15.006 | 159.578 | 29.0071 | 1 | 0 |
| 6016 | 15.1964 | 160.167 | 9.100393 | 1 | 0 |

| Pit Site ID | Central latitude | Central longitude | Area (km$^2$) | Spectral anomaly | Degassing possible |
|---|---|---|---|---|---|
| 6044 | 48.4944 | 139.671 | 275.0594 | 0 | 0 |
| 6049 | 42.4332 | 121.493 | 67.56163 | 0 | 0 |
| 6060 | -5.20355 | 143.593 | 173.7042 | 1 | 0 |
| 6062 | 21.5652 | 145.539 | 89.27543 | 1 | 0 |
| 6062 | 21.8254 | 145.322 | 138.9633 | 1 | 0 |
| 6062 | 21.8296 | 145.806 | 131.2972 | 1 | 0 |
| 6062 | 22.3422 | 146.202 | 347.1419 | 1 | 0 |
| 6064 | -11.0137 | 140.58 | 190.8889 | 1 | 0 |
| 6067* | 16.2076 | 157.299 | 29.56673 | 1 | 0 |
| 6067 | 16.6477 | 156.914 | 8.630827 | 1 | 0 |
| 6071 | 18.1892 | 149.297 | 91.65099 | 1 | 0 |
| 6071 | 18.5236 | 149.558 | 75.27367 | 1 | 0 |
| 6071 | 18.95 | 149.699 | 122.8684 | 0 | 0 |
| 6071 | 19.3648 | 150.156 | 69.15387 | 1 | 0 |
| 6074 | -28.2617 | 146.911 | 86.97006 | 1 | 0 |
| 6074 | -28.1222 | 146.771 | 39.27019 | 1 | 0 |
| 6075 | -52.5569 | 125.647 | 65.11362 | 1* | 0 |
| 6078 | -9.41083 | 154.49 | 21.77587 | 0 | 0 |
| 6078 | -9.13524 | 154.518 | 51.43865 | 1 | 0 |
| 6083 | -28.124 | 136.556 | 47.77071 | 1 | 0 |
| 6084 | 18.3964 | 155.979 | 85.68499 | 0 | 0 |
| 6084 | 18.7995 | 155.201 | 98.384 | 0 | 0 |
| 6086 | -59.7302 | 142.053 | 32.7899 | 1 | 0 |
| 6086 | -59.3725 | 140.439 | 17.64574 | 1 | 0 |
| 6087 | 28.0165 | 138.617 | 40.43325 | 1 | 0 |
| 6090 | -43.7408 | 105.786 | 10.36436 | 1 | 1 |
| 6093 | -42.9966 | 142.619 | 64.47147 | 0 | 0 |
| 6094 | -33.4487 | 136.77 | 43.31107 | 0 | 0 |
| 6096 | -59.905 | 145.325 | 98.92932 | 1 | 0 |
| 6096* | -59.5678 | 145.037 | 14.58474 | 1 | 0 |
| 6096 | -59.391 | 144.899 | 5.595356 | 1 | 0 |
| 6099 | 45.3181 | 144.352 | 26.42387 | 1 | 0 |
| 6100* | -60.6238 | 149.194 | 18.77683 | 1 | 0 |
| 6102 | 28.1036 | 144.639 | 64.39059 | 1* | 0 |
| 6111 | 24.2069 | 148.383 | 176.3917 | 1 | 0 |
| 6112 | 58.7797 | 110.368 | 45.73248 | 0 | 0 |
| 6112 | 59.1613 | 109.692 | 243.3672 | 0 | 0 |
| 6113 | 36.606 | 110.168 | 119.3808 | 1 | 0 |
| 6114 | 60.0608 | 121.052 | 46.56823 | 0 | 0 |

| Pit Site ID | Central latitude | Central longitude | Area (km$^2$) | Spectral anomaly | Degassing possible |
|---|---|---|---|---|---|
| 6115 | 58.2096 | 101.077 | 322.078 | 1 | 0 |
| 6117 | -55.4395 | 142.523 | 122.1151 | 1 | 0 |
| 6117 | -55.2202 | 142.31 | 11.84315 | 1 | 0 |
| 6117 | -55.0796 | 142.766 | 194.5809 | 1 | 0 |
| 6118 | -38.3967 | 129.22 | 39.59973 | 0 | 0 |
| 6119 | -45.7779 | 134.831 | 42.69061 | 1 | 0 |
| 6119 | -45.4469 | 134.807 | 6.867595 | 1 | 0 |
| 6119 | -45.5128 | 135.441 | 86.29905 | 1 | 0 |
| 6119 | -45.152 | 135.074 | 17.51841 | 1 | 0 |
| 6119 | -44.8283 | 134.653 | 23.77232 | 1 | 0 |
| 6119 | -44.7587 | 134.989 | 32.32744 | 1 | 0 |
| 6120 | -40.3315 | 111.341 | 361.583 | 1 | 0 |
| 6123 | -41.9587 | 115.121 | 182.8863 | 1 | 0 |
| 6124 | -51.5263 | 136.546 | 23.04453 | 1 | 0 |
| 6125 | -64.4797 | 144.777 | 14.21397 | 1 | 0 |
| 6125 | -64.2192 | 142.995 | 10.40878 | 1 | 0 |
| 6125 | -64.2007 | 143.589 | 20.67439 | 0 | 0 |
| 6125 | -63.9879 | 143.49 | 10.52402 | 1 | 0 |
| 6125 | -63.8951 | 142.663 | 13.49253 | 1 | 0 |
| 6125 | -64.0419 | 142.066 | 196.8629 | 1 | 0 |
| 6125 | -63.8296 | 143.079 | 36.60424 | 1 | 0 |
| 6125 | -63.6888 | 142.588 | 22.95423 | 1 | 0 |
| 6125 | -63.5328 | 142.566 | 7.930583 | 1 | 0 |
| 6125 | -63.4652 | 142.132 | 34.29798 | 1 | 0 |
| 6125 | -63.4067 | 142.744 | 9.120362 | 1 | 0 |
| 6125 | -63.189 | 142.595 | 23.31592 | 1 | 0 |
| 6125 | -63.0423 | 142.487 | 22.3337 | 1 | 0 |
| 6125 | -62.8526 | 142.489 | 71.17263 | 1 | 0 |
| 6125 | -62.2192 | 142.073 | 15.15347 | 1 | 0 |
| 6125 | -62.0903 | 144.343 | 55.1077 | 1 | 0 |
| 6126 | -65.5415 | 147.641 | 45.62511 | 1 | 0 |
| 6126 | -65.2053 | 147.758 | 170.7535 | 1 | 0 |
| 6127 | -56.3414 | 143.904 | 50.93443 | 1 | 0 |
| 6128 | -60.5485 | 137.566 | 14.84667 | 0 | 0 |
| 6128 | -60.3209 | 137.584 | 5.07265 | 0 | 0 |
| 6128 | -60.0736 | 138.213 | 86.57494 | 0 | 0 |
| 6129 | -66.0803 | 154.141 | 69.48603 | 1 | 0 |
| 6129 | -66.0447 | 154.9 | 82.91517 | 1 | 0 |
| 6129 | -65.7649 | 154.412 | 100.1156 | 1 | 0 |

| Pit Site ID | Central latitude | Central longitude | Area (km$^2$) | Spectral anomaly | Degassing possible |
|---|---|---|---|---|---|
| 6129 | -65.7028 | 153.743 | 83.08073 | 1 | 0 |
| 6130 | -38.6292 | 137.633 | 38.31018 | 1 | 0 |
| 6131 | -38.6423 | 133.703 | 110.1693 | 1 | 0 |
| 6132 | -38.9635 | 134.969 | 43.08629 | 1 | 0 |
| 6132 | -38.8605 | 135.676 | 36.24633 | 1 | 0 |
| 6132 | -38.3249 | 135.266 | 42.70663 | 0 | 0 |
| 6133 | -55.0409 | 147.151 | 21.47244 | 1 | 0 |
| 6134 | -40.1199 | 124.853 | 91.4736 | 1 | 0 |
| 6134 | -39.793 | 124.359 | 9.713194 | 1 | 0 |
| 6136 | -52.2601 | 139.357 | 19.45522 | 1 | 0 |
| 6136 | -52.0487 | 138.572 | 42.33988 | 1 | 0 |
| 6136 | -51.9676 | 139.636 | 34.56625 | 1 | 0 |
| 6136 | -51.8087 | 138.585 | 41.09055 | 1 | 0 |
| 6136 | -51.7253 | 138.946 | 7.732008 | 1 | 0 |
| 6149 | -35.5485 | 143.45 | 5.267842 | 1 | 0 |
| 6149 | -35.1584 | 142.244 | 17.24358 | 1 | 0 |
| 6149 | -34.4755 | 143.483 | 1.318177 | 1 | 0 |
| 6149 | -34.3774 | 143.472 | 2.358897 | 1 | 0 |
| 6151 | -32.5761 | 151.114 | 12.38449 | 1 | 1 |
| 6153 | 17.6497 | 152.572 | 8.914356 | 1 | 1 |
| 6155 | 18.5101 | 150.725 | 2.897938 | 1 | 0 |
| 6155 | 18.5642 | 150.668 | 8.276684 | 1 | 0 |
| 6155 | 18.66 | 151.275 | 9.300803 | 1 | 0 |
| 6156 | 46.8633 | 150.557 | 5.299352 | 1 | 0 |
| 6157 | 17.3591 | 149.951 | 8.030516 | 1 | 0 |
| 6158* | -30.7522 | 153.977 | 1.305446 | 1 | 0 |
| 6158* | -30.7478 | 153.874 | 1.494892 | 1 | 0 |
| 6158* | -30.7198 | 153.858 | 1.096179 | 1 | 0 |
| 6158* | -30.7126 | 153.957 | 1.516913 | 1 | 0 |
| 6158* | -30.6749 | 153.922 | 1.089537 | 1 | 0 |
| 6158* | -30.6698 | 153.862 | 1.211199 | 1 | 0 |
| 6158* | -30.6648 | 153.828 | 0.976398 | 1 | 0 |
| 6160 | 18.5692 | 148.72 | 45.51012 | 0 | 0 |
| 6160 | 19.4503 | 148.342 | 167.7064 | 0 | 0 |
| 6161 | 18.2055 | 148.164 | 52.41707 | 1 | 0 |
| 6161 | 19.2969 | 148.108 | 22.51862 | 1 | 0 |
| 6168* | 26.2547 | 117.85 | 7.567749 | 1 | 1 |
| 7019 | 40.4394 | -100.123 | 79.11648 | 1 | 0 |
| 7019 | 41.2396 | -100.625 | 468.7117 | 1 | 0 |

| Pit Site ID | Central latitude | Central longitude | Area (km$^2$) | Spectral anomaly | Degassing possible |
|---|---|---|---|---|---|
| 7019 | 41.3329 | -101.809 | 53.64364 | 1 | 0 |
| 7019 | 41.0289 | -102.087 | 69.82381 | 1 | 0 |
| 7026 | 35.798 | -111.245 | 845.1376 | 0 | 0 |
| 7031 | 52.5553 | -111.651 | 323.186 | 1 | 0 |
| 7038 | -21.2169 | -89.1973 | 401.7312 | 1 | 0 |
| 7041 | 9.45622 | -137.764 | 97.74036 | 1 | 0 |
| 7042 | 4.42281 | -137.8 | 211.1757 | 1 | 0 |
| 7043 | -47.6161 | -136.332 | 232.4098 | 0 | 0 |
| 7044 | -11.749 | -154.679 | 16.89297 | 1 | 0 |
| 7044 | -11.6991 | -154.584 | 9.136796 | 1 | 0 |
| 7045 | -21.6354 | -156.926 | 65.75627 | 1 | 0 |
| 7046 | -30.4263 | -155.846 | 21.52572 | 1 | 0 |
| 7046 | -30.2902 | -156.018 | 29.10431 | 1 | 0 |
| 7047 | 8.29851 | -113.526 | 105.837 | 1 | 0 |
| 7049* | -28.3823 | -90.1199 | 21.85495 | 1 | 0 |
| 7050 | 0.581327 | -161.901 | 75.39834 | 0 | 0 |
| 7051 | -22.215 | -104.663 | 34.33868 | 1 | 0 |
| 7051 | -21.9876 | -105.06 | 26.2084 | 1 | 0 |
| 7051 | -21.978 | -104.794 | 27.69186 | 1 | 0 |
| 7052 | -57.5395 | -101.703 | 121.3491 | 0 | 0 |
| 7054 | -24.6184 | -156.534 | 12.66526 | 1 | 0 |
| 7054 | -24.6375 | -156.361 | 9.198111 | 1 | 0 |
| 7055 | 42.0109 | -98.5088 | 13.34558 | 1 | 0 |
| 7057 | 21.797 | -67.3702 | 195.0987 | 1 | 0 |
| 7058 | -24.1195 | -105.021 | 92.51473 | 1 | 0 |
| 7074 | -3.54144 | -136.788 | 422.154 | 1 | 0 |
| 7075 | -8.41716 | -135.495 | 238.3135 | 1 | 0 |
| 7090 | 3.80181 | -148.662 | 66.15683 | 1 | 0 |
| 7092 | 23.3835 | -178.354 | 63.47738 | 1 | 0 |
| 7092 | 23.7605 | -178.287 | 34.66247 | 1 | 0 |
| 7092 | 23.8972 | -179.188 | 153.7185 | 1 | 0 |
| 7092 | 24.0086 | -178.294 | 30.40793 | 1 | 0 |
| 7092 | 24.2643 | -178.919 | 296.4913 | 1 | 0 |
| 7092 | 24.6021 | -179.516 | 37.58171 | 1 | 0 |
| 7092 | 24.9394 | -179.203 | 189.0515 | 1 | 0 |
| 7094 | -2.99178 | -147.151 | 12.05755 | 1 | 0 |
| 7094 | -2.95818 | -147.302 | 18.13155 | 1 | 0 |
| 7096 | 4.58257 | -140.668 | 22.81767 | 1 | 0 |
| 7097 | 6.69571 | -142.178 | 148.3202 | 0 | 0 |

| Pit Site ID | Central latitude | Central longitude | Area (km$^2$) | Spectral anomaly | Degassing possible |
|---|---|---|---|---|---|
| 7104 | -16.7501 | -161.611 | 154.7117 | 1 | 0 |
| 7107 | -19.8725 | -161.07 | 26.04765 | 1 | 0 |
| 7109 | -21.0918 | -162.918 | 56.04196 | 1 | 0 |
| 7109 | -20.9983 | -162.674 | 10.65109 | 1 | 0 |
| 7109 | -20.915 | -162.666 | 10.34543 | 1 | 0 |
| 7110 | -6.93046 | -113.798 | 167.2594 | 1 | 0 |
| 7114 | -13.5333 | -129.994 | 89.00266 | 1 | 0 |
| 7115 | -11.5936 | -132.638 | 33.98249 | 1 | 0 |
| 7115 | -11.6032 | -133.03 | 200.6936 | 1 | 0 |
| 7125 | 15.0115 | -112.377 | 195.8582 | 1 | 0 |
| 7141 | -26.7598 | -81.9273 | 699.2833 | 1 | 0 |
| 7146 | 8.59485 | -67.9205 | 33.77271 | 1 | 0 |
| 7160 | -22.8582 | -90.5563 | 867.3482 | 1 | 0 |
| 7162 | 52.501 | -79.3879 | 42.39694 | 0 | 0 |
| 7162 | 52.2481 | -79.555 | 103.8198 | 0 | 0 |
| 7164 | 5.08245 | -139.488 | 5.884468 | 1 | 0 |
| 7165 | 55.9871 | -69.2132 | 13.0608 | 1 | 1 |
| 7165 | 56.0081 | -68.9724 | 5.024762 | 1 | 1 |
| 7166 | -20.2439 | -163.391 | 5.293476 | 1 | 0 |
| 8008 | 48.3288 | -33.9994 | 666.9519 | 1 | 0 |
| 8020 | -59.3734 | -34.4141 | 11.66667 | 1 | 0 |
| 8020 | -59.1551 | -33.9789 | 22.6945 | 1 | 0 |
| 8020 | -59.0245 | -33.1091 | 38.27891 | 1 | 0 |
| 8020 | -58.8822 | -32.5909 | 26.3377 | 1 | 0 |
| 8020 | -58.756 | -32.642 | 15.13003 | 1 | 0 |
| 8020 | -57.9739 | -32.1108 | 119.8899 | 1 | 0 |
| 8020 | -57.8108 | -29.4245 | 8.477087 | 1 | 0 |
| 8020 | -57.86 | -29.8127 | 35.04751 | 1 | 0 |
| 8020 | -57.5594 | -30.7215 | 22.92498 | 1 | 0 |
| 8020 | -57.664 | -32.9988 | 59.96621 | 1 | 0 |
| 8020 | -57.4578 | -29.1158 | 79.28192 | 1 | 0 |
| 8023 | -6.06093 | -13.0714 | 94.6956 | 1 | 0 |
| 8024 | 61.8274 | -10.9485 | 30.63226 | 1 | 0 |
| 8025 | 58.8416 | -32.8942 | 167.7202 | 1 | 0 |
| 8026 | -44.8601 | -12.2601 | 26.77085 | 1 | 0 |
| 8026 | -44.7721 | -12.4973 | 57.8789 | 1 | 0 |
| 8026 | -44.5718 | -12.3276 | 8.132266 | 1 | 0 |
| 8027 | -57.6428 | -37.5427 | 9.746543 | 1 | 0 |
| 8027 | -57.5339 | -37.4753 | 2.528854 | 1 | 0 |

| Pit Site ID | Central latitude | Central longitude | Area (km$^2$) | Spectral anomaly | Degassing possible |
|---|---|---|---|---|---|
| 8029 | -29.4306 | -19.1131 | 236.3528 | 1 | 0 |
| 8031* | -52.5568 | -40.9401 | 3.243678 | 1 | 0 |
| 8031* | -52.5411 | -40.7915 | 3.678445 | 1 | 0 |
| 8031* | -52.4832 | -40.8463 | 3.511014 | 1 | 0 |
| 8031* | -52.4829 | -40.5129 | 2.511593 | 1 | 0 |
| 8034* | -36.8427 | -10.7598 | 3.795242 | 1 | 0 |
| 8034* | -36.8092 | -10.6581 | 7.707808 | 1 | 0 |
| 8167 | 27.0474 | -29.5918 | 468.3054 | 1 | 0 |
| 8172 | -27.7333 | -24.5524 | 10.03598 | 1 | 0 |
| 8178 | -52.3353 | -28.4654 | 18.16994 | 1 | 0 |
| 8178 | -51.666 | -28.176 | 39.77336 | 1 | 0 |
| 8178 | -51.4155 | -27.9447 | 28.12622 | 1 | 0 |
| 8178 | -51.4066 | -27.4618 | 176.8593 | 1 | 0 |
| 8183 | 12.1812 | -44.2048 | 17.31335 | 1 | 0 |
| 8198 | -55.0961 | -30.0106 | 224.5492 | 1 | 0 |
| 8199 | -53.912 | -31.3136 | 121.2622 | 1 | 0 |
| 8199 | -53.0449 | -30.8198 | 61.47804 | 1 | 0 |

**Table C-2 Catalogue of relatively bright, red deposits judged potentially pyroclastic. Pit site ID is as listed in Table C-1. This is an updated version of Table S2 in (*Thomas et al.*, 2014c). * indicates where MESSENGER images released by NASA's Planetary Data System between 5th September 2014 and 5th March 2015 reveal a previously-unidentified deposit or a different extent to the published value.**

| Pit site ID | Deposit Area (km$^2$) |
|---|---|
| 1042 | 2548.533* |
| 1043 | 2847.889 |
| 1045 | 9743.43* |
| 1046 | 219.023 |
| 1047 | 11483.93 |
| 1052 | 202.354 |
| 1065 | 277.176* |
| 1066 | 1662.605 |
| 1067* | 62.641 |
| 1074 | 863.916 |
| 2002 | 183.178* |
| 2006 | 3329.282 |
| 2007 | 2031.571 |

| Pit site ID | Deposit Area (km$^2$) |
|---|---|
| 2029 | 1477.379* |
| 2039 | 1371.818 |
| 2041 | 860.909 |
| 2045 | 423.246 |
| 2046 | 274.757 |
| 2053* | 348.926 |
| 3011* | 335.36 |
| 4001 | 128.727 |
| 4010 | 2092.513 |
| 4010 | 1072.234 |
| 4013 | 249.534 |
| 4013 | 231.395 |
| 4013 | 86.624 |

| Pit site ID | Deposit Area (km²) |
|---|---|
| 4013 | 29.396 |
| 4013 | 29.219 |
| 4014 | 2650.123 |
| 4015 | 5210.971 |
| 4017 | 701.001 |
| 4037 | 79.067 |
| 4038 | 497.569 |
| 4040 | 949.762 |
| 4041 | 898.487 |
| 4041 | 256.306 |
| 4044 | 38.838 |
| 4048 | 375.763 |
| 4048 | 345.355 |
| 4048 | 256.744 |
| 5014 | 824.948 |
| 5014 | 332.608 |
| 5014 | 221.435 |
| 5014 | 202.307 |
| 5014 | 80.526 |
| 5014 | 42.305 |
| 5016 | 942.783 |
| 5020 | 528.897 |
| 5022 | 664.448 |
| 5022 | 268.377 |
| 5023 | 1328.079 |
| 5024 | 673.531 |
| 5034 | 1961.561 |
| 5039 | 7581.485 |
| 5041 | 688.131 |
| 5041 | 504.381 |
| 5041 | 396.54 |
| 5047 | 351.884 |
| 5047 | 58.765 |
| 5053 | 1314.562 |
| 5055 | 657.446 |
| 5061 | 8718.925 |
| 5063 | 716.534 |
| 5066 | 142.483 |
| 5070 | 595.23 |
| 5072 | 136.453 |

| Pit site ID | Deposit Area (km²) |
|---|---|
| 5077 | 1483.78 |
| 5082 | 38589.11 |
| 5083 | 1235.365 |
| 5083 | 672.782 |
| 5084 | 2264.616 |
| 5085 | 2182.915 |
| 5086 | 1196.033 |
| 5086 | 850.09 |
| 5087 | 179.364 |
| 5090 | 534.135 |
| 5091 | 283.142 |
| 5092 | 3229.815 |
| 5094 | 96.056 |
| 5094 | 62.334 |
| 5095 | 848.608 |
| 5096 | 1130.488 |
| 5096 | 823.183 |
| 5096 | 51.22 |
| 5097 | 599.161 |
| 5103 | 824.564 |
| 5104 | 424.303 |
| 6007 | 282.903 |
| 6014 | 646.006 |
| 6016 | 5968.49 |
| 6016 | 108.749 |
| 6060 | 225.924 |
| 6062 | 2507.632 |
| 6062 | 1171.808 |
| 6064 | 124.291 |
| 6064 | 46.374 |
| 6067 | 3027.833 |
| 6071 | 662.424 |
| 6071 | 69.679 |
| 6074 | 186.401 |
| 6075* | 1555.523 |
| 6078 | 120.294 |
| 6083 | 226.471 |
| 6086 | 163.135 |
| 6086 | 14.689 |
| 6087 | 108.062 |

| Pit site ID | Deposit Area (km²) |
|---|---|
| 6090 | 220.669 |
| 6096 | 944.689 |
| 6099 | 81.204 |
| 6100* | 87.671 |
| 6102* | 166.32 |
| 6111 | 418.644 |
| 6113 | 415.005 |
| 6115 | 334.105 |
| 6117 | 485.137 |
| 6119 | 1527.966 |
| 6120 | 817.262* |
| 6123 | 248.592 |
| 6124 | 52.941* |
| 6125 | 4452.764 |
| 6125 | 437.875 |
| 6125 | 154.926 |
| 6126 | 661.386 |
| 6127 | 3062.24 |
| 6129 | 2476.359 |
| 6130 | 87.774 |
| 6131 | 600.378 |
| 6132 | 616.017 |
| 6133 | 69.758 |
| 6134 | 544.625 |
| 6136 | 1455.503 |
| 6149 | 283.794 |
| 6149 | 253.345 |
| 6149 | 165.766 |
| 6149 | 150.661 |
| 6149 | 10.668 |
| 6151 | 191.724 |
| 6153 | 108.256 |
| 6155 | 507.263 |
| 6155 | 55.225 |
| 6156 | 161.829 |
| 6157 | 192.188 |
| 6158* | 84.738 |
| 6160 | 680.515 |
| 6160 | 173.04* |
| 6160 | 82.577 |

| Pit site ID | Deposit Area (km²) |
|---|---|
| 6168* | 55.642 |
| 7019 | 4089.251* |
| 7031 | 1848.849 |
| 7038 | 6989.805 |
| 7041 | 1192.484 |
| 7042 | 731.299 |
| 7044 | 174.361 |
| 7045 | 280.279 |
| 7046 | 499.613 |
| 7047 | 1648.258 |
| 7049* | 48.787 |
| 7051 | 1047.355 |
| 7054 | 157.554 |
| 7055 | 1098.071 |
| 7057 | 3485.665 |
| 7058 | 2358.002 |
| 7074 | 23181.08 |
| 7075 | 2966.497 |
| 7090 | 417.248 |
| 7092 | 11165.961* |
| 7092 | 78.908 |
| 7094 | 1053.608 |
| 7096 | 413.46 |
| 7104 | 1835.675 |
| 7107 | 559.678 |
| 7109 | 728.461 |
| 7110 | 633.923 |
| 7114 | 190.793 |
| 7115 | 110.035 |
| 7125 | 1730.975 |
| 7141 | 2122.314 |
| 7146 | 1820.975 |
| 7160 | 4214.859 |
| 7164 | 67.089 |
| 7165 | 242.038 |
| 7166 | 321.391 |
| 8008 | 1875.548 |
| 8020 | 21035* |
| 8023 | 2086.88 |
| 8024 | 610.964 |

| Pit site ID | Deposit Area (km$^2$) |
|---|---|
| 8025 | 419.7 |
| 8026 | 1228.146 |
| 8027 | 955.305* |
| 8029 | 532.015 |
| 8031* | 357.874 |
| 8034* | 339.974 |
| 8167 | 2331.53 |
| 8172 | 140.18 |
| 8178 | 4360.434* |
| 8183 | 247.876 |
| 8198 | 4363.344* |
| 8199 | 2957.22* |

**Table C-3 Endogenic pits for which I have obtained topographic data. Topographic data quality is indicated by 5 = MLA track, 4 = DEM constrained by several MLA tracks, 3 = DEM constrained by a single MLA track, 2 = DEM unconstrained by MLA points (highest to lowest quality). Data sources are MESSENGER products from which depth and volume values were derived. This is an updated version of Table S3 in (*Thomas et al.*, 2014c) with values added and updated on the basis of topographic products created after publication indicated by *.**

| Pit Site ID | Pit/Host crater name | Pit location in group | DEM resolution | Depth (km) | Volume ($km^3$) | Basis for volume calculation | Topographic data quality (max) | Data source |
|---|---|---|---|---|---|---|---|---|
| 1043 | | | 659 | 0.5 | 14.75* | DEM | 3 | EW0228630864G, EW0243826316G |
| 1045 | Lermontov | N | 802 | 0.4 | 22.26 | DEM | 3 | EW1005485472G, EW1005427796G |
| 2006 | Hemingway | S | 225 | 1.1 | 73.34 | DEM | 3 | EN0235851617M, EN0220847851M |
| 2006 | Hemingway | E | 225 | 1.1 | 45.95 | DEM | 3 | EN0235851617M, EN0220847851M |
| 2007 | | | 368 | 1.0 | 15.90 | DEM | 3 | EN0220502050M, EN0220588493M |
| 2039 | | W | 441 | 0.7 | 6.05 | Cone | 2 | EN0238190873M, EN0253479661M |
| 2039 | | NW | 441 | 0.6 | 3.18 | Cone | 2 | EN0238190873M, EN0253479661M |
| 2039 | | E | 441 | 0.2 | 1.47 | Cone | 2 | EN0238190873M, EN0253479661M |
| 2039 | | SE | 441 | 0.4 | 2.55 | Cone | 2 | EN0238190873M, EN0253479661M |
| 4014 | Navoi | | 649 | 2.4 | 589.30 | DEM | 5 | Interpolation between 16 MLA tracks |
| 4017 | | S | | 0.8 | 64.09 | Hemiellipsoid | 5 | MLASCIRDR1104011436 |
| 4017 | | N | | 0.6 | 20.73 | Hemiellipsoid | 5 | MLASCIRDR1304061605 |
| 4041* | Hauptmann | | 699 | 0.2 | 9.60 | DEM | | EN0213062201M, EN0213235966M |
| 5023 | AP3 | | 486 | 1.3 | 78.38 | DEM | 2 | EN0234067412M, EN0219092124M |
| 5032 | | | 570 | 0.4 | 5.75 | DEM | 3 | EN0219561077M, EN0219391185M |

| Pit Site ID | Pit/Host crater name | Pit location in group | DEM resolution | Depth (km) | Volume (km$^3$) | Basis for volume calculation | Topographic data quality (max) | Data source |
|---|---|---|---|---|---|---|---|---|
| 5053 | | | 728 | 1.9 | 432.68 | DEM | 4 | EW0250391388G, EW0235215701G |
| 5061 | N Rachmaninoff | | 568 | 2.7 | 1026.82 | DEM | 4 | EW1003930329G, EW0254971314G |
| 5066 | | | 615 | 0.3 | 5.50 | DEM | 4 | EW0255000136G, EW0254827390G |
| 5070 | | | 764 | 0.2 | 3.46* | DEM | 2 | EW0222277823G, EN1004273305M |
| 5082 | NE Rachmaninoff | N | | 4.0 | | | 5 | MLASCIRDR1207300710 |
| 5082 | NE Rachmaninoff | S | 665 | 2.0 | 1268.30 | DEM (total pit) | 4 | EW0234664220G, EW0249959465G |
| 5087 | | | 700 | 1.5 | 16.79 | Cone | 3 | EW0254884985G, EW0239956629G |
| 5093 | | W | 623 | 0.5 | 13.19 | Cone | 2 | EN0250039904M, EN0235125575M |
| 5093 | | SE | 623 | 0.9 | 9.19 | Cone | 2 | EN0250039904M, EN0235125575M |
| 6062 | RS-03 | | 880 | 1.2 | 140.52 | DEM | 4 | EW0235938952G, EW0235981373G |
| 6075 | Neruda | | 589 | 0.4 | 7.96* | DEM | 2 | EN0246508161M, EN0231527613M |
| 6083* | | E | 366 | 0.1 | 1.23 | Cone | 2 | EN0215939355M, EN0231526895M |
| 6083* | | N | 366 | 0.2 | 1.07 | Cone | 2 | EN0215939355M, EN0231526895M |
| 6094 | | N | 443 | 0.3 | 3.30 | Hemiellipsoid | 2 | EN0251345872M, EN0250971719M |
| 6117 | | N | 365 | 2.1 | 155.27 | DEM | 2 | EN0231441617M, EN0245930844M |
| 6117 | | S | 365 | 1.5 | 78.16 | DEM | 2 | EN0231441617M, EN0245930844M |
| 6119* | Sher-Gil | NW | 294 | 0.4 | 3.50 | DEM | 2 | EN0231267850M, EN0246045790M |
| 6119* | Sher-Gil | NE | 294 | 0.2 | 3.71 | DEM | 2 | EN0231267850M, EN0246045790M |
| 6119* | Sher-Gil | W | 294 | 0.1 | 0.31 | DEM | 2 | EN0231267850M, EN0246045790M |
| 6119* | Sher-Gil | SW | 294 | 0.6 | 11.48 | DEM | 2 | EN0231267850M, EN0246045790M |

| Pit Site ID | Pit/Host crater name | Pit location in group | DEM resolution | Depth (km) | Volume (km$^3$) | Basis for volume calculation | Topographic data quality (max) | Data source |
|---|---|---|---|---|---|---|---|---|
| 6119* | Sher-Gil | SE | 294 | 0.8 | 38.81 | DEM | 2 | EN0231267850M, EN0246045790M |
| 6120 | | | 531 | 1.3 | 172.84 | DEM | 2 | EN0216331093M, EN0231654904M |
| 6123 | | | 655 | 0.8 | 77.91 | DEM | 2 | EN0216331227M, EN0247054707M |
| 6129 | | NE | 536 | 1.1 | 31.00 | DEM | 2 | EN0246164455M, EN0231615010M |
| 6129 | | NW | 536 | 0.9 | 40.25 | DEM | 2 | EN0246164455M, EN0231615010M |
| 6129 | | SW | 536 | 0.7 | 16.40 | DEM | 2 | EN0246164455M, EN0231615010M |
| 6129 | | E | 536 | 0.6 | 25.15 | DEM | 2 | EN0246164455M, EN0231615010M |
| 6133* | | | 574 | 0.2 | 1.23 | Cone | 2 | EN0261950309M, EN0216680289M |
| 6136* | | WNW | 604 | 0.5 | 7.58 | DEM | 2 | EN0248514857M, EN1012995880M |
| 6136* | | W | 604 | 0.6 | 10.16 | DEM | 2 | EN0248514857M, EN1012995880M |
| 6136* | | NW | 604 | 0.1 | 0.08 | Cone | 2 | EN0248514857M, EN1012995880M |
| 6136* | | N | 604 | 0.2 | 1.88 | DEM | 2 | EN0248514857M, EN1012995880M |
| 6136* | | S | 604 | 0.1 | 0.83 | Cone | 2 | EN0248514857M, EN1012995880M |
| 7026 | Gibran | | 751 | 1.8 | 727.78 | DEM | 5 | EW0242338280G, EW0226964416G |
| 7031 | To Ngoc Van | N | 635 | 2.1 | 223.98 | DEM | 5 | EN0257560167M, EN0211454949M |
| 7038 | | | 675 | 3.2 | 453.87 | DEM | 2 | EN0211497583M, EN0241246615M |
| 7041* | | | 418 | 0.2 | 5.62 | Cone | 2 | EW0247510340G,EW0262632589G |
| 7042 | | NE | 351 | 1.8 | 144.61 | DEM | 3 | EN0242462429M, EN0227217474M |
| 7050 | | | 372 | 0.9 | 25.02 | DEM | 3 | EN0258397916M, EN0227810145M |
| 7057 | Catullus | | 590 | 1.8 | 127.47 | DEM | 4 | EW0238909186G, EW0254051530G |

| Pit Site ID | Pit/Host crater name | Pit location in group | DEM resolution | Depth (km) | Volume (km$^3$) | Basis for volume calculation | Topographic data quality (max) | Data source |
|---|---|---|---|---|---|---|---|---|
| 7058 | | | 535 | 0.9 | 36.61 | DEM | 2 | EN0257560167M, EN0211454949M |
| 7074 | AP1 | | 215 | 2.0 | 341.58 | DEM | 2 | EN0257648861M, EN0227259475M |
| 7075 | AP2 | | 405 | 1.9 | 251.00 | DEM | 2 | EN0242378054M, EN0257763833M |
| 7090 | Tyagaraja | NE | 402 | 0.3 | 2.04 | Cone | 3 | EN0212327110M, EN0227598580M |
| 7090 | Tyagaraja | SW | 402 | 0.5 | 1.77 | Cone | 3 | EN0212327110M, EN0227598580M |
| 7092 | | | | 0.7 | 39.44 | Cone | 5 | MLASCIRDR1201190231 |
| 7094 | Zeami | | 416 | 0.3 | 1.81 | Hemiellipsoid | 2 | EN0242670906M, EN0242378498M |
| 7096 | | | 342 | 0.3 | 1.89* | DEM | 2 | EN0242504201M, EN0227429253M |
| 7097 | | | 619 | 1.2 | 43.47 | DEM | 3 | EN0212196960M, EN0212110008M |
| 7110 | | | 633 | 0.8 | 53.48* | DEM | 3 | EN0232157380M, EN0216884366M |
| 7114* | | | 613 | 0.2 | 3.49 | Cone | 2 | EN0211803825M, EN0227385872M |
| 8008 | | SW | | 0.4 | 44.92 | Hemiellipsoid | 5 | MLASCIRDR1107030619 |
| 8008 | | E | | 0.9 | 71.63 | Hemiellipsoid | 5 | MLASCIRDR1107030619 |
| 8008 | | NW | | 0.5 | 48.17 | Hemiellipsoid | 5 | MLASCIRDR1107030619 |
| 8024 | Abedin | | | 0.2 | 41.25 | V-shaped trench | 5 | MLASCIRDR1112210309 |
| 8025 | | | 594 | 1.9 | 75.02 | DEM | 4 | EW0210851740G, EW0256412124G |
| 8026 | Rilke | W | 566 | 0.6 | 9.82 | Cone | 2 | EN0238275387M, EN0238615040M |
| 8026 | Rilke | SE | 566 | 0.2 | 1.26 | Cone | 2 | EN0238275387M, EN0238615040M |
| 8026* | Rilke | N | 566 | 0.2 | 0.59 | Cone | 2 | EN0238275387M, EN0238615040M |

**Table C-4 Calculated slopes along cross-sections indicated in Table C-5. 'na' denotes not applicable. Topographic data quality is as in Table C-3.**

| Pit Site ID | Pit/Host crater name | Slope (°) | Error (°) | Slope length (km) | Slope height (m) | Width from pit edge (km) | Pit margin | Spectral Anomaly Radius (km) | Topography width/Spectral anomaly width | Topographic data quality | Data source |
|---|---|---|---|---|---|---|---|---|---|---|---|
| 1045 | Lermontov | 0.8 | 0.22 | 1.3 | 120 | 8.8 | N pit NW | 31.6 | 0.3 | 4 | EW1005485472G, EW1005427796G |
| 1045 | Lermontov | 1 | 0.05 | 4 | 246 | 14.4 | N pit SE | 45 | 0.3 | 4 | EW1005485472G, EW1005427796G |
| 2006 | Hemingway | 0.9 | 0.04 | 3.1 | 52 | 4 | SE | 21.6 | 0.2 | 4 | EN0235851617M, EN0220847851M |
| 2006 | Hemingway | 2.1 | 0.07 | 4.5 | 161 | 6.5 | SW | 18.7 | 0.3 | 4 | EN0235851617M, EN0220847851M |
| 2006 | Hemingway | 2.1 | 0.06 | 2.5 | 89 | 5.6 | NE | 20.7 | 0.3 | 4 | EN0235851617M, EN0220847851M |
| 2007 | | 0 | na | na | na | na | na | na | na | 4 | EN0220502050M, EN0220588493M |
| 4014 | Navoi | 1.3 | 0.02 | 4 | 89 | 5.7 | S | 9.7 | 0.6 | 5 | MLASCIRDR1304071605 |
| 4014 | Navoi | 1.2 | 0.03 | 3.4 | 68 | 5.1 | N | 14.2 | 0.4 | 5 | MLASCIRDR1304071605 |
| 5023 | AP3 | 1.1 | 0.2 | 6.9 | 137 | 7.6 | N | 8.2 | 0.9 | 2 | EN0234067412M, EN0219092124M |
| 5053 | | 2.8 | 0.09 | 6 | 288 | 9.5 | E | 11.8 | 0.8 | 4 | EW0250391388G, EW0235215701G |
| 5053 | | 2.2 | 0.07 | 4.1 | 156 | 7.6 | N | 7.6 | 1 | 4 | EW0250391388G, EW0235215701G |
| 5061 | N Rachmaninoff | 6.3 | 0.2 | 5.1 | 567 | 6.8 | W | 36.5 | 0.2 | 4 | EW1003930329G, EW0254971314G |

| Pit Site ID | Pit/Host crater name | Slope (°) | Error (°) | Slope length (km) | Slope height (m) | Width from pit edge (km) | Pit margin | Spectral Anomaly Radius (km) | Topography width/Spectral anomaly width | Topographic data quality | Data source |
|---|---|---|---|---|---|---|---|---|---|---|---|
| 5061 | N Rachmaninoff | 3.8 | 0.11 | 2.6 | 170 | 3.4 | E | 46.6 | 0.1 | 4 | EW1003930329G, EW0254971314G |
| 5082 | NE Rachmaninoff | 2 | 0.07 | 3.7 | 132 | 6.5 | SW | 83.2 | 0.1 | 4 | EW0234664220G, EW0249959465G |
| 5082 | NE Rachmaninoff | 2.1 | 0.07 | 4.7 | 171 | 6.5 | W | 75 | 0.1 | 4 | EW0234664220G, EW0249959465G |
| 6062 | RS-03 | 3.3 | 0.12 | 2.3 | 130 | 2.9 | NW | 24.5 | 0.1 | 4 | EW0220764090G, EW0251171076G |
| 6062 | RS-03 | 2.3 | 0.1 | 1.8 | 73 | 3.6 | SW | 6.4 | 0.6 | 4 | EW0220764090G, EW0251171076G |
| 6117 | | 6.8 | 0.9 | 2.2 | 259 | 2.9 | W | 7.6 | 0.4 | 2 | EN0231441617M, EN0245930844M |
| 6117 | | 8.3 | 1.1 | 1.1 | 159 | 1.4 | N | 13 | 0.1 | 2 | EN0231441617M, EN0245930844M |
| 6117 | | 1.6 | 0.2 | 1.1 | 29 | 1.4 | S | 1.1 | 1.3 | 2 | EN0231441617M, EN0245930844M |
| 6120 | | 1.4 | 0.18 | 5.3 | 128 | 14.2 | E | 18.6 | 0.8 | 2 | EN0216331093M, EN0231654904M |
| 6123 | | 0.7 | 0.1 | 7.8 | 98 | 8.4 | E | 10.5 | 0.8 | 2 | EN0216331227M, EN0247054707M |
| 6129 | | 0 | na | na | na | na | na | na | na | 2 | EN0246164455M, EN0245845207M |

| Pit Site ID | Pit/Host crater name | Slope (°) | Error (°) | Slope length (km) | Slope height (m) | Width from pit edge (km) | Pit margin | Spectral Anomaly Radius (km) | Topography width/Spectral anomaly width | Topographic data quality | Data source |
|---|---|---|---|---|---|---|---|---|---|---|---|
| 7031 | To Ngoc Van | 0.6 | 0.1 | 4.2 | 45 | 4.6 | N | 13.9 | 0.3 | 5 | MLASCIRDR1105170905 |
| 7038 | | 0 | na | na | na | na | na | na | na | 2 | EN0211497583M, EN0241246615M |
| 7057 | Catullus | 0 | na | na | na | na | na | na | na | 4 | EN0131771758M, EW0223701985G |
| 7058 | | 1.8 | 0.23 | 3.2 | 100 | 5.8 | E | 20.4 | 0.3 | 2 | EN0257560167M, EN0211454949M |
| 7075 | AP2 | 5.7 | 0.8 | 3.6 | 363 | 6.4 | NW | 20.2 | 0.3 | 2 | EN0242378054M, EN0257763833M |
| 7075 | AP2 | 3.9 | 0.54 | 4 | 271 | 6.4 | SW | 13.6 | 0.5 | 2 | EN0242378054M, EN0257763833M |
| 7110 | | 2.5 | 0.2 | 1.9 | 84 | 3.1 | NE | 13.2 | 0.2 | 3 | EN0232157380M, EN0216884366M |
| 7110 | | 3.5 | 0.2 | 3.1 | 193 | 5.7 | NW | 10.1 | 0.6 | 3 | EN0232157380M, EN0216884366M |
| 8025 | | 0 | na | na | na | na | na | na | na | 4 | EW0210851740G, EW0256412124G |

**Table C-5 Endogenic pits at which relief due to pyroclastic deposition, if present, should be visible in the topography and my findings at each location. Images: Left: Monochrome image of the pit and surrounding region orthorectified on the basis of a DEM derived from the stereo pair listed in Table C-4 (except where indicated). White rectangle: extent of right image (where present); Right: Hillshade of the circum-pit area. Yellow outline: extent of a spectral anomaly suggesting the presence of pyroclastic deposits, white line: cross-section in the right column, green line: surface trace of thrust fault. Cross-sections: regions where slopes in Table C-4 were calculated are indicated in red. Points: MLA points, lines: smoothed lines through DEM values.**

| Images | Cross-sections |
|---|---|
| **Pits where relief due to pyroclastic deposits is not observed** | |
| (a) 2007 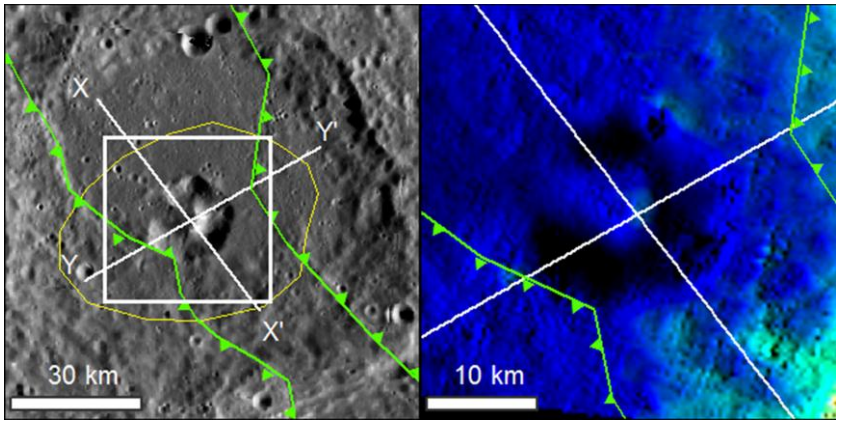  | 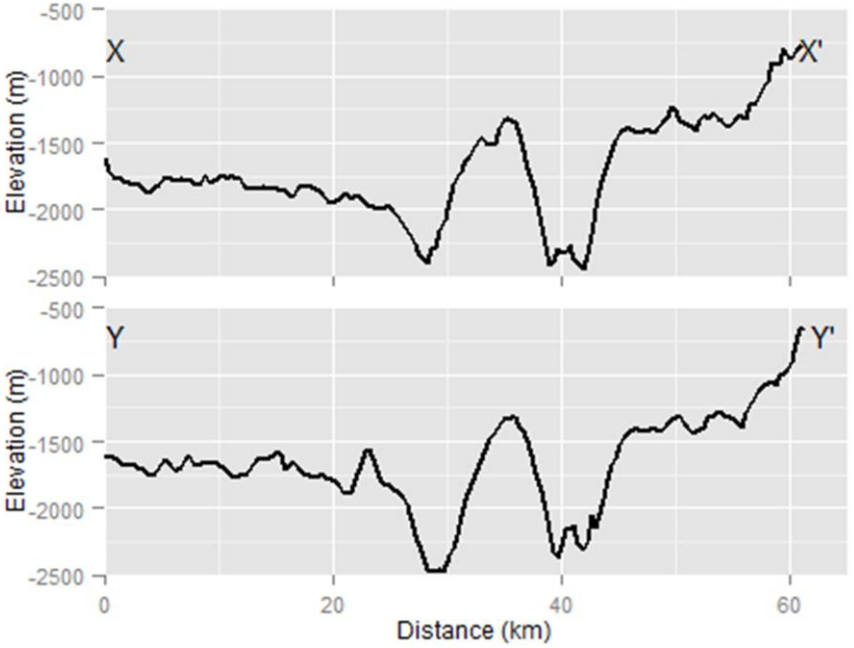  |

(b) 6129 No appreciable relief on the crater floor adjacent to the east rim of the northernmost of Pit Group 6129. Cross-sections were not made elsewhere in the crater because thrust faults or the crater's terraces abut the edge of the other pits.

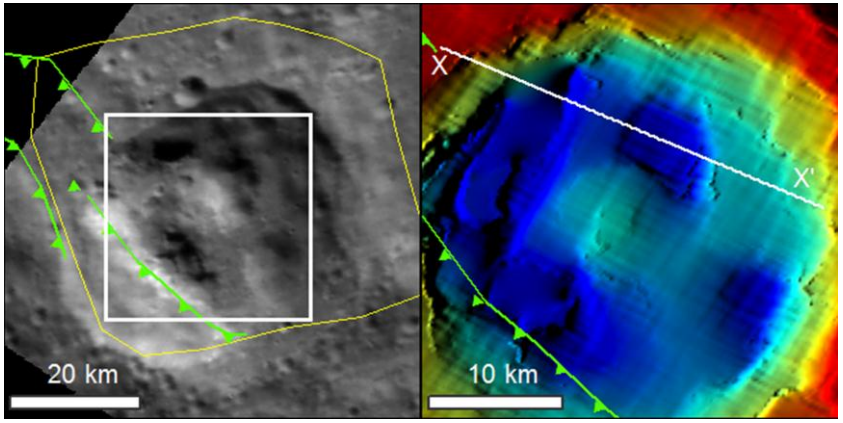


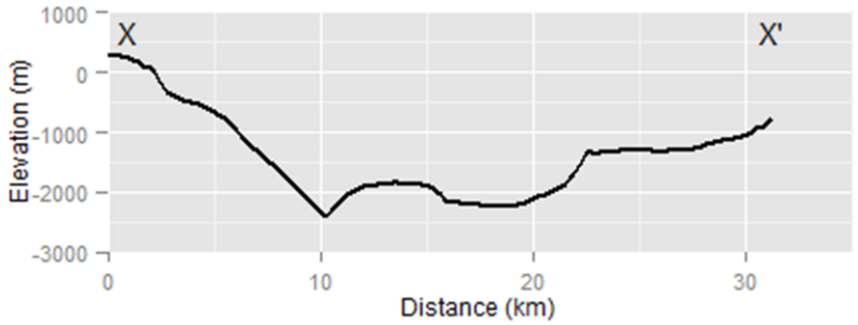


(c) 7031 - To Ngoc Van

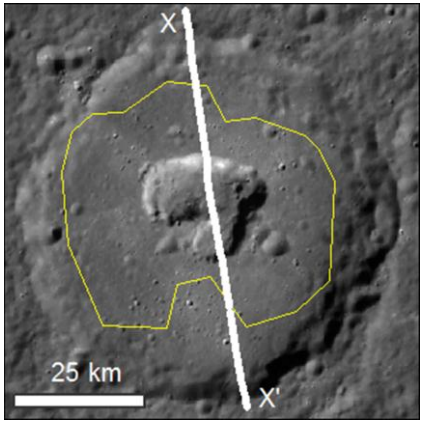


Image: Excerpt from global monochrome mosaic v9

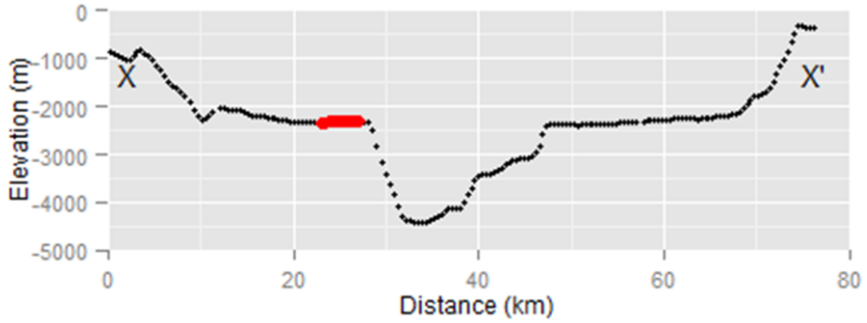

(d) 7038

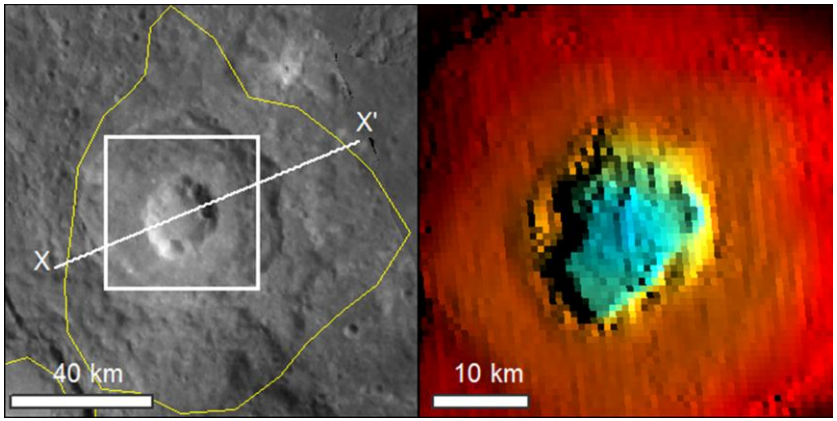
X'
X
40 km
10 km

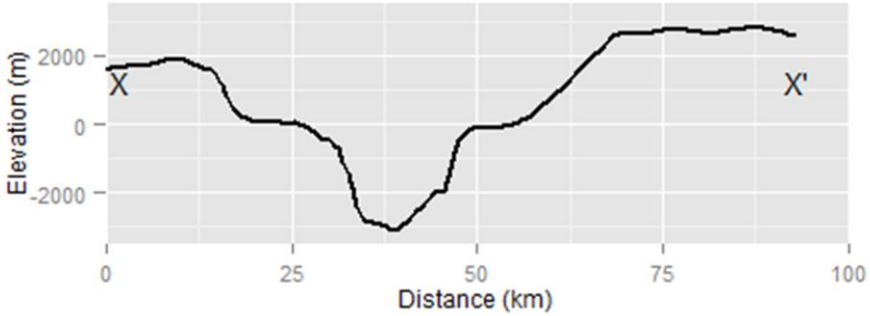
Elevation (m)
2000
0
-2000
X
X'
0
25
50
75
100
Distance (km)

(e) 7057 - Catullus

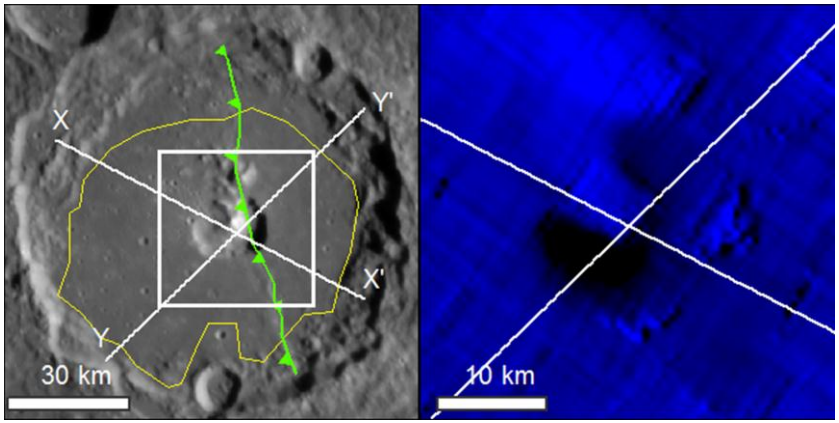


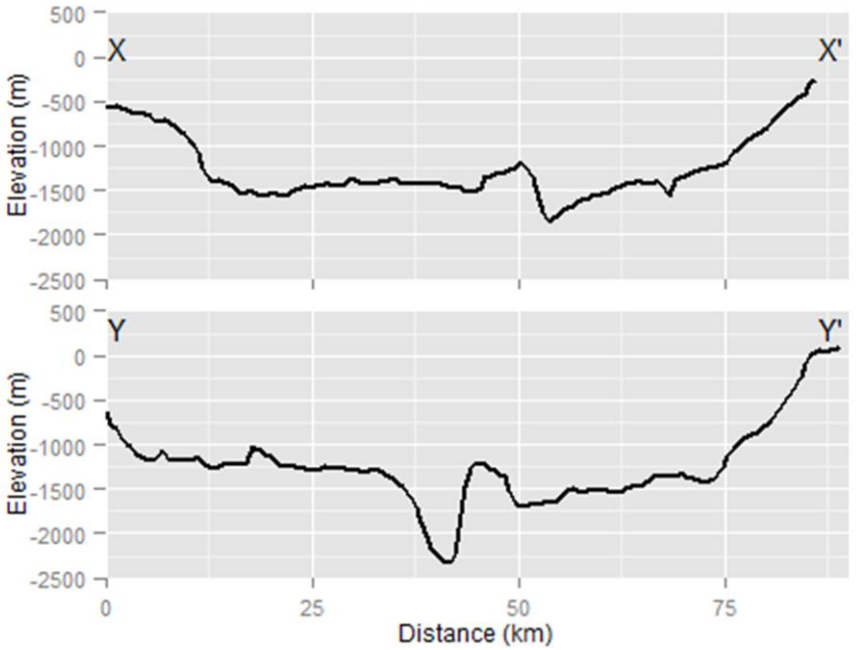

(f) 8025

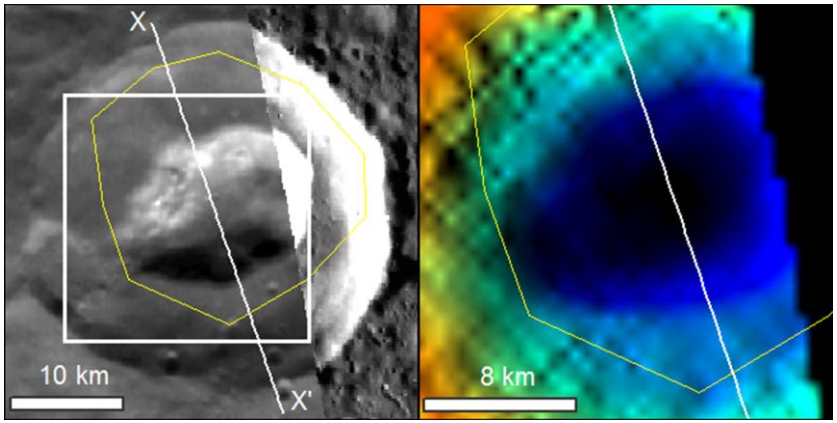


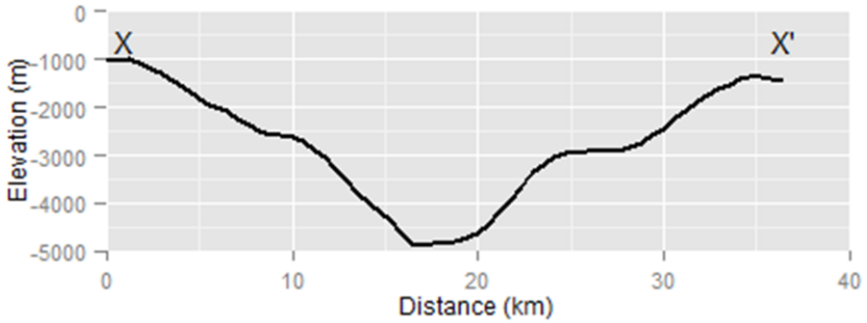


**Pits where outward-dipping circum-pit relief is observed**

(g) 1045 - Lermontov

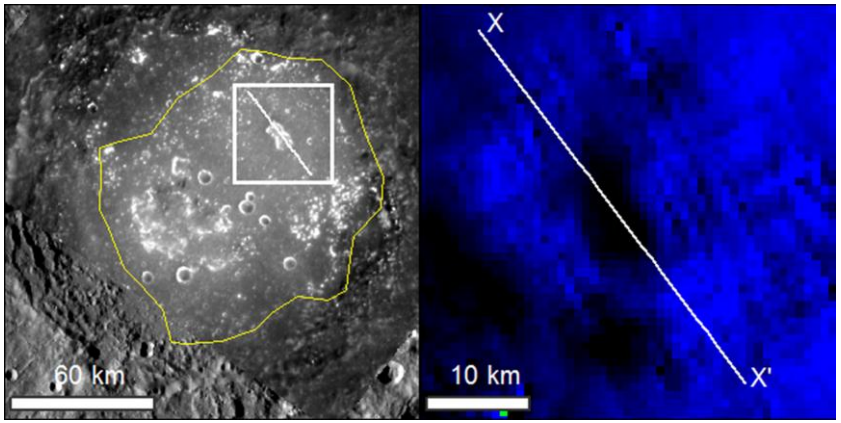


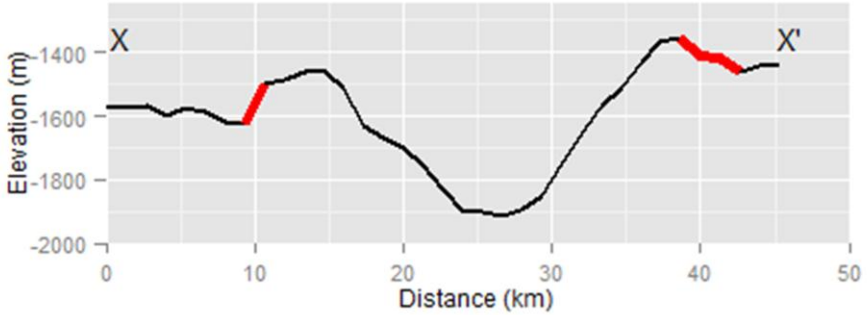

(h) 2006 - Hemingway

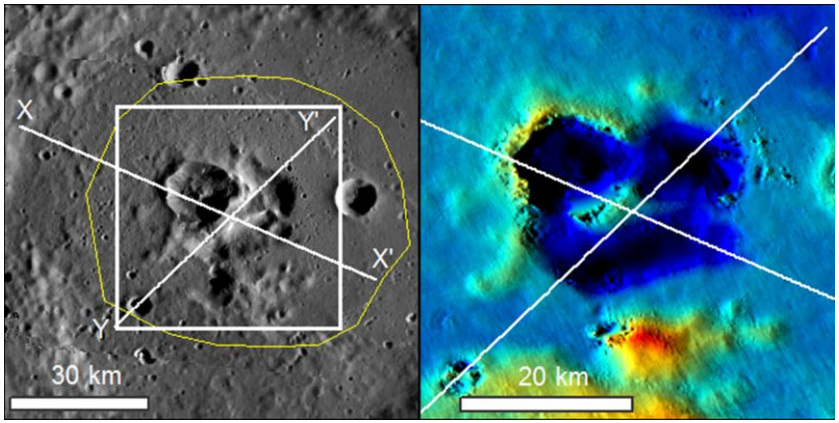


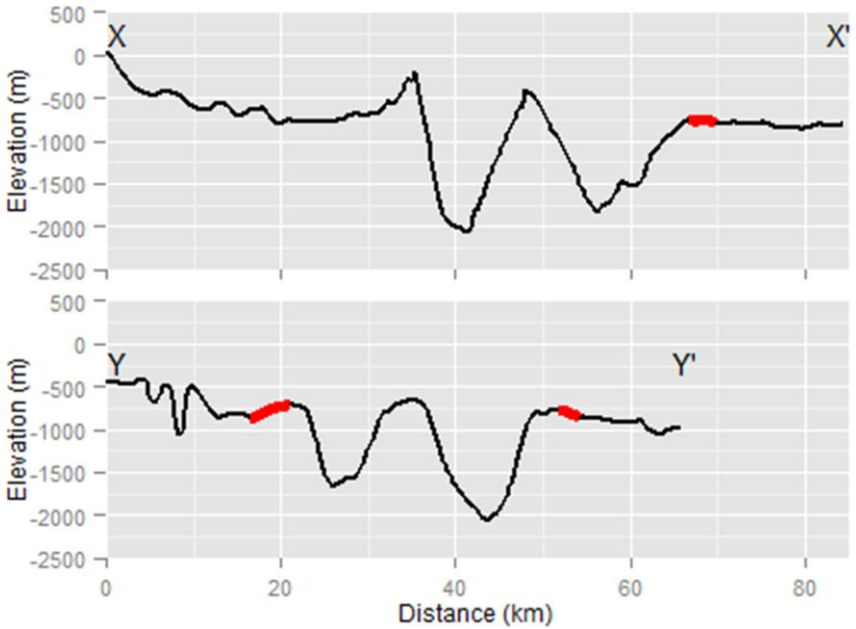

(i) 4014 – Navoi. Cross-section shows points in channels 0-4, but the slope is calculated from channel 0 (minimum noise) points only.

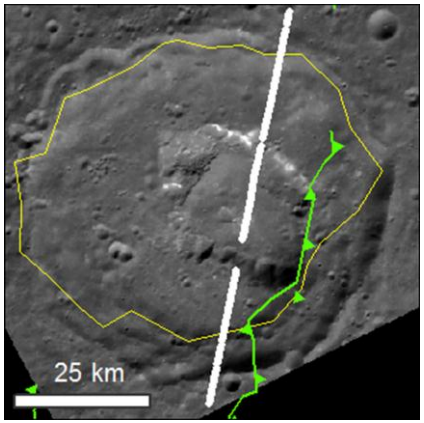


Image: EW0260906200G

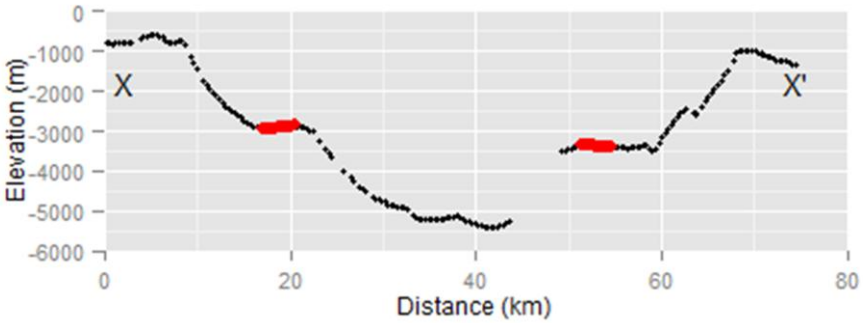

(j) 5023 – AP3. Topography in the east was not attributed to volcanic deposition because the irregular material in the SE may be part of the peak structure.

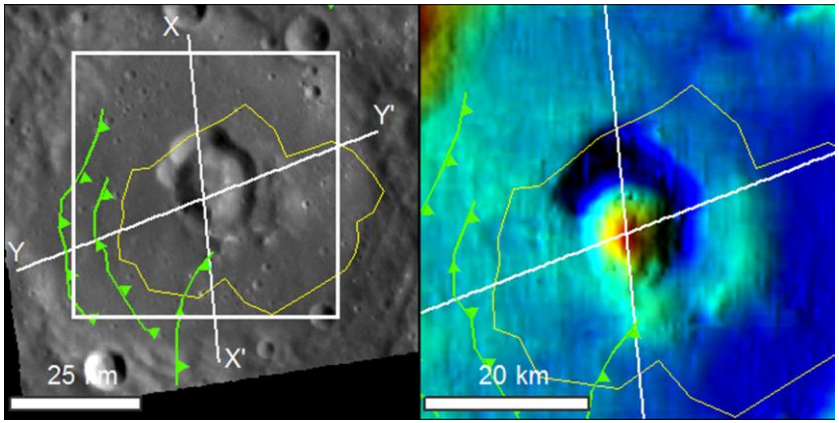


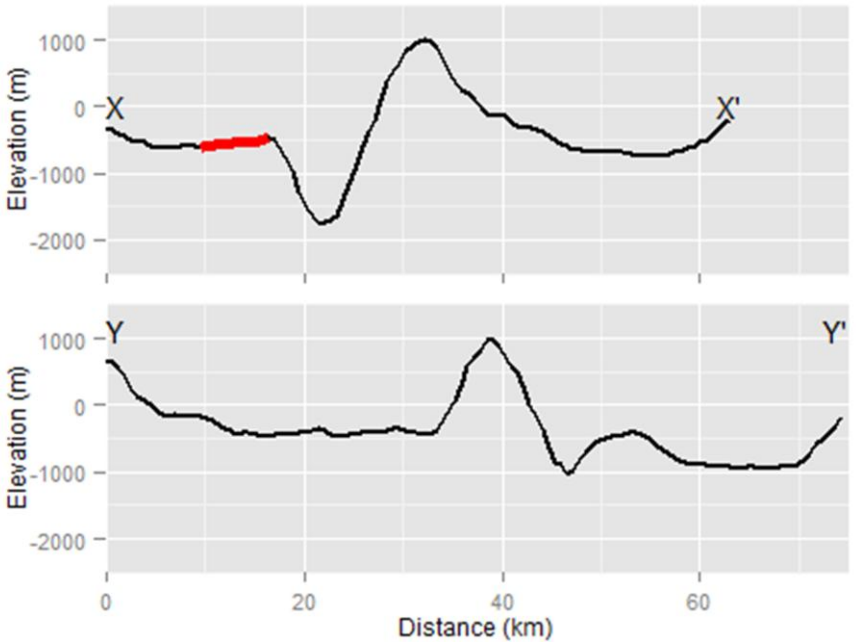

(k) 5053

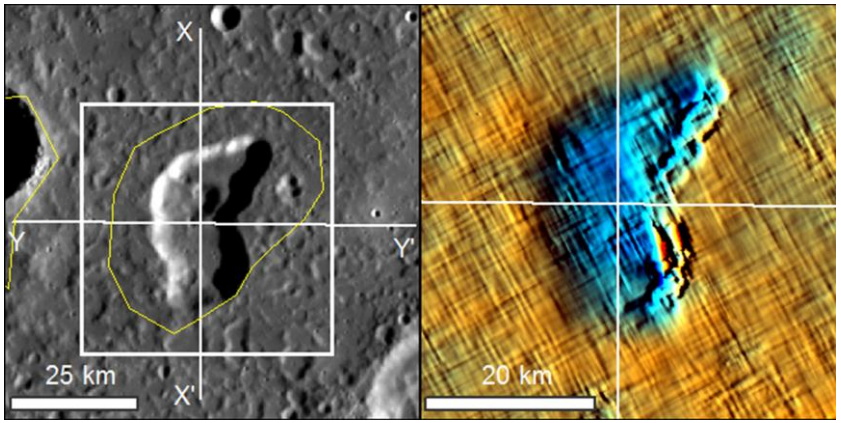
X
Y
Y'
X'
25 km
20 km

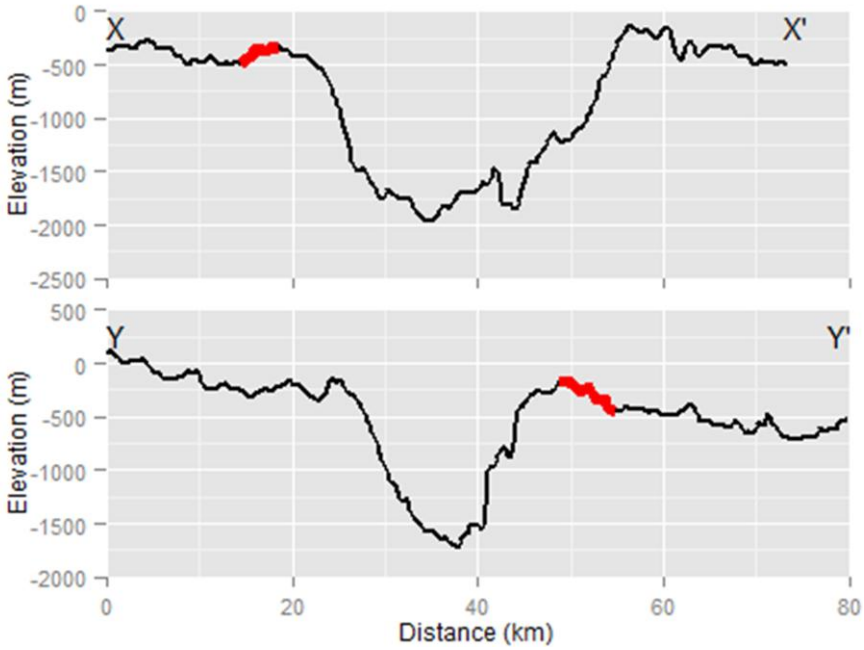
X
X'
Y
Y'
Elevation (m)
0
-500
-1000
-1500
-2000
-2500
500
0
-500
-1000
-1500
-2000
0
20
40
60
80
Distance (km)

(l) 5061 – N Rachmaninoff. Slope could not be used to calculate the relief of pyroclastic deposits in the south because the topography is dominated by an underlying large secondary impact crater

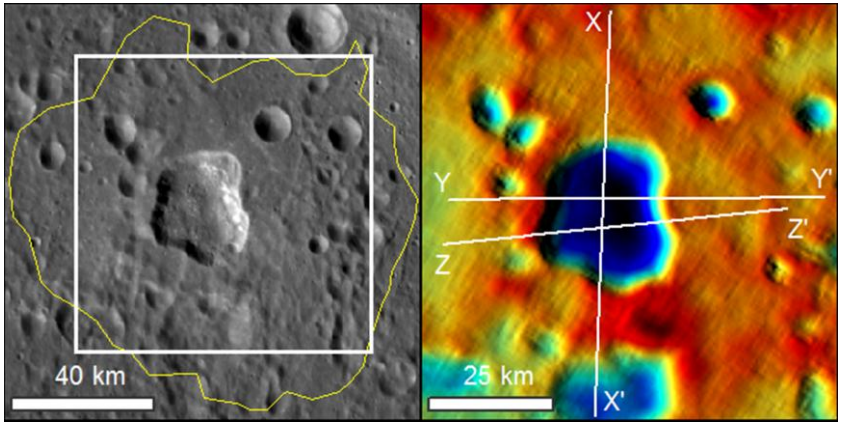


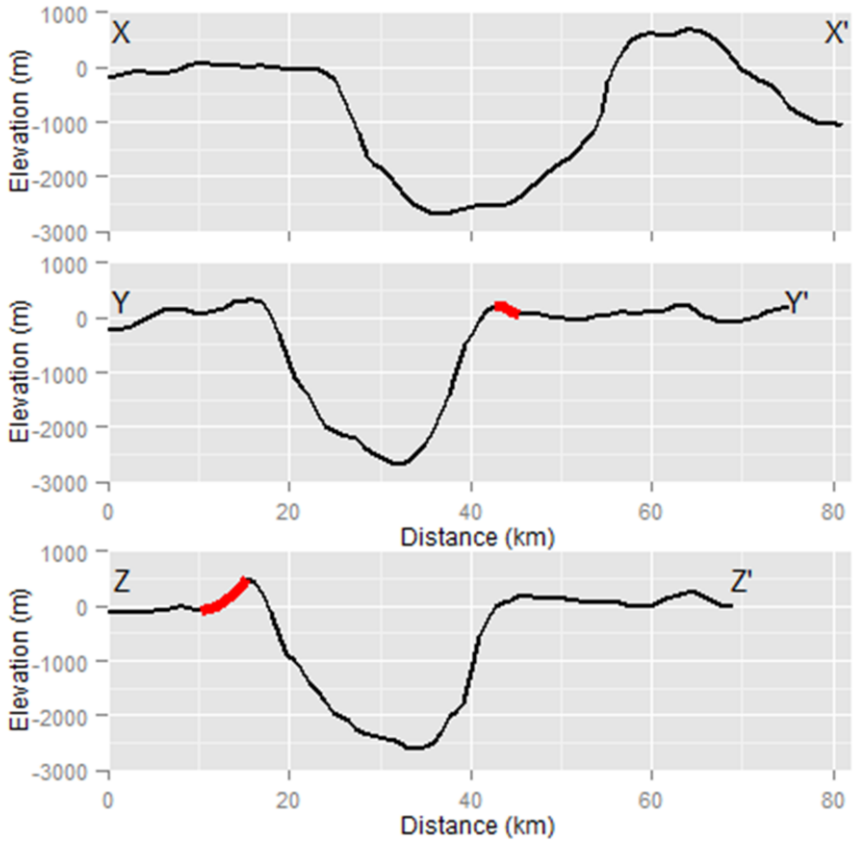

(m) NE Rachmaninoff - 5082

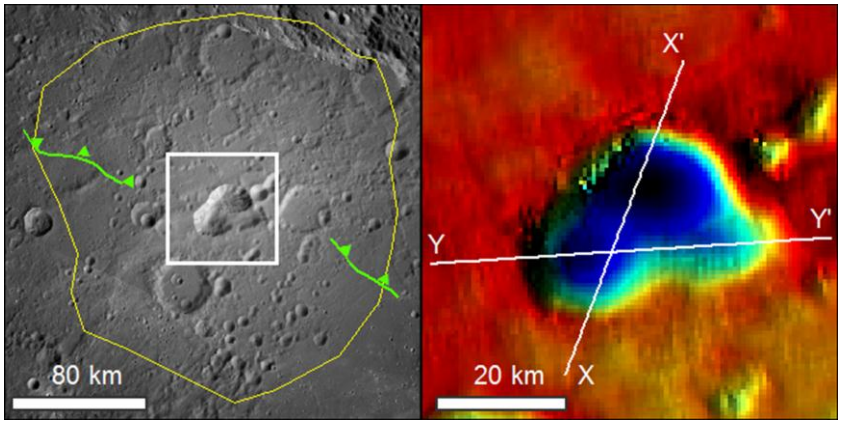


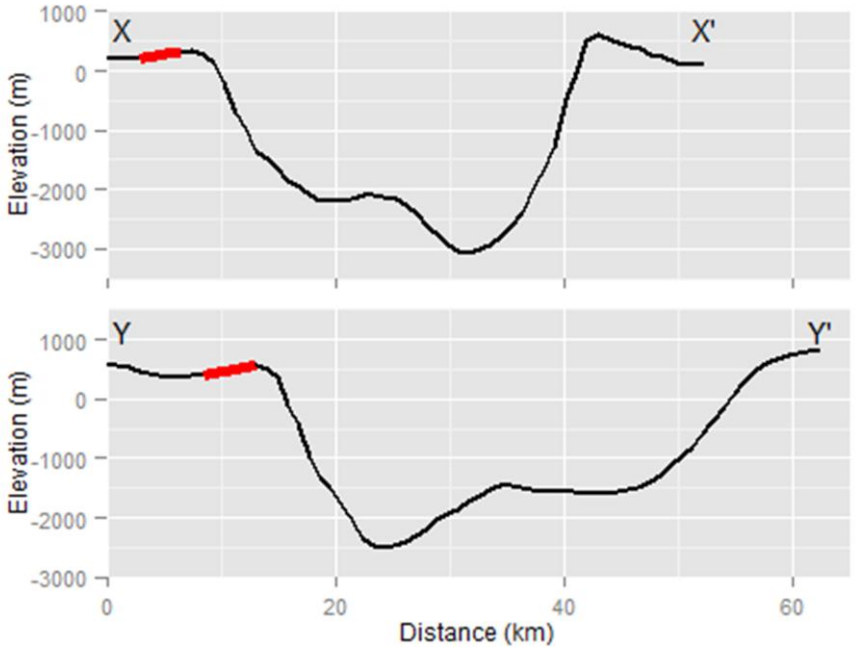

(n) RS-03 – 6062. Slope in the NE was not attributed to deposits due to the presence of a topographic ridge that does not appear to be attributable to pyroclastic deposition.

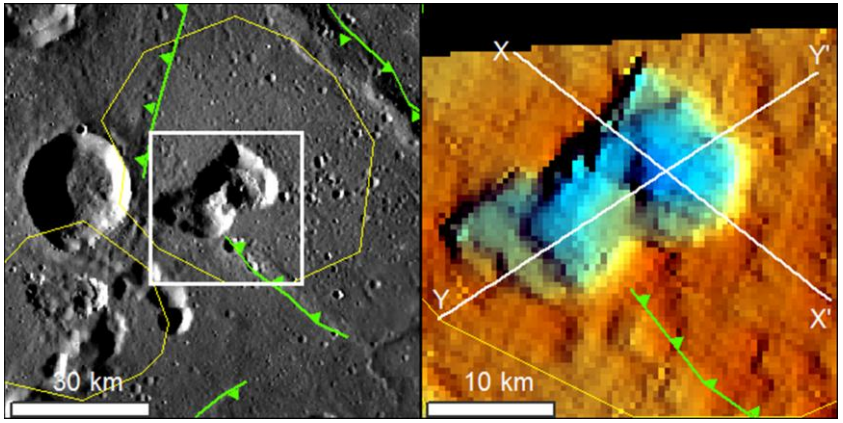


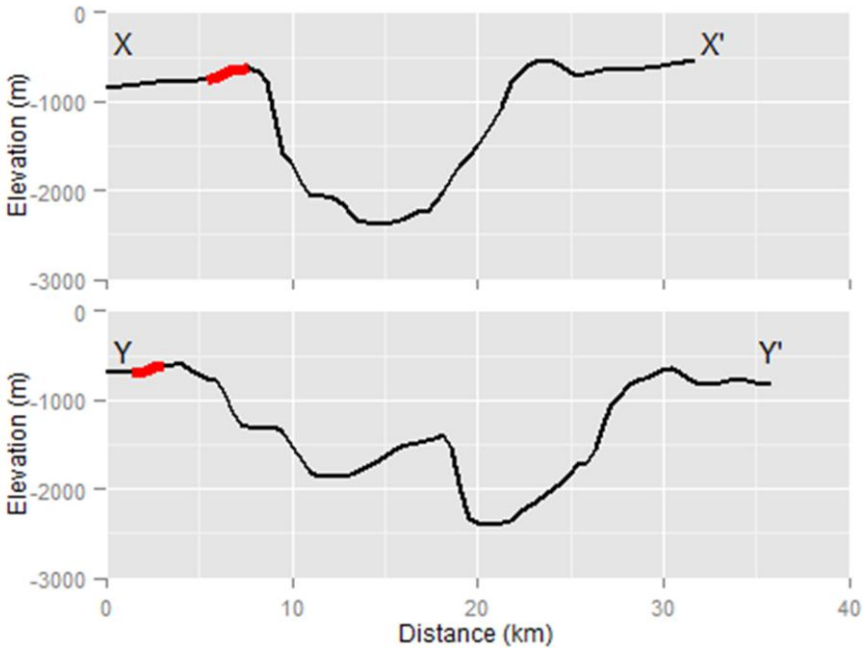

(o) 6117

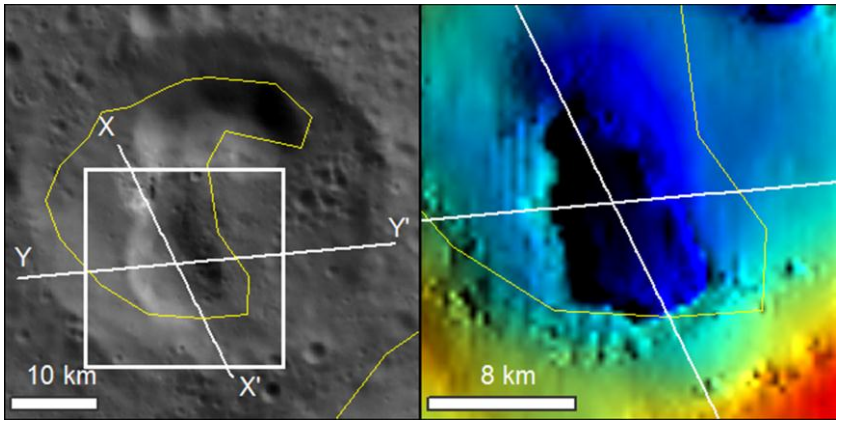
X
X'
Y
Y'
10 km
8 km

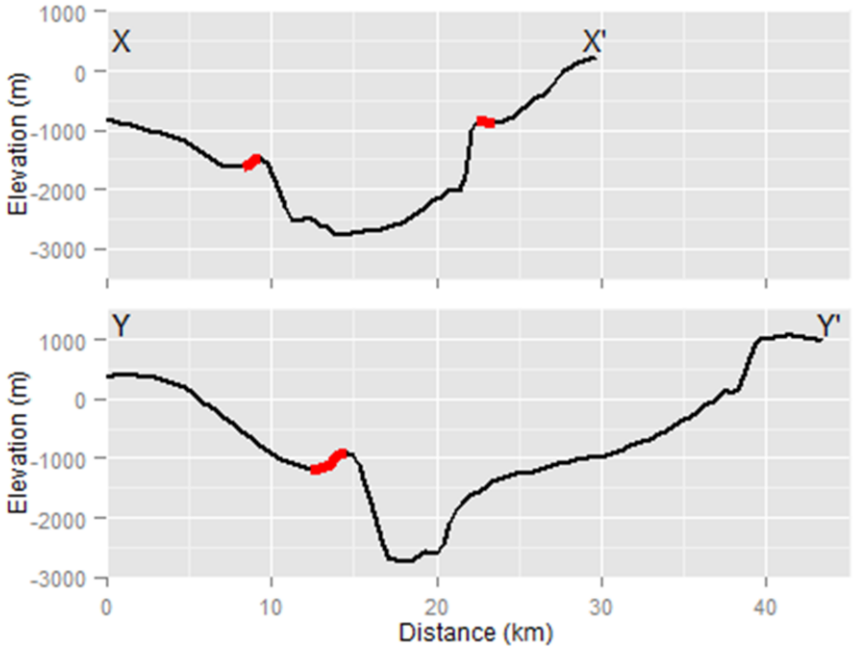
X
X'
Y
Y'
Elevation (m)
1000
0
-1000
-2000
-3000
0
10
20
30
40
Distance (km)

(p) 7058. Topography to the west of the pit is dominated by a lobate scarp.

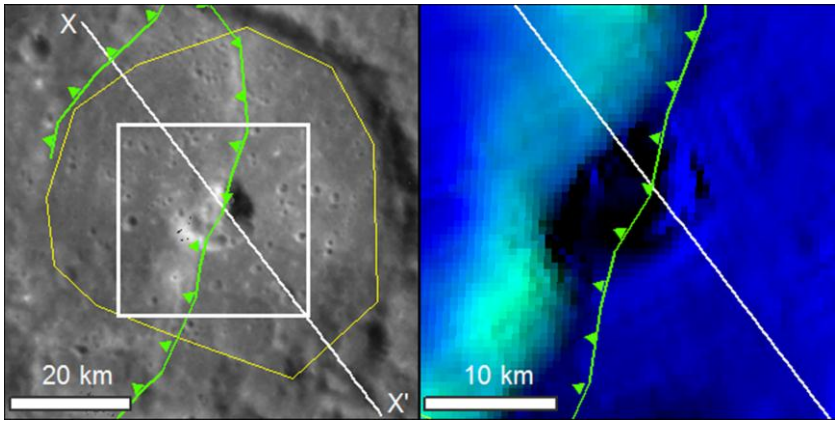


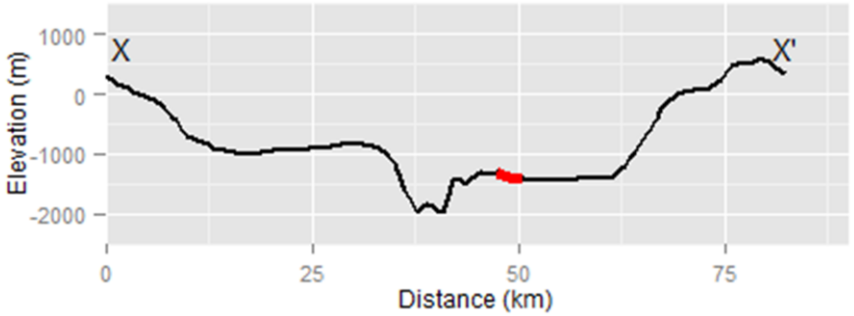

(q) AP2 – 7075. Topography in the east was not attributed to volcanic deposition due to the presence of a lobate scarp.

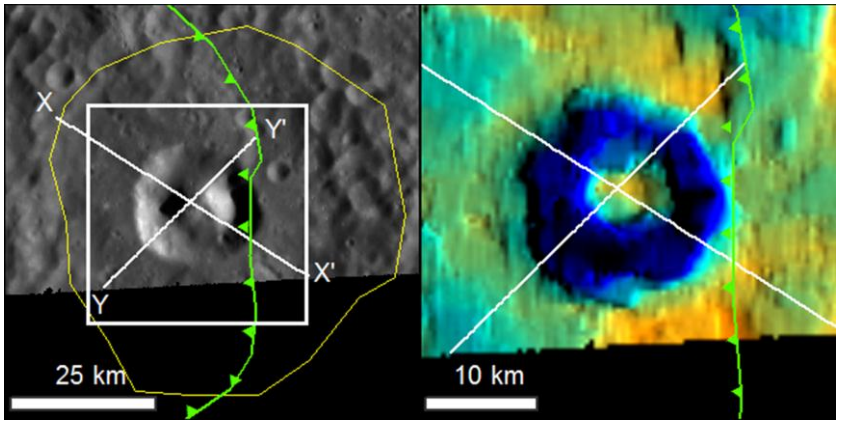


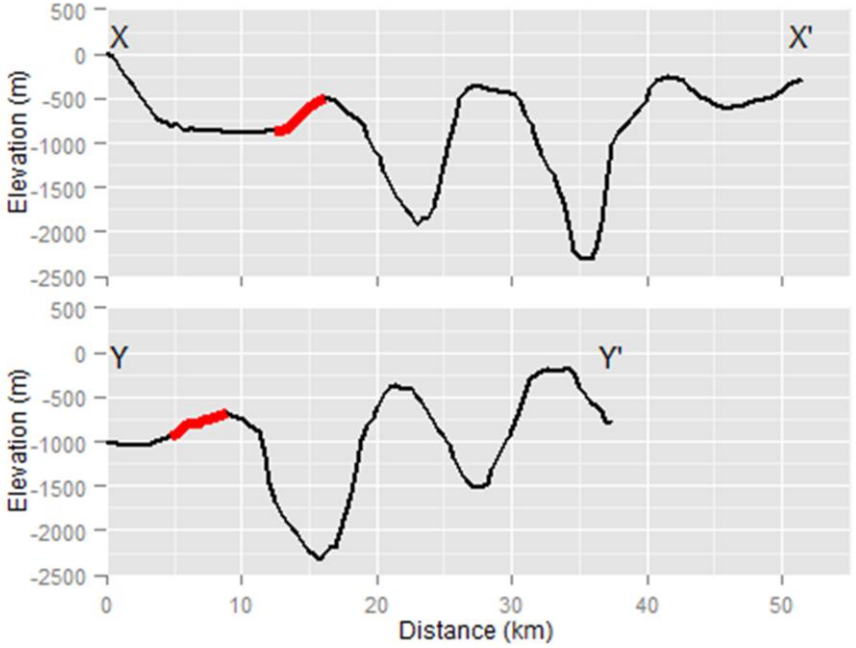

(r) 7110

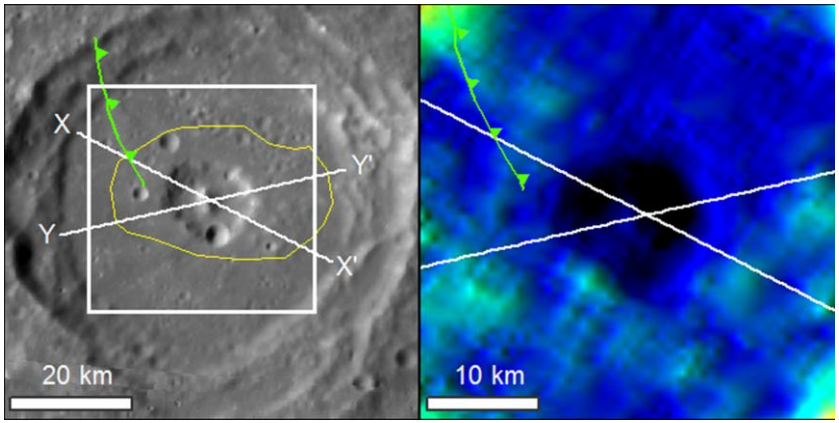
X
Y'
Y
X'
20 km
10 km

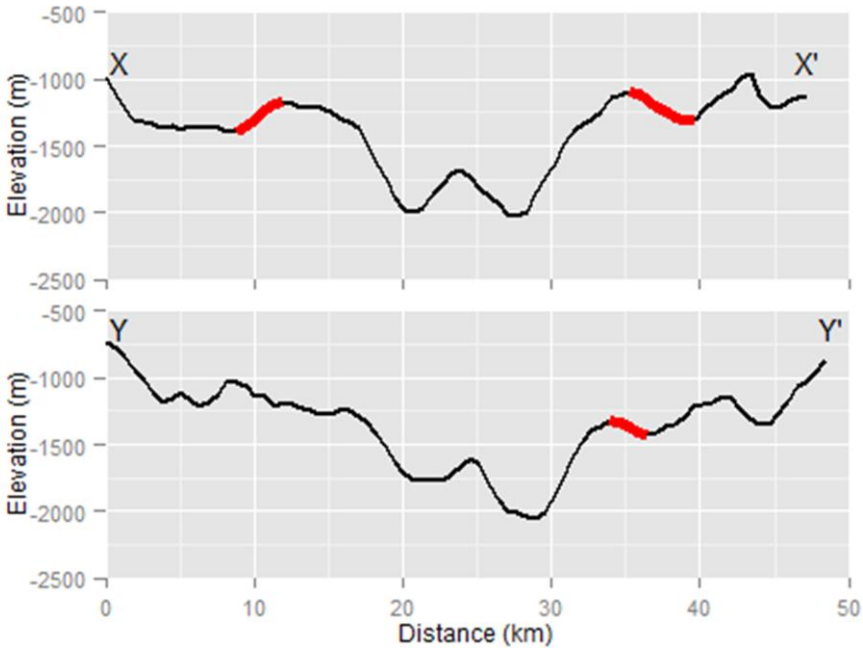
X
X'
Y
Y'
Elevation (m)
-500
-1000
-1500
-2000
-2500
0
10
20
30
40
50
Distance (km)

**Pits with anomalous relief**

(s) 6120

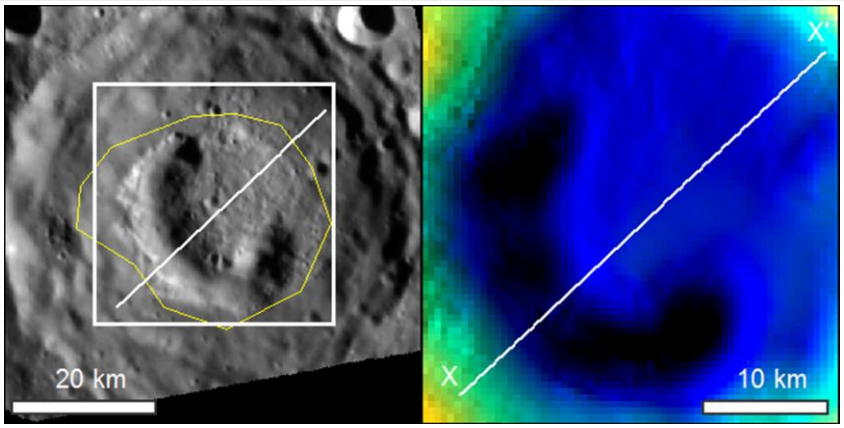


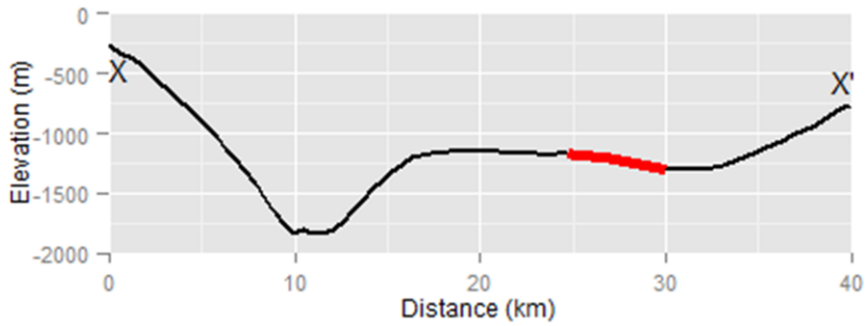


(t) 6123. Slope was taken where indicated because topography to the south is dominated by the crater's central uplift and that to the north, by the crater's terraces.

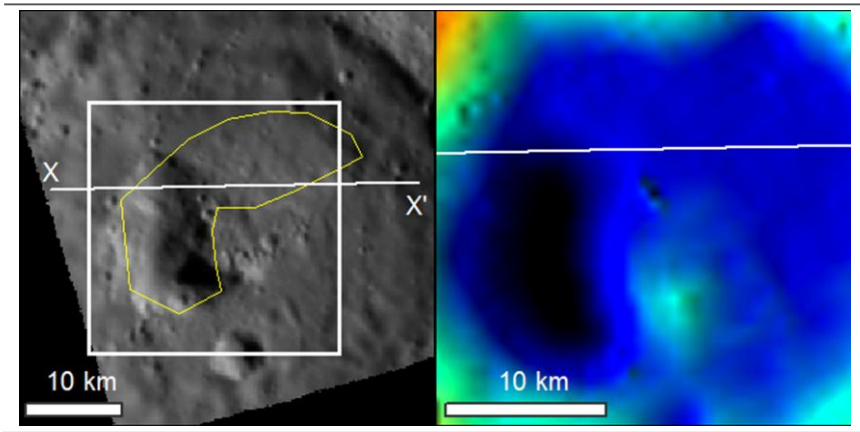


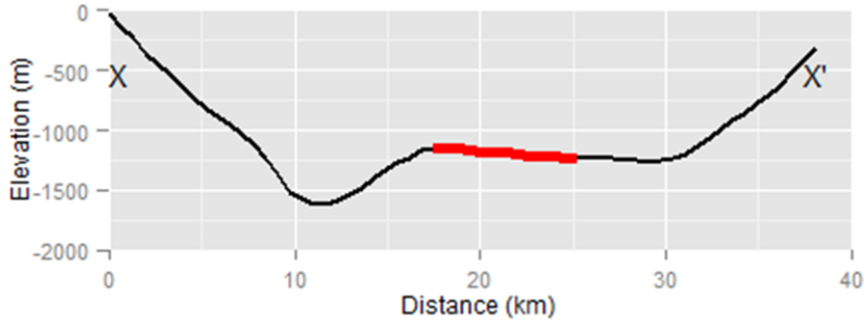

# Appendix D. Sites where putative explosive volcanism occurs at a crater centre

**Table D-1 Sites where endogenic pits are collocated with the uplift structure of an impact crater and are surrounded by a relatively bright and red-sloped spectral anomaly. Types: 1 – at the crater centre or along the peak ring, 2 – concentric to the crater centre or central peak. * indicates sites identified after preparation of (*Thomas et al.*, 2015).**

| Pit group ID | Central latitude | Central longitude | Type |
|---|---|---|---|
| 1045 | 15.0086 | -49.0076 | 1 |
| 1046 | 3.7557 | -56.085 | 1 |
| 1047 | 26.6068 | -59.4069 | 1 |
| 1067* | 12.4442 | -55.814 | 1 |
| 2002 | 27.5251 | 1.19122 | 1 |
| 2006 | 17.4245 | -2.75405 | 2 |
| 2007 | 14.006 | 3.63059 | 2 |
| 2039 | -48.4267 | -6.4235 | 2 |
| 4014 | 58.8242 | 160.686 | 1 |
| 4017 | 60.8055 | 168.064 | 2 |
| 4040 | -28.1626 | 161.933 | 2 |
| 5020 | -51.6599 | 24.4144 | 1 |
| 5022 | -19.0753 | 71.579 | 1 |
| 5023 | -21.0364 | 72.4432 | 2 |
| 5039 | 3.5413 | 50.9792 | 1 |
| 5066 | 36.3165 | 55.2924 | 1 |
| 5070 | -37.5026 | 45.6213 | 1 |
| 5084 | -52.8102 | 38.2961 | 2 |
| 5094 | -36.2284 | 41.1891 | 2 |
| 5097 | -66.8024 | 76.2552 | 1 |
| 6060 | -5.20355 | 143.593 | 2 |
| 6064 | -11.0137 | 140.58 | 2 |
| 6074 | -28.2183 | 146.868 | 2 |
| 6075* | -52.5569 | 125.647 | 1 |
| 6078 | -9.21725 | 154.509 | 2 |
| 6083 | -28.124 | 136.556 | 2 |
| 6099 | 45.3181 | 144.352 | 1 |
| 6117 | -55.2083 | 142.663 | 2 |
| 6120 | -40.3069 | 111.336 | 2 |
| 6130 | -38.6292 | 137.633 | 1 |
| 6133 | -55.0409 | 147.151 | 1 |
| 6168* | 26.2547 | 117.85 | 1 |
| 7019 | 41.1319 | -100.813 | 1 |
| 7026 | 35.8117 | -111.202 | 1 |
| 7031 | 52.5358 | -111.669 | 1 |
| 7038 | -21.2196 | -89.2117 | 1 |
| 7041 | 9.45622 | -137.764 | 2 |
| 7047 | 8.29851 | -113.526 | 2 |
| 7049* | -28.3823 | -90.1199 | 1 |
| 7057 | 21.787 | -67.3412 | 2 |
| 7058 | -24.1346 | -105.024 | 1 |
| 7074 | -3.54144 | -136.788 | 2 |
| 7075 | -8.41149 | -135.493 | 2 |
| 7090 | 3.80181 | -148.662 | 2 |
| 7094 | -2.9716 | -147.242 | 2 |
| 7096 | 4.5811 | -140.681 | 2 |
| 7107 | -19.8725 | -161.07 | 2 |
| 7110 | -6.93635 | -113.785 | 2 |
| 7114 | -13.5333 | -129.994 | 2 |
| 7125 | 15.0115 | -112.377 | 2 |
| 7160 | -22.8582 | -90.5563 | 2 |
| 8008 | 48.3288 | -33.9994 | 2 |
| 8023 | -6.06093 | -13.0714 | 2 |
| 8024 | 61.8274 | -10.9485 | 1 |
| 8025 | 58.8416 | -32.8942 | 1 |
| 8026 | -44.78 | -12.4139 | 2 |
| 8167 | 27.0474 | -29.5918 | 1 |

# Appendix E. Sampled sites of crater-centred explosive volcanism on Mercury and the Moon

**Table E-1 Sites of putative pyroclastic volcanism analysed. Sites are referenced by the name of the host crater on the Moon, and by the (arbitrary) pit group ID (Table C-1) on Mercury. Mercury substrates: LRM = Low-Reflectance Material, IT = Intermediate Terrain.**

| Name | Lat (° N) | Long (° E) | Body | Host crater diameter (km) | Substrate | Maximum ballistic range (km) | Geodetic area (km²) | Vent location | FFC class | Uplift Geometry |
|---|---|---|---|---|---|---|---|---|---|---|
| 1043 | 5.4 | -55.8 | Mercury | 45.8 | LRM | 30.63 | 2847.9 | Mid-floor circumferential | | |
| 2039 | -48.4 | -6.4 | Mercury | 113.2 | LRM | 19.7 | 1371.8 | Central | | |
| 4041 | -23.7 | 179.7 | Mercury | 113 | IT/LRM boundary | 29.76 | 1154.8 | Central | | |
| 5023 | -21 | 72.4 | Mercury | 87.3 | IT | 23.16 | 1328.1 | Central | | |
| 5070 | -37.5 | 45.6 | Mercury | 60 | IT | 14.93 | 595.2 | Central | | |
| 6075 | -52.5 | 125.7 | Mercury | 109.2 | LRM | 27.72 | 1555.5 | Central | | |
| 6083 | -28.1 | 136.6 | Mercury | 46.2 | IT/LRM boundary | 7.23 | 226.5 | Central | | |
| 6119 | -45.4 | 135.1 | Mercury | 78.5 | LRM | 13.6 | 1528 | Central and outer floor by wall | | |
| 6133 | -55 | 147.2 | Mercury | 44.6 | LRM | 3.9 | 69.8 | Central | | |
| 6136 | -52 | 139 | Mercury | 82.2 | LRM | 9.95 | 1455.5 | Central and outer floor by wall | | |
| 7038 | -21.2 | -89.2 | Mercury | 57.6 | IT | 50.27 | 6989.8 | Central | | |
| 7041 | 9.5 | -137.8 | Mercury | 74.7 | IT | 24.8 | 1192.5 | Central | | |

| Name | Lat (° N) | Long (° E) | Body | Host crater diameter (km) | Substrate | Maximum ballistic range (km) | Geodetic area (km²) | Vent location | FFC class | Uplift Geometry | |
|---|---|---|---|---|---|---|---|---|---|---|---|
| 7096 | 4.6 | -140.7 | Mercury | 32.1 | IT | 17.45 | 413.5 | Central | | | |
| 7110 | -6.9 | -113.8 | Mercury | 70.2 | IT | 12.65 | 633.9 | Central | | | |
| 7114 | -13.5 | -130 | Mercury | 96.8 | IT | 5.35 | 190.8 | Central | | | |
| 8026 | -44.8 | -12.4 | Mercury | 80.3 | LRM | 20.93 | 1228.1 | Central | | | |
| Airy | -18.1 | 5.7 | Moon | 33.5 | Highlands | 1.7 | 43.86 | Central | 4a | Convex | |
| Alphonsus | -13.4 | -2.8 | Moon | 113.9 | Highlands /mare boundary | 6.1 | 339.33 | Outer floor by wall | 5 | Slightly convex | |
| Atlas | 46.7 | 44.3 | Moon | 87.1 | Highlands | 15.5 | 712.85 | Outer floor by wall | 1 | Convex | |
| Bohnenberger | -16.2 | 40 | Moon | 32.5 | Highlands /mare boundary | 10.7 | 113.51 | Outer floor by wall | | 4a | Convex |
| Franklin | 38.8 | 47.7 | Moon | 57.9 | Highlands | 17.2 | 805.28 | Outer floor by wall | 5 | Slightly convex | |
| Haldane | -1.7 | 84.1 | Moon | 40 | Mare | 11.7 | 230.68 | Mid-floor circumferential | | 3 | Piston-like, moat |
| Hell | -32.4 | -7.8 | Moon | 34.3 | Highlands | 5.7 | 137.6 | Mid-floor circumferential | | | |
| Komarov | 24.7 | 152.2 | Moon | 83.5 | Highlands | 25.2 | 1720.92 | Outer floor by wall | 3 | Convex | |
| Kopff | -17.4 | -89.7 | Moon | 40.8 | Orientale basin ring | 17.7 | 214.22 | Mid-floor and by wall | 3 (no moat) | Piston-like, no moat | |

| Name | Lat (° N) | Long (° E) | Body | Host crater diameter (km) | Substrate | Maximum ballistic range (km) | Geodetic area (km²) | Vent location | FFC class | Uplift Geometry |
|---|---|---|---|---|---|---|---|---|---|---|
| Lavoisier | 38.1 | -81.2 | Moon | 68.2 | Highlands /mare boundary | 11.5 | 616.87 | Mid-floor and by wall | 3 (no moat) | Piston-like, no moat |
| Lavoisier H | 38.2 | -78.9 | Moon | 30.3 | Highlands /mare boundary | 7.8 | 252.36 | Outer floor by wall | 4a | Convex |
| Mersenius | -21.4 | -49.3 | Moon | 85.8 | Highlands | 3.3 | 72.28 | Outer floor by wall | 4a (unusually large) | Convex |
| Oppenheimer H | -36.8 | -163.4 | Moon | 32.7 | South Pole Aitken Basin | 7.5 | 200.59 | Mid-floor | 4a | Convex |
| Oppenheimer U | -34.4 | -168.2 | Moon | 37.8 | South Pole Aitken Basin | 46.3 | 3948.69 | Mid-floor | 4a | Convex |
| Schluter | -5.9 | -83.4 | Moon | 85.5 | Highlands | 3.6 | 24.83 | Central | 1 | Piston-like, no moat |

# Appendix F. Specific Targets for BepiColombo

An ArcGIS shapefile, Bepi_targets.shp and its associated files are included on the enclosed CD-ROM. This indicates the position and shape of each target listed below. The '.dbf' file can be opened in spreadsheet software and has columns as indicated in Table F-1.

**Table F-1 Data columns in bepi_targets.dbf**

| Column | Description |
|---|---|
| Id | Hollow/pit group ID if applicable |
| C_Lat | Latitude of the shape centroid (°) |
| C_Long | Longitude of the shape centroid (°) |
| Area | Area as measured on a globe ($m^2$) |
| Rationale | Reason for targeting this area; 'rationale codes' are listed under each heading in this Appendix. Comma-separated where more than one rationale applies. |

**Table F-2 Acronyms used in Appendix F**

| | |
|---|---|
| HRIC | High-Resolution Imaging Channel of SYMBIO-SYS |
| STC | STereo and colour imaging Channel of SYMBIO-SYS |
| VIHI | VIsible and near-infrared Hyperspectral Imaging channel of SYMBIO-SYS |
| MERTIS | Mercury Radiometer and Thermal Infrared Spectrometer |
| MIXS | Mercury Imaging X-Ray Spectrometer |
| ISA | Italian Spring Accelerometer |
| MORE | Radio science experiment |
| PPD | Putative Pyroclastic Deposit |

## F.1 Hollows

### F.1.1 Where are hollows?

| | |
|---|---|
| Instrument/s: | HRIC/STC |
| Suggested analyses: | As well as seeking hollows globally (particularly in the southern hemisphere) check those listed below, where MDIS images indicate possible hollows |
| Potential science return: | Site-specific, plus the broader goal of determining whether there are latitudinal/longitudinal variations in the density of hollow-formation, to provide constraints on the probable cause/s of hollow-formation |
| Useful solar incidence: | 45–70° |
| Rationale code: | H |

**Table F-3 Targets were possible hollows require confirmation**

| Longitude (°) | Latitude(°) | Useful resolution (m/px) | Description | Science return |
|---|---|---|---|---|
| -160.62 | 26.31 | < 50 | Small area of low-reflectance material with what appear to be hollows at its centre, but below the resolution of the available images | Constrain formation processes for 'dark spots' (*Xiao et al.*, 2013) |
| -111.54 | 52.71 | < 20 | Possible hollows in a particular substrate in the wall of a major endogenic pit | Provide data regarding the relationship between hollows and explosive volcanism |
| -92.23 | 30.16 | < 100 | Possible hollows in peak material of an impact crater in the hangingwall of a thrust fault | If confirmed, indicates the depth to the hollow-forming lithology at this locality. |
| -65.65 | -52.59 | < 120 | Unusual irregular depressions within an impact crater - could be hollows. | Characterise the process responsible for such landforms |
| -64.53 | -15.59 | < 100 | Possible hollows in the wall of a small crater within an older crater, which is within a peak-ring basin | Determine whether there is hollow-forming material beneath the floor of the large basin |
| -60.22 | 0.08 | < 150 | Possible hollows in walls of several craters | Provide an extra data point for the depth and extent of underlying hollow-forming material in this region |
| -59.39 | 42.37 | < 100 | Possible hollows | Determine the lateral extent of a region with small-extent dispersed hollows and so the extent of hollow-forming material in the subsurface |
| -51.77 | -4.77 | < 100 | Probable hollows in the rim of a small impact crater into an otherwise unhollowed smooth crater floor in an area of smooth plains | Hollow-forming material would not be expected here, so if present, it will require explanation. |
| -51.23 | 26.8 | < 100 | Possible hollow at the margin of peak material of an otherwise unhollowed crater in a region where several craters have interior hollows | Map the extent of hollow-forming material in this region |
| -50.89 | 21.17 | < 100 | Possible hollows on the floor of a very young (Kuiperian) crater, Bek | Constrain rate of hollow-formation using host crater's age and hollow depth |

| Longitude (°) | Latitude(°) | Useful resolution (m/px) | Description | Science return |
|---|---|---|---|---|
| -49.76 | 38.9 | < 100 | Possible hollows in the peak ring of a very old, degraded crater (Hugo) | If confirmed, indicates the composition of material uplifted in an ancient impact |
| -47.24 | 3.07 | < 100 | Possible hollows in the peak ring and wall of an undegraded (late? Mansurian) impact crater | Constrain rate of hollow-formation using host crater's age and hollow depth |
| -23.93 | 20.72 | < 50 | Possible hollows at the rim of an impact crater within a relatively fresh but older crater | Constrain rate of hollow-formation using host crater's age and hollow depth |
| -17.09 | 21.83 | < 100 | Possible hollows at several locations along the old, degraded peak ring of Rodin basin | Map the extent of hollow-forming material in the subsurface in a hollow-rich LRM region |
| -16.03 | 35.04 | < 100 | Probable hollows on a crater floor between the HMR and Northern Plains | Map the extent of hollow-forming material in this region |
| -12.15 | 56.38 | < 100 | Possible hollows in the central uplift of impact crater into the smooth plains | If confirmed, indicates the depth to hollow-forming material beneath the plains in this region |
| -6.01 | 28.73 | < 100 | Probable moderately-extensive hollows in the peak structure and walls of an impact crater | Map the extent of hollow-forming material in the region around an area of smooth plains (ancient basin rim/ring?) |
| -4.4 | -12.24 | < 100 | Possible hollows in the walls of a small crater into the smooth ?volcanic? fill of proposed ancient basin “b38” (*Fassett et al.*, 2012), at the location where a peak ring could be expected | Determine whether this basin exhumed hollow-forming material in its peak ring |
| 1.5 | 27.56 | < 100 | Crater hosting two centres of putative explosive volcanism and uncertain hollows on the east flank | Determine the history of explosive volcanism in the crater, the PPD extent and whether hollows are present. Determine the relationship of this activity with the LRM substrate around the impact crater. |
| 1.55 | 23.54 | < 100 | Possible hollowing in the floor of a small impact crater north of extensively-hollowed de Graft | Determine whether hollow-forming material was present in de Graft ejecta |

| Longitude (°) | Latitude(°) | Useful resolution (m/px) | Description | Science return |
|---|---|---|---|---|
| 10.56 | 30.41 | < 100 | Possible hollows on the sun-facing slope of an impact crater | If hollows are confirmed, determine whether they formed solely on slopes with this aspect |
| 21.29 | -62.12 | < 100 | Possible hollows on the NW terrace of an impact crater into the eastern rim of the proposed “b54” impact basin | Map the extent of hollow-forming material at the eastern margin of “b54” |
| 26.67 | 9.23 | < 100 | Probable hollows in the LRM central peak of a ~Mansurian crater | Confirm or reject hollowing within a crater with a strong LRM spectral signature - if rejected, this would require explanation |
| 38.48 | 54.25 | < 20 | Possible hollows in the wall of a small crater into the ejecta of a larger crater in the Northern Plains | May indicate that volatiles in ejected material were not entirely lost when the larger crater formed |
| 40.45 | 34.58 | < 20 | Probable hollows in the wall of a small impact crater in the floor of a degraded crater to the south of the Northern Plains | If confirmed, would indicate the presence of hollow-forming material in a region that otherwise has no recognised hollows |
| 42.05 | 20.63 | < 20 | Possible hollows around the rim of a small impact crater that is haloed by LRM in moderately-cratered plains | Constrain formation processes for 'dark spots' (*Xiao et al.*, 2013) |
| 45.57 | -37.4 | < 100 | Possible additional hollows in the central uplift of a Mansurian-aged crater that hosts hollows on its floor and an endogenic pit surrounded by a bright, red spectral anomaly in its central peak | Determine the spatial and stratigraphic relationship between explosive volcanism and hollow-formation in the crater |
| 53.75 | 12.77 | < 20 | Possible hollows in the wall of a small crater into the smooth floor fill of an impact crater. This region lacks hollows otherwise. | Indicates the presence of hollow-forming material in this region/in the floor of the larger crater, and its depth |
| 66.11 | -26.71 | < 100 | Possible high density of hollows in the wall and wall slump of an impact crater in smooth plains | Indicates the depth of hollow-forming material beneath the plains surface |

| Longitude (°) | Latitude(°) | Useful resolution (m/px) | Description | Science return |
|---|---|---|---|---|
| 67.56 | 29.51 | < 20 | Possible hollows in the walls of a small crater just inside the margin of some smooth plains | If confirmed, indicates the depth of hollow-forming material beneath the plains surface |
| 68.95 | 73.17 | < 20 | Possible hollows in the rim of a simple crater in the floor of Stieglitz crater in the Northern Plains (only visible in EN0250132980M) | Indicates the presence of hollow-forming material beneath the Northern Plains |
| 125.23 | 72.52 | < 20 | Possible hollows in the rim of a crater in the Northern Plains | Indicates the depth to hollow-forming material beneath the Northern Plains |
| 127.93 | -46.13 | < 100 | Dense group of possible hollows in the ejecta blanket and floor of a ~Mansurian-aged impact crater, which has a bright and red spectral signature | Determine the true nature of the activity in this crater |
| 129.31 | 56.63 | < 20 | Possible hollow at the centre of a low reflectance 'spot' in the wall of a simple crater | Constrain formation processes for 'dark spots' (*Xiao et al.*, 2013) |
| 131.4 | 60.49 | < 20 | Possible hollows in the wall of a small impact crater at the margin of the circum-Caloris plains | Extend the spatial extent of the region of dispersed hollows to the northwest of Caloris |
| 138.51 | 72.72 | < 20 | Possible hollows in the rim of a small crater at the margin of Northern Plains. The crater ejecta has low reflectance beyond the rim at this point | Indicates the depth to a hollow-forming lithology in the region of the Northern Plains |
| 139.63 | -59.47 | < 100 | Possible hollows in a region of abundant putative explosive volcanism, where hollows have not otherwise been recognised | Indicates the presence of hollows in this region of putative explosive volcanic activity |
| 143.46 | 30.59 | < 100 | Several possible hollows on inliers in the Caloris lava infill. | Elucidate the relationship between Caloris and hollow-forming material |
| 150.28 | -20.84 | < 100 | Possible hollows in a small impact crater in a region that otherwise does not have identified hollows | Extend the area in which hollow-forming lithologies are known to be present |

| Longitude (°) | Latitude(°) | Useful resolution (m/px) | Description | Science return |
|---|---|---|---|---|
| 152.17 | 44.34 | < 70 | Possible hollows in the wall of an impact crater in the Caloris interior plains | Constrain the depth to a hollow-forming lithology beneath the Caloris infill |
| 161.73 | -64.87 | < 100 | Potentially extensive hollows in the floor of a southern hemisphere crater | Increase the density of identified hollows in the southern hemisphere |
| 163.62 | 53.59 | < 100 | Potentially extensive hollows in the floor of a crater at the margin of the Caloris exterior plains | Constrain the depth to a hollow-forming lithology beneath the Caloris exterior plains |
| 174.87 | 17.86 | < 100 | Pits that appear too deep to be hollows in the walls of an impact crater at the margins of the Caloris interior plains. There are several areas of LRM around and within the crater | Determine the formation mechanism for these features |
| 176.25 | -46.05 | < 100 | Potentially extensive hollows in the floor of a crater at the margin of the Caloris exterior plains | Constrain the depth to a hollow-forming lithology beneath the Caloris infill |
| 177.97 | 19.62 | < 100 | Possible hollows in the wall of a crater that hosts putative explosive volcanic activity | Determine the relationship between explosive volcanism and hollow-formation |

### F.1.2 What volatile substance is lost in hollow-formation?

Instrument/s: VIHI/MERTIS/STC
Suggested analyses: Investigate the spectral character and implied composition of hollow floors relative to BCFDs and surrounding units
Potential science return: Determine which relatively volatile substance is lost in hollow-formation, potentially aiding investigations into the nature and genesis of LRM.
Useful solar incidence: 20–60°
Useful resolutions: < 200 m/pixel
Rationale code: Hf

**Table F-4 Targets for investigation of flat hollow floors**

| Longitude (°) | Latitude (°) | Name | Description |
|---|---|---|---|
| -142.6 | -4.9 | Theophanes | Crater with dense hollows, with flat floor in the northeast floor. |
| -72.3 | -19 | | Crater with flat-floored hollows in west floor. |
| -56.3 | -38 | Wergeland | Crater with hollows with flat floors |
| -48.8 | -54.4 | | Crater with widespread hollows, MDIS resolution insufficient to determine whether there are flat floors |
| -39.3 | -33.6 | | Crater with dense hollowing, small parts have flat floors |
| -36.4 | 1.2 | Dominici | Crater with dense hollows, potentially with flat-floored regions. |
| -14 | -39.9 | Matabei | Hollows in crater with dark LRM rays. MDIS resolution insufficient to determine whether there are flat floors |
| 5.1 | 25.3 | Kyosai | Crater with dense hollows, flat floors in the north wall. |
| 33.2 | 7.8 | Seuss | Crater with a broad area of flat hollow floor near its wall |
| 119.1 | 27.1 | Raditladi | Basin where MASCS indicates anomalously low UVr for footprints crossing hollows, and where flat hollow floors occur on peak ring |
| 154.5 | 42.4 | Sander | Crater with dense hollows, with flat floors of small areal extent. |

### F.1.3 How does the depth of hollows vary?

Instrument/s: STC/HRIC
Suggested analyses: Investigate the depth of hollow floors through stereo-derived topography and shadow-measurement
Potential science return: Determine whether hollows have different depths in different settings (e.g. crater peak, crater floor) and in different substrates (e.g. pyroclastic, LRM). Estimate the rate of hollow-formation.
Useful solar incidence: 20–70°
Useful resolutions: < 150 m/pixel

**Table F-5 Targets for hollow depth measurement**

| Longitude (°) | Latitude (°) | Name | Description |
|---|---|---|---|
| -148.5 | 3.7 | Tyagaraja | Hollows where there is/is not PPD |
| -138.1 | 40.4 | | Hollows with flat floors in crater wall |
| -39.7 | 50.8 | | Hollows with flat floors at outer crater floor margin |
| -33.4 | 30.5 | | Hollows with clear scarps and flat floors in uneven crater floor |
| -27.1 | -31.5 | | Hollows in wall slumps within a morphologically fresh small crater in the fill of Petrarch basin |
| -14 | -39.9 | Matabei | Hollows in crater with LRM rays - suggests formation in fresh LRM |
| -3.8 | 25.9 | | Hollows in slump from crater wall and around a pit with uneven floor and surrounding spectral anomaly |
| 12.8 | 3.5 | | Hollows in walls and floor of a morphologically fresh crater |
| 22.8 | 35.1 | | Hollows on both LRM crater wall and around pits with uneven floor and surrounding spectral anomalies |
| 33.2 | 7.8 | Seuss | Hollows with flat floors at outer crater floor margin of a morphologically fresh crater |
| 69.2 | 27.4 | | Hollows in and around peak of a morphologically fresh crater |
| 114.4 | 10.7 | Eminescu | Hollows with flat floors on crater floor around peak ring of a morphologically fresh crater |
| 117.9 | -26.5 | Amaral | Hollows in central uplift of a morphologically fresh crater |

| Longitude (°) | Latitude (°) | Name | Description |
|---|---|---|---|
| 119.1 | 27.1 | Raditladi | Flat hollow floors occur on peak ring |
| 123.9 | 41.3 | | Hollows with clear scarps and flat floors in uneven crater floor |
| 125.9 | 57.1 | | Hollows in the LRM ejecta blanket of a morphologically fresh crater |
| 134.8 | 46.1 | Pasch | Flat hollow floors occur on peak ring |
| 154.5 | 42.4 | Sander | Dense hollows on crater floor, some with flat floors |

### F.1.4 What is the relationship between pyroclastic deposits and hollows?

| | |
|---|---|
| Instrument/s: | MIXS/STC/HRIC |
| Suggested analyses: | Investigate stratigraphic relationships between putative pyroclastic deposits (PPDs) and hollows using colour images and high-resolution topography. |
| Potential science return: | Determine whether hollows always post-date explosive volcanism. Determine whether hollows ever form by loss of pyroclastic material |
| Useful solar incidence: | 20–70° |
| Useful resolutions: | Composition: < 2 km/pixel, topography: < 50 m/pixel |
| Rationale code: | Hp |

**Table F-6 Sites at which the relationship of PPDs and hollows can be investigated**

| Longitude (°) | Latitude (°) | Name | Description |
|---|---|---|---|
| -148.6 | 3.8 | Tyagaraja | Crater with large area of hollows, which appear to be more subdued where there is a PPD |
| -60.1 | 27.1 | Praxiteles | Crater with widespread hollows, shallow pits and a large spectral anomaly. |
| -55 | 4.6 | Mistral | Craters with bright spectral anomalies, pits and hollows |
| -48.9 | 15.1 | Lermontov | Crater with widespread hollows, shallow pits and a large spectral anomaly. |
| -30.6 | -55.7 | Hesiod | Line of pits with bright surrounding spectral anomalies and many areas of hollows, adjacent to Kuniyoshi. Putative explosive volcanic activity was probably relatively recent. |
| 87.9 | -41 | Cyllene | Crater at the margin of Rembrandt with a complex association of hollows, a pit and pitted ground |
| 160.5 | 58.8 | Navoi | Large crater-centre pit with hollows around its rim and a surrounding spectral anomaly. |

## F.2 Explosive volcanism

### F.2.1 Composition

#### *F.2.1.1 What is the proportion of juvenile material in putative pyroclastic deposits (PPDs)?*

| | |
|---|---|
| Instrument/s: | MIXS |
| Suggested analyses: | Obtain the composition of PPDs that have a widespread surrounding unit and compare these. |
| Potential science return: | Determine whether the composition of PPDs is that of the products of mantle/crustal melting. Investigate eruption mechanisms. |
| Useful resolutions: | < 1 km/pixel |
| Rationale code: | Pj |

**Table F-7 Targets where there is a widespread PPD**

| Longitude (°) | Latitude (°) | Name | Description |
|---|---|---|---|
| -161.6 | -16.6 | | PPD on the floor of Tolstoj basin |
| -136.6 | -3.4 | AP1 | Second-largest PPD on the planet |
| -37.6 | -57.5 | | Recent PPD at Kuniyoshi crater |
| -31.8 | -58.2 | | PPD near Hesoid proposed to be relative recent |
| -30.7 | -53.4 | | PPD near Hesoid proposed to be relative recent |
| -29.5 | -55.2 | | PPD near Hesoid proposed to be relative recent |
| -28 | -51.8 | | PPD near Hesoid proposed to be relative recent |
| 17.8 | -52.7 | | PPD in LRM region (also analyse other nearby PPDs) |
| 146 | 22.3 | RS-03 | PPD in Caloris volcanic fill |
| 159.4 | 14.3 | | Widespread spectral anomaly in Caloris rim |
| 162.5 | 13.8 | | Widespread spectral anomaly in Caloris rim |

### *F.2.1.2 Do the compositions of PPDs vary consistently on a regional basis?*

Instrument/s: MIXS/MERTIS/VIHI
Suggested analyses: Compare the composition of groups of PPDs that occur within a basin or geochemical unit, or where alignment suggests a similar genesis
Potential science return: Investigate whether the mantle is heterogeneous.
Useful resolutions: < 1 km/pixel
Rationale code: Pr_[region], as below.

**Table F-8 Groups of PPDs that may be geochemically related**

| **High Magnesium Region -Pr_HMR** | | **Caloris basin - Pr_Caloris** | | **Proposed basin "b54" - Pr_b54** | | **Alignment crossing anomalously thick crust - Pr_thick** | |
|---|---|---|---|---|---|---|---|
| **Long (°)** | **Lat (°)** | **Long (°)** | **Lat (°)** | **Long (°)** | **Lat (°)** | **Long (°)** | **Lat (°)** |
| -140.7 | 4.6 | -179.8 | 25.9 | -37.6 | -57.5 | 43.7 | -0.6 |
| -137.9 | 9.4 | -178.5 | 24.5 | -31.8 | -58.2 | 50.8 | 3.9 |
| -137.7 | 4.5 | 138.6 | 28 | -30.7 | -53.4 | 51.8 | -8.4 |
| -136.6 | -3.4 | 144.7 | 28.1 | -29.5 | -55.2 | 52.4 | -9.3 |
| -135.4 | -8.5 | 145.3 | 21.7 | -28 | -51.8 | 54.9 | -11.3 |
| -113.9 | 8.4 | 146.3 | 22.5 | -12.5 | -44.9 | 57 | -5.2 |
| -113.8 | -6.9 | 147.9 | 18.9 | -6.3 | -48.4 | 58.4 | -5.3 |
| -112.4 | 14.9 | 148 | 19.3 | -6.2 | -47.1 | 58.4 | -6.2 |
| -111.7 | 52.5 | 148.1 | 18.3 | 2.2 | -49 | 62.2 | -11.4 |
| -105 | -24.1 | 148.4 | 24.2 | 5.7 | -50 | 65.7 | -15.6 |
| -104.9 | -22.2 | 149.3 | 18.3 | 10.8 | -49.9 | 71.3 | -19.2 |
| -100.6 | 41.1 | 150 | 17.4 | 11.7 | -48.3 | 72.1 | -18.5 |
| -98.5 | 42 | 150.2 | 19.5 | 17.8 | -52.7 | 72.3 | -21.1 |
| -90.8 | -23 | 150.6 | 46.8 | 20.2 | -53.1 | | |
| -89.1 | -21.3 | 150.6 | 18.6 | 23.7 | -68.8 | | |
| -81.9 | -26.7 | 151.3 | 18.7 | | | | |
| -69.2 | 55.9 | 152.6 | 17.6 | | | | |
| -67.8 | 8.5 | 157.1 | 16.7 | | | | |
| -67.5 | 21.8 | 159.4 | 14.3 | | | | |
| -64.3 | 45.5 | 159.6 | 48.7 | | | | |
| -59.4 | 26.6 | 160.8 | 14.5 | | | | |
| -56.1 | 3.7 | 161.2 | 48.4 | | | | |
| -55.6 | 5.4 | 162.5 | 13.8 | | | | |
| -54.2 | 4.3 | 178.1 | 19.5 | | | | |
| -51.4 | 7.5 | 179 | 21.5 | | | | |
| -48.6 | 15.3 | 179.4 | 23.1 | | | | |
| -44.2 | 12.2 | 179.6 | 25.8 | | | | |
| | | 180 | 24.4 | | | | |

### *F.2.1.3 Did the compositions of PPDs vary through time?*

| | |
|---|---|
| Instrument/s: | MIXS/MERTIS/VIHI |
| Suggested analyses: | Compare the compositions of PPDs in spatial groupings that have different apparent surface ages |
| Potential science return: | Determine whether PPDs are sourced from long-lived magma chambers or new batches of magma from the lower crust/mantle |
| Useful resolutions: | < 1 km/pixel |
| Rationale code: | Pct |

**Table F-9 PPDs that may reveal temporal variations in magma composition**

| Longitude (°) | Latitude (°) | Name | Description |
|---|---|---|---|
| -136.6 | -3.4 | AP1 | Large, relatively high reflectance PPD |
| -135.4 | -8.5 | AP2 | Lower-reflectance PPD south of AP1 and in the same terrane |
| 51.2 | 36 | | Smaller PPD aligned with N/NE Rachmaninoff |
| 55.3 | 36.3 | | Smaller PPD aligned with N/NE Rachmaninoff |
| 57.5 | 35.9 | N Rachmaninoff | Surface of PPD appears older than that of NE Rachmaninoff |

### *F.2.1.4 Are PPDs more fractionated than nearby effusive lavas?*

| | |
|---|---|
| Instrument/s: | MIXS/MERTIS/VIHI |
| Suggested analyses: | Compare the composition of PPDs with that of nearby approximately coeval smooth plains units to see if that of the PPDs indicates fractionation of the same parent magma. |
| Potential science return: | Determine whether eruptions become explosive due to a long-duration of magma storage in the shallow subsurface |
| Useful resolutions: | < 1 km/pixel |
| Rationale code: | Pl |

**Table F-10 PPDs near possibly contemporaneous effusive lava deposits**

| Longitude (°) | Latitude (°) | Name | Description |
|---|---|---|---|
| -135.4 | -8.5 | AP2 | PPD that has a similar cratering age as smooth plains to its east |
| -33.5 | 48.4 | Enheduanna | PPD south of the Northern Volcanic Plains |
| -29.5 | 27.1 | Geddes | PPD south of a region of smooth plains |
| 64 | 36 | NE Rachmaninoff | PPD with smooth plains to its north and east, and in the central floor of Rachmaninoff basin to the south |

### F.2.2 How much material was ejected?

| | |
|---|---|
| Instrument/s: | STC |
| Suggested analyses: | Calculate the volume of material forming a PPD |
| Potential science return: | Calculate erupted magma volume and constrain models for melt-generation, transport and storage |
| Useful resolutions: | < 100 m/pixel horizontal, < 10 m vertical |
| Rationale code: | Pv |

**Table F-11 Sites where pyroclastic deposit volume may be amenable to calculation**

| Longitude (°) | Latitude (°) | Name | Description |
|---|---|---|---|
| -113.8 | -6.9 | | PPD on flat crater floor with possible circum-vent relief |
| -111.7 | 52.5 | To Ngoc Van | PPD on flat crater floor with possible circum-vent relief |
| -105 | -24.1 | Rūmī | PPD on flat crater floor with possible circum-vent relief |
| -48.9 | 15.1 | Lermontov | Large-scale PPD on flat crater floor with relief around an endogenic pit in the NE. |
| -2.8 | 17.5 | Hemingway | PPD on flat crater floor with possible circum-vent relief |
| 64 | 36 | NE Rachmaninoff | Large-scale PPD in non-crater setting with circum-vent relief |
| 72.3 | -21.1 | Capote | PPD on flat crater floor with possible circum-vent relief |
| 111.4 | -40.2 | Beckett | PPD on crater floor with relief adjacent to an endogenic pit |
| 115.3 | -41.9 | | PPD on crater floor with relief adjacent to an endogenic pit |
| 146 | 22.3 | RS-03 | PPD with some apparent relief around an endogenic pit in the SW of the Caloris basin floor |

### F.2.3 When did explosive volcanism occur?

| | |
|---|---|
| Instrument/s: | HRIC,STC |
| Suggested analyses: | Calculate model age of PPDs through crater counting. Investigate relative ages where an endogenic pit appears to be less degraded and thus significantly more recent than the host crater. Investigate possible local controls on relatively recent explosive volcanism. |
| Potential science return: | Constrain models for Mercury's secular cooling and investigate possible causes of late-stage melting (e.g. crustal thickening and basal melting). Determine whether crater-formation could have directly triggered explosive volcanism. |
| Useful resolutions: | < 100 m/pixel |
| Useful solar incidence: | 20–70° |
| Rationale code: | Pt |

**Table F-12 Targets for PPD dating**

| Longitude (°) | Latitude (°) | Name | Description |
|---|---|---|---|
| -112.4 | 14.9 | Glinka | PPD centred on an endogenic pit that appears more morphologically-fresh than the host crater |
| -105 | -24.1 | Rūmī | PPD with apparent relief around its central endogenic pit. Relationship of activity with thrust faulting is unclear. |
| -55.6 | 5.4 | | Bright spectral anomaly centred on an endogenic pit that appears fresher than the host crater |
| -54.2 | 4.3 | Mistral | Bright spectral anomaly centred on an endogenic pit that appears fresher than the host crater |
| -48.6 | 15.3 | Lermontov | Large-scale PPD that appears particularly thick around NE endogenic pit |
| -33.5 | 48.4 | Enheduanna | PPD within crater crossed by a thrust fault. Relationship of activity with thrust faulting is unclear. |
| -31.8 | -58.2 | Hesiod | Spectral anomaly near Kuniyoshi that is similarly bright and has a fresh-looking vent, but is within craters that are more degraded than Kuniyoshi |
| -30.7 | -53.4 | Hesiod | Spectral anomaly near Kuniyoshi that is similarly bright and has a fresh-looking vent, but is within craters that are more degraded than Kuniyoshi |
| -29.5 | -55.2 | Hesiod | Spectral anomaly near Kuniyoshi that is similarly bright and has a fresh-looking vent, but is within craters that are more degraded than Kuniyoshi |
| -29.5 | 27.1 | Geddes | PPD within crater crossed by a thrust fault. Relationship of activity with thrust faulting is unclear. |
| -28 | -51.8 | Hesiod | Spectral anomaly near Kuniyoshi that is similarly bright as Kuniyoshi but within a more degraded host crater than Kuniyoshi |
| -13.1 | -6.1 | | PPD within a thrust-faulted crater. Explosive volcanism potentially post-dates thrusting |
| 21.5 | 32.4 | | PPD in a morphologically-fresh crater |
| 33 | 8.2 | Seuss | PPDs on the ejecta blanket of a morphologically-fresh crater that may have formed during crater-formation |
| 38.8 | -52.9 | Donelaitis | Crater in which PPD appears to post-date either faulting or effusive volcanism. Endogenic pits of similar morphological freshness as host crater |
| 43.7 | -0.6 | | PPD around a morphologically-fresh endogenic pit |
| 144.2 | -56.4 | | Bright spectral anomaly around a morphologically-fresh endogenic pit on a cratered plains unit |

### F.2.4 Does explosive volcanism predate effusive volcanism at any site?

| | |
|---|---|
| Instrument/s: | HRIC,STC |
| Suggested analyses: | Examine regions where smooth plains abuts a PPD to determine stratigraphic relationship |
| Potential science return: | Determine the relationship between volatile-rich and -poor magmas locally and globally. |
| Useful resolutions: | < 100 m/pixel |
| Useful solar incidence: | 20–70° |
| Rationale code: | Ppl |

**Table F-13 Targets where smooth plains abut a PPD**

| Longitude (°) | Latitude (°) | Name |
|---|---|---|
| 64 | 36 | NE Rachmaninoff |
| No apparent ambiguity at any other site, but this question should be kept in mind at all other sites. | | |

### F.2.5 What does the distribution of explosive volcanism tell us about the subsurface?

| | |
|---|---|
| Instrument/s: | ISA/MORE/MIXS |
| Suggested analyses: | Derive crustal thickness, gravity anomaly and compositional data for regions with many sites of putative explosive volcanism that may indicate the presence of ancient basins |
| Potential science return: | Reveal the early impact history of Mercury, constrain rates of basin relaxation, determine whether regional groupings of explosive volcanism correlate with crustal setting and so can be used as a surface indication of it |
| Useful resolutions: | < 200 km/pixel |
| Rationale code: | Pss |

**Table F-14 Possible ancient impact basins where subsurface properties require investigation**

| Longitude (°) | Latitude (°) | Description |
|---|---|---|
| -93 | 17 | The High-Magnesium region, potentially an ancient impact basin with sites of explosive volcanism at margins |
| 28 | -79 | Region of anomalously thin crust that could be impact-induced but lacks other evidence for being one or more basin/s |
| 85 | 15 | Region of anomalously thick crust crossed by an unexplained alignment of PPDs and endogenic pits |
| 178 | -48 | Region that appears to be an ancient basin but has above-average crustal thickness in its southern interior on current evidence |

### F.2.6 Volatile-related landforms where genesis is uncertain

#### *F.2.6.1 Spectrally-red pitted ground*

| | |
|---|---|
| Instrument/s: | MIXS/MERTIS/VIHI/STC |
| Suggested analyses: | Investigate whether the composition differs from PPDs and/or from that of the lava deposit it occurs within (if applicable). Investigate stratigraphic relationship with any associated hollows. |
| Potential science return: | Determine whether the terrain forms through degassing of hollow-forming volatiles through lava, by explosive volcanism, or by a third process. |
| Useful solar incidence: | 20–70° |
| Useful resolutions: | Composition: < 2 km/pixel, topography: < 50 m/pixel |
| Rationale code: | SRPg |

**Table F-15 Targets for investigation of spectrally-red pitted ground**

| Longitude (°) | Latitude (°) |
|---|---|
| -179 | 25.6 |
| -62 | -46.6 |
| -53.2 | 18.5 |
| 83.3 | 52.7 |
| 92.3 | -37.3 |
| 58.7 | 25.9 |
| 20.1 | -8.7 |
| 145.1 | -13.2 |
| 122.4 | 58.8 |
| -74.8 | -21.3 |
| -93.4 | 25.2 |
| -91.8 | 50.8 |
| -65.8 | -58.9 |
| -68.6 | 43.8 |
| -97.6 | 32.8 |
| -37.7 | 0.4 |
| 88 | -41.2 |
| 25.9 | -61.5 |
| 129.5 | 72.5 |
| -71.2 | -47.3 |
| 156.8 | -20.7 |
| 152.4 | 17.9 |
| 179.6 | -40.8 |

### *F.2.6.2 Uneven pits in ejecta blankets*

| | |
|---|---|
| Instrument/s: | MIXS/STC/HRIC |
| Suggested analyses: | Investigate composition of spectral anomaly and the morphology of these landforms and their stratigraphic relationship with hollows |
| Potential science return: | Determine whether these form by explosive volcanism, by degassing (potentially of hollow-forming volatiles) through hot crater materials, or by a third process |
| Useful solar incidence: | 20–70° |
| Useful resolutions: | Composition: < 2 km/pixel, topography: < 50 m/pixel |
| Rationale code: | Pej |

**Table F-16 Targets for investigation of uneven pits in ejecta blankets**

| Longitude (°) | Latitude (°) |
|---|---|
| 21.5 | 32.4 |
| 33 | 8.2 |
| -4.2 | 26 |
| 23.1 | 35.5 |
| 23.9 | 37.3 |
| 105.8 | -43.7 |
| 117.8 | 26.3 |
| -6.2 | -47.1 |
| 179.4 | 23.1 |
| 152.6 | 17.6 |
| -51.4 | 7.5 |
| -69.2 | 55.9 |